# From detectors towards systems: enabling clinical TOF-PET with monolithic scintillators

Borghi, G.

**DOI**
10.4233/uuid:e3f9f224-b5fc-4283-85b3-fc8b7d64b5bf

**Publication date**
2021

**Document Version**
Final published version

**Citation (APA)**
Borghi, G. (2021). *From detectors towards systems: enabling clinical TOF-PET with monolithic scintillators*. https://doi.org/10.4233/uuid:e3f9f224-b5fc-4283-85b3-fc8b7d64b5bf

# From detectors towards systems: enabling clinical TOF-PET with monolithic scintillators

# From detectors towards systems: enabling clinical TOF-PET with monolithic scintillators

## Dissertation

for the purpose of obtaining the degree of doctor
at Delft University of Technology,
by the authority of the Rector Magnificus, Prof. dr. ir. T.H.J.J. van der Hagen,
chair of the Board for Doctorates,
to be defended publicly on
Wednesday 22 December 2021 at 15.00 o’clock

by

**Giacomo BORGHI**

Dottore Magistrale in Fisica,
Università degli Studi di Milano-Bicocca, Milano, Italy,
born in Cantù, Italy.

This dissertation has been approved by the promotors.

Composition of the doctoral committee:

| | |
|---|---|
| Rector Magnificus, | chairperson |
| Prof. dr. ir. H. van der Graaf, | Delft University of Technology, promotor |
| Dr. ir. D.R. Schaart, | Delft University of Technology, promotor |
| | |
| *Independent members:* | |
| Prof. dr. ing. C. E. Fiorini, | Politecnico di Milano, Italy |
| Prof. dr.-ing V. Schulz, | RWTH Aachen University, Germany |
| Prof. dr. P. Dorenbos, | Delft University of Technology |
| Prof. dr. ir. A.J. van der Veen, | Delft University of Technology |
| Dr. T. Frach, | Philips Digital Photon Counting, Germany |

The research presented in this thesis was performed at the Department of Radiation Science & Technology, Faculty of Applied Sciences, Delft University of Technology, The Netherlands.
The research was funded by the European Commission through the EU FP7 project SUBLIMA, Grant Agreement 241711

*Printed by:* Proefschriftmaken.nl

*Cover design:* Giacomo Borghi and Lodoviga Giudice

ISBN 978-94-6423-587-6

An electronic version of this dissertation is available at
http://repository.tudelft.nl/.

*Better late than never.*

Popular wisdom

# Contents

# Summary

Nuclear medical imaging (NMI) is the branch of nuclear medicine aimed at imaging the *in-vivo* distribution of specific compounds labeled with radioactive elements (radiotracers) inside animals (preclinical applications) or patients (clinical applications). These compounds are developed to follow metabolic pathways or for binding to receptor systems of interest and are administered to the imaged subject to obtain diagnostic information, such as the functionality of certain organs or the presence of tissues with altered metabolism, e.g. tumors or inflamed tissues. The estimation of the radiotracer distribution is obtained by externally detecting the radiations emitted by the radioactive element attached to the tracer.

Positron emission tomography (PET) is a NMI modality based on radiotracers labelled with a $\beta^+$ emitter. During the decay, the isotope emits a positron that almost immediately annihilates with an electron close to its emission point, obtaining as final products two 511 keV gamma rays emitted at an angle of $\sim$180°. The PET imaging technique is based on the simultaneous detection of these two gamma rays, since the physical constraints of the process allow PET systems to localize the positron annihilation point on the line connecting the interaction points of the two gamma rays (line of response, LOR). PET scanners are usually complete rings of detectors surrounding the imaged subject, so that coincidences along many different directions (projections) can be acquired simultaneously.

The diagnostic value of PET images is determined by how faithfully the tracer distribution can be reconstructed. Spatial resolution, contrast and noise level are physical properties of the images that are used to characterize their quality. Each of these properties is limited by different factors, some of which are intrinsically connected to the physics of $\beta^+$ decay and the subsequent positron annihilation reaction, whereas others are related to the performance of PET detectors, the scanner design, and/or the image reconstruction process.

In particular, image spatial resolution is limited by the positron range, the photon acollinearity (more important for large-bore scanners), and the detector spatial resolution, which also includes their capability to estimate the depth of interaction (DOI). The image contrast and noise are instead dependent on the number of true and false coincidence events registered by the system. A larger number of true events reduces the statistical noise and therefore improve image SNR, whereas false events (random and scatter events) introduce an undesired background and additional statistical fluctuations.

The number of registered true events is largely determined by the detector sensitivity, the scanner geometry, and the detector dead time. The number of false events is instead influenced by the detector energy and timing resolution and by the geometry of the scanner and of the imaged object. Good energy resolution allows the system to better discriminate scattered events, whereas good timing

resolution make it possible to reduce the width of the coincidence window and therefore reduce the number of random events.

A technique that can further improve the image noise is the time-of-flight (TOF) technique: if a PET scanner can measure with sufficient precision the times of interaction of two gamma rays in coincidence, the difference between these times can be used to estimate the position of an annihilation event on its LOR. This information can then be used during image reconstruction to constrain the positron annihilation position on a narrower region on the LOR and enables PET systems to reduce image statistical noise. The better the detector timing resolution, the higher the gain in the image SNR.

Scintillation detectors are a key component in PET systems since their characteristics largely determine the final performance of the scanners. The most important detector characteristics are sensitivity, spatial resolution (including DOI estimation capability), coincidence resolving time, and energy resolution. The influence of these properties on the final quality of the images depends on the geometry of the scanner and of the imaged object. Therefore, different detector optimizations may have to be made depending on the application.

Currently, practically all clinical and pre-clinical PET scanners are built using detectors based on pixelated scintillation crystal arrays, whose performance are determined by crystal pitch, crystal thickness, crystal and reflector arrangement, number of crystal layers, coupling scheme of the crystal array with the photosensor, etc. However, the optimization of pixelated-detector architectures for spatial and DOI resolution often causes a degradation of the timing and energy resolution.

An alternative to pixelated detectors is represented by monolithic scintillator detectors, which are based on wide unsegmented crystals read out by pixelated photosensors. In these detectors, the position of interaction is estimated from the light distribution caused by a scintillation event on the photosensor pixels. The main advantage of these detectors is that they have a faster and more efficient light collection compared to pixelated detectors, since fewer reflections are usually needed to collect all photons. Therefore, they can obtain at the same time excellent timing performance, high spatial resolution, DOI capability and good energy resolution.

At the beginning of this project, it had already been demonstrated that monolithic detectors could provide good spatial resolution (~1 mm in 10-mm-thick crystals), DOI estimation, and excellent CRTs (~200 ps in 20-mm-thick crystals). However, no one had demonstrated yet the possibility to combine all these characteristics in a single detector with high sensitivity. Moreover, these detectors required lengthy calibration procedures and computationally demanding statistical algorithms to estimate the position of interaction, both of which hampered their use in real scanners.

The research conducted in the scope of this thesis is aimed at demonstrating that monolithic scintillator detectors can be practically calibrated and operated and that they are a suitable alternative to pixelated detectors in clinical PET systems, both for whole-body and for organ-dedicated high-resolution applications. A further goal of this work is to characterize the performance of monolithic detectors not only at the single-detector level but also in a tomographic setup, in order to demonstrate their imaging capabilities in whole-body TOF-PET systems.

A first improvement of the calibration procedures is presented in Chapter 2, in which a new calibration method for k-nearest neighbor (k-NN) position-estimation algorithm is experimentally tested and validated for the first time. The traditional calibration procedure used for most of the statistical position-estimation algorithms is based on the acquisition of reference events on a fine 2D grid of reference positions using a narrow pencil beam. The new method is based on fan-beam irradiation, which can provide an event-acquisition rate much higher than pencil beam irradiation. The new method is tested with two monolithic detectors having a footprint of 16 mm × 16 mm and a thickness of 10 mm and 20 mm. In both cases, the performance of the new method is shown to be equivalent to the previous method based on pencil-beam calibration, enabling the detectors to achieve outstanding spatial resolutions of ~1.1 mm FWHM and of ~1.5 mm FWHM for the 10 mm and 20 mm thick detectors, respectively. Moreover, the new calibration method proved to be more than one order of magnitude faster than the previous one and can potentially be sped up by another order of magnitude with simple modifications of the calibration setup.

The detector calibration procedures are further revised and optimized in Chapter 3, in which the techniques used to calibrate the algorithms for estimating the position of interaction (DOI included) and the time of interaction are modified so that the complete detector calibration can be performed by means of fan-beam irradiations and flood irradiations only.

Further improvements of the techniques to operate the monolithic detectors are also introduced in Chapter 3. First, the k-NN position-estimation method is revised and accelerated, introducing an analytical algorithm that pre-selects only the most useful events from the reference dataset before the k-NN algorithm is applied. This modification reduces the computational burden for position estimation by more than two orders of magnitude compared to the previously used k-NN algorithm. Then, a new technique is presented that allows the detector to use also the events in which the light signals or the timestamps of some photosensor pixels are missing (e.g. due to dead time), so as to further increase system sensitivity.

Still in Chapter 3, all these methods are then applied to a large monolithic detector based on a wide monolithic crystal (32 mm × 32 mm × 22 mm, LYSO) read out from the back side by a DPC digital SiPM array. When only events with complete light distributions are considered, the detector achieves a spatial resolution of 1.7 mm FWHM, an average DOI resolution of 3.7 mm FWHM, a CRT of 214 ps and an energy resolution of ~9.9%. The performance of the detector are also characterized when events with a variable number of missing pixels are used. If events missing up to 25% of the pixel data are accepted, the detector sensitivity improves accordingly, while the other performance parameters deteriorate by less than 2%. This monolithic detector in back-side-readout (BSR) configuration therefore shows an excellent match with the requirements of whole-body clinical TOF-PET imaging, demonstrating a unique combination of characteristics such as high sensitivity, excellent timing and energy resolution, good spatial resolution, DOI estimation capability, ease of assembly, and cost comparable to (or lower than) pix-

elated detectors.

In Chapter 4, the same calibration and characterization methods presented in Chapter 3 are applied to an ultra-high performance monolithic detector, which is developed for possible applications in high-resolution PET scanners, such as pediatric scanners and dedicated brain or breast scanners. This detector is based on a monolithic 32 mm × 32 mm × 22 mm LYSO crystal and on two DPC arrays, which read out the crystal from the front and back surface in the so-called dual-sided readout (DSR) configuration. The detector achieves unprecedented performance for such large monolithic crystals, demonstrating a spatial resolution of ~1.1 mm FWHM, a DOI resolution of ~2.4 mm FWHM, an energy resolution of 10.2% FWHM, and a coincidence resolving time of 147 ps FWHM.

Lastly, in Chapter 5, the imaging capabilities of the BSR monolithic detector are investigated in a 70-cm-diameter PET geometry. Two complete PET modules (2 × 2 detectors) are developed, calibrated and employed in a tomographic setup representative of a whole-body clinical scanner. The fully automated setup, based on two coaxially rotating arms and a central rotating phantom table, sequentially acquires all possible LORs of a complete detector ring, using a step-and-shoot acquisition approach. During a complete tomographic acquisition of a $^{22}$Na point source, the system demonstrates a CRT of ~212 ps and an average energy resolution of 10.2%. The system spatial resolution is quantitatively assessed imaging a $^{22}$Na point source at different radial distances from the system axis, obtaining excellent radial and tangential resolutions of ~2.9 mm at the center of the imaged region. Thanks to the DOI estimation capability of the monolithic detectors, the resolution remains almost constant in the whole FOV: at a radial distance of 20 cm, the radial and tangential spatial resolutions are 3.2 mm and 4.0 mm, respectively, whereas at 25 cm they become 3.3 mm and 4.7 mm. The system spatial resolution is also qualitatively assessed by imaging a high-resolution Derenzo-like phantom at different locations within the FOV. The images show that the system is able to resolve 3-mm-diameter hot rods up to 25 cm radial distance.

In conclusion, the results presented in this thesis demonstrate that monolithic scintillator detectors can be practically calibrated and operated in clinical PET systems. Moreover, these detectors can outperform state-of-the-art pixelated detectors for whole-body and organ-dedicated applications and can achieve superior imaging performance compared to current state-of-the-art whole-body scanners. Therefore, monolithic scintillator detectors could be the enabling technology to develop the next generation of clinical PET scanners, both for whole-body or high-resolution systems.

# Samenvatting

Nucleaire medische beeldvorming (NMB) is de tak van nucleaire geneeskunde die is gericht op *in-vivo* beeldvorming van de distributie van specifieke met radionucliden gelabelde tracers (radiofarmacon) in zowel dieren (pre-klinische toepassingen) als patiënten (klinische toepassingen). Deze tracers zijn zo ontworpen dat ze metabole routes volgen of aan bepaalde receptoren binden. Ze worden toegediend met als doel het vergaren van diagnostische informatie, zoals de functionaliteit van bepaalde organen of de aanwezigheid van weefsel met een afwijkend metabolisme, zoals tumoren of ontstekingen. Met behulp van een externe detector die de door de radionuclide uitgezonden straling detecteert, wordt een schatting van de distributie van het radiofarmacon bepaald.

Positronemissietomografie (PET) is een NMB modaliteit gebaseerd op radionucliden die bij verval een positron uitzenden ($\beta^+$-emitters). Dit uitgezonden positron annihileert vrijwel meteen met een elektron tot twee gammafotonen van 511 keV die in vrijwel exact tegenovergestelde richting worden uitgezonden. De PET-techniek is gebaseerd op de simultane detectie van deze twee gammafotonen, waarbij de annihilatie dan op de lijn tussen de twee detectiepunten (LOR, line of response) heeft plaatsgevonden. Een PET-detector bestaat typisch uit complete ringen van detectoren die het af te beelden object geheel omsluiten. Dankzij deze geometrie kunnen coïncidenties (*events*) in veel verschillende richtingen (projecties) tegelijk worden vastgelegd.

De diagnostische waarde van PET-beelden hangt af van hoe getrouw de distributie van het radiofarmacon kan worden gereconstrueerd. De kwaliteit van de beelden wordt uitgedrukt in fysieke eigenschappen zoals de spatiële resolutie, het contrast en het ruisniveau. Elk van deze eigenschappen kent beperkende factoren, waarvan sommige intrinsiek zijn aan de fysica van bètaverval en de daaropvolgende positron-annihilatie, en anderen gerelateerd zijn aan de prestaties van de PET detectoren, het ontwerp van de PET-scanner en/of het proces van beeldreconstructie.

De spatiële resolutie van PET-beelden hangt in het bijzonder af van het positronbereik, de acolineariteit van de annihilatiefotonen (belangrijker naarmate de diameter van de PET-scanner groter is) en de spatiële resolutie van de detector. Onder dat laatste valt ook de nauwkeurigheid waarmee de diepte van de interactie in de detector kan worden bepaald (DOI, depth of interaction). Het contrast en de ruis van het beeld hangen af van het aantal *true* en *false events* die het systeem registreert. Een groter aantal *trues* leidt tot minder statistische ruis en, daardoor, een betere signaal-ruisverhouding. False events (toevallig en door verstrooiing) leiden tot een verhoogde achtergrond en additionele statistische fluctuaties.

Het aantal geregistreerde trues hangt grotendeels af van de gevoeligheid van de detector, de geometrie van de scanner en de dode tijd van de detector. Het aantal false events wordt bepaald door zowel de energie- en tijdsresolutie van de detectoren als door de geometrie van de scanner en het af te beelden object. Met een goede energieresolutie kan het systeem verstrooiing beter onderscheiden. Met een goede tijdsresolutie kan het tijdsinterval voor coïncidentie worden teruggebracht, waardoor er minder toevallige coïncidenties zullen worden geregistreerd.

Een andere techniek voor het verminderen van beeldruis is de zogenoemde time-of-flight (TOF) techniek: Als een PET-scanner met voldoende nauwkeurigheid de tijdstippen van interactie van de twee gammafotonen kan bepalen, dan kan het tijdsverschil tussen deze twee interacties gebruikt worden om de positie van de annihilatie langs de LOR te schatten. Tijdens de beeldreconstructie kan deze informatie worden gebruikt om statistische beeldruis te reduceren. Hoe beter de tijdsresolutie, hoe hoger de signaal-ruisverhouding.

Scintillatiedetectoren behoren tot de belangrijkste componenten van een PET-systeem omdat hun karakteristieken voor een groot deel de uiteindelijke prestaties van het systeem bepalen. De belangrijkste karakteristieken van deze detectoren zijn hun gevoeligheid, spatiële resolutie (inclusief DOI), energieresolutie en *coincidence resolving time* (CRT). De mate waarin deze eigenschappen de uiteindelijke beeldkwaliteit beïnvloeden hangt af van de geometrie van de scanner en van het af te beelden object. De optimale detectorgeometrie hangt dus af van de uiteindelijke toepassing.

Op dit moment maken vrijwel alle klinische en pre-klinische PET-scanners gebruik van detectoren die bestaan uit gepixelleerde arrays van scintillatiekristallen. De prestaties van deze arrays hangen af van de hartafstand tussen aangrenzende kristallen, de kristaldikte, de rangschikking van de kristallen en reflectoren, het aantal kristallagen, de koppeling tussen kristalarray en fotosensor, enz. Helaas gaat de optimalisatie van het ontwerp van dit type detectoren op bijvoorbeeld spatiële resolutie (en DOI) al snel ten koste van de tijds- en energieresolutie, en vice-versa.

Een alternatief ten opzichte van gepixelleerde detectoren is het gebruik van monolithische scintillatiedetectoren – gebaseerd op brede, ongesegmenteerde kristallen die worden uitgelezen met gepixelleerde fotosensoren. In deze detectoren wordt de positie van interactie van het foton binnen het kristal geschat aan de hand van de verdeling van de scintillatiefotonen over de fotosensorpixels. Het belangrijkste voordeel van deze detectoren is de snellere en efficiëntere detectie van de scintillatiefotonen, omdat deze typisch minder vaak hoeven te reflecteren vóór detectie. Deze detectoren kunnen daardoor een uitmuntende tijdsresolutie combineren met een hoge spatiële resolutie, de mogelijkheid om de DOI te bepalen, en een goede energieresolutie.

Bij aanvang van dit project was al aangetoond dat monolytische detectoren in staat zijn tot een goede spatiële resolutie ($\sim$1 mm in kristallen met een dikte van 10 mm), schatting van de DOI, en uitmuntende CRTs ($\sim$200 ps in kristallen met een dikte van 20 mm). Tot nu toe heeft echter niemand de combinatie van deze karakteristieken laten zien in een kristal met hoge gevoeligheid. De eerste detectorprototypes vereisten bovendien een tijdrovende kalibratieprocedure en het gebruik van rekenintensieve statistische algoritmes voor het schatten van de interactiepositie. Beide nadelen beperkten de mogelijkheden tot gebruik ervan in echte (commerciële) scanners.

Het onderzoek dat ten grondslag lag aan dit proefschrift was erop gericht om aan te tonen dat monolithische kristallen op een praktisch-acceptabele manier kunnen worden gekalibreerd en gebruikt en dat ze daarom een bruikbaar alternatief bieden voor gepixelleerde detectoren in klinische PET-systemen – bij zowel *whole-body* als orgaanspecifieke toepassingen. Een tweede doel was om de prestaties van deze kristallen niet alleen in een *stand-alone* setting te karakteriseren, maar juist ook in een tomografische setup – om zo hun beeldvormende potentie aan te tonen voor TOF-PET-systemen voor klinische whole-body scans.

In Hoofdstuk 2 wordt een eerste verbetering in de kalibratieprocedure beschreven. Hierin wordt voor het eerst een nieuwe kalibratiemethode voor een *k-nearest neighbor* (k-NN) positiebepalings-algoritme experimenteel getest en gevalideerd. De kalibratiemethode die traditioneel gezien het meest gebruikt wordt voor statistische positiebepalings-algoritmes is gebaseerd op de acquisitie van een fijnmazig 2D rooster van referentiedata met behulp van een smalle *pencil beam*. De nieuwe methode maakt gebruik van bestraling met een "waaiervormige" bundel (*fan-beam*), waarmee de acquisitiesnelheid veel hoger ligt. De nieuwe methode is getest voor twee monolitische kristallen met elk een oppervlakte van 16 mm × 16 mm en een dikte van respectievelijk 10 mm en 20 mm. De nieuwe methode laat in beide gevallen prestaties zien die vergelijkbaar zijn met de kalibratiemethode gebaseerd op pencil-beams, resulterend in een uitstekende spatiële resolutie van ∼1,1 mm FWHM en ∼1,5 mm FWHM voor respectievelijk de 10 mm en 20 mm dikke detector. De nieuwe kalibratiemethode was bovendien een orde van grootte sneller dan de oude methode en kan zo mogelijk nog een orde van grootte worden versneld met enkele eenvoudige aanpassingen aan de kalibratie-setup.

De kalibratieprocedures voor de detector worden in Hoofdstuk 3 verder aangepast en geoptimaliseerd. Dit hoofdstuk beschrijft aangepaste technieken voor het kalibreren van de algoritmes die gebruikt worden voor het schatten van de interactiepositie (inclusief DOI) en het tijdstip van interactie. Dankzij deze aanpassingen kan de gehele detector worden gekalibreerd met uitsluitend gebruik van fan-beams en brede bundels (*flood beams*).

Hoofdstuk drie behandelt ook verbeteringen die betrekking hebben op het gebruik van monolitische detectoren. Allereerst wordt de k-NN positiebepalingsmethodiek aangepast en versneld. Hiervoor introduceren we een analytisch algoritme dat alleen de meest nuttige coïncidenties uit de referentie-dataset selecteert voordat het k-NN algoritme wordt toegepast. Deze aanpassing vermindert de benodigde rekenkracht voor positiebepaling met meer dan twee ordes van grootte in vergelijking met het eerder gebruikte k-NN algoritme. Daarna wordt een nieuwe techniek gepresenteerd waarmee de detector ook gebruik kan maken van coïncidenties waarbij de data van enkele fotosensorpixels ontbreekt (ten gevolge van bijvoorbeeld dode tijd) om zo de gevoeligheid van het systeem nog verder te vergroten.

Al deze methoden worden vervolgens (nog steeds in Hoofdstuk 3) toegepast op een grote monolithische detector gebaseerd op een 32 mm × 32 mm × 22 mm LYSO kristal, aan de achterkant uitgelezen door een digitale SiPM array. Als alleen coïncidenties zonder ontbrekende pixels worden meegenomen dan behaalt de detector een spatiële resolutie van 1,7 mm FWHM, een gemiddelde DOI-resolutie van 3,7 mm FWHM, een CRT van 214 ps en een energieresolutie van ~9,9%. De prestaties van de detector zijn ook gekarakteriseerd in het geval dat coïncidenties met een variabel aantal ontbrekende pixels worden meegenomen. Als alle events worden meegenomen waarbij tot 25% van de pixeldata ontbreekt, dan verbetert de detectorgevoeligheid dienovereenkomstig terwijl de overige prestatie-parameters met minder dan 2% verslechteren. De configuratie van een monolitische detector met *backside readout* (BSR) laat een unieke combinatie van karakteristieken zien, zoals een hoge gevoeligheid, uitstekende tijds- en energieresolutie, goede spatiële resolutie, de mogelijkheid tot het schatten van de DOI, eenvoudig assemblage en kosten die vergelijkbaar zijn met (of lager dan) die van gepixelleerde detectoren. Deze detector matcht dan uitstekend met de eisen die worden gesteld aan whole-body klinische TOF-PET.

In Hoofdstuk 4 worden de methodes voor kalibratie en karakterisatie (zoals gepresenteerd in Hoofdstuk 3) toegepast op een zeer hoogwaardige monolitische detector, speciaal ontworpen voor mogelijke toepassing in hoge-resolutie PET-scanners – zoals pediatrische scanners en scanners specifiek voor beeldvorming van de hersenen of borsten. Deze detector is gebaseerd op een monolytisch 32 mm × 32 mm × 22 mm LYSO-kristal en twee digitale SiPM arrays die het kristal aan zowel de voor- als achterzijde uitlezen in een zogenoemde *dual-sided readout* (DSR) configuratie. Deze detector behaalt ongekende prestaties voor zulke grote monolitische kristallen; een spatiële resolutie van ~1,1 mm FWHM, een DOI-resolutie van ~2,5 mm FWHM, een energieresolutie van 10,2% FWHM en een CRT van 147 ps FWHM.

In hoofdstuk 5 worden tenslotte de beeldvormingskarakteristieken van de BSR monolitische detector onderzocht in een 70-cm-diameter PET-geometrie. Hiervoor zijn twee complete PET-modules (2 × 2 detectoren) ontwikkeld, gekalibreerd en toegepast in een tomografische setup die representatief is voor een whole-body klinische scanner. De volledig geautomatiseerde setup, gebaseerd op twee in het coaxiale vlak roterende armen en een centraal-roterend fantoomplatform, vergaart met een *step-and-shoot* aanpak sequentieel alle mogelijk LORs van een complete detectorring. Bij de complete tomografische acquisitie van een $^{22}$Na puntbron vertoont het systeem een CRT van ~212 ps en een gemiddelde energieresolutie van 10,2%. De spatiële resolutie van het systeem is kwantitatief bepaald met een $^{22}$Na-puntbron op verschillende radiale afstanden van de centrale as van het systeem. Hierbij zijn uitstekende radiale en tangentiele resoluties van ~2,9 mm behaald, in het centrum van het beeldvormingsgebied. Dankzij het vermogen van deze monolitische detectoren tot het schatten van de DOI blijft deze resolutie vrijwel constant over het gehele field-of-view. Op een radiale afstand van 20 cm zijn de radiale en tangentiële spatiële resolutie respectievelijk 3,2 mm en 4,0 mm. Op een afstand van 25 cm zijn deze respectievelijk 3,3 mm en 4,7 mm. De spatiële resolutie van het systeem is eveneens kwalitatief bepaald door een beeldvormende test met een hoge-resolutie Derenzo-achtig fantoom op verschillende posities in het field-of-view. Hiermee is aangetoond dat het systeem *hot rods* met een diameter van 3 mm tot op een radiale afstand van 25 cm goed kan onderscheiden.

De in dit proefschrift gepresenteerde resultaten tonen aan dat monolithische scintillatordetectoren op een praktisch-acceptabele manier kunnen worden gekalibreerd en toegepast in klinische PET-systemen. Deze detectoren kunnen bovendien state-of-the-art gepixelleerde detectoren overtreffen in zowel whole-body als orgaanspecifieke toepassingen en ze kunnen een superieure beeldkwaliteit bereiken in vergelijking met huidige state-of-the-art whole-body scanners. Monolithische scintillatordetectoren kunnen daarom de *enabling* technologie zijn voor het ontwikkelen van de volgende generatie klinische PET-scanners, voor zowel whole-body als hoge-resolutie systemen.

# List of abbreviations

| | |
|---|---|
| **APD** | Avalanche photodiodes |
| **BP** | Back-projection |
| **BSR** | Back-side readout *or* Back-sided readout |
| **CDF** | Cumulative distribution function |
| **CFD** | Constant fraction discrimination |
| **COG** | Center of gravity |
| **CRT** | Coincidence resolving time |
| **CT** | Computed tomography |
| **DCR** | Dark count rate |
| **DOI** | Depth of interaction |
| **DPC** | Digital photon counter |
| **dSiPM** | Digital silicon photo-multiplier |
| **DSR** | Dual-sided readout *or* Double-side readout *or* Double-sided readout |
| **ECT** | Emission computed tomography |
| **EEG** | Electroencephalography |
| **FB** | Fan beam |
| **FBP** | Filtered back-projection |
| **FFDD** | First photon detection delay |
| **FI** | Flood irradiation |
| **f-MR** | Functional magnetic resonance |
| **FOV** | Field of view |
| **FPGA** | Field-programmable gate array |
| **FWHM** | Full width at half maximum |
| **FWTM** | Full width at tenth maximum |

| | |
|---|---|
| **GTB** | Gradient tree boosting |
| **KDE** | Kernel-density estimation |
| **k-NN** | k-nearest neighbor |
| **LED** | Leading edge discrimination |
| **LY** | Light yield |
| **LOR** | Line of response |
| **LUT** | Look-up table |
| **MAE** | Mean absolute error |
| **MAP** | Maximum-a-posteriori |
| **MC** | Monte Carlo |
| **MCP-PMT** | Micro-channel plate PMT |
| **ML** | Maximum likelihood |
| **ML-EM** | Maximum likelihood expectation maximization |
| **MLITE** | Maximum-likelihood interaction time estimation |
| **MPPC** | Multi-pixel photon counter |
| **MR** | Magnetic resonance |
| **MRI** | Magnetic resonance imaging |
| **NECR** | Noise equivalent counting rate |
| **NEMA** | National Electrical Manufacturers Associations |
| **NMI** | Nuclear medical imaging |
| **OSEM** | Ordered subset expectation maximization |
| **PB** | Pencil beam |
| **PCA** | Principal components analysis |
| **PDE** | Photon detection efficiency |
| **PDF** | Probability distribution function |
| **PET** | Positron emission tomography |
| **PMT** | Photomultiplier tube |
| **PNECR** | Peak noise equivalent counting rate |
| **PSF** | Point spread function |
| **PS-PMT** | Position-sensitive photomultiplier tube |

| | |
|---|---|
| **QE** | Quantum efficiency |
| **ROI** | Region of interest |
| **SiPM** | Silicon photomultiplier |
| **SNR** | Signal-to-noise-ratio |
| **SOM** | Self-organizing map |
| **SPAD** | Single photon avalanche diode |
| **SPECT** | Single photon emission computed tomography |
| **SPTR** | Single photon timing resolution |
| **SSPI** | Sum of the squared pixel intensity |
| **SSPM** | Solid state photomultiplier |
| **TDC** | Time-to-digital converter |
| **TOF** | Time of flight |
| **VOR** | Volume of response |

# 1

# Introduction

**Abstract** - *This thesis deals with the development of innovative detectors for positron emission tomography (PET). Therefore, this introductory chapter gives a general overview of the field, focusing on the topics that are most important for optimizing the performance of gamma-ray detectors for clinical PET applications. In the first part of the chapter, the basic principles behind the different nuclear medical imaging (NMI) techniques are illustrated. In particular, the radiotracer principle is explained, the most common imaging techniques are described, and some concepts of image reconstruction techniques are introduced. The concept of multi-modality imaging is also defined and the most common clinical and research applications of NMI are reported. In the second part, a more focused description of positron emission tomography technique is given and the criteria used to define image quality in PET are discussed. The factors limiting spatial resolution, noise, contrast and quantitative imaging are then analyzed in detail and the concept of time-of-flight (TOF) PET is introduced. In the third part of this chapter, the discussion focuses on PET instrumentation. First, the working principle of scintillation detectors is described, focusing on the most important characteristics that scintillating crystals and photosensors should have for PET applications. In particular, the detector performance parameters are related to different aspects of image quality and there is a brief discussion of which parameters have to be optimized for different types of PET scanners. Then, the different scintillation detector architectures used in PET systems are reported and their main advantages and drawbacks are analyzed. Finally, the characteristics of state-of-the-art clinical PET scanners are described. In the last part of this chapter, the thesis research objectives are discussed and the general structure of the thesis is outlined.*

## 1.1. Nuclear medical imaging (NMI)

In general, nuclear medicine can be defined as the medical field in which radioactive substances are used to diagnose, image or treat different types of physiological functions or diseases. In particular, nuclear medical imaging (NMI) is the branch of nuclear medicine aimed at imaging specific physiological processes with non-invasive techniques employing trace amounts of radioactive compounds.

### 1.1.1. The radiotracer principle in NMI

The basic principle on which all NMI applications are based is that it is possible to measure the in-vivo distribution of a defined compound inside a patient (or an animal) if this compound is labeled with a radioactive element that emits a radiation which can be detected outside the patient.

In practice, the compounds employed in NMI applications are pharmaceuticals developed to follow definite metabolic pathways or for binding to precise receptor systems or molecules. These compounds, called radiopharmaceuticals or (radio)tracers, are usually marked with gamma- or positron-emitting isotopes. Once they are administered to the patients, they follow the targeted physiological processes and are accumulated by the different patients' tissues in different concentrations, depending on the kinematic of the tracer uptake inside these tissues. While these tracers follow the targeted metabolic paths, the radioactive nuclides bind to the radiopharmaceuticals decay and emit gamma rays whose energy is high enough for having a good probability to escape from the patient's body without interactions. Using specific scanners based on particle detectors, the radiation emitted by the tracers can be detected and used to create a planar or tomographic image of the estimated tracer distribution inside the body. This image can then be used to obtain diagnostic information such as the functionality of certain organs or the presence of tissues with altered metabolism, e.g. tumors or inflamed tissues.

The radiotracer principle and the targeting mechanism on which all NMI applications are based can be more clearly explained using as an example the $^{18}$F-Fluorodeoxyglucose ($^{18}$F-FDG), a compound that is one of the most commonly used radiotracers for clinical applications. FDG is a glucose analog and is used to study glucose metabolism in tissues, since the two compounds have a very similar chemical structure and have a similar kinetic until they are delivered to the individual cells. However, once FDG is absorbed by the cells it cannot be further metabolized because of the presence of the $^{18}$F in place of a –OH group and therefore it cannot leave the cell. As a consequence, FDG distribution in different tissues reflects their different glucose uptakes. Therefore, FDG scans are used to detect regional specific alterations in glucose metabolism, which can be caused by several pathologic conditions. In particular, FDG scans are employed in clinical routine for the detection, staging and re-staging of cancer, since most tumors have an abnormally high glucose metabolism and therefore cancer tissues can be recognized as bright spots in the images where a high $^{18}$F activity is concentrated.

Even though there is a large number of isotopes that could possibly be used in NMI applications, due to practical reasons only few of them are routinely employed in clinical practice. In particular, useful isotopes are selected considering [1]:

Table 1.1: List of the most common radioisotopes used in NMI. For each isotope the decay mode, the half-life ($T_{1/2}$) and the energy of the emitted gamma rays ($E_\gamma$) are reported. For $\beta^+$ emitters, in the $E_\gamma$ column the energy of the positron annihilation photons is reported together with the energy of the de-excitation gamma ray emitted by the daughter nucleus. (EC: electron capture; IT: isomeric transition)

| Radionuclide | Decay mode | $T_{1/2}$ | $E_\gamma$ (keV) |
|---|---|---|---|
| $^{11}$C | $\beta^+$ | 20.4 min | 511, 960 |
| $^{13}$N | $\beta^+$ | 10.0 min | 511, 1190 |
| $^{15}$O | $\beta^+$ | 2.0 min | 511, 1723 |
| $^{18}$F | $\beta^+$ | 110 min | 511, 635 |
| $^{67}$Ga | EC | 3.26 d | 93, 185, 300 |
| $^{68}$Ga | $\beta^+$ | 67.6 min | 511, 1900 |
| $^{82}$Rb | $\beta^+$ | 1.3 min | 511, 3350 |
| $^{99m}$Tc | IT | 6.0 h | 141 |
| $^{111}$In | EC | 2.8 d | 171, 247 |
| $^{123}$I | EC | 13.2 h | 159 |
| $^{201}$Tl | EC | 3.06 d | 69-82 (X-rays), 167 |

- type and energy of the emitted radiation, since radiation should have a reasonable likelihood to escape from the patient's body;
- physical half-life (usually in the range from few minutes up to few days), which should be long enough to prepare and inject the tracers but short enough to obtain an high activity during the examination time and a quick decay of the tracer afterwards, in order to minimize the dose to the patient;
- the possibility to produce the isotope with a high specific activity and a high radionuclide purity;
- the cost and complexity of preparation.

The most commonly used radioisotopes are reported in Table 1.1 [2].

### 1.1.2. Imaging techniques in NMI

In NMI, the simplest method to obtain an image of the tracer distribution inside a patient consists in selecting only the gamma rays emitted from the patient along a defined direction and in measuring the spatial distribution of the flux of these photons on the plane perpendicular to that direction. If a large number of photons is collected, the spatial distribution of the flux corresponds to a 2D projection along the selected direction of the 3D tracer distribution inside the patient. A pictorial explanation of this method is shown in Figure 1.1. The main issue of this approach is that a 2D projection of the tracer distribution does not provide clear information, since it is not possible to determine the depth of the image features and some structures might be obscured by other overlying or underlying structures.

To solve this issue, a more sophisticated approach called tomographic imaging can be used. In practice, if many projections of the same distribution are measured along different directions, mathematical algorithms can be used to estimate the 3D

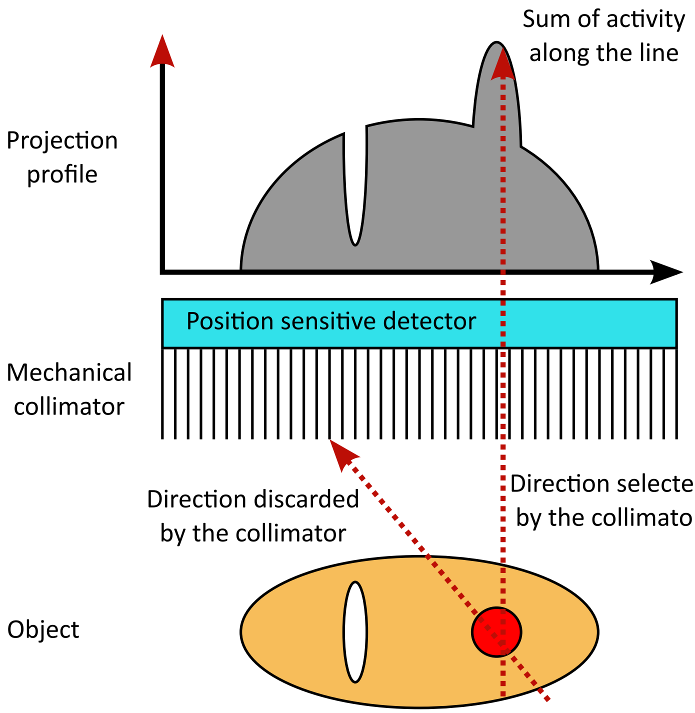

Figure 1.1: Technique used to acquire a projection of the radioactive tracer distribution inside an object. A collimation technique (in this case a mechanical collimator) is used to select only the radiation emitted along a certain direction. A position sensitive detector is used to detect the radiation and to determine its position of interaction. The plot of the spatial distribution of the recorded activity represents the projected image of the tracer distribution.

spatial distribution of the tracer and to obtain a tomographic image (see section 1.1.3). With this approach, full information on the position of the imaged features inside the patient's body can be obtained, dramatically improving the diagnostic value of the examination. In NMI there are two different tomographic imaging techniques, whose main differences consists in the type of radioisotope employed to produce the tracers and in the mechanism used to determine the gamma-ray incoming direction during the scan.

The first technique is called single photon emission computed tomography (SPECT) and is based on single-photon-emitting isotopes, i.e. isotopes that decay through $\beta^-$ emission (e.g. $^{131}$I), electron capture (e.g. $^{67}$Ga, $^{111}$In, $^{123}$I) or isomeric transitions (e.g. $^{99m}$Tc) and have among their final decay products a single gamma-ray whose energy is in between 50/100 keV and 500/600 keV. In SPECT, the information about the direction of the detected gamma rays is obtained by using mechanical collimators made of dense material (such as Pb, W or Au), which allow gamma rays coming only from definite directions or regions to be detected (Figure 1.2). Depending on the application, different collimator geometries can be used: most common ones are parallel hole collimators, which are designed to select only gamma rays coming from a definite direction. However, more sophisticated collimator geometries can also be used, e.g. pinhole collimators that make possible to magnify the imaged object on the detectors in order to improve spatial resolution. With this imaging technique, considering the point of interaction of a gamma-ray on the detector and the collimator geometry, the point of emission of the photon can be localized along a certain line of response (LOR) or, if the detector is made of discrete elements, within a certain volume of response (VOR). Different collimator types have different advantages and drawbacks in terms of sensitivity, spatial resolution and image uniformity and therefore the optimization of their geometry is a complex task that is strongly dependent on the final application.

The second tomographic imaging technique is called positron emission tomography (PET) and is based on radio-isotopes that undergo to β+ decay, i.e. that decay emitting a positron (e.g. $^{11}$C, $^{18}$F and $^{82}$Rb). After the emission, positrons are first slowed down and stopped into the patient's body and then they annihilate with an electron of the surrounding tissue. The final products of this process are two 511 keV gamma rays that are emitted at an angle of ~180° from the annihilation point. PET exploits this peculiarity of annihilation photons to determine their direction: if the two gamma rays are detected in coincidence, knowing the point of interaction of both gamma rays it is possible to univocally determine the LOR (or VOR) containing the point from which the photons have been emitted, as illustrated in Figure 1.3. Selecting only the events along LORs having a defined orientation, a certain projection of the tracer distribution can be obtained without any physical collimator. This mechanism is called electronic collimation and allows PET to achieve a sensitivity even two or three orders of magnitude higher than SPECT. More details on PET working principles can be found in section 1.2.1.

SPECT and PET techniques have many differences in terms of sensitivity, cost and complexity of the scanners, final image resolution, etc. Therefore, the choice of one or the other technique depends on the requirements of the final application.

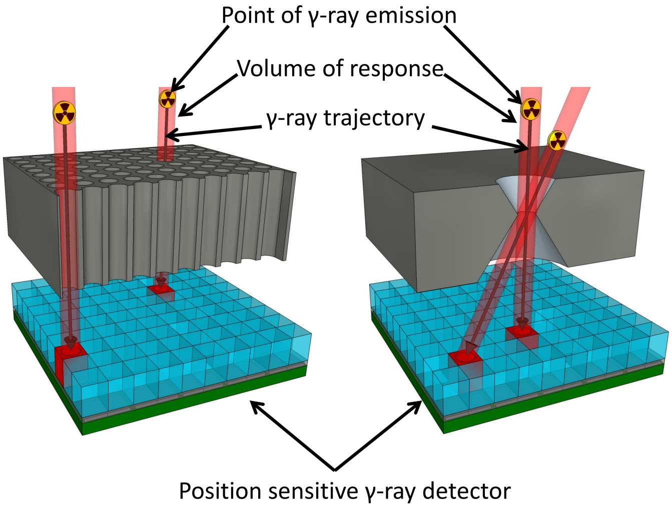

Figure 1.2: Working principle of single photon emission computed tomography (SPECT). Gamma photons reach the detectors passing through a collimator, e.g. a parallel hole collimator in the left image or a pinhole collimator in the right one. The volume of response from which a photon is coming is determined by considering the detector element in which the radiation interacts and the collimator geometry.

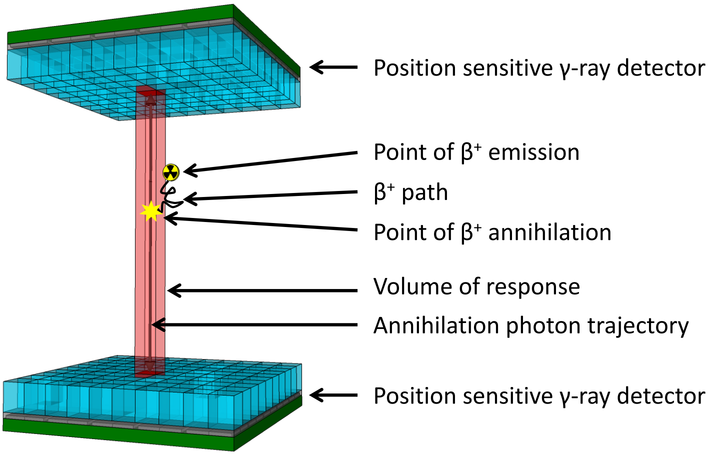

Figure 1.3: Working principle of positron emission tomography (PET). An element that undergoes to a $\beta^+$ decay emits a positron and, when it annihilates with an electron, a pair of annihilation photons are emitted in opposite directions. The volume of response containing the point of annihilation can be determined as the volume defined by the two detector elements in which the photons interact.

However, most of the time the choice is driven by the availability of dedicated tracers, since tracers suitable to investigate a definite physiological process can often be labelled only with isotopes that can be imaged with just one of the two techniques.

### 1.1.3. Image reconstruction in emission computed tomography

In general, tomographic imaging is an imaging technique that makes it possible to obtain the 2D representation of a plane within a 3D object by measuring several 1D projections of this plane along different directions. If more consecutive planes are reconstructed, a complete 3D representation of the object can be obtained. This technique can also be applied in NMI to estimate the 3D radiotracer distribution inside a patient by using a set of projections of this distribution along different directions. These projections are obtained by collimating the emitted photons and selecting them based on their incoming direction. As already mentioned in section 1.1.2, there are two different types of tomographic procedures in NMI, SPECT and PET, which use different types of tracers and collimation strategies and are collectively referred to as emission computed tomographies (ECT).

The principle used to measure the projection of the activity distribution in a certain plane is shown in Figure 1.1. A collimation system is used to select only the photons having a certain direction (among all the gamma rays emitted isotropically by the tracer) and a detector is used to measure their position of interaction. The collimation system can be either a mechanical collimator (SPECT), which physically stops all gamma rays except those that enter from a specific direction, or a coincidence system, which records annihilation photons detected by opposite detectors (PET). Using this collimation system, each event can be associated with a LOR, i.e. the line along which the decay of a tracer molecule has to occur in order to be registered by the detector in a specific position. Thus, the number of interactions registered at a given point on the detector is proportional to the integrated tracer activity along the LOR. The profile of the numbers of events measured for all possible LORs, for a given position of the detector, is called a projection. By rotating the collimator-detector system around the object it is possible to acquire a projection for every possible direction.

Obviously, the profiles that are measured during real ECT scans are not perfect projections of the tracer distribution, since there are many effects that contributes to blur and add noise to the measurement. These effects are due to the finite and discrete positioning accuracy of detectors, the finite collimation capability of the collimation techniques, photon scattering, the finite counting statistics, etc. (see sections 1.2.3 and 1.2.4). However, in first instance these effects can be neglected to outline the most widespread image reconstruction techniques, which can be divided into two major families.

The first family comprehends all analytical algorithms, which are basically mathematical transformation that map the data contained in the projection space, i.e. the data measured in all the different detector positions, to the image space, i.e. the image representing the region of interest for which the tracer distribution has to be estimated.

The simplest analytical method is called back-projection (BP). As discussed above, each point in each projection profile corresponds to the intensity of the total activity along a certain LOR. In BP, all the pixels of the image along the LOR are considered to equally contribute to the measured value. Therefore, during image reconstruction each value in the projection profiles is equally distributed to all the image pixels along the corresponding LOR. Repeating this back-projection operation for all the measured values in all acquired projections, a reconstructed image can be obtained. This method is simple and straightforward: however, it results in a blurred image because of the homogeneous projection of the measured values on the LORs. Mathematically, it can be shown that this blurring effect corresponds to the convolution of the image with a $1/r$ filter.

To solve this issue, a more refined method was developed, which is called filtered back-projection (FBP). In this method, the blurring effect is removed first by calculating the Fourier transform of all the projections, then by applying a ramp filter to the transformed projections, and finally by calculating the inverse Fourier transform of each filtered profile and by applying standard back projection. It can be mathematically demonstrated that the filtering step in the frequency domain corresponds to the deconvolution of the $1/r$ filter in the image space and that this method can exactly reconstruct the original image, if a sufficient number of perfect projections are acquired. However, in practice this method is quite sensitive to high-frequency noise and therefore modified frequency filters are needed in order to avoid image artifacts during real ECT reconstructions. Moreover, the method is quite sensitive to missing data (e.g. due to a detector malfunctioning) and to low counting statistics and cannot directly include information about attenuation and scattered events (see section 1.2.4). Despite these limitations, FBP has been for a long time one of the most widely used reconstruction method since it is fast, has limited computational requirements and is relatively simple to be implemented.

Starting from the 1980s-1990s, a second family of reconstruction algorithms has been developed, which rely on a model-based statistical approach and use iterative algorithms to obtain an image. These algorithms can solve many of the issues connected with the analytical methods; however, they are more computationally intensive than FBP and so they reached widespread use in the clinical practice only in recent years. Basically, all iterative algorithms start with an assumed tracer distribution (which might be an educated guess or even an homogeneous distribution) and then calculate the projections that are expected to be measured for this distribution using the system under study (forward projection). Those calculated profiles are then compared with the profiles that have been actually measured and, if they do not agree, the image is updated so that the forward-projected profiles become closer to the measured data. This process can be repeated indefinitely until the difference between the forward-projected profiles and the measured profiles is smaller than a pre-defined level.

In practice, all iterative methods are based on three fundamental elements:

- a system model that can be used to forward project the estimated images and calculate their profiles; this system model should take into account the scanner geometry, the detector resolution and efficiency, the attenuation of gamma-rays into the imaged object and other physical effects such as photon scattering, positron range and photon acollinearity, etc. (see sections 1.2.3 and 1.2.4);

- a cost function that provides a measure of the difference between the forward-projected profiles and the measured profiles;
- a search or update function that uses the output of the cost function to create a new iteration of the image; the update functions has to provide an image whose forward-projected profiles are more similar to the measured ones compared to the forward-projected profiles obtained with the image of the previous iteration.

One of the earliest iterative algorithm is the maximum likelihood expectation maximization algorithm (ML-EM), which uses a (log) likelihood function as cost function and an expectation maximization algorithm to update the images. This approach provides a stable convergence to the most probable solution but converges quite slowly. Therefore, a modified version of this approach was introduced, which divides the projection data into subsets and applies EM to each subset. This method is called ordered subset expectation maximization (OSEM) and guarantees a much faster convergence. Another class of iterative methods is based on maximum-a-posteriori (MAP) estimators, which include also a statistical model for the image and therefore enforce an a priori model of the image distribution (e.g. some smoothness constraints) in the image reconstruction.

Over the years, many sophisticated image-reconstruction methods have been developed and introduced into clinical practice and this is still a very active research field. For example, full 3D reconstruction techniques (both analytical and statistical) have been developed, which do not reconstruct separately each 2D plane of the image but perform a simultaneous reconstruction of the whole imaged volume. The introduction of these techniques, in which all LORs crossing the FOV are used for image reconstruction, was required to reconstruct data acquired in 3D mode, i.e. an acquisition modality that registers coincidence along all possible directions and not just the ones that are perpendicular to the scanner axis (see section 1.2.1). An exhaustive review of these methods is outside the scope of this thesis. For interested readers, a more detailed review of these techniques can be found in several reference books [1, 3, 4] and articles [5, 6].

### 1.1.4. Multi-modality or hybrid medical imaging techniques

NMI techniques can image physiological processes but do not provide any accurate anatomical information. This lack of precise anatomical references is a severe limitation for accurately localizing the features of interest of the functional images. To overcome this limitation, currently a large fraction of SPECT scanners and virtually all PET systems are integrated with other imaging modalities that provide anatomical images, such as computed tomography (CT) scanners and magnetic resonance (MR) systems. These multi-modality scanners can acquire both images (almost) simultaneously without moving the patient from the bed and can produce perfectly-aligned “fused” images. These combined images contain at the same time the anatomical and functional information and therefore significantly increase the diagnostic capabilities of the NMI procedures.

Currently, the most common multi-modality PET scanners are integrated PET-CT systems: these systems were first developed at the end of the 1990s [7] and quickly found a wide diffusion into clinical practice thanks to their evident added value in comparison with standalone PET scanners [8]. They essentially consists in two independent PET and CT systems mounted on the same gantry, which acquire coaxial scans. In these systems, CT scans do not only provide anatomical information but are also used to calculate in a very reliable way the attenuation maps for PET image correction (see section 1.2.4.5), which in standalone PET scanners were obtained (with lower quality) with lengthy transmission scans based on external radioactive sources. Attenuation correction is of utmost importance to obtain reliable quantitative estimations of the tracer uptake, which e.g. in FDG scans is used to properly stage tumors and evaluate patient’s response to treatments. Therefore, integrated PET-CT systems have significant advantages over systems which cannot directly measure the attenuation map.

Combined PET-MR scanners are, instead, still a niche solution. Despite they were proposed approximately at the same time of PET-CT scanners (early-mid 1990s), the integration of PET and MR turned out to be a much more challenging task due to the mutual disturbance that the two systems cause to each other [9] and to the fact that MR images cannot provide reliable information for attenuation correction in a straightforward manner. For this reason, the first commercial PET-MR scanner appeared only at the beginning of the 2010s [10].

In principle, this multi-modality imaging technique can offer several advantages compared to PET-CT systems, such as the superior resolution and soft-tissue contrast of MR images, the possibility to spare the CT dose to patients, and the capability of MR systems to obtain complementary functional and molecular information. Despite these advantages, PET-MR so far encountered a smaller success than PET-CT, due to its significantly higher costs and the absence of demonstrated benefits in routine clinical practice. However, currently there are many promising applications that are under investigation and might significantly widen the application fields of PET-MR systems, e.g. clinical evaluation of neuro-oncological and neurodegenerative diseases [11], research on human brain function [12], and pediatric oncology, where children could fully benefit of the significant dose reduction over many different imaging sessions [13, 14].

A newly proposed development of integrated PET-MR scanners that is also interesting to report is a tri-modality imaging systems combining PET, MR and electroencephalography (EEG) [15]. This scanner is currently under investigation to add the peculiar functional-imaging capabilities of EEG to PET-MR scanners for some brain-imaging and neuroscience applications. In these applications, PET-MR scanners already provide clear advantages, thanks to the possibility to simultaneously obtain metabolic (PET), functional (functional-MR, fMR) and high-resolution anatomical (MR) information of the brain, and EEG integration could further improve the capabilities of such systems.

### 1.1.5. Clinical and research applications of NMI

A wide variety of tracers has been developed during the years and currently NMI techniques are used for studying a broad range of biological processes with diagnostic applications mainly in the fields of oncology, neurology and cardiovascular disease, both in clinical and research practice.

In particular, most common clinical SPECT applications comprehend studies of myocardial perfusion to assess coronary artery disease and heart functionality, cerebral perfusion studies to investigate cerebrovascular disease, dementia, brain tumors, etc., and oncological studies to visualize primary and metastatic lesions. Other applications in which SPECT is commonly employed are imaging of inflammation and infection and measurements of kidney and liver functionality. SPECT is also widely used in research studies, preclinical studies and basic biomedical research [1].

As regards PET, FDG scans for oncological applications are by far the most common procedures in clinical environments. As described in section 1.1.1, these procedures are widely used for the detection and staging of cancer and for tumor re-staging during treatments in many different types of oncological diseases, such as lymphomas, lung cancer, breast cancer, brain cancer, etc.

Besides oncological applications, PET is also commonly used in neurology: for example, it can be used for diagnostic purposes in neurodegenerative diseases (e.g. Alzheimer and Parkinson disease), dementia, epilepsy, movement disorders [16], and other neuropsychiatric illnesses. For these applications, many different tracers are used such as FDG, which allows physicians to evaluate brain functionality, $^{18}$F-6-Fluorodopa ($^{18}$F-dopa), which is used for studying the dopaminergic system in movement disorders, 18F-florbetapir, a specific tracer to image amyloid plaque in Alzheimer's patients, and many other tracers that are ligands for specific neuro-receptors subtypes. Moreover, PET has also several diagnostic applications in cardiology, where FDG is used in conjunction with other blood flow tracers (e.g. $^{13}$N-ammonia or $^{82}$Rb-Cl) for studying myocardial viability, and for diagnosing and monitoring inflammatory and infectious diseases.

PET is also widely used in pre-clinical and clinical research studies, e.g. to study particular receptor systems, to study the pharmacokinetic of new drugs or for developing new pharmaceuticals. Recent studies indicate that new applications for PET are also emerging due to the recent introduction of integrated PET-MR scanners, especially in the field of neuro-imaging and in some oncological applications [17–19].

For interested readers, thorough reviews of the different fields in which PET is used can be found in the following references: [1, 3, 4, 20].

## 1.2. Positron emission tomography - PET

### 1.2.1. General concepts of PET imaging

As briefly described in section 1.1.2, PET examinations are performed using radiotracers labeled with $\beta+$ emitters (see Figure 1.3). When a positron is emitted from a radiotracer inside the patient's body, it is slowed down by electrostatic interactions with the electrons and nuclei of the surrounding tissue and, after losing most of its kinetic energy, it undergoes mutual annihilation with an electron. The products of this reaction are two simultaneous gamma rays, each one carrying an energy equal to the rest-mass energy of a positron/electron (511 keV). In order to respect the momentum conservation principle, the photons are emitted in opposite directions in the frame of reference in which the $e^-/e^+$ system has no linear momentum. PET imaging technique is based on the simultaneous detection of the two gamma rays originating from the $\beta+$ decay, since the physical constraints of the process allow PET systems to localize the positron annihilation point on the line connecting the two points of interaction of the gamma rays on the detectors, i.e. the LOR.

The simplest system that can be used to perform PET imaging is composed of a couple of opposite planar gamma-ray detectors operated in coincidence. These detectors estimate the position of interaction, the time of interaction and the deposited energy of each interacting photon (single event or single). Then, a coincidence unit sorts all the events and pairs up the couples of singles (from different detectors) that have been registered in a predetermined time window to define the coincidence events (or coincidences). The width of the time window is chosen considering three parameters:

- the maximum possible variation of the difference between the times of interaction of the photons, which is derived considering the maximum difference in distance travelled by the two photons (~3.3 ns for imaged objects having a diameter ~50 cm);
- the detector precision in measuring the arrival time of a photons (i.e. the detector timing resolution);
- other possible time uncertainties, such as additional jitters introduced during analog signal transmission, etc.

In clinical scanners, coincidence timing windows usually have a width of 6-10 ns.

The major drawback of a dual-detector system is that it can acquire a single projection (or a limited number of projections) per detectors position. Therefore, to obtain a tomographic reconstruction it is necessary to rotate the detectors around the patient and perform several acquisitions, which is a lengthy and inefficient process.

A more efficient approach is to build a complete ring of detectors around the patient and to operate each detector in coincidence with multiple modules on the opposite side (see Figure 1.4). In this way, many projections are acquired at the same time, greatly improving the system sensitivity and reducing other possible issues connected with the sequential acquisition of different projections, such as

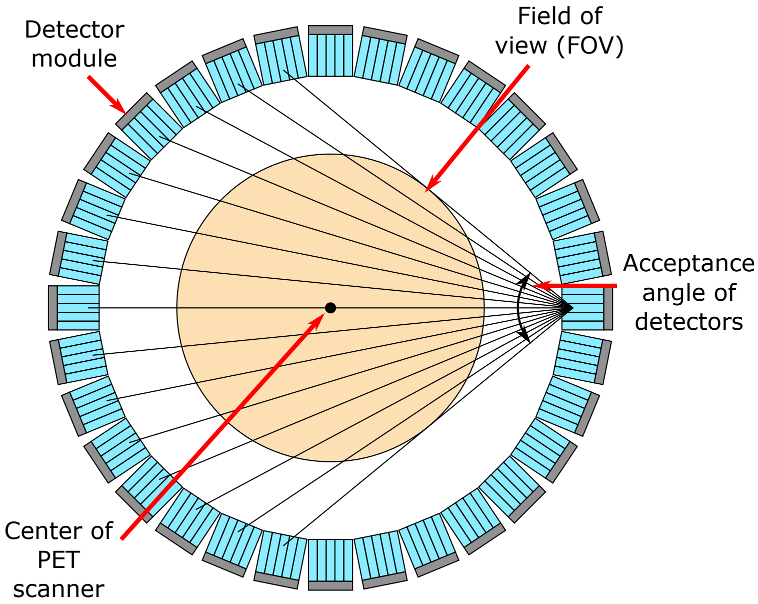

Figure 1.4: Illustration of a PET system composed of a complete ring of detector units. The field of view (FOV) of the scanner is defined by the acceptance angle of the detectors, which defines the couples of detectors for which it is allowed to acquire coincidences.

changes in the total activity, patient movement, etc. The maximum angle between detectors (with respect to their perpendicular direction) for which coincidences are allowed defines the useful field of view (FOV) of an annular scanner. Therefore, the wider is the FOV relatively to the ring diameter, the larger is the possible incidence angle of gamma rays on the detectors.

Modern ring PET scanners usually have a bore diameter from 70 cm up to 90 cm and an axial length which ranges from 15 cm up to 40 cm. Since there are several rings of detector elements along the axial direction of the scanner, two data acquisition techniques are possible in PET scanners. With the first technique, only elements in the same detector ring are allowed to acquire coincidence events, i.e. only the LORs in the planes which are perpendicular to the scanner axis can be acquired. This acquisition technique is usually called 2D data acquisition and most often employs collimators or septa between the detector rings to mechanically collimate the gamma rays with an oblique direction, in order to reduce the single count rate on the detectors. If 2D data acquisition is used, image reconstruction can be performed separately for each acquired plane and requires a limited amount of computational power.

The second acquisition technique is called 3D data acquisition and allows PET systems to register coincidences between all detector rings (at least up to a certain plane angle). Using this technique, image reconstruction cannot be done any more for each separate projection plane but has to be performed at the same time for the whole imaged volume. There are both analytical and iterative methods that can handle this task, however they have much higher computational requirements since the matrices and the amount of data that have to be handled are much larger than for 2D image reconstruction. Three dimensional data acquisition also has other drawbacks, e.g. a higher count rate of random events (see section 1.2.4.1). Despite these issues, scanners implementing 3D data acquisition can provide a much higher image quality thanks to their greatly enhanced sensitivity; for this reason, 3D data acquisition is currently the most used technique in modern clinical scanners.

### 1.2.2. Image quality in PET

The purpose of a PET scanner is to provide a representation as faithful as possible of the tracer distribution inside a patient, in order to obtain diagnostic information. However, PET scanners can be employed for a large variety of tasks, e.g. to locate a tumor or to measure the metabolism of the brain, and each task has different requirements from the imaging point of view: in some cases it might be more important to visualize and resolve small features in the image whereas in others it might be more useful to obtain a precise estimation of the amount of the tracer in a wider region. Moreover, in clinical applications the final images are evaluated by physicians and clinical physicists, therefore the performance of PET scanners are both task- and observer-dependent. For this reason, to assess the image quality of a PET scanner is a very challenging issue.

In general, two different approaches can be followed to determine the performance of a PET system. The first approach consists in characterizing certain physical properties of the images that can be quantitatively measured (and that are correlated to the quality of the images used for diagnostic purposes) such as:

- spatial resolution, i.e. the capability to resolve small details in the imaged object;
- contrast, i.e. the capability to accurately reproduce different levels of tracer uptake in the color intensity of the final image;
- noise level, i.e. the system uncertainties or fluctuations in estimating the amount of activity in each image pixel/voxel, which usually determine an high-frequency disturbance in the image.

A series of standardized tests have been developed to singularly assess these parameters: the most widely accepted and used ones are the tests developed by the (American) National Electrical Manufacturers Associations (NEMA), which are periodically revised and published in a dedicated manual [21]. Those tests are often used to define the scanner performance and to compare different scanner models. However, they are usually based on imaging tasks that can be quite different from the tasks performed in clinical applications: for example, spatial resolution is measured by acquiring images of stand-alone point sources, which is a condition that never happens in real diagnostic acquisitions.

A second approach for assessing image quality relies instead on observer performance studies that are based on well-defined imaging tasks. These tasks are closer to the tasks that are accomplished in a real clinical environment, e.g. it is required to determine if a small structure with higher activity (lesion) is present or not in a phantom filled with an homogeneous background activity. Measuring the fraction of correctly recognized images as a function e.g. of the lesion dimension or contrast (i.e. the ratio between the lesion activity and the homogeneous phantom activity), it is possible to draw conclusions on the imaging capabilities of different scanners or to compare different acquisition conditions. These studies can be performed either using human observers, i.e. showing the images to trained physicians or medical physicists, or computer observers, i.e. computer algorithms that are developed to mimic human observer and can be used when to set up a study with human observers is not practical. Two different typologies of observer tasks are commonly used, the detection tasks and the quantitation tasks. The detection tasks require observers to decide whether a certain feature is present or not, whereas quantitation tasks require to make a quantitative estimate of the tracer uptake in certain region of interest (ROI). A complete review of the possible observer performance studies is outside the scope of this thesis, interested readers can find more details in [1].

Despite the two approaches to assess PET image quality are correlated, it has to be noted that each observer task is differently influenced by the physical properties of the images. Since physical properties are interdependent and often to improve one of them comes at the expense of deteriorating another one, it is important to know which factors influence spatial resolution, noise and contrast in order to make the best compromises when designing a PET scanner for a defined task.

### 1.2.3. Limiting factors for PET image spatial resolution

In PET scanners, image spatial resolution is usually defined as the width that a point source assumes in a reconstructed image in different positions of the FOV. This parameter is connected to the smallest distance at which two separate features can be distinguished in a diagnostic image. There is a series of factors that limit the achievable spatial resolution in PET imaging: some of them are intrinsically connected to the physics of $\beta^+$ decay and of the following positron annihilation reaction, whereas others are more connected to the performance of the PET detectors, to the scanner design and to the image reconstruction process. In the following, some of these factors are briefly described and analyzed. A more comprehensive exposition of the factors limiting spatial resolution can be found for example in [22] and [1].

#### 1.2.3.1. Positron range

In $\beta^+$ decays, positrons are emitted by the nuclei with a certain kinetic energy and therefore they travel for a certain distance before they are slowed down by Coulomb interactions and they annihilate, creating the two gamma rays that define the LORs. For this reason, LORs usually do not intersect the original tracer position and a blurring effect is introduced in the final PET image, whose magnitude depends on the positron range (i.e. the distance between the positron emission point and the

Table 1.2: List of the maximum positron energy ($E^{\beta}_{max}$) and of the FWHM/FWTM of the 1D positron-range distribution for six of the most common PET radio-isotopes.

| Isotope | $E^{\beta}_{max}$ (MeV) | FWHM (mm) | FWTM (mm) |
|---|---|---|---|
| $^{11}$C | 0.970 | $0.29 \pm 0.06$ | $2.24 \pm 0.10$ |
| $^{13}$N | 1.19 | $0.38 \pm 0.05$ | $2.89 \pm 0.09$ |
| $^{15}$O | 1.72 | $0.57 \pm 0.07$ | $4.12 \pm 0.12$ |
| $^{18}$F | 0.635 | $0.16 \pm 0.02$ | $1.34 \pm 0.04$ |
| $^{68}$Ga | 1.89 | $0.62 \pm 0.07$ | $4.61 \pm 0.13$ |
| $^{82}$Rb | 3.15 | $0.88 \pm 0.13$ | $8.58 \pm 0.26$ |

positron annihilation point). The influence of this effect on PET spatial resolution can be estimated by calculating the probability distribution of positron ranges, which can be obtained for different isotopes and for different surrounding materials using Monte-Carlo simulations. These simulations take also into account the continuous energy spectra of the emitted positrons and the fact that positrons do not travel in straight paths. Such distributions have a cusp-like shape, with a sharp peak and long tails, and a final PET image can be considered as the convolution of this function with the original tracer distribution. In Table 1.2, the FWHM and FWTM of the 1D positron-range probability distributions (i.e. the distribution of the absolute distances of the positron emission points from the annihilation points) in water for six of the most common PET isotopes are reported; a more comprehensive discussion on the topic can be found in [23] and [24].

#### 1.2.3.2. Photon acollinearity

When a positron and an electron annihilate, their center of mass might not be completely at rest in the reference system of the PET scanner, due to the residual energy of the positron or to the kinetic energy of the electron. Therefore, since the total momentum is preserved in the process, the two annihilation photons might not be emitted exactly in opposite directions. Recent measurements showed that the angular distribution of the photons can be considered a double-Gaussian function whose main component has a FWHM ~0.6° [25]. This phenomenon, called photon acollinearity, introduces a Gaussian blurring in the final PET image, since the LORs calculated using the photon interaction points do not always intersect the annihilation points. The magnitude of this blurring, $R_{acollinearity}$, is linearly dependent on the detector separation $D$ and can be estimated as $R_{acollinearity} \approx 0.0024 \times D$. The effect is therefore maximum at the center of the scanner FOV and larger for scanner with a wider bore: for example, $R_{acollinearity}$ is ~2 mm at the center of the FOV of a scanner having a diameter of 80 cm.

#### 1.2.3.3. Detector spatial resolution and DOI effect

Another factor that contributes to degrade PET image spatial resolution is the error made by particle detectors in determining the 3D position of interaction of gamma rays. This error directly influences the system accuracy in determining the LORs and can be considered composed by two contributions.

The first contribution is due to the detector accuracy in determining the $x - y$ coordinates of interaction on the detector plane. This accuracy depends on the type of detector employed and on the technique used to decode the interaction point (see sections 1.3.3.1 and 1.3.3.2). If a detector has a spatial resolution equal to $D_{xy}$, it can introduce a degradation in the spatial resolution of the final image ($R_{detector}$) that ranges from $D_{xy}/2$ up to $D_{xy}$, depending on the shape of the error distribution and on the position in the FOV (see [1] for a more detailed discussion). For example, the most common detectors used in PET clinical scanner are made of small, discrete elements (pixelated detectors, see section 1.3.3.1) and their intrinsic spatial resolution can be considered to be equal to the element dimension, which is usually ~3/4 mm. These detectors determine a $R_{detector}$ equal to $D_{xy}/2$ (~1.5/2 mm) at the center of the FOV and equal to $D_{xy}$ (~3/4 mm) at the edges of the FOV. Further degradations of this resolution are usually determined by the unavoidable photon scattering inside the detector material (see section 1.3.2.1) and by errors made in decoding the hit element, if a multiplexed readout system is used.

The second contribution comes from the uncertainty in determining the depth-of-interaction (DOI) of gamma rays inside the detectors. This uncertainty introduces an additional error in defining the LORs for gamma rays that are not perpendicularly incident on the detectors, which is commonly referred to as parallax error. This issue can be better explained referring to Figure 1.5, were pixelated detectors made of small, discrete elements are considered. Usually, these elements have a thickness ~20 mm (to achieve a good sensitivity) and detectors do not provide any estimation of the DOI. If a coincidence happens between two opposite elements in the detector ring, the region where the annihilation could have taken place (volume of response, VOR) is defined only by the lateral dimension of the elements. However, if a coincidence happens between two elements which are not opposite one to each other, the VOR is defined also by the element thickness and becomes wider. This broadening of the VOR for non-perpendicular gamma rays introduces an additional deterioration in the PET image resolution, which is more important at larger radial distances from the center of the FOV. The effect of the parallax error can be reduced by increasing the ring diameter, since this reduces the angle of incidence of gamma rays for a defined diameter of the FOV. However, this solution increases the cost and complexity of the scanner if the sensitivity has to be maintained constant. Therefore, the best way to reduce this issue would be to introduce in PET scanners detectors that can estimate the DOI, since simulation studies show that already a 2-level DOI information can improve image spatial resolution in the outer regions of the FOV and image homogeneity [26, 27].

#### 1.2.3.4. Sampling and reconstruction filters

Other factors influencing PET image spatial resolution are connected to the scanner architecture and to image reconstruction methods. For example, if PET detectors made of small (~4 mm), discrete elements (pixelated detectors, see section 1.3.3.1) are used, some distortion can be introduced into the image due to the sampling interval between parallel projection lines and to the inhomogeneous sampling of the imaged space due to the finite size of the detector elements. Another element that could introduce a deterioration in image spatial resolution are the filters that

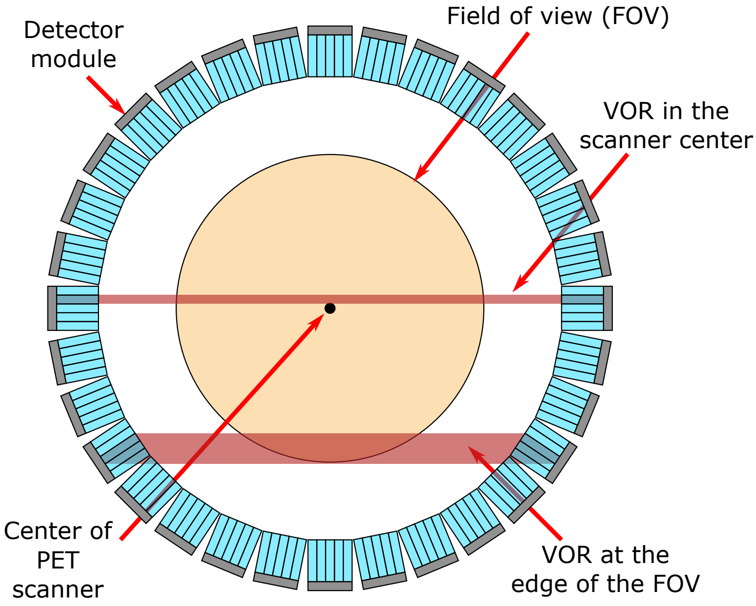

Figure 1.5: Illustration of the parallax error introduced by the uncertainty in determining the DOI in case of a scanners composed of pixelated detectors (no DOI information). At the center of the scanner, for perpendicularly incident gamma rays, the VOR is determined only by the lateral dimensions of the detector elements. At the border of the scanner, instead, for non-perpendicularly incident gamma rays, the VOR is broadened due to the uncertainty in determining the DOI inside the crystal elements.

are used on the data (especially in FBP) or on the final image to reduce the image noise. These factors have a variable influence on the final image resolution and usually can be reduced by properly taking them into account during the system design, e.g. introducing some appropriate expedients in the sampling scheme. More details regarding these issues can be found in [1].

### 1.2.4. Factors affecting noise, contrast and quantitative estimations in PET imaging

Besides spatial resolution, the other physical parameters that influence PET image quality are the noise and the contrast. The noise is connected to the capability of the system to provide clear images without excessive random fluctuation in the pixel values, which might hide small details or create false high- or low-activity spots. The contrast instead defines the system capability to correctly represent different levels of tracer uptake without introducing any bias, which is important to obtain accurate quantitative measurements of different physiological processes (e.g. tumor metabolic activity and therefore response to treatments). Despite these parameters have different effects on the image, they are closely related since both of them are strongly dependent on phenomena that introduce wrong information (i.e. counts on LORs that do not correspond to the position of a real annihilation event) in the data used for image reconstruction. Noise is also strongly dependent on the total amount of information that is acquired. The most important factors influencing image noise, contrast and quantitative measurements are briefly described in the following sections.

#### 1.2.4.1. Random events

Prompt coincidences are registered by PET scanners whenever two gamma rays are detected within a defined time window $\tau$, i.e. if they have a maximum time separation equal to $\tau$. Prompt coincidences can be divided into true coincidences or true events, i.e. coincidences determined by two gamma rays coming from the same annihilation event, and random coincidences or random events, i.e. coincidences in which two gamma rays coming from two unrelated annihilation events are detected by chance within the coincidence time window (see Figure 1.6).

The random count rate $r_{rnd}$ of a detector pair is given by:

$$r_{rnd} = r_{d1} \cdot r_{d2} \cdot \tau \tag{1.1}$$

where $r_{d1}$ and $r_{d2}$ are the single count rate of the two detectors.

Few considerations can be drawn from this formula. First, the random count rate linearly depends on the width of the coincidence timing window $\tau$, therefore the shorter is $\tau$ the smaller is the amount of randoms. As mentioned in section 1.2.1, $\tau$ cannot be reduced below a certain value because of the possible difference in time-of-flight of the coincidence photons. However, any improvement in the timing accuracy of the detectors determines a correspondent reduction of $\tau$. Moreover, a coincidence resolving time (CRT) significantly smaller than $\tau$ can also be used to improve the final image quality using the time-of-flight technique, as described in section 1.2.5. For these reasons, CRT is an important performance parameter

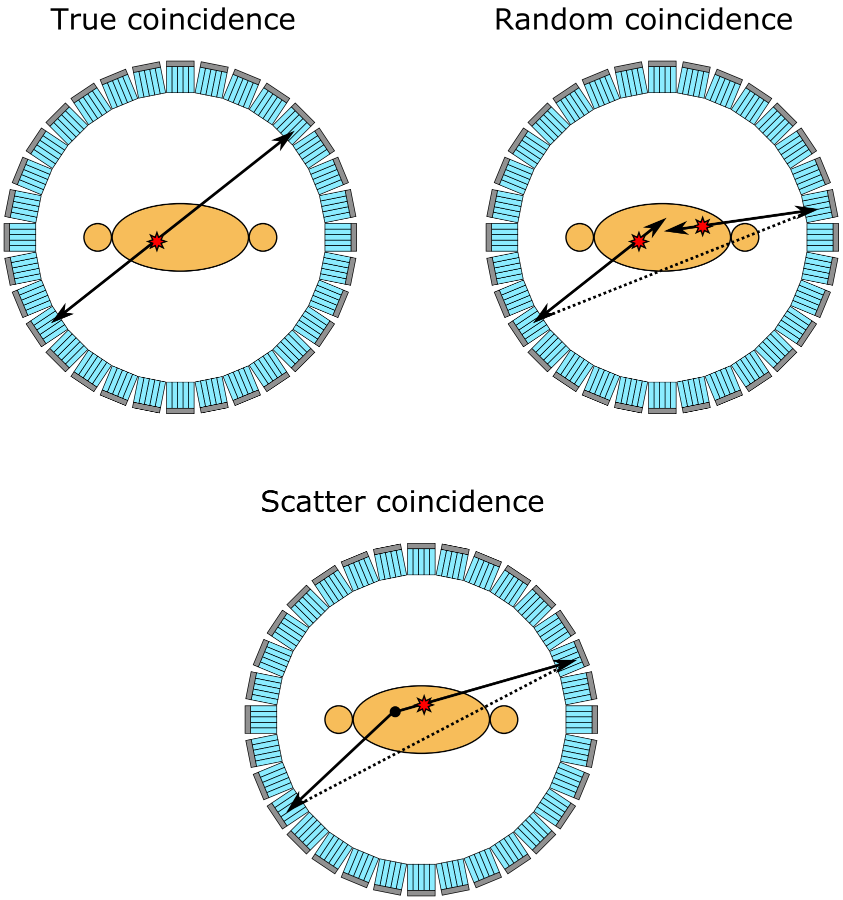

Figure 1.6: Pictorial representation of a *true* coincidence event (left), a *random* coincidence event (center) and a *scatter* coincidence event (right). Random and scatter coincidence events introduce false coincidences in the acquired data and contribute to a uniform background and an increased noise.

for PET detectors. Second, since $r_{d1}$ and $r_{d2}$ depend both linearly on the total amount of activity, the random rate depends quadratically on it. In general, $r_{d1}$ and $r_{d2}$ depend on the geometry of the scanner and of the imaged object in a complex manner, therefore each system has to be optimized in a different way to maximize the true to random events ratio. However, any expedient that can be used to reduce the single count rate without reducing the true coincidence count rate can be beneficial to improve the image quality. For example, a shielding of the detector ring that reduces the incoming number of photons from the area outside the FOV can significantly help in reducing the random count rate.

Since coincidence events due to random events add counts into the projection data but do not add any meaningful information, the effect of randoms is to add a more or less continuous background to the image and therefore reduce the image contrast. Moreover, they contribute to the statistical noise of the image (see section 1.2.4.4). There are several techniques to estimate the expected number of random events and subtract their contribution during image reconstruction [28]: however, these techniques cannot reduce the increased statistical noise and could leave a remaining bias. Therefore, randoms should always be minimized as much as possible during PET acquisitions.

#### 1.2.4.2. Scattered events

Compton scattering is an inelastic collision between a photon and a charged particle (most often an electron of the medium in which the photon is propagating), during which the photon transfers parts of its energy to the particle and deflects from its original trajectory by an angle $\Theta$. The energy of the scattered photon $E_{sc}$ and the scattering angle $\Theta$ can be related using the laws of conservation of momentum and energy. For the case of a scattering event with an electron, the relation is given by:

$$E_{sc} = \frac{E_0}{1 + \frac{E_0}{(m_0 c^2)}(1 - \cos\Theta)} \tag{1.2}$$

where $E_0$ is the original photon energy and $m_0 c^2$ is the rest mass of the electron. The scattering angle can assume any value between 0 (no energy transfer) and $\pi$ (maximum energy transfer); however, the angular distribution of the scattered photons is not isotropic and depends on the energy of the incident photon. More details on the shape of this distribution can be found for example in [29]. For PET applications, it is important to notice that 511 keV photons are more likely scattered in the 'forward' direction, i.e. with a small angle $\Theta$ and a relatively small energy loss.

Compton scattered photons introduce false coincidences (scattered events), since the resulting LOR does not intersect the annihilation point (see Figure 1.6). In theory, scattered photons can be discriminated and filtered out by measuring the photon energy. However, the energy resolution of average PET detectors is in the order of 10-15%, which corresponds to a scattering angles of ~27°-35°. Therefore, it is necessary to compromise on the scanner capability to identify and discard Compton events in order not to filter out also full-energy events. Moreover, Compton interactions can also happen in the detector absorbing material, yielding to an incomplete energy absorption in the detector. Since incomplete energy absorption can be quite frequent in PET detectors, usually the energy threshold used to select the events is quite low in order not to limit excessively the scanner sensitivity. For these reasons, an efficient discrimination of photons scattered in the imaged object is difficult in PET scanners.

Unlike random coincidences, the fraction of scattered events does not depend on the amount of activity but only on the geometry of the imaged object and of the scanner (since scattering can also happen in the scanner passive components, e.g. the patient bed and the structure of the scanner). In practice, the larger (and more dense) is the object to be imaged, the larger is the fraction of scattered events. For example, in abdominal imaging the scattering to true coincidence ratio can range from 0.4 up to 2, depending on the size of the patient and the type of acquisition that is used (2D or 3D acquisition).

LORs defined by a coincidence event in which one of (or both) the photons underwent to Compton scattering do not carry any useful spatial information on the position of the annihilation event. Therefore, Compton scattered events have an effect similar to random events, even if in this case the additional background tends to be more concentrated in the central part of the image. As for random events, there are techniques that can be used to estimate and subtract the contribution of (non-discriminated) scattered events from the final image [30–32]. However, also in this case scattered events contribute to increase the statistical noise (see section 1.2.4.4) and could introduce some bias in the image.

#### 1.2.4.3. Dead time of PET detectors and dead-time correction

As most detectors, also PET detectors require that two events are separated by a minimum amount of time in order to be able to correctly record them as separate interactions. This time interval is needed for example by photosensors to be recharged and restore their full sensitivity or by readout electronics to correctly acquire, process, transmit and record the signals. If an event happens during this minimum separation time, called dead time, it will be lost and it might even spoil the acquisition of the previous event (pile-up) or of the following event.

Two different models are usually defined to describe the dead-time behavior of radiation detectors: the nonparalyzable and paralyzable response. In the first model, each event recorded during the "live time" of the detectors is followed by a fixed amount of time ($\tau$) during which the detector is not sensitive to any other event. Events occurring during this period are not recorded and do not modify/extend the duration of the dead period of the detector. In the paralyzable model, instead, if an event occurs during the dead period $\tau$ following a true event, this event is not recorded and it also extends the dead period of another period $\tau$ after its interaction. The two behaviors determine different event losses, especially at high count rates. In nonparalyzable detectors, the observed-event rate as a function of the true-event rate increases asymptotically toward the maximum value $1/\tau$. In nonparalyzable detectors, instead, the observed-event rate reaches a maximum value equal to $1/(e \cdot \tau)$ and then decreases with a further increase in the true-event rate, approaching a value of zero for an infinite true-event rate. In any case, they are idealized models and real detectors might have a behavior that show a combination of elements of both of them. A thorough discussion of these models is outside the scope of this thesis and can be found in [29] and in [1].

At scanner level, the event loss due to detector dead time determines an error in the quantitative estimation of the tracer uptake in the different regions of the image, in particular during high-count-rate acquisitions. Therefore, a dead-time correction is usually performed during image reconstruction, which compensates for the event loss and makes it possible to obtain more reliable and accurate estimations of the activity. These corrections can be performed fitting paralyzable or non-paralyzable models to the whole system, to each detector pair or to singular detectors and can be as large as a factor of 2, especially if regions with high activity are imaged (e.g., close to the bladder) or an initial high activity is used (e.g., for studies employing $^{15}$O).

Despite these corrections, detector dead time can determine errors in the quantitative estimation of the activity and can introduce additional statistical noise (see section 1.2.4.4). Therefore, in PET scanners dead time should always be minimized as much as possible in all the levels of the signal-acquisition chain (detector hardware, front-end electronics, acquisition and processing electronics, etc.) in order to obtain the best possible image quality.

#### 1.2.4.4. Statistical noise and NECR

In a PET scanner, data acquisition consists essentially of a counting process that registers the number of times each possible couple of detector elements (i.e. each possible LOR) detects a coincidence. This counting process is usually assumed to follow Poisson statistics: therefore, for a given LOR, the standard deviation $\sigma_\lambda$ on the number of the measured true coincidences $n_\lambda$ can be estimated to be $\sigma_\lambda = \sqrt{n_\lambda}$. This uncertainty is called statistical noise and affects the noise of the final reconstructed image. If only true coincidences are considered, the signal-to-noise-ratio (SNR) for each pixel in the projection space (i.e. each LOR) corresponds to $\sqrt{n_\lambda}$ and this error determines the noise of the final image during the image reconstruction process. For example, in FBP the value assigned to each image voxel corresponds to the weighted sum of the counts registered by all the LORs intersecting the voxel and therefore the variance of each image voxel value corresponds to the weighted sum of the variances of all the LORs. The minimum noise level that can be achieved in a PET image is therefore strictly determined by the number of measured coincidences, which is limited in different ways by the maximum amount of activity that can be administered to the patient, the scanner sensitivity and the total duration of the scan. In clinical scanners, statistical noise is often one of the most important limiting factor also for image resolution because it determines a lower limit on the dimension of the image voxels, since the smaller is the voxel the smaller is also the statistics for that voxel and therefore the SNR.

In normal acquisition conditions, further statistical noise is added to each LOR by random and scattered events that are registered along with true events. Also random and scattered events follow Poisson statistics and therefore, even if their average contribution can be subtracted from the final image (see sections 1.2.4.1 and

1.2.4.2), their variance increases the statistical noise on the number of measured coincidences and determines a degradation of the final SNR. In general, statistical noise can be improved by increasing the system sensitivity and reducing as much as possible the influence of random and scattered events, e.g. improving the system CRT and energy resolution.

Performance parameters that are commonly measured and quoted in PET scanners are the noise equivalent counting rate (NECR) curve and its peak value, which give an indication of the SNR achievable at image level by the system. The NECR is a parameter that accounts for the statistical noise due to real events, random events and scattered events in a single value: it is defined as the equivalent counting rate of only true events that would yield the same statistical noise obtained for the observed counting rate after random and scattered coincidences have been corrected for [1]. The formula to calculate the NECR is:

$$NECR = \frac{R_{true}^2}{R_{true} + a \cdot R_{Compton} + b \cdot R_{random}} \tag{1.3}$$

where $R_{true}$, $R_{Compton}$ and $R_{random}$ are the true, scattered and random event rate, $a$ is the fraction of the projection occupied by the imaged object and $b$ is equal to 1 or 2, depending from the method used to determine the random count rate.

Usually, the NECR is measured with a standard homogeneous phantom as a function of the total activity. The NECR curve has a complex dependence on the total amount of activity since true-, scatter- and random-event rates depend in a different way on the total amount of activity, the geometry of the scanner and of the imaged object, the detector dead time, etc. Figure 1.7 shows an example of a NECR curve, plotted together with the true-event rate ($R_{true}$), the scatter-event rate ($R_{scatter}$), and the random-event rate ($R_{random}$) curves. If detectors had no dead time, the true-event rate and the scatter-event rate curves should increase linearly with the activity whereas the random-event rate should increase quadratically with the activity. However, detector dead time reduces the acquisition rates for all event types, modifying the behavior of these curves and determining also the value at with the NECR curve achieves its maximum.

When the imaged object is a cylindrical phantom filled with homogeneous activity, it can be demonstrated that the SNR of the estimated activity values is roughly proportional to the square root of the NECR [1]. Therefore, a comparison of the NECR curves of two scanners gives an indication of the system that can obtain images with lower noise: if a scanner has an higher NECR value for a certain activity level, this should correspond to the capability of the scanner to achieve an higher equivalent count rate of true events and therefore a better SNR at image level. Equivalently, the peak value of the NECR curve is considered a performance parameter that gives an indication of the best SNR achievable at image level by the system; the value at which the peak NECR is obtained, instead, suggests the amount of activity that provides the images with the best SNR. These considerations are true for a simplified model of the system and of the imaged objects and do not take into account other techniques that can improve the image noise, e.g. the time-of-flight (TOF) technique (see section 1.2.5). However, NECR curves and

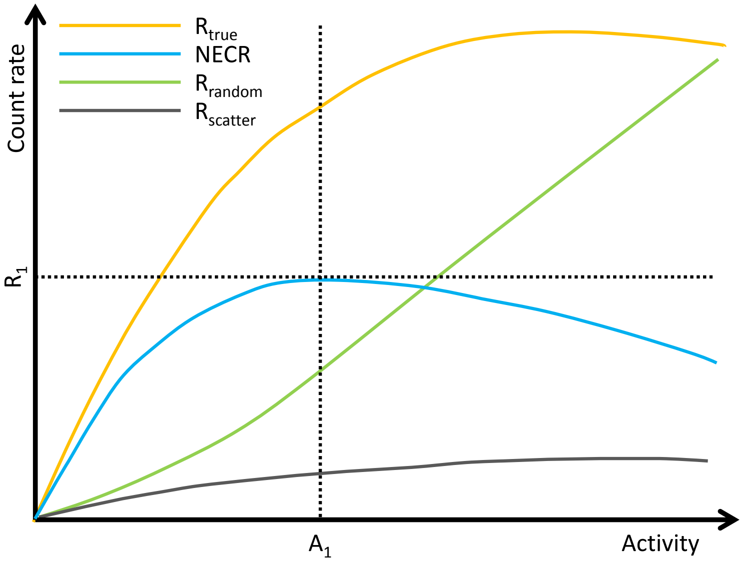

Figure 1.7: Example of a noise equivalent counting rate (NECR) curve as a function of the activity, plotted together with the true-event rate ($R_{true}$), the scatter-event rate ($R_{scatter}$), and the random-event rate ($R_{random}$). The curve predicts that, for the phantom and the system used to measure the curves, the best signal-to-noise ratio in the image (i.e. the peak of the NECR curve) will be obtained for an activity equal to $A_1$

peak NECR values are still parameters that can be useful to consider to have e first comparison of different systems and to guide the development of new scanners.

### 1.2.4.5. Normalization, attenuation correction and dead time correction

During the image reconstruction process, a system model is used to relate the acquired data with the image and perform the back- or forward-projection operations. To obtain accurate quantitative estimations and avoid image artifacts, the system model has to accurately define the probability that a certain pair of detector elements (i.e. a pixel in the projection space) registers an annihilation event from a certain image voxel. This probability depends on the geometry and performance of the scanner but also on the total amount of activity and on the geometry of the imaged object. Usually, two corrections are needed to properly define the system model.

The first correction is usually called normalization and compensates for non-uniformities in the single and coincidence detection efficiency of the detector elements. These non-uniformities can be due to inaccuracies in the calibration procedures and in the scanner manufacturing or to small variations in the effective efficiencies of different elements, due for example to the different incidence angles of the incoming photons. This correction is usually performed by imaging well defined calibration sources and determining the ratio between the expected number of coincidences for each LOR and the number of coincidences actually measured. A detailed review on the effects that can be determined on the final image by a non-uniform detector response and of the methods used to perform normalization correction can be found in [33].

The second correction that is needed to obtain accurate images is attenuation correction, which compensates for the photons absorbed or scattered by the materials of the imaged object. Note that the probability to register an event along a certain LOR depends on the amount and density of the materials along that LOR. Therefore, to properly reconstruct the tracer distribution, attenuation coefficients have to be calculated for each detector pair so that the number of measured coincidences can be corrected for this effect. Originally, attenuation maps were obtained with transmission scans using external radioactive sources. However, this technique required lengthy acquisitions and contributed to introduce additional statistical noise. Currently, all PET scanners are integrated with complementary anatomical imaging systems such as CT scanners or MR systems (see section 1.1.4) and so these images are the most common source of information used to compute the attenuation maps.

For CT scans, the conversion between CT image units (Hounsfield units) and attenuation coefficients for 511 keV photons ($\mu$) is relatively straightforward, since CT scans are also transmission scans based on x-rays (even if CT beams have lower energies and are not mono-energetic). Currently, the most common conversion method is based on a continuous mapping between CT units and $\mu$, which is obtained with a piece-wise linear transformation [34].

For MR scanners the problem is less trivial, since MR-image intensity values are determined by proton density and tissue relaxation properties which cannot be directly related to electron densities, i.e. the quantity determining the linear attenuation coefficients for annihilation photons. Several different methods have been developed to overcome this problem, either based on an elaboration of MR images (e.g. image segmentation and tissue recognition) or on separate emission/transmission measurements [4, 9]. Currently, none of these method can provide the same accuracy as obtained with CT scans. However, this is an active field of research and future improvements are expected to definitely solve the issue.

### 1.2.5. Time-of-flight (TOF) PET

Since annihilation photons are emitted simultaneously, in principle it is possible to determine the position of an annihilation event on its LOR by using the time-of-flight (TOF) technique. With this technique, the distance $\Delta x$ of the annihilation point from the center of the LOR can be calculated measuring the difference $\Delta t$ between the times of interaction of the two gamma-rays with the detectors, using the following formula:

$$\Delta x = \frac{c \cdot \Delta t}{2} \tag{1.4}$$

where $c$ is the speed of light.

However, the finite timing resolution of PET detectors, i.e. the finite accuracy in determining the time of interaction of the gamma rays (see section 1.3.1), determines a consequent inaccuracy in estimating the position of interaction. If PET detectors have a CRT equal to $\sigma_t$, i.e. an uncertainty of $\sigma_t$ in determining the value $\Delta t$, an error equal to:

$$\sigma_x = \frac{c \cdot \sigma_t}{2} \tag{1.5}$$

is made in determining the position of the annihilation point.

In practice, if TOF information is used during image reconstruction the probability that the annihilation happened on a certain point of the LOR is not considered uniform any more but a certain probability distribution is assigned for each point of the LOR, which is related to the expected probability distribution of the error made in measuring $\Delta t$. This information is then used during image reconstruction as a weighting factor during back- or forward-projection and enables PET systems to reduce image statistical noise, since the signal of each coincidence is 'dispersed' on a smaller number of voxels.

Obviously, to provide a meaningful improvement TOF information should provide a positioning accuracy $\sigma_t$ significantly smaller than the diameter of the imaged object. For example, a timing resolution equal to 1 ns corresponds to a positioning accuracy equal to 15 cm. Therefore, in clinical applications, timing resolution in the order of 500 ps or better are needed to obtain meaningful improvements from the TOF technique.

In general, theoretical models show that for simplified systems (phantoms) the gain in the SNR of the image is proportional to the square root of the ratio between the diameter of the imaged object $D$ and the positioning accuracy $\sigma_x$:

$$SNR_{gain} = \frac{SNR_{TOF}}{SNR_{nonTOF}} \propto \sqrt{D/\sigma_x} \tag{1.6}$$

Therefore, the better is the CRT and the larger is the imaged object, the higher is the gain. A detailed discussion on the effects of TOF on the image noise is outside the scope of this thesis, interested readers can refer for example to [35–38].

Nowadays, state-of-the-art PET scanners have a CRT in the order of 200-400 ps (see section 1.3.4), providing a $SNR_{gain}$ estimated in the order of 2-4 for objects having a diameter ≥30 cm [35]. Single optimized detectors in optimal laboratory conditions can instead reach a CRT in the order of 60 ps for small crystal dimensions (see section 1.3.3.1): however, such values seem to be hardly achievable in practical PET scanners in the near future.

Recently, a community of researchers focused their efforts to further improve the timing performance of PET detectors, aiming at achieving a CRT in the order of 10 ps [39]. To achieve this value, they proposed a variety of novel approaches that are not based on standard scintillation detectors (see [40] for a comprehensive review). A CRT of 10 ps has been proposed because such a value would enable PET systems to localize the annihilation position along the LOR with an uncertainty in the order of ~1.5 mm, a dimension smaller or comparable to the voxel dimension used in image reconstruction in clinical PET. Therefore, the measurement would no longer consist of projections of the activity distribution but would be a list of 3D points of annihilation, which could be directly assigned to the image voxels. Therefore, a tomographic reconstruction from projections would not be needed anymore and, if no scatter and attenuation corrections were considered, a single back-projection step would be sufficient to reconstruct the images taking into account the system sensitivity. In any case, image reconstruction would still be required to obtain a reliable, quantitative estimation of the activity, since it would be necessary to perform scatter and random corrections. Moreover, advanced image reconstruction techniques could improve the image resolution by including the detector PSF and could also be used to directly estimate the attenuation map [40].

## 1.3. Gamma-ray detectors for PET

### 1.3.1. Detector requirements

As discussed in the previous sections, there are many factors that influence image resolution and noise in PET imaging. Some of these factors are directly dependent on the characteristics and the performance of the detectors employed to build PET scanners. The main detector features that have to be considered when a scanner is designed are:

- detector sensitivity ($\epsilon$), i.e. the probability to (correctly) detect an annihilation photon impinging on the detector surface;
- detector spatial resolution (eventually including the DOI estimation capability), i.e. the detector capability to correctly estimate the 2D (or 3D) points of first interaction of gamma-rays;
- coincidence resolving time (CRT), i.e. the uncertainty with which a couple of detectors can resolve the difference in time of interaction of two gamma rays in a coincidence event;

- energy resolution, i.e. the detector precision in measuring the gamma-ray energies.

Other detector characteristics that have to be taken into account are maximum count-rate and dead-time behavior, insensitivity to magnetic fields (in case of integrated PET/MR scanners), temperature of operation, overall power consumption, computational/memory requirements for data acquisition and data processing. Besides these technical features, other important characteristics are detector robustness and reliability, easiness of production/calibration/operation, and, of course, cost.

Since in different scanners each detector property has a different influence on the final quality of the images, different tradeoffs have to be made depending on the application. For example, in whole-body clinical PET the detectors are required to have excellent sensitivity, excellent CRT, good spatial resolution and good energy resolution.

High sensitivity $\epsilon$ is the foremost requirement since statistical noise is currently one of the most significant limiting factors for this application (see section 1.2.4.4). Therefore, to maximize the number of detected events is vital in order to improve the image SNR, also considering that the true coincidence count rate scales with $\epsilon^2$.

Excellent timing resolution is also very important since it enables PET scanners to reduce the width of the coincidence window and therefore the number of random events; moreover, good CRT also significantly reduces the image noise if it enables scanners to use the TOF technique (see section 1.2.5).

The requirements on the detector spatial resolution are, instead, not too demanding since a spatial resolution in the order of 2-3 mm in the plane perpendicular to the radial direction of the scanner (x-y spatial resolution) is usually considered the lowest limit that is necessary to target for clinical PET detectors. In fact, any further improvement in spatial resolution would yield a limited gain because of the influence of many other unavoidable limiting factors such as positron range, photon acollinearity, and the minimum dimension of the image voxel, which cannot be indefinitely reduced for statistical reasons. However, detectors that could provide DOI information would be a very useful improvement in clinical PET scanners, since they would enable PET systems to improve the spatial resolution in the external regions of the FOV and to provide a more homogeneous response throughout the whole imaged area. Finally, an energy resolution of or below 12% is usually considered adequate, since most of the times the width of the energy window is determined not by the energy resolution but by sensitivity requirements (see sections 1.2.4.2 and 1.2.4.4).

For comparison, in small-animal PET systems usually the detector requirements are quite different compared to clinical systems, due to the very different geometrical dimensions and constraints of the scanners. For this application, the foremost requirement is an excellent x-y spatial resolution, even in the order of 0.5 mm for some small-bore scanners, and possibly DOI estimation. Timing resolution, instead, is usually not required to be excellent, since TOF technique cannot be used for small-FOV systems (a CRT in the order of few tens of ps would be needed to profitably use TOF information). An energy resolution ≤20-25 % is usually considered adequate, since few Compton scatters are expected in small imaged objects and therefore energy windows are usually very wide, in order to acquire also the photons scattered in the detectors. Finally, also the detector sensitivity can be reduced compared to clinical scanners, if this yields an improvement in the spatial resolution. A lower detector sensitivity can be usually compensated for by covering a wider solid angle with the PET scanner, which for small-radius systems can be done with a limited increase in the total cost.

### 1.3.2. Scintillation detectors: working principles and main components

Practically, all PET detectors employed in research and in commercial scanners are scintillation detectors based on inorganic scintillation crystals read out by fast photosensors. Scintillation crystals are particular crystals having the property to convert the energy deposited by ionizing radiation interacting with them into a number N of (near-)visible photons, proportional to the absorbed energy. Therefore, by measuring the light emitted by a scintillation crystal it is possible to detect the interaction of gamma rays and to estimate their energy and time of interaction.

In PET applications, these crystals are usually read out by fast photodetectors with internal gain such as photomultiplier tubes (PMTs) and silicon photomultipliers (SiPMs). These sensors can convert the weak light signals produced by scintillation crystals (in the order of thousands of photons are typically emitted) into usable current pulses without introducing substantial noise in the signal.

In a standard scintillation detector, the crystal is usually coupled to the photosensor by means of a transparent glue or grease, which has an index of refraction that facilitates the transmission of the light from the crystal towards the photosensor. Tipically, the crystal is also wrapped with reflective material (either specular or diffusive) that reflects back the light impinging on the crystal surfaces not coupled to the photosensor and maximizes the light collected by the photosensor.

Besides inorganic scintillation detectors, several other detector technologies have been proposed for PET applications and have been investigated by means of simulations or with experimental measurements. These technologies comprehend organic scintillation detectors [41, 42], semiconductor detectors [43], resistive plate chambers (RPCs, i.e. fast gaseous detectors) [44, 45], scintillation detectors based on liquid Xenon [46] and pure Cherenkov detectors [47, 48]. Currently, none of these technologies has demonstrated to be able to provide better system performance compared to inorganic scintillation detectors; however, research is still ongoing and some of them could demonstrate some advantages, for example in specific dedicated PET systems.

A hybrid approach has also been recently proposed, which is based on inorganic scintillation detectors that also use the Cherenkov signal produced by the interaction of gamma rays inside the crystals in order improve the timing resolution [49]. This topic is currently an active field of research and initial calculations predicted that this approach might make possible to develop new innovative detectors with excellent TOF capabilities (≤50 ps) based on crystals (e.g. BGO) that do not have fast scintillation properties [39, 50, 51]. Despite more recent calculations showed that these predictions might be too optimistic [52], several experimental works demonstrated that indeed Cherenkov emission can improve timing performance of BGO crystals [53–56]. The hybrid Cherenkov/scintillation approach might therefore be a viable approach to obtain cost-effective TOF-PET detectors based on relatively inexpensive materials like BGO.

#### 1.3.2.1. Scintillation crystals for PET applications

As briefly described in the previous section 1.3.2, inorganic scintillation crystals are particular types of crystals that can convert the energy released inside them by ionizing radiation into a faint light signal. In practice, when gamma rays interact with a scintillation crystal via a photoelectric or a Compton interaction, they transfer all or part of their energy to an electron. This resulting high-energy electron ionizes the crystal creating electron-hole pairs that, in turn, transfer the deposited energy to luminescent centers. These centers are particular sites of the crystal lattice characterized by energy levels whose de-excitation results in the emission of a (near-)visible photon. The final result of the process is the emission of a number N of low energy photons, N being (roughly) proportional to the deposited energy E. The wavelength of these photons is usually in the range between 350 nm and 600-700 nm, depending on the scintillation materials, even if higher or lower wavelengths are also possible.

Usually, the time profile of the light signal emitted by a scintillation crystal can be modeled as the convolution of two exponential functions representing the energy transfer mechanism (rising edge of the signal, defined by the rise time constant $\tau_r$) and the radiative decay (defined by the decay time constant $\tau_d$). However, many crystals show two or more exponential components both for the rise and the decay part of the signal, each of them determined by different energy-transfer or radiative-emission mechanisms [51].

The most important properties which have to be considered when choosing an inorganic scintillator for PET applications are:

- Light yield (LY), i.e. the number of photons emitted per unit of absorbed energy: LY is usually measured in photons/MeV and can range from a few hundred photons/MeV up to $\sim 10^5$ photons/MeV;

- Energy linearity, i.e. how constant is the LY depending on the amount of energy deposited in a single point of the crystal;

- Intrinsic energy resolution, i.e. the best energy resolution that can be achieved for 511 keV photons (which is determined by the LY and the linearity of the crystal);

- Density and effective atomic number ($Z_{eff}$), which determine the stopping power of the material for annihilation photons and the photoelectric interaction probability;

- Rise ($\tau_r$) and decay ($\tau_d$) time(s) of the scintillation pulse;

- Emission spectrum, i.e. the wavelength distribution at which the scintillation photons are emitted;

- Absorption spectrum, i.e. the wavelengths that are absorbed by the crystal, which might determine a partial self-absorption of the light signal if the emission and absorption spectra significantly overlap;

- Practical aspects, such as hygroscopy, easiness of production in large dimensions and large quantities, cost, etc.

As discussed in section 1.3.1, PET detectors for clinical applications should have high sensitivity, fast CRT, good spatial resolution and good energy resolution.

In order to achieve high sensitivity the crystals should have an high gamma-photon detection efficiency, which is determined by their density, effective atomic number and total thickness. Spatial resolution, CRT and energy resolution usually deteriorate for thicker crystals, since on average photons undergo a larger number of reflections before being detected by the photo-sensor. This introduces a larger variance on their time of arrival on the photo-sensors and also on their number, due to inefficiencies in the reflection process. For this reason, scintillators with high density and high $Z_{eff}$ are usually preferred for PET applications, since they allow detectors to achieve higher efficiency with thinner crystals.

An additional advantage of high-density and high-$Z_{eff}$ scintillators is that they have an higher photoelectric-interaction probability and an higher stopping power for photons that underwent Compton scattering inside the crystals. Thanks to this property, the gamma-ray energy is (on average) deposited in a smaller volume, further improving the spatial resolution and detection efficiency.

Besides high density and $Z_{eff}$, crystals used in PET applications should also have high LY, since this characteristic usually improves the spatial resolution and the energy resolution, the latter of which is also strongly dependent on the energy linearity. High LY is also a key parameter to obtain fast timing, alongside with fast rise and decay time, as demonstrated in [57].

In Table 1.3, a brief list of some scintillation materials that are used or are considered for medical applications is reported. In first PET scanners, NaI used to be the most commonly used scintillator, thanks to its high light yield, low cost, and easiness of production. However, due to its relatively low density, this material is sub-optimal for high-energy gamma detection. When denser scintillators were developed, BGO became the standard material for commercial scanners thanks to its higher stopping power and photoelectric interaction probability. However, its relatively low light yield and especially its rather long decay time make it unsuitable for TOF applications. Currently, the most commonly used materials in PET scanners are lutetium-based scintillators (LSO, LYSO, LFS), since they can combine a rather high density, high light yield and fast rise and decay time.

For interested readers, updated reviews of the trends and advances in inorganic scintillators, also for medical applications, can be found in [58] and [59].

Table 1.3: Most common scintillation materials which are used or are considered for medical applications.

| Crystal | Density (g/cm$^3$) | $Z_{eff}$ | Attenuation length (mm) @511 KeV | Photo-Electric prob (%) | Light Yield ($10^3$ ph/MeV) | Rise time ($\tau_r$, ps) | Decay time ($\tau_d$, ns) | Peak emission ($\lambda_{max}$, nm) | Hygro-scopic | Index of refraction |
|---|---|---|---|---|---|---|---|---|---|---|
| NaI:Tl | 3.67 [1] | 50 [1] | 29.1 [60] | 17 [60] | 38 [58] | - | 230 [1, 60] | 410 [60] | Yes [1, 60] | 1.85 [1] |
| CsI:Tl | 4.51 [1] | 54 [1] | 22.9 [60] | 21 [60] | 54 [58] | - | 1000 [1] / 800 [60] | 550 [60] | Slightly [1, 60] | 1.8 [1] |
| BGO | 7.13 [1] | 73 [1] | 10.4 [60] | 40 [60] | 9 [58] | - | 300 [1, 60] | 480 [60] | No [1, 60] | 2.15 [1] |
| LSO:Ce | 7.40 [1] | 66 [1] | 11.4 [60] | 32 [60] | 27 [58] | 50-90 [51] | 40 [51] | 420 [60] | No [1, 60] | 1.82 [1] |
| LSO:Ce,Ca (0.2%) | see LSO:Ce | see LSO:Ce | see LSO:Ce | see LSO:Ce | - | ≤ 10 [51] | 33-35 [51] | - | No [1, 60] | - |
| LYSO:Ce | 7.2 [58] | - | - | - | 30-32 [58] | 65-80 [51] | ~ 40 [51] | - | No [1, 60] | - |
| GSO:Ce | 6.71 [1] | 59 [1] | 14.1 [60] | 25 [60] | 12.5 [58] | - | 60 [1, 60] | 440 [60] | No [1, 60] | 1.85 [1] |
| LuAP:Ce | 8.34 [1] | 65 [1] | 10.5 [60] | 30 [60] | 10 [58] | - | 18 [1, 60] | 365 [60] | No [1, 60] | 1.97 [1] |
| LaBr3:Ce | 5.3 [1] | 46 [1] | 21.3 [60] | 13 [60] | 61 [58] | 270 (72%) [61] | 15 [61] | 360 [60] | Yes [1, 60] | 1.9 [1] |

#### 1.3.2.2. Photosensors for PET applications

Besides scintillation crystals, PET detector performance is also strongly influenced by the characteristics of photodetectors used to read out the scintillation light. One of the most important photodetector properties that has to be optimized for PET applications is the photon detection efficiency (PDE), i.e. the probability that a photon impinging on the sensor surface is converted into a measureable electric signal. The main factors that contribute to the sensor PDE are the geometrical efficiency, i.e. the ratio between the active area of the photosensor and its total area, the optical efficiency, i.e. the probability that a photon impinging on the active area of the sensors surface is transmitted to the active volume, and finally the internal quantum efficiency (QE), i.e. the probability that a photon absorbed in the active volume gives rise to a detectable electric signal. It has to be noted that optical efficiency and QE depend on the photon wavelength, thus photosensors have variable PDE for photons of different energies in the (near) visible spectrum. It is therefore important to optimize photosensor characteristics so that their PDE is maximized for the emission spectrum of the chosen scintillation crystal.

Besides high PDE, photosensors should also have a fast timing response in order to best use the timing information contained in the scintillation photons. Usually the timing performance of a photodetector is characterized by the so-called single photon timing resolution (SPTR), which describes the photosensor accuracy in measuring the time of arrival of a single photon.

Considering that usually only few thousand photons are detected for each scintillation event, the corresponding charge that would be created in a photosensor without internal gain (i.e. in which a single electron is created for each detected scintillation photon) is in the order of about 0.1-1 fC. To measure this small amount of charge and its time of arrival with high accuracy would pose extreme requirements on the readout electronics, since usually it is difficult to minimize the electronic noise in fast readout electronics. For this reason, high internal gain ($>10^5$) is usually desirable in photosensors for PET applications, in order to minimize the influence of electronic noise on the measurement of the intensity and the time of arrival of the light signal.

Finally, other important characteristics for photon detectors are ruggedness, cost, easiness of operation (e.g. necessity of high voltage or temperature stabilization), number of readout channels and, in case of integrated PET/MRI, insensitivity to magnetic fields.

Originally, the most used photosensors for PET applications were photomultipliers tubes (PMTs), first introduced in the 1930's [62]. These sensors are composed by a transparent entrance window covered with a photo-emissive substance, called photo-cathode, and a series of metal electrodes, called dynodes, that are contained into an evacuated body and are biased using a voltage divider. The photo-emissive substance has the property to emit an electron when a (near-)visible photon interacts with it. The emitted electron is then accelerated by the electric field created between the photo-cathode and the metal electrodes and is focused on the first dynode. The kinetic energy gained by the electron determines the extraction from the first dynode of a number of secondary electrodes ($\sim$10), which are then accelerated towards the following dynodes and are further multiplied until they are collected on the last electrode, called anode.

PMTs usually can achieve a gain $\geq 10^6$ and a PDE in the order of 20-30% for the wavelength of maximum sensitivity. Timing properties of PMTs usually depend on the dimension of the sensitive area and on the dynode structure: typical SPTR values are in the order of 0.2-1 ns.

An evolution of standard PMTs are the position-sensitive PMTs (PS-PMTs), which have different series of dynodes positioned in a grid so that each series separately multiply electron extracted from different positions on the photocathode. This structure makes it possible to reduce the spread in the electron transit time, improving timing performance, and to obtain information on the spatial distribution of the light signal.

Some of the major disadvantages of PMTs and PS-PMTs for PET applications are their bulky dimensions, the high voltage (> 1 kV) required to operate them, their limited PDE, which cannot be higher than 35-40%, and their extreme sensitivity to magnetic fields, which makes them unsuitable for integrated PET-MRI.

Another type of photosensor based on a concept similar to standard PMTs is the micro-channel plate PMT (MCP-PMT), in which the metal dynodes are substituted with a 2D array of glass micro channels [63, 64]. These glass channels are only few microns wide, are polarized with a potential difference across their extremities and act as continuous dynodes along their entire length. In practice, electrons produced by a photocatode are first accelerated towards the micro-channels and then multiplied inside these structures by multiple interactions with the channel walls (which act as secondary electron emitter) while they move towards the exit of the channels. The major advantages of MCP-PMTs compared to standard PMTs are their excellent timing properties (SPTR $\leq$ 100 ps) combined with the possibility to obtain spatial information if the readout anode below the micro-channels is segmented. However, their relatively high cost has limited their application in commercial PET systems.

A different class of photosensors used in PET applications are solid-state silicon photosensors with internal multiplication. The simplest type are avalanche photodiodes (APDs), which are reverse biased photodiodes with internal, proportional multiplication. The multiplication is obtained by designing the internal structure of APDs so that at high reverse bias voltages (300-400 V) a depleted region with high-intensity electric field is created. In this region, the charge carriers created by the interaction of scintillation photons in silicon are multiplied by means of the impact ionization mechanism and a gain in the order of $10^2$-$10^3$ is obtained.

APDs can achieve a very high QE (even in the order of 80%), are virtually insensitive to magnetic fields, and are much more compact and rugged than PMTs. However, their low gain poses higher requirements on the readout electronics compared to PMTs and usually determines a lower signal-to-noise ratio for the scintillation signals. This characteristic, in combination with their high capacity, leads also to worse timing resolution compared to optimized PMTs. Moreover, the gain of APDs has a strong dependence on the operating temperature and APDs suffer of a much larger noise compared to PMTs, due to the dark current generated in silicon by thermal excitation of charge carriers. These issues can be mitigated by cooling the sensor, finely stabilizing the temperature and designing compensation mechanisms that maintain a constant gain by adjusting the bias voltage. However, these requirements add up to the complexity of the system and make APDs more difficult to be operated compared to PMTs.

Due to their poor timing resolution and the difficulty to operate them, APDs have never found widespread application in PET systems. In the past they have been used only in few small animal scanners [65], which benefit from their compactness, and also in the first integrated clinical PET-MR scanner [10], which used APDs because they were the only photosensors that could be operated in a strong magnetic field at the time.

A different type of silicon photosensor with internal multiplications is the silicon photomultiplier (SiPM) (Figure 1.8), also called solid state photomultiplier (SSPM) or multi pixel photon counter (MPPC), which has been introduced at the beginning of 2000s [66, 67]. SiPMs are large arrays of single photon avalanche diodes (SPADs, also referred to as Geiger-mode avalanche photodiodes, GM-APDs), i.e. small APDs specifically designed to be operated above their breakdown voltage, whose dimension is usually comprised between 10 $\mu$m and 100 $\mu$m. In such a meta-stable condition, when a carrier is generated into the depleted region by a (near-)visible photon and drifts into the high-electric-field region, it triggers a divergent multiplication which becomes self-sustaining and spreads across the whole diode. This discharge is then quenched by an integrated external circuit, which can either be passive (a quenching resistor) or active (a transistor that actively quenches and resets the SPAD). The amount of charge generated in an avalanche is constant and independent of the number of initial carriers; therefore, to have a quantitative measurement of the number of photons hitting an SiPM, the light signal has to be spread on many micro-cells so that on average less than one photon is hitting a single SPAD. In such a condition, the number of firing micro-cells is proportional to the intensity of the light signal.

Two different types of SiPMs are currently used in medical imaging applications, analog SiPMs and digital SiPM. Analog SiPMs are arrays of passively quenched SPADs connected in parallel to a common output: such devices provide as output a current signal whose total amount of charge is proportional to the number of firing micro-cells. Digital SiPMs, instead, are arrays of actively quenched SPADs, which usually have an integrated circuitry that can count the number of triggered cells and outputs this value as a digital signal. A complete discussion on the working principle and the characteristics of analog and digital SiPMs is outside the scope of this thesis; however, interested readers can find updated reviews of analog and digital SiPMs technologies in [68, 69] and in [70], respectively.

SiPMs can achieve a high peak PDE (even higher than 60%), can be operated using low bias voltage ($\leq$50 V), and they can be used to produce segmented arrays with different pixel dimensions (1-5 mm pitch). Single SPADs can achieve SPTRs in the order of 20-30 ps and even with large area SiPMs (3 mm × 3 mm) SPTRs $<$ 100 ps can be obtained [71]. Similarly to APDs, SiPMs are also compact, rugged and insensitive to magnetic fields. Analog SiPMs are characterized by very high gain

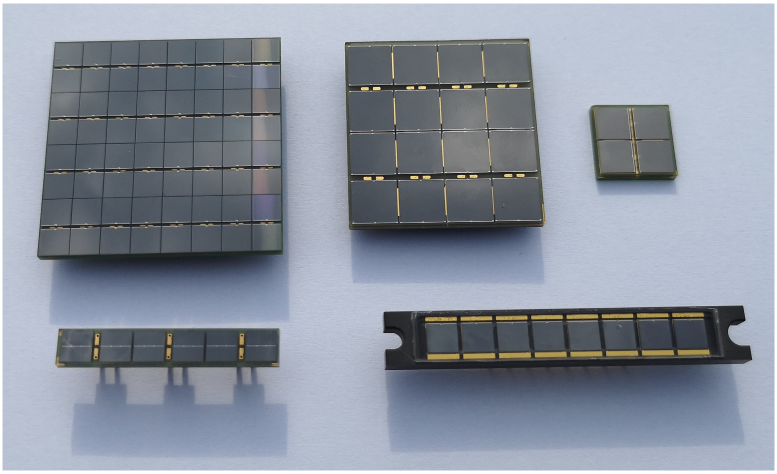

Figure 1.8: Picture of different SiPM arrays produced by Fondazione Bruno Kessler (FBK).

(~$10^5$-$10^6$), whereas digital SiPMs have integrated readout electronics to count the number of fired cells and acquire time stamps. Thanks to these favorable characteristics, analog or digital SiPMs are currently employed in the high-end clinical PET scanners of essentially all commercial manufacturers at the time of writing.

### 1.3.3. Detector architectures

Different scintillation detector architectures have been developed and used over the last decades to build research and commercial PET systems [4]. The first PET scanners employed single, wide scintillation crystals (~ 5 cm wide) one-to-one coupled to single PMTs [72, 73]. These detectors had limited spatial resolution and efficiency and therefore, in the first large-area scanners, they were substituted by optimized versions of the gamma camera (Figure 1.9) developed by Hal Anger for SPECT applications [74]. In particular, thicker crystals were introduced to increase the efficiency for 511 keV photons. The Anger camera is a detector composed of a single, wide slab of scintillator (e.g. NaI) read out by an array of PMTs, in which the position of interaction is estimated by using a weighted centroid algorithm.

In the following developments, the unsegmented scintillators used in gamma cameras were substituted by segmented blocks, partially or completely subdivided into smaller pixels. In these detectors, the position would still be decoded by an array of photosensors using light-sharing techniques and weighted centroid algorithms. Segmented scintillators were introduced in order to confine the light into relatively small crystal elements, so that the spread of the light on the photosensors could be controlled also with thicker crystals, allowing detectors to achieve higher sensitivity without deteriorating the spatial resolution. One of the most successful architectures based on this concept was the so-called block detector [75] (Figure 1.9): this detector is based on a single block of BGO in which partial cuts of different depths are introduced in the crystal and in the light guide in order to control the

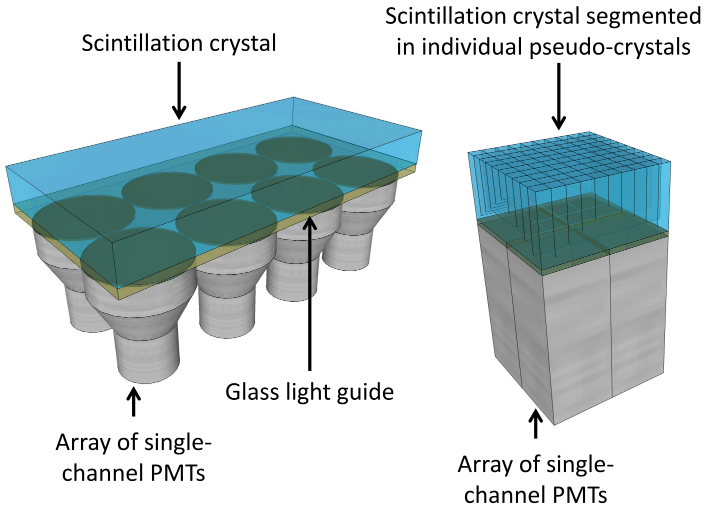

Figure 1.9: Schematic drawing of a gamma or Anger camera (left) and of a block detector (right) for PET applications.

light spread on an array of 4 PMTs. These pixelated detectors allowed to achieve a spatial resolution in the order of 5-10 mm, depending on the segmentation of the crystals and the module architecture.

Current PET detectors are basically the evolution of these two different detector architectures, one based on unsegmented (or monolithic) crystals and the other one on pixelated crystal matrixes. In both cases, modern detectors benefit from the progresses made in the field of scintillating materials and of photosensors technologies. In the following sections, a more detailed description of the advantages, the limitations and the possible developments of detectors based on pixelated or unsegmented crystals are reported. For interested readers, an excellent historical review on the developments of PET detectors and PET systems can be found in [76]. A very complete review of the state of the art in PET instrumentation can instead be found in [77], together with a thorough discussion of the possible developments that could impact the field.

#### 1.3.3.1. Pixelated detectors

Pixelated detectors are usually built coupling an array of crystals with high aspect ratio, optically isolated by a reflecting material, to an array of photosensors via a thin light guide (Figure 1.10, left). The pixelated photosensor, usually an array of SiPMs, an array of PMTs, or a PS-PMT, is often composed of elements with wider pitch compared to the crystal array and the position decoding is usually performed using a weighted centroid algorithm and a look-up table (LUT).

An alternative architecture for pixelated detectors is based on a one-to-one cou-

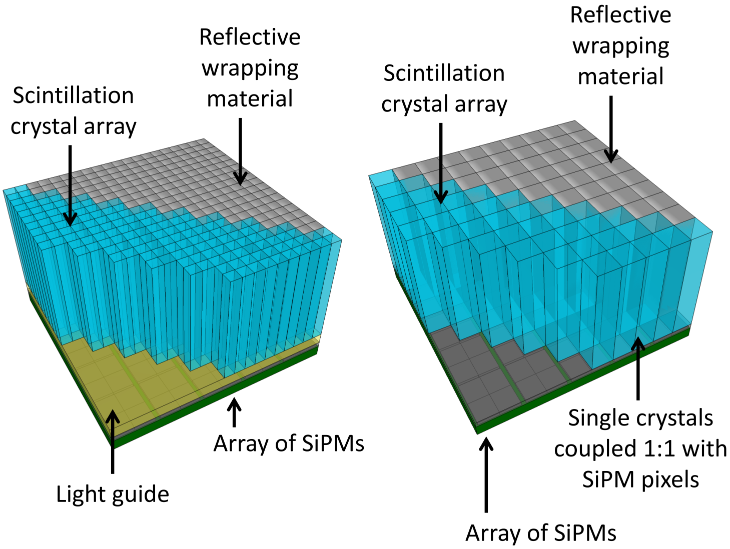

Figure 1.10: Schematic drawing of two differet pixelated-detector architectures. On the left side, the crystal array is coupled to the SiPM array through a thin light guide: the scintillation light coming from a single crystal is shared among different SiPM pixels and position decoding is performed using a weighted centroid algorithm. On the right side, the scintillation crystals are 1:1 coupled with the SiPM pixels and therefore the whole light coming from a single crystal is read out by a single photosensor channel.

pling scheme (Figure 1.10, right) in which each separate crystal pixel is directly coupled to a single photodetector element. In this scheme, no positioning algorithm is needed and the count rate can be maximized. Moreover, for detectors with the same crystal dimensions, the one-to-one coupling technique is expected to have better timing resolution than the light-sharing technique, since the light signal is focused on a single sensor. However, the one-to-one coupling scheme requires a larger number of readout channels, increasing the complexity and cost of the detectors.

In both configurations, usually the time of interaction is estimated from the rising edge of the photodetector signal(s) by using standard techniques such as leading edge discrimination (LED) or constant fraction discrimination (CFD), which require low processing resources.

Currently, all detectors used in state-of-the-art commercial clinical PET scanners are based on pixelated detectors read out by SiPMs arrays. These detectors typically have a crystal pitch of 3-4 mm and a crystal thickness of ~ 20-25 mm, do not provide DOI estimation, have an energy resolution of 10-12% FWHM and achieve a CRT in the range of 200-400 ps FWHM (see section 1.3.4).

Pixelated detectors are also common in pre-clinical and high-resolution systems: in these applications they usually have a pitch of ~1-2 mm, a thickness of ~10 mm, an energy resolution ~15-20 %, and do not provide TOF information. Some of those systems are also able to provide DOI information (e.g. the dedicated brain scanner ECAT HRRT [78]), even if in most of pre-clinical scanners thin crystals are used (~10 mm) in order to reduce the parallax error, at the expense of some sensitivity.

Focusing on detectors for clinical applications, at present most research effort is focused on developing detectors with better timing performance and with DOI capability, preserving or slightly improving the current spatial resolution.

As regards timing, the most recent improvements of the single detector components (scintillation crystals, photosensors and readout electronics) are pushing the limits that can be obtained with a standard detector architecture. As a result, outstanding CRTs of ~60 ps for small crystals (2 mm × 2 mm × 3 mm) and of ~100 ps for thicker crystals (2 mm × 2 mm × 20 mm) have been recently presented [55], thanks to the most recent advances in SiPM technologies and to optimized readout electronics. Besides these developments, other research group are also trying to improve the time estimation techniques by using statistical methods, showing promising results [79, 80].

All these developments will probably make it possible to obtain incremental improvements in timing performance of future scanners. However, it will be difficult to achieve exactly the same results in real detector modules and complete scanners, since in crystal matrixes it is usually difficult to obtain the same light collection efficiency as with single crystals, which are usually coupled to larger photosensors. Moreover, most of the techniques used in these developments require the use of front-end electronics with high power consumption and/or to digitize the complete sensor waveforms with high sampling rate, both of which cannot be easily implemented in systems with thousands of channels.

Another approach to improve the timing performance of pixelated detector consists in using a double-sided readout scheme to read out the scintillator array: this architecture makes it possible to obtain a faster and more efficient extraction of the light from both the sides of the crystals and provides the possibility to obtain multiple timestamps [81, 82]. An additional advantage of this method is that it can also provide DOI information. However, also this techniques presents relevant practical difficulties to be implemented in real scanners, due to the additional costs and complexity determined by the double number of sensors and readout channels and to the mechanical challenges for integrating the photodetectors in the inner part of the scanner bore.

As regards the spatial resolution and the DOI capability, many prototype pixelated detectors with superior performance compared to the current state-of-the-art detectors used in clinical PETs have been presented in literature. For example, several research groups presented pixelated detectors based on small pixels, having dimensions around 2 mm, and thickness suitable for clinical applications [83–85].

Numerous detector designs have also been proposed to obtain DOI information. The most commonly proposed architectures are based on stacking different layers of crystals one on top of each other, optically coupling them and reading them out with a single pixelated photosensor at the bottom of the stack. In phoswich detectors, different scintillation material with different physical properties (such as decay time or light yield) are used in the different layers and DOI estimation is achieved by discriminating the pulse shape produced by the different layers with the readout electronics [86, 87]. In other architectures, mostly used in pre-clinical or high resolution scanners, the crystal arrays are stacked in shifted positions and with different reflector arrangements. These configurations determine that each pixel in each layer produces a unique light distribution on the photosensor, making it possible to identify them using center-of-gravity (COG) positioning algorithms [88, 89].

Other DOI techniques are based on single-layer crystal arrays in which reflectors and light guides are used to modulate the amount of light shared among different crystals as a function of the depth of interaction. For example, in the detector presented in [84] the reflector between the crystals has a triangular shape that modulates the light sharing between them as a function of the DOI, encoding the DOI in the width of the registered light distribution. In the detector presented in [90], instead, an array of depolished crystals is used, coupled on one side with an SiPM array and on the other side with a glass light guide. In depolished crystals, the amount of amount of light extracted from the two ends of the crystals is strongly dependent on the DOI. Therefore, in this detector DOI is encoded in the amount of light redirected and shared among multiple crystals by the light guide.

Another approach consists in using crystals partially coated by phosphor, which absorbs and re-emits with a certain delay the scintillation light and therefore makes it possible to estimate the DOI using pulse-shape discrimination [91, 92].

More complicated techniques that require two or more photosensor arrays have also been proposed. These techniques range from previously mentioned double-sided readout detectors [81, 82] to stacked layers of thin detectors [93] and complicated 3D arrays of small crystals read out from many sides [94]. An extensive review of the different detectors developed for DOI estimation can be found in [95].

The major drawback to implementing high-resolution and especially DOI-capable pixelated detectors for clinical applications is that most of the proposed architectures require to use crystals with high aspect ratio and materials/readout schemes which hamper a fast and efficient collection of the scintillation light. In thin and long crystals, in crystal arrays composed of several layers and in detectors that use light-sharing techniques, most of the photons have to undergo numerous reflections before they reach the photosensor. These tortuous paths introduce delays and jitters in the time of arrival of the scintillation photons and reduce the overall light collection efficiency.

For these reasons, most of the techniques described above result in a serious degradation of the energy resolution and, more importantly, of the timing performance of the detectors. This can be an acceptable trade-off in pre-clinical scanners and high resolutions scanner, which do not exploit TOF; however, it is undesirable in clinical scanners, whose performance is often limited by statistical noise and greatly rely on TOF to improve image quality.

Therefore, pixelated detectors seem to be inherently limited in achieving at the same time excellent timing resolution, good spatial resolution, DOI capability, and good energy resolution. Most technologies able to obtain this necessitate using more than one photosensor per crystal, which is difficult to implement in clinical scanners.

#### 1.3.3.2. Monolithic detectors

Monolithic detectors are detectors based on unsegmented scintillation crystals and segmented photosensors (Figure 1.11). In these detectors, the position of interaction is estimated from the light distribution determined by a scintillation event, i.e. the intensity of the light signals acquired by each pixel of the photosensor. A simplified illustration of the working principle of these detectors is shown in Figure 1.12: if the interaction points shifts laterally from one side of the crystal to the other side, the peak of the light distribution is expected to shift accordingly, with the highest intensity measured on the photosensor pixels which are closer to the interaction point. Similarly, if the interaction point changes depth, the light distribution is expected to change width, resulting in a narrower light distribution when the interaction is closer to the photosensor and a wider light distribution when the interaction is further from it. It should be emphasized that real light distributions are strongly influenced by reflections on the faces of the crystal not coupled with the photosensor. Moreover, they suffer from noise due to photon statistics, photosensor noise and discrete sampling on (relatively wide) photosensor pixels. Because of these reasons, position estimation in monolithic detectors is a complex task and position-estimation algorithms play an important role in determining the performance of a detectors.

Many different methods have been proposed to estimate the position of interaction of gamma rays inside monolithic detectors, which are either based on analytical algorithms, on statistical algorithms or on algorithms based on machine learning techniques. Analytical algorithms range from the simple center-of-gravity

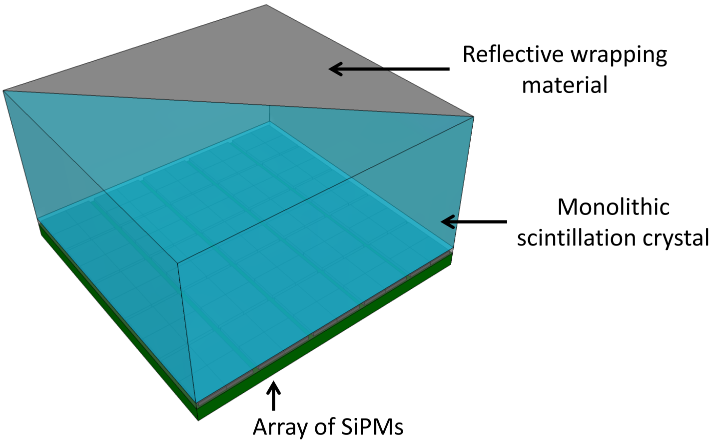

Figure 1.11: Schematic drawing of a monolithic scintillator detector.

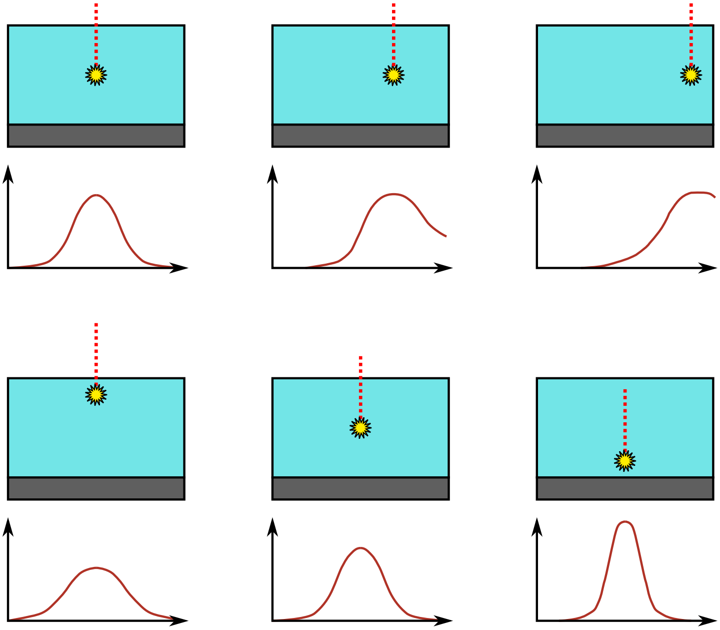

Figure 1.12: Simplified illustration of the working principle of monolithic scintillator detectors: if the position of interaction shifts laterally, the peak of the light distribution is expected to shift accordingly (top row); if the interaction point changes depth, the light distribution is expected to change width, resulting in a narrower light distribution when the interaction is closer to the photosensor.

(COG) method, used in standard gamma cameras, to more complex algorithms, which for example model expected light distributions as a function of the 3D position of interaction, considering geometrical efficiencies of the photosensor pixels and reflections on the crystal edges [96, 97].

Statistical algorithms and algorithms based on machine learning techniques, instead, comprehend methods based on maximum likelihood (ML) estimation [98–102], neural networks [103–106], support vector machines [107], k-nearest neighbor (k-NN) algorithm [108, 109], self-organizing maps (SOMs) [110], gradient tree boosting [111], and hybrid methods that combine some of the algorithms previously mentioned [112, 113].

An advantage of monolithic crystals over finely pixelated crystals is that scintillation photons usually undergo a lower number of reflections before reaching the photosensor. This favors an efficient light collection, which in turn enables monolithic detectors to achieve good timing performance and good energy resolution. Of course, the light signal is spread over a larger surface, therefore low-noise photosensors are needed to fully exploit this advantage. However, there are no intrinsic limitations to obtain at the same time good timing performance, high spatial resolution, DOI capability and good energy resolution. Actually, if photosensor used in monolithic detectors can acquire more than one timestamp (e.g. one timestamp per pixel), dedicated methods can also be used to improve the estimation of the time of interaction by making use of the information contained in the light distribution, in the estimated position of interaction and in the multiple time measurements. For example, in [114] a statistical method for time-of-interaction estimation has been proposed which can correct for DOI effects and for any jitter in the photosensor pixel response, improving the performance that can be obtained with standard analytical methods (e.g. an average of timestamps).

Considering the historical development of monolithic detectors, the gamma camera proposed by Anger was the first detector which used this architecture [74]. Gamma cameras found wide utilization in early SPECT and also PET scanners: however, their performance could not keep up with the developments of the block detectors and the pixelated detectors, which became the detectors of choice in PET scanners during the 1980s. A remarkable development of the monolithic detector technology was made possible only in more recent years thanks to the introduction of finely segmented photosensors, such as PS-PMTs and arrays of solid-state light sensors (APDs and SiPMs), which made it possible to obtain a better sampling of the light distribution. Thanks to these improvements, since the beginning of the 2000s monolithic detectors have been extensively considered as possible high-resolution detectors for pre-clinical applications [103, 108, 115–119]. At the beginning of 2010s, monolithic scintillator detectors had already shown the capability to achieve a spatial resolution in the order of 1 mm FWHM [120] in relatively thin crystals (~10 mm), as well as timing resolutions below 200 ps [114].

These results have brought, in more recent years, to the development of several pre-clinical scanners that show performance comparable to or even better than the performance of pre-clinical scanners based on pixelated detectors [121–124]. However, most of these results have been obtained with relatively thin crystals

(~10 mm), which are not a viable option for clinical applications. At the beginning of this research project, many problems on how to practically calibrate and operate monolithic detectors were still open and there were no detector prototypes which could combine all the requirements of PET clinical detectors, mainly a high sensitivity combined with excellent CRT and good spatial resolution (with DOI estimation).

### 1.3.4. State-of-the-art commercial and research clinical PET scanners

Main hardware characteristics and performance indicators of recent, state-of-the-art whole-body clinical TOF-PET scanners produced by the most popular commercial vendors are reported in Table 1.4. All of these scanners are built using pixelated detectors based on L(Y)SO scintillator crystals coupled to SiPMs. These detectors typically have a crystal pitch of 3-5 mm, a crystal thickness of ~16/25 mm, employ standard readout architectures (Anger logic or 1:1 coupling), and do not provide DOI estimation.

All the scanners have an axial extension between 16 cm and 27 cm and a transaxial dimension in between 72 cm and 79 cm, except the Signa PET/MR scanner which has a smaller bore (~62 cm) to fit inside the MR system, while the uEXPLORE scanner has a much longer axial extent, as described in detail below. These systems achieve a spatial resolution between 3.0 mm and 4.5 mm at the center of the FOV, which degrades to 4-8 mm (in the radial direction) at 20 cm off-center. They also provide CRTs in the range of 200-400 ps FWHM and energy resolution in the order of 10-12%.

In research, much of the recent efforts in the field of whole-body PET scanners are directed towards building clinical systems with extended axial length (>1 m), in order to boost sensitivity of more than one order of magnitude compared to current commercial scanners. This development would make it possible to improve current image quality thanks to the much higher statistics or to obtain the same quality with reduced dose to the patients or reduced acquisition times. More importantly, such high sensitivity systems could open up completely new possibilities in clinical applications of PET imaging and in the field of tracer kinetic studies [137].

The well-known collaboration which is focusing on this development is the EXPLORER consortium, which has already promoted the construction of two high-sensitivity scanners based on different architectures. The first scanner is based on the same technology of the Philips VEREOS PET/CT scanner and is basically assembled stacking several scanner rings along the axial direction [138]. This scanner features and axial FOV of 70 cm, which is planned to be further extended in future up to 140 cm. Thanks to an improved cooling system, this scanner can also achieve a CRT of 250/280 ps (depending on the total activity), which is slightly better than the CRT obtained with the standard VEREOS systems.

The second scanner has been built from scratch and is based on pixelated detectors having a crystal pitch of 2.85 mm, in order to be able to exploit the higher sensitivity also to increase the image spatial resolution. This scanner features a ring diameter of ~79 cm, an axial FOV of 194 cm, achieves a CRT of ~430 ps and an energy resolution of ~11.7% [131]. The scanner is built by the company United

Table 1.4: Main hardware and performance characteristics of state-of-the-art commercial whole-body clinical TOF-PET scanners offered by the most important vendors (part 1).
$^{*}$ transversal / axial (transversal is the average between radial and tangential)
$^{**}$ in a miniblock

| | Scanner model - producing company | Discovery MI PET/CT (5 ring) – GE [125] | Signa PET/MR – GE [126] | Vereos PET/CT – Philips [127] | Vision PET/CT – Siemens [128] |
|---|---|---|---|---|---|
| Systems specifications | Axial/Transaxial dim. (cm) | 25/74.4 | 25/62.4 | 16.4/76.4 | 26.1/78 |
| | Photosensors type | analog SiPM (Hamamatsu?) | analog SiPM (Hamamatsu) | digital SiPM (DPC) | analog SiPM |
| | Scintillator type | LYSO | LYSO | LYSO | LSO |
| | Scintillator thickness (mm) | 25 | 25 | 19 | 20 |
| | Scintillator size (mm × mm) | 3.95 × 5.3 | 3.95 × 5.3 | 4 × 4 | 3.2 × 3.2 |
| | N. modules | 34 | 28 | 18 | 19 |
| | N. blocks per module | 4 × 5 | 4 × 5 | 4 × 5 | 2 × 8 (each block is 4 × 2 miniblocks ) |
| | Integrated anatomical imaging modality | CT | MR | CT | CT |
| Detector block | N. crystals pixels per detector block | 4 × 9 | 4 × 9 | 8 × 8 | 5 × 5 $^{**}$ |
| specifications | N. photosensor pixels | 3 × 6 | 3 × 6 | 8 × 8 | 4 × 4 $^{**}$ |
| | Positioning scheme | Anger logic | Anger logic | 1:1 coupling | Anger logic |
| Spatial resolution (FBP) | 1 cm, FWHM (mm) R/T/A | 4.3/4.3/5.0 | 4.4/4.1/5.3 | 4.24/4.17 $^{*}$ | 3.7/3.7/3.6 |
| | 10 cm, FWHM (mm) R/T/A | 5.5/4.6/6.5 | 5.8/4.4/6.7 | 4.55/4.35/4.39 | 4.6/3.9/4.3 |
| | 20 cm, FWHM (mm) R/T/A | 7.4/5.0/6.6 | 8.4/5.2/7.3 | 5.84/4.92/4.60 | 6.0/3.6/4.6 |
| Sensitivity (cps/kBq) | Center | 20.8 | 23.1 | 5.1 | 16.4 |
| | 10 cm | 20.6 | 22.5 | 5.2 | 16.3 |
| Counting rate statistics | Peak NECR (kcps) | 266 | 217 | 153.4 | 306 |
| | Peak NECR activity (kBq/ml) | 20.8 | 17.8 | 54.9 | 32.6 |
| | Scatter fraction at PNECR (%) | 40.2 | 43.8 | 33.9 | 38.7 |
| Energy resolution | FWHM (%) | 9.55 | 10.3 | 11.2 | - |
| CRT | FWHM (ps) | 382 | 386 | 310 | 210 |

Table 1.4: Main hardware and performance characteristics of state-of-the-art commercial whole-body clinical TOF-PET scanners offered by the most important vendors (part 2).
$^{***}$ low activity / peak NECR
$^{****}$ single LOR / system)

| | Scanner model - producing company | uMI550 PET/CT – United Imaging [129] | uEXPLORER PET/CT – United Imaging [130–134] | Cartesion Prime PET/CT – Canon [135, 136] |
|---|---|---|---|---|
| Systems specifications | Axial/Transaxial dim. (cm) | 24.0 / 72.2 | 194.8 / 78.6 | 27 / 78 |
| | Photosensors type | analog SiPM (SensL) | analog SiPM (SensL) | analog SiPM |
| | Scintillator type | LYSO | LYSO | LYSO |
| | Scintillator thickness (mm) | 16.3 | 18.1 | 20.0 |
| | Scintillator size (mm × mm) | 2.85 × 2.85 | 2.85 × 2.85 | 4.2 × 4.2 |
| | N. modules | 24 | 24 (× 8 rings) | 48 |
| | N. blocks per module | 5 × 14 | 5 × 14 | 1 × 5 |
| | Integrated anatomical imaging modality | CT | CT | CT |
| Detector block | N. crystals pixels per detector block | 6 × 7 | 6 × 7 | 12 × 12 |
| specifications | N. photosensor pixels | 2 × 2 | 2 × 2 | 12 × 12 |
| | Positioning scheme | Anger logic | Anger logic | 1:1 coupling |
| Spatial resolution (FBP) | 1 cm, FWHM (mm) R/T/A | 2.98 / 2.91 / 2.97 | 3.0 / 3.0 / 2.8 | NA |
| | 10 cm, FWHM (mm) R/T/A | 3.29 / 3.09 / 2.97 | 3.4 / 3.1 / 3.2 | NA |
| | 20 cm, FWHM (mm) R/T/A | 4.14 / 4.08 / 3.13 | 4.7 / 4.0 / 3.2 | NA |
| Sensitivity (cps/kBq) | Center | 10.24 | 174 | 13.5 |
| | 10 cm | 10.32 | 177 | 13.5 |
| Counting rate statistics | Peak NECR (kcps) | 124.4 | 1524 | 144.7 |
| | Peak NECR activity (kBq/ml) | 18.85 | 17.3 | 9.6 |
| | Scatter fraction at PNECR (%) | 36.65 | 36.3 | 36 |
| Energy resolution | FWHM (%) | 12 | 11.7 | 11.4 |
| CRT | FWHM (ps) | 372 / 419 $^{***}$ | 412 / ~500 $^{****}$ | 255 |

Imaging and is also commercially available.

Both of these scanners are currently operational [139, 140] and are already showing the new research and clinical possibilities that such high-sensitivity systems can open up.

Recently, other interesting research scanners have been proposed that focused on developing new detectors to improve the system spatial resolution, either by using small crystals [85] or by developing scanners with DOI capabilities [141].

Besides high-resolution and high-sensitivity whole-body scanners, many research efforts are currently committed to developing new instrumentation and scanner architectures for clinical systems dedicated to brain or breast imaging. These tasks require to image with high resolution and high SNR well-defined anatomical regions and would therefore benefit of dedicated solutions.

For brain imaging, for example, scanners with smaller radial dimensions that cover only the patient's head are the best option, since they can achieve a good solid-angle coverage with reduced detector material and can reduce spatial-resolution degradation due to photon acollinearity compared to large-radius scanner. In order to achieve the best imaging performance, detectors optimized for these scanners should have high sensitivity (~20 mm L(Y)SO crystal thickness), high spatial resolution (<2 mm), good DOI estimation capabilities (~3-5 mm) and possibly excellent timing resolution (<200 ps), so that TOF information can be exploited also in the small FOV (~20 cm) imaged by such systems.

Several scanners dedicated to brain imaging were developed since the beginning of the 80s and the interest in this research field has significantly increased since the beginning of the 2000s. In the last 15-20 years many different brain scanners have been proposed and a thorough review of these devices can be found in [142]. The most well know-known of these systems is the ECAT HRRT [78, 143], the first commercially-available brain scanner, whose performance are still competitive also compared to the most recent whole-body PET scanners. Since there is a clear advantage in having combined PET and MR information for brain imaging, several efforts have also been made to develop systems which are compatible with MR scanners [144]. More recently, new research systems based on non-cylindrical scanners and on detectors with enhanced DOI capabilities have been proposed [93, 145] and also the EXPLORER consortium developed a small-radius scanner which might be used for human brain imaging [132]. However, to date none of the proposed solution can combine all the requirements previously listed, leaving room for further improvements in the field.

As regards breast imaging, dedicated PET systems are currently considered as possible tools that could aid in the diagnosis, staging and treatment evaluation of breast cancer, especially in some specific situations in which functional molecular imaging could provide higher sensitivity and specificity compared to standard x-ray mammograms [146, 147]. The challenges in breast imaging are similar to brain imaging, since systems with high detection efficiency and high spatial resolution are required also for this task. Additional geometrical challenges are posed in these systems by the necessity to image close to the chest wall, being as much sensitive as possible also to the tissues close to the chest. Different scanner geometries have been proposed, some based on parallel plate detectors with limited angle information and others which are instead fully tomographic systems. An accurate review of these systems can be found in [147]. Due to the limited angle coverage and the non-circular shape of the scanners, these system could additionally benefit of DOI-capable detectors and TOF estimation, in order to achieve high spatial resolution and compensate for missing projection angles in image reconstruction.

## 1.4. Thesis research objectives

In the clinical practice, PET imaging is an invaluable tool for the diagnosis and the management of oncological disease; new important applications are also under development in the field of neurodegenerative disease. Furthermore, PET is widely used in research both for pre-clinical and clinical studies, e.g. to investigate the pharmacokinetics of new drugs or for developing new pharmaceuticals.

The diagnostic value of PET images crucially depends on how accurately the distribution of the radiotracer inside the patient can be estimated, i.e. on the spatial resolution, the contrast and the noise level of the reconstructed images. Besides some physical limitations (e.g. positron range and photon acollinearity), the image quality is fundamentally limited by the number of detected coincidence events, the ratio between the true and the false (random and scattered) events used for image reconstruction, and the accuracy in measuring the time and position of interaction of (true) gamma photons inside the detectors. These limiting factors are largely determined by the performance of the detectors used in the scanners, in particular by their sensitivity and by their timing, energy and spatial resolution, the latter of which comprises also the capability to estimate the DOI.

It is important to stress that PET scanners for different purposes are differently influenced by the detector properties and therefore, for each application, a different optimization of the detector architecture has to be performed. This has to be carefully considered when a system is designed since, often, improvements in one of the detector performance parameters negatively affects other ones. For example, as discussed in section 1.3.3.1, many of the architectures that can provide DOI estimation in pixelated detectors severely degrade light collection efficiency and therefore degrade timing performance and energy resolution. Moreover, new detector developments should not come at the expense of an excessive increase in cost or complexity, since the technologies that are applied in real scanners have to be affordable in price and practical as far as their calibration and their operation is concerned.

The research conducted in the scope of this thesis is aimed at demonstrating that monolithic scintillator detectors are a suitable alternative to pixelated detectors in clinical PET systems, both in whole-body and in dedicated high-resolution scanners (e.g. for brain and breast imaging). In whole-body clinical PET, detectors are required to have excellent sensitivity, excellent CRT, good spatial resolution and good energy resolution; moreover, they have to be relatively inexpensive and simple in their construction and operation, since a large number of detectors has to be assembled and operated in a full scanner. In dedicated high-resolution scanners, instead, detectors are required to have an improved spatial resolution and, possibly, timing resolution compared to whole body scanners. These improvements could be obtained even at the cost of some added price and complexity, since this additional complexity can be cost-effective in such applications, especially considering that a more limited number of detectors is used.

At the beginning of this project, which started in 2011 and 2012, monolithic detectors had already demonstrated (often in separate studies) that they could achieve good spatial resolution, that they could be used to estimate DOI, and that they could obtain excellent CRTs. However, no one had demonstrated yet the possibility to combine all these characteristics in a single detector with high sensitivity. In this thesis, the possibility to develop such detectors for whole-body and high-resolution clinical applications is explored. Furthermore, several improvements aimed at making the calibration and operation of monolithic detectors more practical are investigated. A particular objective is to demonstrate the capabilities of this technology not only at the single-detector level but also in a tomographic setup that can demonstrate the potential of monolithic detectors in whole-body TOF-PET systems.

## 1.5. Thesis outline

The research presented in this thesis, whose aims were outlined in section 1.4, is organized as follows.

In Chapter 2, the experimental validation of a new calibration method for k-nearest neighbor position estimation is presented. This method aims to speed up the traditional procedure used to collect the reference dataset for the k-NN algorithm, which requires to collect reference data on a fine 2D grid of reference position using a narrow pencil beam (PB). The new method is based on fan-beam (FB) irradiation and is demonstrated to provide the same positioning accuracy obtained with the PB method, accelerating the calibration procedure of more than one order of magnitude and making it possible to calibrate single detectors in just few hours (and potentially in few minutes).

In Chapter 3, all the methods developed in our group to estimate the 3D position of interaction, the time of interaction and the energy deposited inside monolithic detectors are systematically reviewed and made more practical and consistent. In particular, all the calibration procedures are modified so that only fan-beam irradiations and flood irradiations are required for a full detector calibration. The k-NN position-estimation method is also accelerated, reducing the computational burden by more than two orders of magnitude. Finally, a new technique is presented to allow the use of events in which some of the photosensor pixel values and/or timestamps are missing (e.g. due to dead time), so as to further increase system sensitivity. All these methods are then applied to a large monolithic detector, based on a 32 mm × 32 mm × 22 mm LYSO crystal and a DPC digital SiPM array in back-side readout (BSR) configuration, which is developed for clinical whole-body PET applications.

In Chapter 4, the same calibration and characterization methods presented in Chapter 3 are applied to an ultra-high performance monolithic detector, which is developed for possible applications in high-resolution PET scanners, such as pediatric scanners and dedicated brain or breast scanner. This detector is also based on a monolithic 32 mm × 32 mm × 22 mm LYSO crystal, this time read out using two DPC digital SiPM arrays on the front and back surface, in the so-called dual-sided readout (DSR) configuration.

In Chapter 5, the detector architecture presented in Chapter 3 is used to assemble two detector modules, each one composed by 2 × 2 detectors. These modules are employed in a tomographic setup to demonstrate the performance of such monolithic detectors in a real imaging system. In this work, we emulate a whole-body clinical scanner having a bore diameter of 70 cm and we characterize its CRT, its energy resolution and its spatial resolution with point sources and resolution phantoms, demonstrating an almost uniform spatial resolution throughout the FOV thanks to the use of the DOI information.

Finally, Chapter 6 summarizes the most important findings achieved in the scope of this thesis, discussing them in the context of the current status-of-the-art technologies for clinical PET. An outlook is also provided of the developments which are still needed in the monolithic detectors technology to make it a viable option for commercial clinical systems.

## References

[1] S. Cherry, J. Sorenson, and M. Phelps, *Physics in Nuclear Medicine*, 4th ed. (Elsevier (Saunders), 2012) p. 544.

[2] S. M. Qaim, *Nuclear data for production and medical application of radionuclides: Present status and future needs,* Nuclear Medicine and Biology **44**, 31 (2017).

[3] G. B. Saha, *Basics of PET Imaging*, 3rd ed. (Springer, 2016).

[4] M. M. Khalil, *Basic Science of PET Imaging*, 1st ed. (Springer, 2017).

[5] A. J. Reader and H. Zaidi, *Advances in pet image reconstruction,* PET Clinics **2**, 173 (2007).

[6] S. Tong, A. M. Alessio, and P. E. Kinahan, *Image reconstruction for pet/ct scanners: past achievements and future challenges,* Imaging in medicine **2**, 529 (2010).

[7] T. Beyer, D. W. Townsend, T. Brun, P. E. Kinahan, M. Charron, R. Roddy, J. Jerin, J. Young, L. Byars, and R. Nutt, *A combined pet/ct scanner for clinical oncology,* Journal of Nuclear Medicine **41**, 1369 (2000).

[8] T. Beyer and D. W. Townsend, *Putting 'clear' into nuclear medicine: a decade of pet/ct development,* European Journal of Nuclear Medicine and Molecular Imaging **33**, 857 (2006).

[9] S. Vandenberghe and P. K. Marsden, *Pet-mri: a review of challenges and solutions in the development of integrated multimodality imaging,* Physics in Medicine and Biology **60**, R115 (2015).

[10] G. Delso, S. Fürst, B. Jakoby, R. Ladebeck, C. Ganter, S. G. Nekolla, M. Schwaiger, and S. I. Ziegler, *Performance measurements of the siemens mmr integrated whole-body pet/mr scanner,* Journal of Nuclear Medicine **52**, 1914 (2011).

[11] P. Werner, H. Barthel, A. Drzezga, and O. Sabri, *Current status and future role of brain pet/mri in clinical and research settings,* European Journal of Nuclear Medicine and Molecular Imaging **42**, 512 (2015).

[12] H. F. Wehrl, M. Hossain, K. Lankes, C.-C. Liu, I. Bezrukov, P. Martirosian, F. Schick, G. Reischl, and B. J. Pichler, *Simultaneous pet-mri reveals brain function in activated and resting state on metabolic, hemodynamic and multiple temporal scales,* Nat Med **19**, 1184 (2013).

[13] S. Purz, O. Sabri, A. Viehweger, H. Barthel, R. Kluge, I. Sorge, and F. W. Hirsch, *Potential pediatric applications of pet/mr,* Journal of Nuclear Medicine **55**, 32S (2014).

[14] K. Zukotynski, F. Fahey, M. Kocak, L. Kun, J. Boyett, M. Fouladi, S. Vajapeyam, T. Treves, and T. Y. Poussaint, *18f-fdg pet and mr imaging associations across a spectrum of pediatric brain tumors: A report from the pediatric brain tumor consortium,* Journal of Nuclear Medicine (2014), 10.2967/jnumed.114.139626.

[15] I. Neuner, R. Rajkumar, C. R. Brambilla, S. Ramkiran, A. Ruch, L. Orth, E. Farrher, J. Mauler, C. Wyss, E. R. Kops, J. Scheins, L. Tellmann, M. Lang, J. Ermert, J. Dammers, B. Neumaier, C. Lerche, K. Heekeren, W. Kawohl, K. Langen, H. Herzog, and N. J. Shah, *Simultaneous pet-mr-eeg: Technology, challenges and application in clinical neuroscience,* IEEE Transactions on Radiation and Plasma Medical Sciences **3**, 377 (2019).

[16] V. Sossi, J. Cheng, and I. S. Klyuzhin, *Imaging in neurodegeneration: Movement disorders,* IEEE Transactions on Radiation and Plasma Medical Sciences **3**, 262 (2019).

[17] C. B. Hruska and M. K. O'Connor, *Nuclear imaging of the breast: Translating achievements in instrumentation into clinical use,* Medical Physics **40**, 050901 (2013), https://aapm.onlinelibrary.wiley.com/doi/pdf/10.1118/1.4802733 .

[18] F. Fraioli and S. Punwani, *Clinical and research applications of simultaneous positron emission tomography and mri,* The British Journal of Radiology **87**, 20130464 (2014).

[19] H. Jadvar and P. M. Colletti, *Competitive advantage of pet/mri,* European Journal of Radiology **83**, 84 (2014).

[20] H. Zhuang and I. Codreanu, *Growing applications of fdg pet-ct imaging in non-oncologic conditions,* The Journal of Biomedical Research **29**, 13 (2015).

[21] NEMA-NU2, *Performance Measurements of Positron Emission Tomographs (PETS),* NEMA Standards Publication NU 2-2018 (National Electrical Manufacturers Association (NEMA), 2018).

[22] W. W. Moses, *Fundamental limits of spatial resolution in pet,* Nuclear Instruments and Methods in Physics Research Section A: Accelerators, Spectrometers, Detectors and Associated Equipment **648, Supplement 1**, S236 (2011).

[23] H. Peng and C. S. Levin, *Study of pet intrinsic spatial resolution and contrast recovery improvement for pet/mri systems,* Physics in Medicine and Biology **57**, N101 (2012).

[24] J. Cal-González, J. L. Herraiz, S. España, P. M. G. Corzo, J. J. Vaquero, M. Desco, and J. M. Udias, *Positron range estimations with penelopet,* Physics in Medicine and Biology **58**, 5127 (2013).

[25] K. Shibuya, E. Yoshida, F. Nishikido, T. Suzuki, T. Tsuda, N. Inadama, T. Yamaya, and H. Murayama, *Annihilation photon acollinearity in pet: volunteer and phantom fdg studies,* Physics in Medicine and Biology **52**, 5249 (2007).

[26] H. Thoen, V. Keereman, P. Mollet, R. V. Holen, and S. Vandenberghe, *Influence of detector pixel size, tof resolution and doi on image quality in mr-compatible whole-body pet,* Physics in Medicine and Biology **58**, 6459 (2013).

[27] S. Surti, A. R. Shore, and J. S. Karp, *Design study of a whole-body pet scanner with improved spatial and timing resolution,* Nuclear Science, IEEE Transactions on **60**, 3220 (2013).

[28] D. Brasse, P. E. Kinahan, C. Lartizien, C. Comtat, M. Casey, and C. Michel, *Correction methods for random coincidences in fully 3d whole-body pet: Impact on data and image quality,* Journal of Nuclear Medicine **46**, 859 (2005).

[29] G. F. Knoll, *Radiation detection and measurement* (Wiley, New York, NY, 2010) p. 830.

[30] J. M. Ollinger, *Model-based scatter correction for fully 3d pet,* Physics in Medicine and Biology **41**, 153 (1996).

[31] C. C. Watson, *New, faster, image-based scatter correction for 3d pet,* IEEE Transactions on Nuclear Science **47**, 1587 (2000).

[32] C. Watson, *Extension of single scatter simulation to scatter correction of time-of-flight pet,* IEEE Transactions on Nuclear Science **54**, 1679 (2007).

[33] L. Theodorakis, G. Loudos, V. Prassopoulos, C. Kappas, I. Tsougos, and P. Georgoulias, *A review of pet normalization: striving for count rate uniformity,* Nuclear Medicine Communications **34**, 1033 (2013).

[34] J. P. J. Carney, D. W. Townsend, V. Rappoport, and B. Bendriem, *Method for transforming ct images for attenuation correction in pet/ct imaging,* Medical Physics **33**, 976 (2006).

[35] L. Eriksson and M. Conti, *Randoms and tof gain revisited,* Physics in Medicine and Biology **60**, 1613 (2015).

[36] S. Surti, *Update on time-of-flight pet imaging,* Journal of Nuclear Medicine **56**, 98 (2015).

[37] S. Vandenberghe, E. Mikhaylova, E. D'Hoe, P. Mollet, and J. S. Karp, *Recent developments in time-of-flight pet,* EJNMMI Physics **3**, 3 (2016).

[38] D. R. Schaart, G. Schramm, J. Nuyts, and S. Surti, *Time of flight in perspective: Instrumental and computational aspects of time resolution in positron emission tomography,* IEEE Transactions on Radiation and Plasma Medical Sciences , 1 (2021).

[39] P. Lecoq, *Pushing the limits in time-of-flight pet imaging,* IEEE Transactions on Radiation and Plasma Medical Sciences **1**, 473 (2017).

[40] P. Lecoq, C. Morel, J. O. Prior, D. Visvikis, S. Gundacker, E. Auffray, P. Križan, R. M. Turtos, D. Thers, E. Charbon, J. Varela, C. de La Taille, A. Rivetti, D. Breton, J.-F. Pratte, J. Nuyts, S. Surti, S. Vandenberghe, P. Marsden, K. Parodi, J. M. Benlloch, and M. Benoit, *Roadmap toward the 10 ps time-of-flight PET challenge,* Physics in Medicine & Biology **65**, 21RM01 (2020).

[41] P. Moskal, S. Niedźwiecki, T. Bednarski, E. Czerwiński, . Kapłon, E. Kubicz, I. Moskal, M. Pawlik-Niedźwiecka, N. G. Sharma, M. Silarski, M. Zieliński, N. Zoń, P. Białas, A. Gajos, A. Kochanowski, G. Korcyl, J. Kowal, P. Kowalski, T. Kozik, W. Krzemień, M. Molenda, M. Pałka, L. Raczyński, Z. Rudy, P. Salabura, A. Słomski, J. Smyrski, A. Strzelecki, A. Wieczorek, and W. Wiślicki, *Test of a single module of the j-pet scanner based on plastic scintillators,* Nuclear Instruments and Methods in Physics Research Section A: Accelerators, Spectrometers, Detectors and Associated Equipment **764**, 317 (2014).

[42] P. Moskal, D. Alfs, T. Bednarski, P. Bialas, C. Curceanu, E. Czerwiński, K. Dulski, A. Gajos, B. Glowacz, M. Gorgol, B. Hiesmayr, B. Jasińska, D. Kamińska, G. Korcyl, P. Kowalski, T. Kozik, W. Krzemień, E. Kubicz, M. Mohammed, M. Pawlik-Niedźwiecka, S. Niedźwiecki, M. Palka, L. Raczyński, Z. Rudy, O. Rundel, N. G. Sharma, M. Silarski, J. Smyrski, A. Strzelecki, A. Wieczorek, W. Wiślicki, B. Zgardzińska, and M. Zieliński, *J-pet: A novel tof-pet detector based on plastic scintillators,* in *2016 IEEE Nuclear Science Symposium, Medical Imaging Conference and Room-Temperature Semiconductor Detector Workshop (NSS/MIC/RTSD)* (2016) pp. 1–3.

[43] S. Del Sordo, L. Abbene, E. Caroli, A. M. Mancini, A. Zappettini, and P. Ubertini, *Progress in the development of cdte and cdznte semiconductor radiation detectors for astrophysical and medical applications,* Sensors **9** (2009), 10.3390/s90503491.

[44] P. Martins, A. Blanco, P. Crespo, M. F. F. Marques, R. F. Marques, P. M. Gordo, M. Kajetanowicz, G. Korcyl, L. Lopes, J. Michel, M. Palka, M. Traxler, and P. Fonte, *Towards very high resolution rpc-pet for small animals,* Journal of Instrumentation **9**, C10012 (2014).

[45] S. Razaghi, S. Saramad, and M. Shamsaei, *Simulation study of resistive plate chamber's (rpcs) capability for medical imaging applications,* Journal of Instrumentation **14**, P01024 (2019).

[46] P. Ferrario, *Liquid xenon in nuclear medicine: state-of-the-art and the petalo approach,* Journal of Instrumentation **13**, C01044 (2018).

[47] I. Somlai-Schweiger and S. I. Ziegler, *Cherencube: Concept definition and implementation challenges of a cherenkov-based detector block for pet,* Medical Physics **42**, 1825 (2015).

[48] R. Ota, K. Nakajima, I. Ogawa, Y. Tamagawa, H. Shimoi, M. Suyama, and T. Hasegawa, *Coincidence time resolution of 30 ps FWHM using a pair of cherenkov-radiator-integrated MCP-PMTs,* Physics in Medicine & Biology **64**, 07LT01 (2019).

[49] S. E. Brunner, L. Gruber, J. Marton, K. Suzuki, and A. Hirtl, *Studies on the cherenkov effect for improved time resolution of tof-pet,* IEEE Transactions on Nuclear Science **61**, 443 (2014).

[50] S. Gundacker, E. Auffray, K. Pauwels, and P. Lecoq, *Measurement of intrinsic rise times for various l(y)so and luag scintillators with a general study of prompt photons to achieve 10 ps in tof-pet,* Physics in Medicine and Biology **61**, 2802 (2016).

[51] S. Gundacker, R. M. Turtos, E. Auffray, and P. Lecoq, *Precise rise and decay time measurements of inorganic scintillators by means of x-ray and 511 kev excitation,* Nuclear Instruments and Methods in Physics Research Section A: Accelerators, Spectrometers, Detectors and Associated Equipment **891**, 42 (2018).

[52] D. R. Schaart, *Physics and technology of time-of-flight PET detectors,* Physics in Medicine & Biology **66**, 09TR01 (2021).

[53] S. I. Kwon, A. Gola, A. Ferri, C. Piemonte, and S. R. Cherry, *Bismuth germanate coupled to near ultraviolet silicon photomultipliers for time-of-flight pet,* Physics in Medicine and Biology **61**, L38 (2016).

[54] S. E. Brunner and D. R. Schaart, *Bgo as a hybrid scintillator / cherenkov radiator for cost-effective time-of-flight pet,* Physics in Medicine and Biology **62**, 4421 (2017).

[55] S. Gundacker, R. M. Turtos, E. Auffray, M. Paganoni, and P. Lecoq, *High-frequency SiPM readout advances measured coincidence time resolution limits in TOF-PET,* Physics in Medicine & Biology **64**, 055012 (2019).

[56] S. Gundacker, R. M. Turtos, N. Kratochwil, R. H. Pots, M. Paganoni, P. Lecoq, and E. Auffray, *Experimental time resolution limits of modern SiPMs and TOF-PET detectors exploring different scintillators and cherenkov emission,* Physics in Medicine & Biology **65**, 025001 (2020).

[57] S. Seifert, H. T. v. Dam, and D. R. Schaart, *The lower bound on the timing resolution of scintillation detectors,* Physics in Medicine and Biology **57**, 1797 (2012).

[58] P. Lecoq, *Development of new scintillators for medical applications,* Nuclear Instruments and Methods in Physics Research Section A: Accelerators, Spectrometers, Detectors and Associated Equipment **809**, 130 (2016).

[59] C. Dujardin, E. Auffray, E. Bourret-Courchesne, P. Dorenbos, P. Lecoq, M. Nikl, A. N. Vasil'ev, A. Yoshikawa, and R. Zhu, *Needs, trends, and advances in inorganic scintillators,* IEEE Transactions on Nuclear Science **65**, 1977 (2018).

[60] C. W. E. van Eijk, *Inorganic scintillators in medical imaging,* Physics in Medicine and Biology **47**, R85 (2002).

[61] S. Seifert, J. H. L. Steenbergen, H. T. v. Dam, and D. R. Schaart, *Accurate measurement of the rise and decay times of fast scintillators with solid state photon counters,* Journal of Instrumentation **7**, P09004 (2012).

[62] V. K. Zworykin, G. A. Morton, and L. Malter, *The secondary emission multiplier-a new electronic device,* Proceedings of the Institute of Radio Engineers **24**, 351 (1936).

[63] G. W. Goodrich and W. C. Wiley, *Continuous channel electron multiplier,* Review of Scientific Instruments **33**, 761 (1962).

[64] R. C. Blase, R. R. Benke, and K. S. Pickens, *Review of measured photon detection efficiencies of microchannel plates,* IEEE Transactions on Nuclear Science **65**, 2839 (2018).

[65] S. I. Ziegler, B. J. Pichler, G. Boening, M. Rafecas, W. Pimpl, E. Lorenz, N. Schmitz, and M. Schwaiger, *A prototype high-resolution animal positron tomograph with avalanche photodiode arrays and lso crystals,* European Journal of Nuclear Medicine **28**, 136 (2001).

[66] P. Buzhan, B. Dolgoshein, L. Filatov, A. Ilyin, V. Kantzerov, V. Kaplin, A. Karakash, F. Kayumov, S. Klemin, E. Popova, and S. Smirnov, *Silicon photomultiplier and its possible applications,* Nuclear Instruments and Methods in Physics Research Section A: Accelerators, Spectrometers, Detectors and Associated Equipment **504**, 48 (2003).

[67] V. Golovin and V. Saveliev, *Novel type of avalanche photodetector with geiger mode operation,* Nuclear Instruments and Methods in Physics Research Section A: Accelerators, Spectrometers, Detectors and Associated Equipment **518**, 560 (2004).

[68] C. Piemonte and A. Gola, *Overview on the main parameters and technology of modern silicon photomultipliers,* Nuclear Instruments and Methods in Physics Research Section A: Accelerators, Spectrometers, Detectors and Associated Equipment **926**, 2 (2019).

[69] F. Acerbi and S. Gundacker, *Understanding and simulating sipms,* Nuclear Instruments and Methods in Physics Research Section A: Accelerators, Spectrometers, Detectors and Associated Equipment **926**, 16 (2019).

[70] D. R. Schaart, E. Charbon, T. Frach, and V. Schulz, *Advances in digital sipms and their application in biomedical imaging,* Nuclear Instruments and Methods in Physics Research Section A: Accelerators, Spectrometers, Detectors and Associated Equipment **809**, 31 (2016).

[71] J. W. Cates, S. Gundacker, E. Auffray, P. Lecoq, and C. S. Levin, *Improved single photon time resolution for analog SiPMs with front end readout that reduces influence of electronic noise,* Physics in Medicine & Biology **63**, 185022 (2018).

[72] M. M. Ter-Pogossian, M. E. Phelps, E. J. Hoffman, and N. A. Mullani, *A positron-emission transaxial tomograph for nuclear imaging (pett),* Radiology **114**, 89 (1975).

[73] E. J. Hoffman, M. E. Phelps, N. A. Mullani, C. S. Higgins, and M. M. Ter-Pogossian, *Design and performance characteristics of a whole-body positron transaxial tomograph,* Journal of Nuclear Medicine **17**, 493 (1976).

[74] H. O. Anger, *Scintillation camera,* Review of Scientific Instruments **29**, 27 (1958).

[75] M. E. Casey and R. Nutt, *A multicrystal two dimensional bgo detector system for positron emission tomography,* IEEE Transactions on Nuclear Science **33**, 460 (1986).

[76] T. Jones and D. Townsend, *History and future technical innovation in positron emission tomography,* Journal of Medical Imaging **4**, 011013 (2017).

[77] E. Berg and S. R. Cherry, *Innovations in instrumentation for positron emission tomography,* Seminars in Nuclear Medicine **48**, 311 (2018).

[78] H. W. A. M. de Jong, F. H. P. van Velden, R. W. Kloet, F. L. Buijs, R. Boellaard, and A. A. Lammertsma, *Performance evaluation of the ecat hrrt: an lso-lyso double layer high resolution, high sensitivity scanner,* Physics in Medicine and Biology **52**, 1505 (2007).

[79] M. Ruiz-Gonzalez, V. Bora, and L. R. Furenlid, *Maximum-likelihood estimation of scintillation pulse timing,* IEEE Transactions on Radiation and Plasma Medical Sciences **2**, 1 (2018).

[80] E. Berg and S. R. Cherry, *Using convolutional neural networks to estimate time-of-flight from PET detector waveforms,* Physics in Medicine & Biology **63**, 02LT01 (2018).

[81] S. Seifert and D. R. Schaart, *Improving the time resolution of tof-pet detectors by double-sided readout,* Nuclear Science, IEEE Transactions on **PP**, 1 (2014).

[82] H. G. Kang, G. B. Ko, J. T. Rhee, K. M. Kim, J. S. Lee, and S. J. Hong, *A dual-ended readout detector using a meantime method for sipm tof-doi pet,* IEEE Transactions on Nuclear Science **62**, 1935 (2015).

[83] R. Marcinkowski, S. España, R. V. Holen, and S. Vandenberghe, *Optimized light sharing for high-resolution tof pet detector based on digital silicon photomultipliers,* Physics in Medicine and Biology **59**, 7125 (2014).

[84] M. S. Lee and J. S. Lee, *Depth-of-interaction measurement in a single-layer crystal array with a single-ended readout using digital silicon photomultiplier,* Physics in Medicine and Biology **60**, 6495 (2015).

[85] W.-H. Wong, H. Li, Y. Zhang, R. Ramirez, S. An, C. Wang, S. Liu, Y. Dong, and H. Baghaei, *A high-resolution time-of-flight clinical pet detection system using a gapless pmt-quadrant-sharing method,* Nuclear Science, IEEE Transactions on **62**, 2067 (2015).

[86] J. P. Schmall, S. Surti, and J. S. Karp, *Characterization of stacked-crystal pet detector designs for measurement of both tof and doi,* Physics in Medicine and Biology **60**, 3549 (2015).

[87] C.-M. Chang, J. W. Cates, and C. S. Levin, *Time-over-threshold for pulse shape discrimination in a time-of-flight/depth of interaction phoswich pet detector,* in *2016 IEEE Nuclear Science Symposium, Medical Imaging Conference and Room-Temperature Semiconductor Detector Workshop (NSS/MIC/RTSD)* (2016) pp. 1–3.

[88] H. Liu, T. Omura, M. Watanabe, and T. Yamashita, *Development of a depth of interaction detector for γ-rays,* Nuclear Instruments and Methods in Physics Research Section A: Accelerators, Spectrometers, Detectors and Associated Equipment **459**, 182 (2001).

[89] T. Tsuda, H. Murayama, K. Kitamura, N. Inadama, T. Yamaya, E. Yoshida, F. Nishikido, M. Hamamoto, H. Kawai, and Y. Ono, *Performance evaluation of a subset of a four-layer lso detector for a small animal doi pet scanner: jpet-rd,* IEEE Transactions on Nuclear Science **53**, 35 (2006).

[90] M. Pizzichemi, G. Stringhini, T. Niknejad, Z. Liu, P. Lecoq, S. Tavernier, J. Varela, M. Paganoni, and E. Auffray, *A new method for depth of interaction determination in pet detectors,* Physics in Medicine and Biology **61**, 4679 (2016).

[91] H. Du, Y. Yang, J. Glodo, Y. Wu, K. Shah, and S. R. Cherry, *Continuous depth-of-interaction encoding using phosphor-coated scintillators,* Physics in Medicine and Biology **54**, 1757 (2009).

[92] S. I. Kwon, A. Ferri, A. Gola, E. Berg, C. Piemonte, S. Cherry, and E. Roncali, *Reaching 200-ps timing resolution in a time-of-flight and depth-of-interaction positron emission tomography detector using phosphor-coated crystals and

*high-density silicon photomultipliers,* Journal of Medical Imaging **3**, 043501 (2016).

[93] M. Watanabe, A. Saito, T. Isobe, K. Ote, R. Yamada, T. Moriya, and T. Omura, *Performance evaluation of a high-resolution brain PET scanner using four-layer MPPC DOI detectors,* Physics in Medicine & Biology **62**, 7148 (2017).

[94] T. Yamaya, T. Mitsuhashi, T. Matsumoto, N. Inadama, F. Nishikido, E. Yoshida, H. Murayama, H. Kawai, M. Suga, and M. Watanabe, *A sipm-based isotropic-3d pet detector x'tal cube with a three-dimensional array of 1 mm3crystals,* Physics in Medicine and Biology **56**, 6793 (2011).

[95] I. Mohammadi, I. F. C. Castro, P. M. M. Correia, A. L. M. Silva, and J. F. C. A. Veloso, *Minimization of parallax error in positron emission tomography using depth of interaction capable detectors: methods and apparatus,* Biomedical Physics & Engineering Express **5**, 062001 (2019).

[96] T. Ling, T. H. Burnett, T. K. Lewellen, and R. S. Miyaoka, *Parametric positioning of a continuous crystal pet detector with depth of interaction decoding,* Physics in Medicine and Biology **53**, 1843 (2008).

[97] Z. Li, M. Wedrowski, P. Bruyndonckx, and G. Vandersteen, *Nonlinear least-squares modeling of 3d interaction position in a monolithic scintillator block,* Physics in Medicine and Biology **55**, 6515 (2010).

[98] T. Ling, T. K. Lewellen, and R. S. Miyaoka, *Depth of interaction decoding of a continuous crystal detector module,* Physics in Medicine and Biology **52**, 2213 (2007).

[99] W. C. J. Hunter, H. H. Barrett, and L. R. Furenlid, *Calibration method for ml estimation of 3d interaction position in a thick gamma-ray detector,* Nuclear Science, IEEE Transactions on **56**, 189 (2009).

[100] H. H. Barrett, W. C. J. Hunter, B. W. Miller, S. K. Moore, C. Yichun, and L. R. Furenlid, *Maximum-likelihood methods for processing signals from gamma-ray detectors,* Nuclear Science, IEEE Transactions on **56**, 725 (2009).

[101] Y. Wang, X. Cheng, and D. Li, *Improved statistics based positioning scheme for continuous thick crystal pet detectors,* Nuclear Science, IEEE Transactions on **60**, 1527 (2013).

[102] S. España, R. Marcinkowski, V. Keereman, S. Vandenberghe, and R. V. Holen, *Digipet: sub-millimeter spatial resolution small-animal pet imaging using thin monolithic scintillators,* Physics in Medicine and Biology **59**, 3405 (2014).

[103] P. Bruyndonckx, S. Leonard, L. Jiangui, S. Tavernier, P. Szupryczynski, and A. Fedorov, *Study of spatial resolution and depth of interaction of apd-based pet detector modules using light sharing schemes,* Nuclear Science, IEEE Transactions on **50**, 1415 (2003).

[104] P. Bruyndonckx, S. Leonard, S. Tavernier, C. Lemaitre, O. Devroede, Y. Wu, and M. Krieguer, *Neural network-based position estimators for pet detectors using monolithic lso blocks,* Nuclear Science, IEEE Transactions on **51**, 2520 (2004).

[105] Y. Wang, W. Zhu, X. Cheng, and D. Li, *3d position estimation using an artificial neural network for a continuous scintillator pet detector,* Physics in Medicine and Biology **58**, 1375 (2013).

[106] P. Conde, A. Iborra, A. J. González, L. Hernández, P. Bellido, L. Moliner, J. P. Rigla, M. J. Rodríguez-Álvarez, F. Sánchez, M. Seimetz, A. Soriano, L. F. Vidal, and J. M. Benlloch, *Determination of the interaction position of gamma photons in monolithic scintillators using neural network fitting,* IEEE Transactions on Nuclear Science **63**, 30 (2016).

[107] P. Bruyndonckx, C. Lemaitre, D. J. van der Laan, M. Maas, D. Schaart, W. Yonggang, L. Zhi, M. Krieguer, and S. Tavernier, *Evaluation of machine learning algorithms for localization of photons in undivided scintillator blocks for pet detectors,* Nuclear Science, IEEE Transactions on **55**, 918 (2008).

[108] M. C. Maas, D. Van der Laan, D. R. Schaart, J. Huizenga, J. C. Brouwer, P. Bruyndonckx, S. Leonard, C. Lemaitre, and C. W. E. Van Eijk, *Experimental characterization of monolithic-crystal small animal pet detectors read out by apd arrays,* Nuclear Science, IEEE Transactions on **53**, 1071 (2006).

[109] H. T. van Dam, S. Seifert, R. Vinke, P. Dendooven, H. Löhner, F. J. Beekman, and D. R. Schaart, *Improved nearest neighbor methods for gamma photon interaction position determination in monolithic scintillator pet detectors,* Nuclear Science, IEEE Transactions on **58**, 2139 (2011).

[110] S. España, K. Deprez, R. V. Holen, and S. Vandenberghe, *Fast calibration of spect monolithic scintillation detectors using un-collimated sources,* Physics in Medicine and Biology **58**, 4807 (2013).

[111] F. Müller, D. Schug, P. Hallen, J. Grahe, and V. Schulz, *Gradient tree boosting-based positioning method for monolithic scintillator crystals in positron emission tomography,* IEEE Transactions on Radiation and Plasma Medical Sciences **2**, 411 (2018).

[112] P. Bruyndonckx, S. Leonard, C. Lemaitre, S. Tavernier, and Y. Wu, *Performance study of a pet detector module based on a continuous scintillator,* Nuclear Science, IEEE Transactions on **53**, 2536 (2006).

[113] Y. Wang, D. Li, X. Lu, X. Cheng, and L. Wang, *Self-organizing map neural network-based nearest neighbor position estimation scheme for continuous crystal pet detectors,* Nuclear Science, IEEE Transactions on **61**, 2446 (2014).

[114] H. T. van Dam, G. Borghi, S. Seifert, and D. R. Schaart, *Sub-200 ps crt in monolithic scintillator pet detectors using digital sipm arrays and maximum*

*likelihood interaction time estimation,* Physics in Medicine and Biology **58**, 3243 (2013).

[115] P. Bruyndonckx, C. Lemaitre, S. Leonard, D. R. Schaart, D. J. van der Laan, M. C. Maas, O. Devroede, W. Yibao, M. Krieguer, and S. Tavernier, *Initial characterization of a nonpixelated scintillator detector in a pet prototype demonstrator,* Nuclear Science, IEEE Transactions on **53**, 2543 (2006).

[116] T. Ling, K. Lee, and R. Miyaoka, *Performance comparisons of continuous miniature crystal element (cmice) detectors,* Nuclear Science, IEEE Transactions on **53**, 2513 (2006).

[117] D. R. Schaart, H. T. v. Dam, S. Seifert, R. Vinke, P. Dendooven, H. Löhner, and F. J. Beekman, *A novel, sipm-array-based, monolithic scintillator detector for pet,* Physics in Medicine and Biology **54**, 3501 (2009).

[118] R. S. Miyaoka, X. Li, W. Hunter, L. A. Pierce, W. McDougald, P. E. Kinahan, and T. K. Lewellen, *Resolution properties of a prototype continuous miniature crystal element (cmice) scanner,* Nuclear Science, IEEE Transactions on **58**, 2244 (2011).

[119] S. Seifert, H. T. v. Dam, J. Huizenga, R. Vinke, P. Dendooven, H. Löhner, and D. R. Schaart, *Monolithic labr 3 :ce crystals on silicon photomultiplier arrays for time-of-flight positron emission tomography,* Physics in Medicine and Biology **57**, 2219 (2012).

[120] S. Seifert, G. v. d. Lei, H. T. v. Dam, and D. R. Schaart, *First characterization of a digital sipm based time-of-flight pet detector with 1 mm spatial resolution,* Physics in Medicine and Biology **58**, 3061 (2013).

[121] F. Sánchez, A. Orero, A. Soriano, C. Correcher, P. Conde, A. González, L. Hernández, L. Moliner, M. J. Rodríguez-Alvarez, L. F. Vidal, J. M. Benlloch, S. E. Chapman, and W. M. Leevy, *Albira: A small animal pet/spect/ct imaging system,* Medical Physics **40**, 051906 (2013).

[122] A. J. González, A. Aguilar, P. Conde, L. Hernández, L. Moliner, L. F. Vidal, F. Sánchez, S. Sánchez, C. Correcher, C. Molinos, J. Barberá, K. Lankes, S. Junge, T. Bruckbauer, P. Bruyndonckx, and J. M. Benlloch, *A pet design based on sipm and monolithic lyso crystals: Performance evaluation,* IEEE Transactions on Nuclear Science **63**, 2471 (2016).

[123] P. Mollet, K. Deprez, B. Vandeghinste, S. Neyt, R. Marcinkowski, S. Vandenberghe, and R. Van Holen, *The β-cube, a high-end compact preclinical benchtop pet for total body imaging,* Journal of Nuclear Medicine **58**, 393 (2017).

[124] S. Krishnamoorthy, E. Blankemeyer, P. Mollet, S. Surti, R. V. Holen, and J. S. Karp, *Performance evaluation of the MOLECUBES β-CUBE—a high spatial resolution and high sensitivity small animal PET scanner utilizing mono-*

*lithic LYSO scintillation detectors,* Physics in Medicine & Biology **63**, 155013 (2018).

[125] T. Pan, S. A. Einstein, S. C. Kappadath, K. S. Grogg, C. Lois Gomez, A. M. Alessio, W. C. Hunter, G. El Fakhri, P. E. Kinahan, and O. R. Mawlawi, *Performance evaluation of the 5-ring ge discovery mi pet/ct system using the national electrical manufacturers association nu 2-2012 standard,* Medical Physics **46**, 3025 (2019).

[126] A. M. Grant, T. W. Deller, M. M. Khalighi, S. H. Maramraju, G. Delso, and C. S. Levin, *Nema nu 2-2012 performance studies for the sipm-based tof-pet component of the ge signa pet/mr system,* Medical Physics **43**, 2334 (2016).

[127] I. Rausch, A. Ruiz, I. Valverde-Pascual, J. Cal-González, T. Beyer, and I. Carrio, *Performance evaluation of the vereos pet/ct system according to the nema nu2-2012 standard,* Journal of Nuclear Medicine **60**, 561 (2019).

[128] J. van Sluis, J. de Jong, J. Schaar, W. Noordzij, P. van Snick, R. Dierckx, R. Borra, A. Willemsen, and R. Boellaard, *Performance characteristics of the digital biograph vision pet/ct system,* Journal of Nuclear Medicine **60**, 1031 (2019).

[129] S. Chen, P. Hu, Y. Gu, H. Yu, and H. Shi, *Performance characteristics of the digital umi550 pet/ct system according to the nema nu2-2018 standard,* EJNMMI Physics **7**, 43 (2020).

[130] R. Badawi, W. Liu, E. Berg, Y. Lv, T. Xu, S. An, Y. Dong, X. Zhang, M. Judenhofer, J. Qi, T. Jones, A. Tarantal, J. Bao, H. Li, and S. Cherry, *Progress on the explorer project: towards a total body pet scanner for human imaging,* Journal of Nuclear Medicine **59**, 223 (2018).

[131] R. D. Badawi, H. Shi, P. Hu, S. Chen, T. Xu, P. M. Price, Y. Ding, B. A. Spencer, L. Nardo, W. Liu, J. Bao, T. Jones, H. Li, and S. R. Cherry, *First human imaging studies with the explorer total-body pet scanner*,* Journal of Nuclear Medicine **60**, 299 (2019).

[132] Y. Lv, X. Lv, W. Liu, M. S. Judenhofer, A. Zwingenberger, E. Wisner, E. Berg, S. McKenney, E. Leung, B. A. Spencer, S. R. Cherry, and R. D. Badawi, *Mini EXPLORER II: a prototype high-sensitivity PET/CT scanner for companion animal whole body and human brain scanning,* Physics in Medicine & Biology **64**, 075004 (2019).

[133] S. Vandenberghe, P. Moskal, and J. S. Karp, *State of the art in total body pet,* EJNMMI Physics **7**, 35 (2020).

[134] B. A. Spencer, E. Berg, J. P. Schmall, N. Omidvari, E. K. Leung, Y. G. Abdelhafez, S. Tang, Z. Deng, Y. Dong, Y. Lv, J. Bao, W. Liu, H. Li, T. Jones, R. D. Badawi, and S. R. Cherry, *Performance evaluation of the uexplorer total-body pet/ct scanner based on nema nu 2-2018 with additional tests to*

*characterize long axial field-of-view pet scanners,* Journal of Nuclear Medicine , jnumed.120.250597 (2020).

[135] X. Li, W. Qi, M. Miyahara, and J. Kolthammer, *Performance characterization of an sipm-based time-of-flight canon pet/ct scanner,* Journal of Nuclear Medicine **61**, 14 (2020).

[136] S. Surti and J. S. Karp, *Update on latest advances in time-of-flight pet,* Physica Medica: European Journal of Medical Physics **80**, 251 (2020).

[137] S. R. Cherry, T. Jones, J. S. Karp, J. Qi, W. W. Moses, and R. D. Badawi, *Total-body pet: Maximizing sensitivity to create new opportunities for clinical research and patient care,* Journal of Nuclear Medicine **59**, 3 (2018).

[138] J. S. Karp, V. Viswanath, M. J. Geagan, G. Muehllehner, A. R. Pantel, M. J. Parma, A. E. Perkins, J. P. Schmall, M. E. Werner, and M. E. Daube-Witherspoon, *Pennpet explorer: Design and preliminary performance of a whole-body imager,* Journal of Nuclear Medicine **61**, 136 (2020).

[139] X. Zhang, Z. Xie, E. Berg, M. S. Judenhofer, W. Liu, T. Xu, Y. Ding, Y. Lv, Y. Dong, Z. Deng, S. Tang, H. Shi, P. Hu, S. Chen, J. Bao, H. Li, J. Zhou, G. Wang, S. R. Cherry, R. D. Badawi, and J. Qi, *Total-body dynamic reconstruction and parametric imaging on the uexplorer,* Journal of Nuclear Medicine **61**, 285 (2020).

[140] A. R. Pantel, V. Viswanath, M. E. Daube-Witherspoon, J. G. Dubroff, G. Muehllehner, M. J. Parma, D. A. Pryma, E. K. Schubert, D. A. Mankoff, and J. S. Karp, *Pennpet explorer: Human imaging on a whole-body imager,* Journal of Nuclear Medicine **61**, 144 (2020).

[141] G. Akamatsu, H. Tashima, Y. Iwao, H. Wakizaka, T. Maeda, A. Mohammadi, S. Takyu, M. Nitta, F. Nishikido, H. Rutherford, A. Chacon, M. Safavi-Naeini, E. Yoshida, and T. Yamaya, *Performance evaluation of a whole-body prototype PET scanner with four-layer DOI detectors,* Physics in Medicine & Biology **64**, 095014 (2019).

[142] C. Catana, *Development of dedicated brain pet imaging devices: Recent advances and future perspectives,* Journal of Nuclear Medicine **60**, 1044 (2019).

[143] K. Wienhard, M. Schmand, M. E. Casey, K. Baker, J. Bao, L. Eriksson, W. F. Jones, C. Knoess, M. Lenox, M. Lercher, P. Luk, C. Michel, J. H. Reed, N. Richerzhagen, J. Treffert, S. Vollmar, J. W. Young, W. D. Heiss, and R. Nutt, *The ecat hrrt: performance and first clinical application of the new high resolution research tomograph,* IEEE Transactions on Nuclear Science **49**, 104 (2002).

[144] A. Kolb, H. F. Wehrl, M. Hofmann, M. S. Judenhofer, L. Eriksson, R. Ladebeck, M. P. Lichy, L. Byars, C. Michel, H.-P. Schlemmer, M. Schmand, C. D. Claussen, V. Sossi, and B. J. Pichler, *Technical performance evaluation of a human brain pet/mri system,* European Radiology **22**, 1776 (2012).

[145] H. Tashima, E. Yoshida, Y. Iwao, H. Wakizaka, T. Maeda, C. Seki, Y. Kimura, Y. Takado, M. Higuchi, T. Suhara, T. Yamashita, and T. Yamaya, *First prototyping of a dedicated PET system with the hemisphere detector arrangement,* Physics in Medicine & Biology **64**, 065004 (2019).

[146] W. A. Berg, *Nuclear breast imaging: Clinical results and future directions,* Journal of Nuclear Medicine **57**, 46S (2016).

[147] D. F. Hsu, D. L. Freese, and C. S. Levin, *Breast-dedicated radionuclide imaging systems,* Journal of Nuclear Medicine **57**, 40S (2016).

# 2

# Experimental validation of an efficient fan-beam calibration procedure for k-nearest neighbor position estimation in monolithic scintillator detectors

This chapter has been published as:
G. Borghi, V. Tabacchini, S. Seifert, and D. R. Schaart, "Experimental Validation of an Efficient Fan-Beam Calibration Procedure for k-Nearest Neighbor Position Estimation in Monolithic Scintillator Detectors," IEEE Trans. Nucl. Sci., vol. 62, no. 1, pp. 57–67, Feb. 2015.
DOI: 10.1109/TNS.2014.2375557

***Abstract*** *- Monolithic scintillator detectors can achieve excellent spatial resolution and coincidence resolving time. However, their practical use for positron emission tomography (PET) and other applications in the medical imaging field is still limited due to drawbacks of the different methods used to estimate the position of interaction. Common statistical methods for example require the collection of an extensive dataset of reference events with a narrow pencil beam aimed at a fine grid of reference positions. Such procedures are time consuming and not straightforwardly implemented in systems composed of many detectors. Here, we experimentally demonstrate for the first* *time a new calibration procedure for k-nearest neighbor (k-NN) position estimation that utilizes reference data acquired with a fan beam. The procedure is tested on two detectors consisting of 16 mm × 16 mm × 10 mm and 16 mm × 16 mm × 20 mm monolithic, Ca-codoped LSO:Ce crystals and digital photon counter (DPC) arrays. For both detectors, the spatial resolution and the bias obtained with the new method are found to be practically the same as those obtained with the previously used method based on pencil-beam irradiation, while the calibration time is reduced by a factor of ∼20. Specifically, a FWHM of ∼1.1 mm and a FWTM of ∼2.7 mm were obtained using the fan-beam method with the 10 mm crystal, whereas a FWHM of ∼1.5 mm and a FWTM of ∼6 mm were achieved with the 20 mm crystal. Using a fan beam made with a ∼4.5 MBq* $^{22}$*Na point-source and a tungsten slit collimator with 0.5 mm aperture, the total measurement time needed to acquire the reference dataset was ∼3 hours for the thinner crystal and ∼2 hours for the thicker one.*

## 2.1. Introduction

Gamma-ray detectors based on bright monolithic scintillation crystals such as L(Y)SO:Ce(Ca) and $LaBr_3$:Ce coupled to position-sensitive light sensors such as multi-anode photomultipliers tubes (PMTs), arrays of avalanche photodiodes (APDs) and silicon photomultipliers (SiPMs) are currently being investigated for several applications in the medical imaging field. Mainly, these detectors have been considered for small-animal positron emission tomography (PET) [1–5] and dedicated PET systems [6]. However, monolithic crystals are also considered for clinical PET [7] and Compton cameras for dose monitoring during hadron therapy treatments [8]. Moreover, advances in gamma-ray detectors can be applied in single photon emission computed tomography (SPECT) [9].

Monolithic scintillator detectors have already shown the capability to achieve good spatial resolution and excellent timing resolution even with thick (~15 mm - 20 mm) crystals. For example, several research groups have obtained spatial resolutions better than 2 mm FWHM in crystals with a thickness of 10 mm - 15 mm [10–12], while coincidence resolving times (CRT) well below 200 ps FWHM have recently been achieved with 10 mm and 20 mm thick LSO:Ce(Ca) crystals [13]. Moreover, monolithic scintillator detectors provide good energy resolution [11, 14], show better sensitivity compared to high-resolution crystal matrices due to the absence of dead space, and can estimate the depth of interaction (DOI) from the shape of the light distribution [15–20]. In fact, the main advantage of detectors based on continuous crystals is that they can provide all of these results simultaneously, whereas detectors based on pixelated crystals typically require a tradeoff between spatial resolution on the one hand and sensitivity, time resolution and energy resolution on the other.

At present, the practical use of monolithic scintillator detectors is still hampered by drawbacks of the different techniques used to estimate the position of interaction, which can be broadly subdivided into two classes: parametric methods and statistical methods. The first class comprehends the positioning algorithms based on modelling of the relation between the 3D position of the light source inside the crystal and the light distribution measured by the photosensor [17, 19]. The main advantage of these methods is that they need little or no calibration data, since they are based on geometrical and physical considerations. However, these models usually have difficulties in positioning events close to the edges of the crystals, due to the truncation of the measured light distribution [17] and might not be robust in case of non-ideal response of the detectors. Also, they require quite intensive computational power, since for each unknown event a function with several fitting parameters has to be minimized or maximized. Moreover, to our knowledge, they have not yet been demonstrated for crystals thicker than 10 mm.

Common statistical methods include maximum likelihood (ML) positioning [16, 18], neural networks [21, 22], and the k-nearest neighbor (k-NN) method [2, 23]. These position estimation techniques are based on a thorough experimental characterization of the detector response as a function of the gamma-photon incidence position, which is usually performed by irradiating the detectors at precise positions with a narrowly collimated pencil beam of annihilation photons. These methods take into account the non-ideal response of the individual detector as well as the statistical properties of the signals, either incorporating them in a model (ML) or finely sampling the possible response for the same class of events (k-NN and neural networks). These methods can achieve excellent positioning performance. However, the complex and time demanding calibration procedures needed to acquire a set of reference events still impose a significant drawback for their application. Moreover, ML positioning and k-NN algorithms also require intense computational power.

Recently, a new statistical position estimation approach based on self-organizing maps (SOMs) was demonstrated by España *et al.* [9] in a 5 mm thick NaI(Tl) monolithic scintillator detector for SPECT. This method employs reference events acquired by flood irradiation and therefore requires a calibration measurement considerably more practical than other approaches. However, this SOM technique has been demonstrated only for estimating the 2D position of interaction of low-energy (141 keV) photons in thin crystals and thus has not yet been demonstrated for PET applications.

In this work, we focus on the k-NN method that is known to give good results in monolithic scintillator PET detectors [11, 14, 24, 25]. An early implementation of the k-NN method [2] made use of multiple reference datasets, each acquired at a different angle of incidence on the detector. Although this approach had the ability to estimate the entry point of the gamma-ray, thus avoiding parallax errors resulting from depth of interaction (DOI) variations, the total number of reference events required was very large.

More recently it was shown that the DOI in monolithic scintillators can be estimated directly based on the shape of the measured light distribution [20]. This approach requires only perpendicular calibration events and thus makes it possible to use a single perpendicular reference dataset both for training the DOI classifier and for estimating the x-y position of interaction using the k-NN method. This DOI estimation method thus removes the need to acquire reference events at multiple angles of incidence and reduces the time needed for detector calibration substantially.

Further acceleration of the k-NN approach was achieved by van Dam *et al.* [23], who reported on a number of modified k-NN methods that required a significantly smaller amount of reference data than the standard k-NN method while giving similarly good results. However, the reference events were still collected with a narrow pencil beam aimed at a fine grid of reference positions covering the entire crystal surface. Implementation of this approach in a completely assembled clinical or preclinical PET system is not straightforward. Similar pencil-beam calibration is also used with ML methods and methods based on neural networks, which therefore suffer from the same practicality problem.

van Dam *et al.* [23] therefore suggested, but did not experimentally test, a potential approach to further speed up and facilitate the calibration process. They described how an adaptation of the k-NN algorithm might enable the use of reference events acquired with a line source or a fan beam. Due to the higher count rate obtained with a fan beam, the acquisition of calibration events could be much faster. In addition, it was foreseen that fan beams could be realized in a practical way within clinical scanners, e.g. through electronic or mechanical collimation of line sources.

Here, k-NN estimation of the position of interaction in monolithic scintillator detectors utilizing reference data acquired with a fan beam is tested experimentally for the first time. The spatial resolution obtained with this new approach is compared to that obtained with pencil beams in order to determine if fan-beam irradiation can be considered a valid option for the calibration of monolithic scintillators.

## 2.2. Material and methods

### 2.2.1. Experimental setup

#### 2.2.1.1. Digital silicon photomultiplier array

The detectors used in this work were based on Digital Photon Counter (DPC) arrays (version DPC-3200-44-22), a type of digital silicon photo-multiplier (dSiPM) array developed by Philips Digital Photon Counting (PDPC). This array measures 32.6 mm × 32.6 mm and consists of 4 × 4 autonomous sensors (dies), each divided into 2 × 2 pixels. Each pixel comprises a total of 3200 microcells arranged into 64 columns and 50 rows, grouped into 2 × 2 equal sub-pixels.

Each DPC microcell is composed of a single photon avalanche photodiode (SPAD) and logic circuitry that actively quenches and recharges the SPAD after a discharge. The circuitry is also used to read out the state of the SPAD and can enable or disable it, giving the possibility to switch off the diodes that show an abnormally high dark count rate (DCR). A more detailed description of the DPC array can be found in [26, 27].

The acquisition sequence of a die is started by a trigger, whose threshold can be set by the user. In this work, the trigger level $MT_{=1}$ was used, i.e. a trigger is generated every time that a single cell discharges on the die. Whenever a trigger is generated, a time stamp is acquired and the die goes into the validation phase. During this phase, the sensor waits for a user-selected time interval and then checks if a higher threshold criterion, also selected by the user, is reached. In this work, the validation interval was set to 20 ns. The validation threshold was set such that the event is acquired if at least one pixel has at least one fired cell on each of its sub-pixels (DPC threshold notation: '0x7F:AND'). If none of the pixels reaches the validation criterion, the die undergoes to a fast recharge and reset, which takes about 20 ns. If the die is validated, the acquisition sequence is completed. First, the die waits for a user-defined integration time, which in this work was set to 165 ns. Afterwards, during the readout phase (680 ns), the number of fired cells is counted row-by-row and the summed number of cells per pixel is acquired. Finally, a recharge and reset sequence is performed. Therefore, when an event is acquired, a die provides one time stamp as well as the number of fired cells on each of its pixels.

Before the detectors were assembled, the DCR of the DPC arrays used in this work was measured at the temperature used for the measurements (-25°C). The measurement was performed following the procedure described in [26] and was used to disable the noisiest 5% of the cells.

#### 2.2.1.2. Monolithic scintillator detectors

Two monolithic scintillator detectors were tested in this work. These detectors were assembled using Ca-codoped (0.2% in the melt) LSO:Ce crystals [28], which were produced at the Scintillation Materials Research Center, University of Tennessee and provided by Agile Engineering Inc. (Knoxville, TN, USA). The crystals had polished surfaces, a base area of 16 mm × 16 mm and a thickness of 10 mm or 20 mm.

The scintillators were positioned on the four central dies of a DPC array (covering 4 × 4 pixels in total) and were optically coupled to the photosensor using a transparent silicone material (Sylgard 527, Dow Corning). In both cases, the four lateral faces of the crystal were covered with a specular reflector foil (Vikuiti ESR, 3M), whereas the top face was covered with Teflon tape. A coincidence detector was assembled using the same procedure with a standard LSO:Ce crystal (Agile Engineering Inc., Knoxville, TN, USA) having dimensions of 16 mm × 16 mm × 20 mm.

#### 2.2.1.3. Measurement / irradiation setup

A paired-collimator system was designed in order to obtain the 511 keV annihilation-photon beams needed to calibrate and test the detectors. This system is based on a central tungsten housing that contains an encapsulated 22Na point-source (⌀ 0.5 mm, ∼4.5 MBq, IDB Holland BV), surrounded in each direction by at least 3 cm of tungsten or lead (Figure 2.1, Figure 2.2). On one side of this housing, two different 80 mm long tungsten collimators can be mounted in order to define the beam used to irradiate the detector under test. On the other side, two corresponding 70 mm long lead collimators are used to reduce the count rate on the reference detector and to minimize the chance of random coincidences.

The first tungsten collimator has a cylindrical aperture having a diameter of 0.5 mm and it is paired to a lead collimator which has a 3 mm diameter cylindrical aperture (Figure 2.1). This set of collimators is used to create a narrow pencil beam for which both the x and y positions of interaction of the gamma-photons in the irradiated crystal are accurately known.

The second tungsten collimator has a rectangular aperture 0.5 mm wide and ∼35 mm long (Figure 2.2). Its paired lead collimator, instead, has a trapezoidal aperture, which is 3 mm wide and ∼29 mm long on the side further from the source.

This set of collimators is used to obtain a fan beam. Since the whole collimator system can rotate by an angle of 90°, the fan beam can be aligned perpendicularly to the x or y axis of the detector under test (Figure 2.3). In this manner, the x or y position of interaction of the gamma-photons in the crystal is known, while the fan beam irradiates the crystal approximately uniformly in the other direction.

The detectors to be tested were fixed on two linear x-y stages with a range of 100 mm and a precision ≤10 $\mu$m, driven by stepper-motors (Physics Instruments, M-403.42S stages with C-663 controllers). These stages were used to move the detectors in the plane perpendicular to the beam direction and to automatically acquire the reference/test events in all required positions.

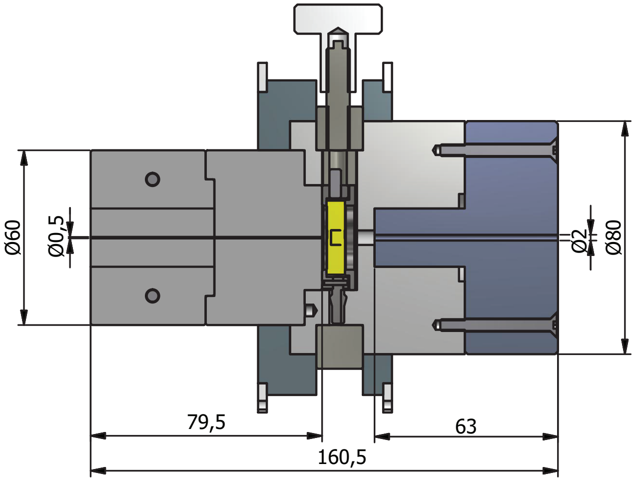

Figure 2.1: Design of the collimator used to create a pencil beam having a diameter of 0.5 mm (all dimensions in mm).

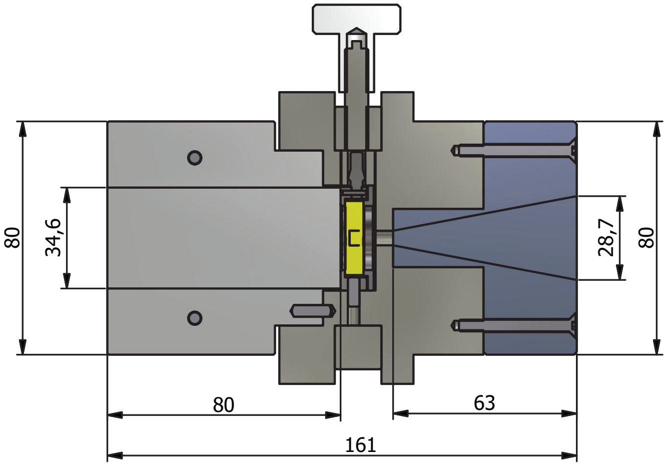

Figure 2.2: Design of the collimator used to create the fan beam having a width of 0.5 mm (all dimensions in mm).

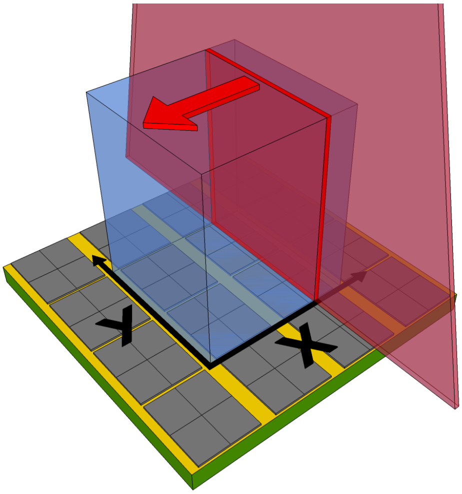

Figure 2.3: Illustration of the acquisition of the x-reference dataset with a fan beam. The narrow fan beam is aligned perpendicularly to the x axis and moved in the small steps along the x direction. For each x position a fixed number or event is acquired.

The setup was assembled inside a light-tight temperature chamber (Weiss WT 450/70). To reduce the DCR on the sensors, the ambient temperature was set to -25 °C. In order to dissipate the heat produced by the dSiPMs during operation, Peltier elements were coupled to the backsides of the sensors. The Peltier elements were regulated by a PI (proportional-integral) feedback system keeping the detector temperature stable within ~0.1° C.

### 2.2.2. Data acquisition

Two different sets of events were acquired for each detector. The first set was obtained by irradiating the entire front surface of the crystals with the pencil beam at a grid of 64 × 64 reference positions, at a pitch of 0.25 mm. For each point, 250 events were registered for which all the dies below the crystal were acquired and the full 511 keV energy was deposited. The energy selection was performed by creating an energy spectrum of the events acquired on all the positions and considering only the interactions comprised in the full width at tenth maximum (FWTM) of the photo-peak.

The second set was obtained by irradiating the crystals with the fan beam. First, the fan beam was aligned perpendicularly to the crystal x-axis and measurements were acquired at a series of 64 reference positions spaced 0.25 mm apart along the x-direction. At each position, 6400 full-energy, all-dies events were registered in order to obtain a first subset, hereafter referred as the x-subset. Subsequently, the fan beam was rotated by 90° and the y-subset was acquired using a similar procedure.

The light distributions of the events acquired with both of the irradiation methods were normalized to the sum of all pixel values before further processing and analysis.

## 2.2.3. Data processing and analysis

### 2.2.3.1. Position estimation

Four position estimation methods were used in this study, all based on the k-NN algorithm. Two established methods using reference dataset acquired with a pencil-beam irradiation were used as a benchmark for the methods based on fan-beam calibration [23]:

i) **Standard k-NN (Max 2D)**. This method calculates the Euclidean distance of the light distribution of the unknown event to those of all the events in the reference dataset. The k reference events having the smallest distances (nearest neighbors) are selected and a 2D histogram of their (x,y) irradiation coordinates is subsequently made. The position of the unknown events is estimated as the position of the 2D histogram for which there is the maximum number of entries. In case of multiple maxima, one of them is selected randomly.

ii) **Smoothed k-NN (Smoothed 2D)**. This method is similar to the standard one but a moving average filter is used to smooth the 2D histogram of the coordinates of the k nearest neighbors before locating the maximum. The filter is a square $n \times n$ filter which is cropped at crystal edges when necessary. In this work $n = 5$; therefore in the Smoothed 2D histogram each bin is the average of an area of 25 bins of the original histogram, except at the crystal borders.

The two methods based on a fan-beam irradiation are:

iii) **Standard k-NN 1D (Max 1D)**. To determine x, this method calculates the Euclidean distance between the light distribution of the unknown event and those of all events contained in the x-subset. The k events having the most similar light distributions are selected and a 1D histogram of their x coordinates is made. The x coordinate of the unknown event is estimated as the position in the histogram that has the most entries. In case of multiple maxima, one of them is selected at random. The procedure is then repeated to estimate the y coordinate using the y-subset.

iv) **Smoothed k-NN 1D (Smoothed 1D)**. The position estimation is performed similarly as for the 1D Max method, except that the 1D histograms are smoothed with a moving average filter that is n bins wide. When the filter approaches the edge of the histogram, its dimensions are reduced on the edge side. In this work, $n = 5$.

For both crystals, the entire dataset acquired with the pencil beam (250 events per grid position) was used as a test set and the positions of all events were estimated using the four different methods.

For the Max 2D and the Smoothed 2D algorithms, part of the same pencil-beam dataset was used as reference set, namely 100 fixed events per position. Whenever the positions of events belonging to the reference set were estimated, the leave-one-out method described in [24] was applied, whereas in all other cases the entire reference set was used.

For the Max 1D and the Smoothed 1D algorithms, the x- and y-subsets acquired with the fan beam, containing 6400 events per position, were used as reference set. Each subset, therefore, had the same number of events included in the pencil-beam reference dataset.

Since the fan beam is obtained by mechanical collimation of a point source, the crystal is not irradiated truly perpendicularly and uniformly along the entire length of the irradiated line. The uniformity of the acquired reference events along this line is additionally compromised by the increased escape probability of the scattered photon following a Compton interaction in the neighborhood of a crystal edge. To verify the influence of these effects, the Max 1D and the Smoothed 1D algorithms were additionally tested with an idealized 1D reference dataset containing perpendicularly incident events distributed uniformly along the irradiated line. This idealized fan-beam dataset is constructed from the pencil-beam dataset used as a reference for the 2D position estimation methods by alternately grouping together all events with the same x or y position on the grid. These experiments are referred to as Max $1D_{\mathrm{ideal}}$ and Smoothed $1D_{\mathrm{ideal}}$, respectively.

For all methods, the position estimation was performed selecting the 100 closest matches (k = 100) for building the 1D or 2D histograms of the nearest neighbors. Both the number of reference events and the number of closest matches were optimized in order to approach the best achievable results without excessively increasing the reference dataset.

#### 2.2.3.2. Misalignment correction

Before each measurement, a procedure based on count rate profiles was performed to align the collimator and the detector under test. The alignment procedure defines a coordinate system using the edges of the crystal as a reference. However, small differences in the alignments performed for different measurements (in the order of 0.1-0.2 mm) cannot be avoided completely. If the coordinate systems used to acquire test and reference events are not perfectly aligned, this may result in a bias when the accuracy of the position estimation is checked.

In this work, no bias is expected for the 2D and the $1D_{\mathrm{ideal}}$ methods, since the test and reference events are acquired during the same measurement. However, for the Max 1D and the Smoothed 1D methods the test events and reference events are acquired separately. Therefore, a procedure was developed to compare the alignment of the coordinate system used during fan-beam irradiation with the coordinate system used during pencil-beam irradiation and, if necessary, to correct for their differences. This procedure is described in Appendix A, section 2.5.

#### 2.2.3.3. Spatial resolution

Detector point spread functions (PSFs) were determined as the normalized 2D histograms of the differences between the estimated positions of the test events and their true irradiation coordinates. The measures that are used for the x and y spatial resolution are the full width at half maximum (FWHM) and the full width at

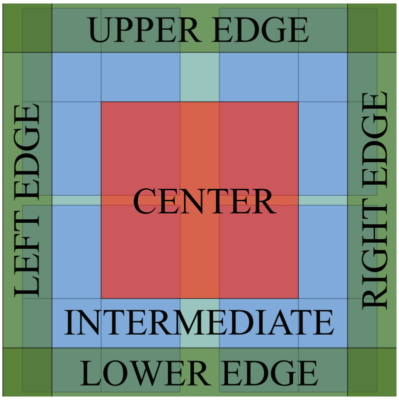

Figure 2.4: The different regions defined to study the variation of the spatial resolution and bias across the detector area. The center region is 8 mm × 8 mm wide and the edge regions are defined as the 2 mm borders on each side of the crystal. The intermediate region is the area not covered by the center and edge regions.

tenth maximum (FWTM) of the corresponding cross-sections of the PSF through its maximum.

For each of the two detectors, in combination with each of the six position estimation methods, the whole-detector PSF (containing the errors of all test events acquired over the entire detector surface) was built. The overall spatial resolutions were then estimated by interpolating the PSF cross-sections with a 1D cubic spline. For the Max 1D and the Smoothed 1D methods, the PSFs were built after applying the misalignment correction described in Appendix A, section 2.5.

In previous research, it has been shown that the spatial resolution of monolithic scintillator detectors depends on the position of interaction and usually degrades towards the edges of the crystal [11, 14, 24]. This problem was investigated for fan-beam calibration and compared with a standard position estimation method. To this end, a detailed analysis of small regions of the crystals was performed for both detectors, considering only the Smoothed 1D and the Smoothed 2D methods. Specifically, the front surface of the crystals was divided into six different regions, shown in Figure 2.4, and for each region a separate PSF was built. The regional FWHM and FWTM were then calculated and used to compare the different calibration methods.

#### 2.2.3.4. Bias

For both crystals, the bias in the position estimation obtained with the Smoothed 1D and the Smoothed 2D methods were analyzed. This study was performed using a method similar to the one described in [11, 14]. For each irradiation position $\mathbf{v}_{i,j}$, the bias vector $\mathbf{b}(\mathbf{v}_{i,j})$ was calculated as the mean error of the estimated positions:

$$\mathbf{b}(\mathbf{v}_{i,j}) = \begin{bmatrix} \frac{\sum_{m=1}^{M}(\hat{x}_m(\mathbf{v}_{i,j}) - x_{i,j})}{M} \\ \frac{\sum_{m=1}^{M}(\hat{y}_m(\mathbf{v}_{i,j}) - y_{i,j})}{M} \end{bmatrix} \tag{2.1}$$

where $m$ is the m$^{\text{th}}$ test event acquired at position $\mathbf{v}_{i,j} = (x_{i,j}, y_{i,j})$ ($i$ and $j$ being the row and column indexes of the grid), $\hat{\mathbf{v}}_m = (\hat{x}_m, \hat{y}_m)$ is its estimated position and $M$ is the number of events per positions. No further selection was made on the estimated events, so, for each point, $M = 250$. The crystal surface was divided in areas 0.5 mm × 0.5 mm wide, each containing four irradiation points, and the average bias vector was calculated for each of them. The vector magnitudes were calculated as their Euclidean norm.

## 2.3. Results and discussion

### 2.3.1. Calibration time

The coincidence event rate measured during fan-beam irradiation equals ~200 Hz for the 10 mm thick crystal and ~300 Hz for the 20 mm thick one. In both cases this is ~40 times higher than the coincidence event rate registered with the pencil beam, as expected from the ratio of the different irradiated areas. Since the x- and y-subsets acquired with the fan beam contain the same number of events as the pencil-beam reference set (see section 2.2.2), the fan-beam calibration procedure is ~20 times faster for 16 mm × 16 mm crystals. It has to be emphasized that the same point source was used for both measurements and only the paired collimators were changed. The measurement time needed to acquire the total fan-beam dataset was ~3 hours for the thinner crystal and ~2 hours for the thicker one.

### 2.3.2. Spatial resolution

The overall spatial resolutions obtained with the six different position estimation methods (see section 2.2.3.1) are reported in Table 2.1 and Table 2.2 for the 16 mm × 16 mm × 10 mm and the 16 mm × 16 mm × 20 mm crystal, respectively. Using the fan-beam (Smoothed 1D) method, a FWHM of ~1.1 mm and a FWTM of ~2.7 mm were obtained with the thinner crystal in both the x and y directions. With the 20 mm thick crystal, the fan-beam method resulted in a FWHM of ~1.5 mm and a FWTM of ~6 mm.

For both detectors, the results were practically the same as those obtained with the pencil-beam (Smoothed 2D) method. Moreover, the smoothing procedure appears to significantly improve the positioning accuracy compared to the Max 1D method, similar to what was found for the corresponding 2D algorithms [23].

The results obtained with the Max 1D$_{\text{ideal}}$ and Smoothed 1D$_{\text{ideal}}$ datasets (see section 2.2.3.1) are essentially equal to those achieved using the corresponding datasets obtained with the mechanically collimated fan beam (Max 1D and Smoothed 1D, respectively). This indicates that a reference dataset acquired with a realistic fan beam performs similarly well as a dataset acquired under idealized conditions,

Table 2.1: Overall spatial resolutions obtained with the position estimation methods described in section 2.2.3.1 for the 16 mm × 16 mm × 10 mm crystal

| Method | Beam | x direction | | y direction | |
|---|---|---|---|---|---|
| | | FWHM (mm) | FWTM (mm) | FWHM (mm) | FWTM (mm) |
| Max 2D | Pencil | 1.25 | 3.05 | 1.27 | 3.17 |
| Smoothed 2D | Pencil | 1.07 | 2.63 | 1.07 | 2.75 |
| Max $1D_{ideal}$ | Pencil | 1.17 | 2.88 | 1.18 | 2.98 |
| Smoothed $1D_{ideal}$ | Pencil | 1.07 | 2.67 | 1.06 | 2.78 |
| Max 1D | Fan | 1.21 | 2.88 | 1.21 | 2.97 |
| Smoothed 1D | Fan | 1.08 | 2.70 | 1.10 | 2.75 |

Table 2.2: Overall spatial resolutions obtained with the position estimation methods described in section 2.2.3.1 for the 16 mm × 16 mm × 20 mm crystal

| Method | Beam | x direction | | y direction | |
|---|---|---|---|---|---|
| | | FWHM (mm) | FWTM (mm) | FWHM (mm) | FWTM (mm) |
| Max 2D | Pencil | 1.92 | 6.66 | 1.91 | 7.30 |
| Smoothed 2D | Pencil | 1.49 | 5.85 | 1.50 | 6.22 |
| Max $1D_{ideal}$ | Pencil | 1.73 | 6.40 | 1.79 | 6.63 |
| Smoothed $1D_{ideal}$ | Pencil | 1.54 | 6.02 | 1.57 | 6.22 |
| Max 1D | Fan | 1.77 | 6.50 | 1.84 | 7.30 |
| Smoothed 1D | Fan | 1.51 | 5.94 | 1.57 | 6.38 |

i.e. with all reference events incident perpendicularly to the crystal and distributed uniformly along the irradiated line.

The FWHM and FWTM values obtained from the regional PSFs are given in Table 2.3 and Table 2.4 for the 10 mm and 20 mm thick crystals, respectively. For the thinner crystal, the Smoothed 1D method yields FWHM values comparable to the Smoothed 2D method in almost all cases. Only in the edge regions slightly worse FWHM values are found for the coordinate perpendicular to the edge considered. In most of the crystal regions, the 1D method furthermore yields slightly (0.1 mm - 0.2 mm) higher values of the FWTM. However, the differences are small and the two methods can be assumed to be substantially equivalent.

The FWHM values obtained in the edge regions of the 20 mm thick crystal show similar trends as in the 10 mm thick one. As for the FWTM values, their comparison becomes more difficult for this detector, since the PSFs are wider and therefore suffer from statistical fluctuations on their tails. However, a trend for slightly higher FWTM values for the 1D position estimation method can again be noticed, which in any case does not substantially deteriorate the positioning performance.

The actual shapes of the PSFs obtained with 1D and 2D position estimation are also found to be practically equivalent. As an example, a comparison of the cross-sections in the y-direction of the PSFs obtained in four selected regions are shown in Figure 2.5 for the 10 mm thick crystal and in Figure 2.6 for the 20 mm thick one. These findings demonstrate that the new 1D position estimation procedure based on calibration data acquired with a fan beam can achieve results similarly good as

Table 2.3: FWHM and FWTH values of regional PSFs in the regions indicated in 2.4 for the 16 mm × 16 mm × 10 mm crystal. The smoothed 1d and smoothed 2d k-nn position estimation algorithms were used.

| Region | x direction | | | | y direction | | | |
|---|---|---|---|---|---|---|---|---|
| | FWHM (mm) | | FWTM (mm) | | FWHM (mm) | | FWTM (mm) | |
| | 1D | 2D | 1D | 2D | 1D | 2D | 1D | 2D |
| Left edge | 1.61 | 1.62 | 4.10 | 4.02 | 1.02 | 1.03 | 2.61 | 2.60 |
| Right edge | 1.56 | 1.39 | 3.80 | 3.69 | 1.00 | 1.00 | 2.59 | 2.53 |
| Upper edge | 1.07 | 1.02 | 2.57 | 2.46 | 1.74 | 1.38 | 4.07 | 3.88 |
| Lower edge | 1.01 | 1.05 | 2.43 | 2.44 | 1.65 | 1.58 | 4.08 | 4.26 |
| Center | 0.98 | 0.97 | 2.01 | 1.99 | 0.99 | 0.96 | 2.06 | 2.02 |
| Intermediate | 1.11 | 1.08 | 2.55 | 2.53 | 1.11 | 1.13 | 2.71 | 2.66 |
| Total | 1.08 | 1.07 | 2.70 | 2.63 | 1.10 | 1.07 | 2.75 | 2.75 |

Table 2.4: FWHM and FWTH values of regional PSFs in the regions indicated in 2.4 for the 16 mm × 16 mm × 20 mm crystal. The smoothed 1d and smoothed 2d k-nn position estimation algorithms were used.

| Region | x direction | | | | y direction | | | |
|---|---|---|---|---|---|---|---|---|
| | FWHM (mm) | | FWTM (mm) | | FWHM (mm) | | FWTM (mm) | |
| | 1D | 2D | 1D | 2D | 1D | 2D | 1D | 2D |
| Left edge | 2.13 | 2.04 | 6.41 | 6.21 | 1.51 | 1.61 | 6.02 | 6.66 |
| Right edge | 1.96 | 1.84 | 6.26 | 5.67 | 1.67 | 1.54 | 6.27 | 6.39 |
| Upper edge | 1.59 | 1.59 | 6.27 | 6.25 | 2.12 | 1.89 | 6.92 | 6.33 |
| Lower edge | 1.54 | 1.42 | 6.21 | 5.81 | 2.21 | 1.86 | 7.28 | 6.63 |
| Center | 1.22 | 1.31 | 6.24 | 4.91 | 1.22 | 1.29 | 8.31 | 5.27 |
| Intermediate | 1.54 | 1.51 | 6.40 | 6.48 | 1.58 | 1.56 | 6.73 | 7.33 |
| Total | 1.51 | 1.49 | 5.94 | 5.85 | 1.57 | 1.50 | 6.38 | 6.22 |

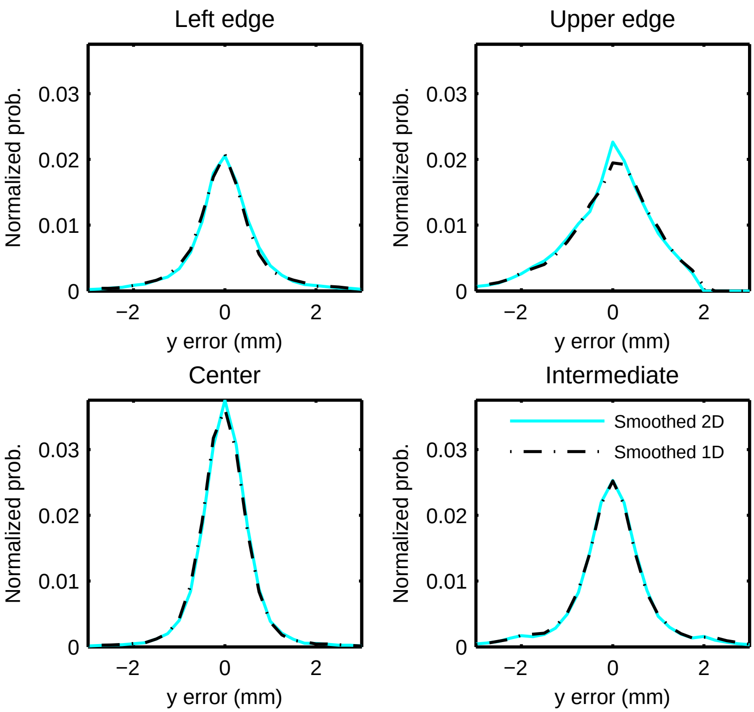

Figure 2.5: Cross-sections in the y-direction through the maximum of the regional PSFs obtained with the 1D (black) and 2D (cyan) Smoothed k-NN methods for the 10 mm thick crystal. From left to right, top to bottom, they correspond to the left-edge region, top-edge region, central region, and intermediate region.

the method using pencil-beam calibration data.

The results obtained here with a 16 mm × 16 mm × 10 mm LSO:Ce,0.2%Ca crystal mounted on a DPC-3200-44-22 array are similar to the best values reported in literature for ~10 mm thick crystals. Seifert *et al.*, for example, in [11] characterized a detectors similar to the one presented in this work, which was based on a 24 mm × 24 mm × 10 mm LSO:Ce,0.2%Ca crystal coupled to DPC-6400-44-22 array. Also for that detector the FWHM obtained in the center region of the crystal was a little smaller than 1 mm FWHM, while the FWTM was ~2 mm. Averaged over the entire 24 mm × 24 mm × 10 mm crystal, a FWHM of ~1 mm and a FWTM of ~2.3 mm were achieved. The slightly higher average values obtained in the present work can be attributed to the increased influence of the intermediate and edge regions in a detector with a smaller surface area. Cabello *et al.* [12] reported a spatial resolution of ~0.7 mm FWHM and ~2.0 mm FWTM for a detector based on a 12 mm × 12 mm × 10 mm LYSO crystal and a 8 × 8 pixels analog SiPM array. These excellent results may have been due to the small photosensor pixel size of 1.5 mm × 1.4 mm, which enables a very fine sampling of the light distribution. Ling *et al.* [17] achieved a spatial resolution of ~1.1 mm FWHM in the central part of

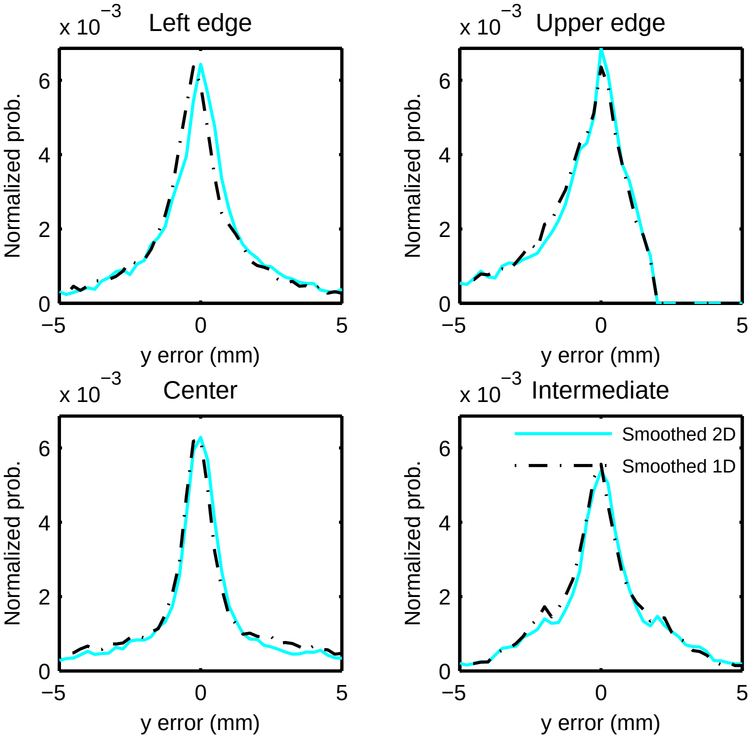

Figure 2.6: Cross-sections in the y-direction through the maximum of the regional PSFs obtained with the 1D (black) and 2D (cyan) Smoothed k-NN methods for the 20 mm thick crystal. From left to right, top to bottom, they correspond to the left-edge region, top-edge region, central region, and intermediate region.

the crystal and ∼1.3 mm FWHM in the corners of the detector for a detector based on a 50 mm × 50 mm × 8 mm LYSO crystal and a 64-channel flat-panel PMT.

The results obtained with the 16 mm × 16 mm × 20 mm crystal are considered highly promising since, to our knowledge, this is the first time a FWHM better than 2 mm is achieved with a ≥20 mm thick monolithic crystal with back-side readout (BSR). So far, this had only been demonstrated with monolithic scintillator detectors employing double-side readout (DSR) [24]. Previously, the thickest detector having single-side readout which demonstrated a FWHM resolution <2 mm was the one described by Li *et al.*, in [10], which was based on a 50 mm × 50 mm × 15 mm LYSO crystal and a 64-channel flat-panel PMT and had a spatial resolution of ∼1.5 mm FWHM.

Still, the PSFs obtained for the 20 mm thick detector presented in this paper show long tails, which determine the value of ∼6 mm for the FWTMs. The tails probably have two causes. The first refers to events for which the gamma-ray undergoes a Compton interaction and is subsequently absorbed in a position distant from the original line of irradiation. Due to the crystal thickness, this distance can be significant in the x- and y- directions even for relatively small scattering angles. The second reason refers to the aspect-ratio of the crystal, which is rather high compared to its width. This crystal shape determines that the cone of direct light (i.e. the photons having an angle of incidence with the photosensors surface smaller than the critical angle) created by events taking place in the top part of the crystal is distorted and truncated by reflections on the side surfaces of the crystal. Therefore, the change of the light distribution with position, which determines the lower bound on the variance on the estimated interaction coordinates [29, 30], becomes worse compared to the situation in a crystal with lower aspect ratio, where at least one side of the direct light distribution is never truncated. The FWTM values could therefore improve significantly in lower-aspect-ratio crystals.

Looking at the regional PSF of both detectors, it is possible to notice a worsening in the spatial resolution in the edge regions of the crystal compared to the resolution observed in the central region. This deterioration, which happens for both reconstruction methods, is limited to the coordinate perpendicular to the considered edge and is consistent with previous results [10, 11, 14, 25]. A detailed discussion about the causes underlying this phenomenon can be found in [14].

### 2.3.3. Bias

The plots of the bias vectors $\mathbf{b}(\mathbf{v}_{i,j})$, calculated as described in section 2.2.3.4 for the Smoothed 1D and the Smoothed 2D methods applied to the 10 mm thick crystal, are shown in Figure 2.7. No considerable differences are observed. Only the regions near the corners show a slightly (<0.3 mm) higher bias towards the center for the Smoothed 1D method. Both of the position estimation methods reach remarkable results; except for the border regions (distance ≤1 mm from the edges) the bias is always smaller than 0.5 mm.

For the 20 mm thick crystal (Figure 2.8) the bias is ≤1.1 mm in the center and intermediate regions for both position estimation methods. The bias becomes more pronounced in the edge regions, where it is between 1 mm and 2 mm, and in the

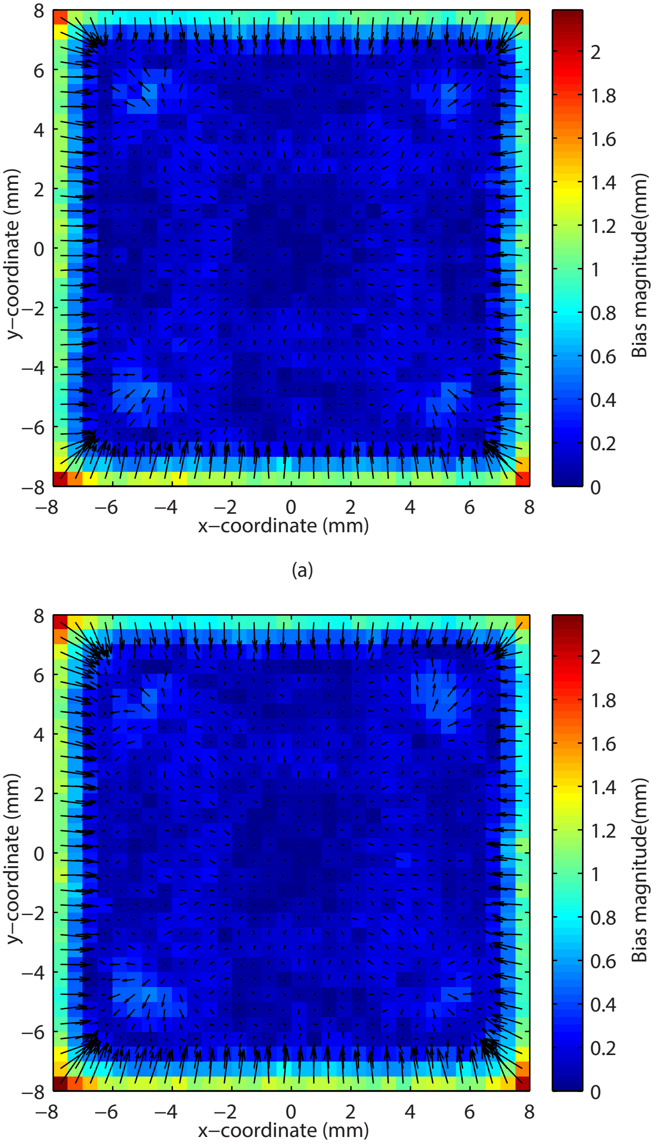

(a)

(b)

Figure 2.7: Direction and magnitude of the bias vectors $\mathbf{b}(\mathbf{v}_{i,j})$ obtained with the Smoothed 1D (a) and the Smoothed 2D (b) position estimation methods for the 10 mm thick crystal. The bias vectors are averaged over an area of 0.5 mm × 0.5 mm, i.e. over 2 × 2 irradiation positions. The color scale represents the vector magnitude.

corners, where it can reach almost 4 mm. Also for this detector the Smoothed 1D method shows a slightly higher bias in the corners. The difference with the Smoothed 2D method is ≤0.5 mm and occurs at distances of less than 2 mm from the corners only. For this detector, a small difference between the position estimation methods can be noticed in the central region as well; in this area the 1D positioning method seems to perform slightly better.

The hypothesis that the increased bias found with the Smoothed 1D method in the corner regions is due to the non-uniform distribution of the reference events along the lines irradiated with the fan beam has been considered and tested. This non-uniformity is due to the higher escape probability of the scattered photon following a Compton interaction near the edges (see also section 2.2.3.1). In principle this could result in a higher possibility to select events from the central region during position estimation, especially in the corner regions. To test this hypothesis, the bias plot was calculated also for the Smoothed $1D_{\text{ideal}}$ method, which makes use of the reference dataset acquired for the pencil-beam calibration. Since in this calibration procedure the irradiation times are adjusted to acquire the same number of full-energy events in each grid point, the reference dataset used for the Smoothed $1D_{\text{ideal}}$ method is uniform along each line. However, approximately the same increased bias in the corners was observed also for this dataset and therefore the hypothesis is rejected.

The independent estimation of the x- and the y-coordinates in the Smoothed 1D method therefore seems a more likely cause of the increased bias in the corners. In those regions the variation of light distribution with one of the coordinates probably is no longer independent of the other coordinate and the correlated estimation of the x- and y-coordinates by the Smoothed 2D method may yield better results. Anyway, the differences in bias between the different calibration methods are small and therefore are not expected to change the detector performance significantly.

## 2.4. Conclusions

A new method to estimate the position of interaction of 511 keV gamma-photons in monolithic scintillator detectors was tested experimentally for the first time. This method is based on a modified (Smoothed 1D) k-NN algorithm that enables efficient acquisition of reference events by means of a fan beam. The new method was compared to a method based on pencil-beam irradiation (Smoothed 2D) that has previously been shown to give good results in 10 mm thick crystals [11, 14, 23]. The new method was tested using two detectors based on DPC arrays and LSO:Ce(0.2%Ca) monolithic crystals having dimensions of 16 mm × 16 mm × 10 mm and 16 mm × 16 mm × 20 mm.

With both crystals, the Smoothed 1D method essentially achieved the same performance as the Smoothed 2D method with respect to the overall spatial resolution, the spatial resolution of selected detector regions, and the positioning bias. With the 10 mm thick crystal, an overall spatial resolution of ~1.1 mm FWHM and ~2.7 mm FWTM was achieved, whereas a FWHM of ~1.5 mm and a FWTM of ~6 mm were obtained with the 20 mm thick crystal.

The new calibration method proved to be more than one order of magnitude

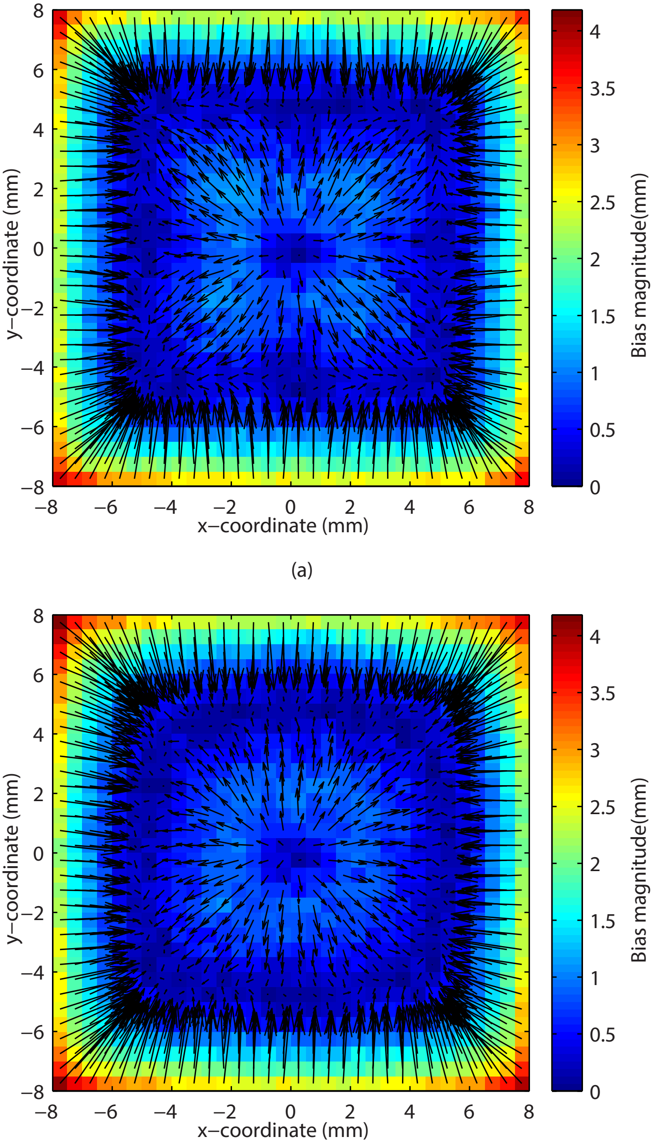

(a)

(b)

Figure 2.8: Direction and magnitude of the bias vectors $\mathbf{b}(\mathbf{v}_{i,j})$ obtained with the Smoothed 1D (a) and the Smoothed 2D (b) position estimation methods for the 20 mm thick crystal. The bias vectors are averaged over an area of 0.5 mm × 0.5 mm, i.e. over 2 × 2 irradiation positions. The color scale represents the vector magnitude.

faster than the previous one using the same point source. Moreover, a fan beam similar to the one used in this experiment could be obtained with a collimated line source. A line source can be produced with a total activity much higher than a point source since the radioactive volume is larger at the same source diameter. Therefore, if necessary, detector calibration could be made even faster if line sources were employed.

The fan-beam method reduces the complexity of the calibration procedure considerably. With a pencil beam the total number of reference positions is $n_{pos} \times n_{pos}$, whereas with a fan beam it equals $n_{pos} + n_{pos}$ only, where $n_{pos}$ is the number of reference positions along one crystal axis. This is particularly important when implementing a procedure for acquiring the reference events in an assembled PET scanner. Using multiple line-sources in combination with mechanical and/or electronic collimation, irradiation condition similar to those used in this work could be obtained in a PET ring in order to simultaneously calibrate all the detectors. Calibration of a full scanner with pencil beams, instead, would be a much more complex and time consuming task.

In conclusion, the new calibration method may enable the acquisition of reference datasets in a reasonable time period also in a clinical environment. Thus, fan-beam calibration could eliminate the calibration problems that have so far hampered the application of monolithic detectors in clinical PET systems. The actual implementation of such a procedure will require further investigations, e.g. to determine the optimum number of sources and the geometry needed to simultaneously calibrate all the detectors.

## 2.5. Appendix: misalignment correction

In this experiment, the coordinate systems defined during the pencil-beam irradiation and the fan-beam irradiation could be slightly misaligned. Therefore, to correctly determine the error in the interaction positions estimated with the Max 1D and Smoothed 1D methods, the irradiation positions of the reference events, i.e. the possible estimated positions, have to be determined in the coordinate system of the test events.

Let us define the coordinate system used during the fan-beam irradiation as $X''Y''$ and the coordinate system used during the pencil-beam irradiation as $XY$ (see Figure 2.9). Both of them are centered approximately in the center of the crystal. The misalignment between them can be described as a linear coordinate transformation. The corresponding translation vector $\mathbf{t} = (t_x, t_y)$ and the rotation angle $\alpha$ can be determined using the following assumption. If the calibration and test coordinates are aligned perfectly, then the x-error distributions for two positions that are located symmetrically with respect to the crystal y-axis should be symmetric with respect to the zero error axis. The mean value of their summed error distributions should therefore be 0. Similar arguments apply in the orthogonal direction. Therefore, if the crystal is irradiated at a rectangular grid of positions uniformly distributed over a rectangular region centered on the crystal center, the mean x-error on each grid row, the mean y-error on each grid column, and, therefore, the total mean error, should be zero. Even if the reference and test grids are

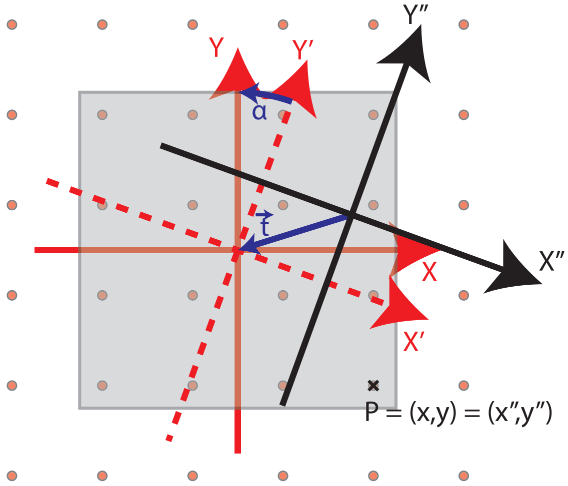

Figure 2.9: Sketch of the transformation of the coordinate system applied to the estimated positions of the test events obtained with the fan-beam methods, to make them consistent with the positions of the pencil-beam irradiation; $X''Y''$ is the coordinate system used during the fan-beam irradiation and $XY$ is the coordinate system used during the pencil-beam irradiation. The red dots represents the grid positions of the pencil-beam irradiation and the grey square contains the grid positions selected for the correction.

slightly rotated and/or translated with respect to the crystal edges, this assumption still holds within good approximation in the crystal region that is not affected by significant bias (see section 2.2.3.4 for a definition of bias). Therefore, a potential translation between the reference and test coordinate systems can be corrected by imposing:

$$\mathbf{e} = \begin{bmatrix} \dfrac{\sum_{i,j,m}((\hat{x}''_m(\mathbf{v}_{i,j}) - t_x) - x_{i,j})}{I \times J \times M} \\ \dfrac{\sum_{i,j,m}((\hat{y}''_m(\mathbf{v}_{i,j}) - t_x) - y_{i,j})}{I \times J \times M} \end{bmatrix} = 0 \tag{2.2}$$

where $m$ is the $m^{th}$ test event at position $\mathbf{v}_{i,j} = (x_{i,j}, y_{i,j})$ ($i$ and $j$ being the row and column indexes of the grid), $\hat{\mathbf{v}}''_m = (\hat{x}''_m, \hat{y}''_m)$ is its estimated position, $M$ is the number of events per positions, and $I$ and $J$ are the number of grid positions in the x- and y-direction, respectively.

Subsequently, a potential rotation $R_\alpha$ can be estimated from the sum of the x-errors on each grid row and of the y-errors on each grid column. The angle $\alpha$ can be determined as:

Table 2.5: Components of the translation vector **t** = $(t_x, t_y)$ and rotation angle $\alpha$ necessary to align the coordinate systems used during the pencil-beam scan and the fan-beam scan

| Crystal | Method | $t_x$ (mm) | $t_y$ (mm) | $\alpha(^\circ)$ |
|---|---|---|---|---|
| 16 mm × 16 mm × 10 mm | Max 1D | -0.04 | -0.11 | 0.96 |
| | Smoothed 1D | -0.04 | -0.11 | 0.93 |
| 16 mm × 16 mm × 20 mm | Max 1D | 0.00 | -0.05 | 0.00 |
| | Smoothed 1D | -0.01 | -0.04 | 0.00 |

$$\alpha = \arg\min_{\alpha} \left\{ \sum_{i} \left| \frac{\sum_{j,m} R_\alpha(\hat{x}'_m(\mathbf{v}_{i,j})) - x_{i,j}}{I \times J \times M} \right| + \sum_{j} \left| \frac{\sum_{i,m} R_\alpha(\hat{y}'_m(\mathbf{v}_{i,j})) - y_{i,j}}{I \times J \times M} \right| \right\} \tag{2.3}$$

Previous studies [11, 14] showed that the central region of monolithic detectors is usually not affected significantly by bias. Therefore, the events acquired during the pencil-beam irradiation having coordinates x and y between -4 mm and 4 mm from the crystal center (in the system of coordinate $XY$ of the pencil-beam irradiation) were selected to calculate the corrections for the Max 1D and the Smoothed 1D k-NN methods in both the crystals.

The components of the translation vector $\mathbf{t} = (t_x, t_y)$ and the rotation angle $\alpha$ necessary to align the coordinate systems of the fan-beam scans to the coordinate systems of the pencil-beam scans are given in Table V for both of the 1D methods. For both crystals the values obtained with the two different algorithms are consistent.

## References

[1] P. Bruyndonckx, C. Lemaitre, S. Leonard, D. R. Schaart, D. J. van der Laan, M. C. Maas, O. Devroede, W. Yibao, M. Krieguer, and S. Tavernier, *Initial characterization of a nonpixelated scintillator detector in a pet prototype demonstrator,* Nuclear Science, IEEE Transactions on **53**, 2543 (2006).

[2] M. C. Maas, D. Van der Laan, D. R. Schaart, J. Huizenga, J. C. Brouwer, P. Bruyndonckx, S. Leonard, C. Lemaitre, and C. W. E. Van Eijk, *Experimental characterization of monolithic-crystal small animal pet detectors read out by apd arrays,* Nuclear Science, IEEE Transactions on **53**, 1071 (2006).

[3] R. S. Miyaoka, X. Li, W. Hunter, L. A. Pierce, W. McDougald, P. E. Kinahan, and T. K. Lewellen, *Resolution properties of a prototype continuous miniature crystal element (cmice) scanner,* Nuclear Science, IEEE Transactions on **58**, 2244 (2011).

[4] M. Carles, C. W. Lerche, F. Sánchez, A. Orero, L. Moliner, A. Soriano, and J. M. Benlloch, *Performance of a doi-encoding small animal pet system with monolithic scintillators,* Nuclear Instruments and Methods in Physics Research Section A: Accelerators, Spectrometers, Detectors and Associated Equipment **695**, 317 (2012).

[5] G. Llosá, P. Barrillon, J. Barrio, M. G. Bisogni, J. Cabello, A. Del Guerra, A. Etxebeste, J. E. Gillam, C. Lacasta, J. F. Oliver, M. Rafecas, C. Solaz, V. Stankova, and C. de La Taille, *High performance detector head for pet and pet/mr with continuous crystals and sipms,* Nuclear Instruments and Methods in Physics Research Section A: Accelerators, Spectrometers, Detectors and Associated Equipment **702**, 3 (2013).

[6] I. Sarasola, P. R. Mendes, P. Garcia de Acilu, M. Canadas, O. Vela, J. M. Cela, J. C. Oller, L. Nunez, C. Willmott, and J. M. Perez, *Pet demonstrator for a human brain scanner based on monolithic detector blocks,* Nuclear Science, IEEE Transactions on **58**, 2190 (2011).

[7] M. Kaul, S. Surti, and J. S. Karp, *Combining surface treatments with shallow slots to improve the spatial resolution performance of continuous, thick lyso detectors for pet,* Nuclear Science, IEEE Transactions on **60**, 44 (2013).

[8] G. Llosá, J. Cabello, S. Callier, J. E. Gillam, C. Lacasta, M. Rafecas, L. Raux, C. Solaz, V. Stankova, C. de La Taille, M. Trovato, and J. Barrio, *First compton telescope prototype based on continuous labr3-sipm detectors,* Nuclear Instruments and Methods in Physics Research Section A: Accelerators, Spectrometers, Detectors and Associated Equipment **718**, 130 (2013).

[9] S. España, K. Deprez, R. V. Holen, and S. Vandenberghe, *Fast calibration of spect monolithic scintillation detectors using un-collimated sources,* Physics in Medicine and Biology **58**, 4807 (2013).

[10] X. Li, W. C. J. Hunter, T. K. Lewellen, and R. S. Miyaoka, *Use of cramer–rao lower bound for performance evaluation of different monolithic crystal pet detector designs,* IEEE Transactions on Nuclear Science **59**, 3 (2012).

[11] S. Seifert, G. v. d. Lei, H. T. v. Dam, and D. R. Schaart, *First characterization of a digital sipm based time-of-flight pet detector with 1 mm spatial resolution,* Physics in Medicine and Biology **58**, 3061 (2013).

[12] J. Cabello, P. Barrillon, J. Barrio, M. G. Bisogni, A. Del Guerra, C. Lacasta, M. Rafecas, H. Saikouk, C. Solaz, P. Solevi, C. de La Taille, and G. Llosá, *High resolution detectors based on continuous crystals and sipms for small animal pet,* Nuclear Instruments and Methods in Physics Research Section A: Accelerators, Spectrometers, Detectors and Associated Equipment **718**, 148 (2013).

[13] H. T. van Dam, G. Borghi, S. Seifert, and D. R. Schaart, *Sub-200 ps crt in monolithic scintillator pet detectors using digital sipm arrays and maximum likelihood interaction time estimation,* Physics in Medicine and Biology **58**, 3243 (2013).

[14] S. Seifert, H. T. v. Dam, J. Huizenga, R. Vinke, P. Dendooven, H. Löhner, and D. R. Schaart, *Monolithic labr 3 :ce crystals on silicon photomultiplier arrays for time-of-flight positron emission tomography,* Physics in Medicine and Biology **57**, 2219 (2012).

[15] C. Lerche, J. Benlloch, F. Sanchez, N. Pavon, B. Escat, E. Gimenez, M. Fernandez, I. Torres, M. Gimenez, A. Sebastia, and J. Martinez, *Depth of gamma-ray interaction within continuous crystals from the width of its scintillation light-distribution,* IEEE Transactions on Nuclear Science **52**, 560 (2005).

[16] T. Ling, T. K. Lewellen, and R. S. Miyaoka, *Depth of interaction decoding of a continuous crystal detector module,* Physics in Medicine and Biology **52**, 2213 (2007).

[17] T. Ling, T. H. Burnett, T. K. Lewellen, and R. S. Miyaoka, *Parametric positioning of a continuous crystal pet detector with depth of interaction decoding,* Physics in Medicine and Biology **53**, 1843 (2008).

[18] W. C. J. Hunter, H. H. Barrett, and L. R. Furenlid, *Calibration method for ml estimation of 3d interaction position in a thick gamma-ray detector,* Nuclear Science, IEEE Transactions on **56**, 189 (2009).

[19] Z. Li, M. Wedrowski, P. Bruyndonckx, and G. Vandersteen, *Nonlinear least-squares modeling of 3d interaction position in a monolithic scintillator block,* Physics in Medicine and Biology **55**, 6515 (2010).

[20] H. T. van Dam, S. Seifert, R. Vinke, P. Dendooven, H. Löhner, F. J. Beekman, and D. R. Schaart, *A practical method for depth of interaction determination in monolithic scintillator pet detectors,* Physics in Medicine and Biology **56**, 4135 (2011).

[21] P. Bruyndonckx, S. Leonard, S. Tavernier, C. Lemaitre, O. Devroede, Y. Wu, and M. Krieguer, *Neural network-based position estimators for pet detectors using monolithic lso blocks,* Nuclear Science, IEEE Transactions on **51**, 2520 (2004).

[22] P. Bruyndonckx, C. Lemaitre, D. J. van der Laan, M. Maas, D. Schaart, W. Yonggang, L. Zhi, M. Krieguer, and S. Tavernier, *Evaluation of machine learning algorithms for localization of photons in undivided scintillator blocks for pet detectors,* Nuclear Science, IEEE Transactions on **55**, 918 (2008).

[23] H. T. van Dam, S. Seifert, R. Vinke, P. Dendooven, H. Löhner, F. J. Beekman, and D. R. Schaart, *Improved nearest neighbor methods for gamma photon interaction position determination in monolithic scintillator pet detectors,* Nuclear Science, IEEE Transactions on **58**, 2139 (2011).

[24] M. C. Maas, D. R. Schaart, D. J. v. d. Laan, P. Bruyndonckx, C. Lemaître, F. J. Beekman, and C. W. E. v. Eijk, *Monolithic scintillator pet detectors with intrinsic depth-of-interaction correction,* Physics in Medicine and Biology **54**, 1893 (2009).

[25] D. R. Schaart, H. T. v. Dam, S. Seifert, R. Vinke, P. Dendooven, H. Löhner, and F. J. Beekman, *A novel, sipm-array-based, monolithic scintillator detector for pet,* Physics in Medicine and Biology **54**, 3501 (2009).

[26] T. Frach, G. Prescher, C. Degenhardt, R. de Gruyter, A. Schmitz, and R. Ballizany, *The digital silicon photomultiplier - principle of operation and intrinsic detector performance,* in *Nuclear Science Symposium Conference Record (NSS/MIC), 2009 IEEE* (2009) pp. 1959–1965.

[27] T. Frach, G. Prescher, C. Degenhardt, and B. Zwaans, *The digital silicon photomultiplier - system architecture and performance evaluation,* in *Nuclear Science Symposium Conference Record (NSS/MIC), 2010 IEEE* (2010) pp. 1722–1727.

[28] M. A. Spurrier, P. Szupryczynski, Y. Kan, A. A. Carey, and C. L. Melcher, *Effects of ca2+ co-doping on the scintillation properties of lso:ce,* Nuclear Science, IEEE Transactions on **55**, 1178 (2008).

[29] D. Van der Laan, M. C. Maas, D. R. Schaart, P. Bruyndonckx, S. Leonard, and C. W. E. Van Eijk, *Using cramer-rao theory combined with monte carlo simulations for the optimization of monolithic scintillator pet detectors,* Nuclear Science, IEEE Transactions on **53**, 1063 (2006).

[30] D. J. van der Laan, M. C. Maas, P. Bruyndonckx, and D. R. Schaart, *Limits on the spatial resolution of monolithic scintillators read out by apd arrays,* Physics in Medicine and Biology **57**, 6479 (2012).

# 3

# Towards monolithic scintillator based TOF-PET systems: practical methods for detector calibration and operation

This chapter has been published as:
G. Borghi, V. Tabacchini, and D. R. Schaart, "Towards monolithic scintillator based TOF-PET systems: practical methods for detector calibration and operation," Phys. Med. Biol., vol. 61, no. 13, pp. 4904–4928, Jul. 2016.
DOI: 10.1088/0031-9155/61/13/4904

***Abstract*** - *Gamma-ray detectors based on thick monolithic scintillator crystals can achieve spatial resolutions <2 mm full-width-at-half-maximum (FWHM) and coincidence resolving times (CRTs) better than 200 ps FWHM. Moreover, they provide high sensitivity and depth-of-interaction (DOI) information. While these are excellent characteristics for clinical time-of-flight (TOF) positron emission tomography (PET), the application of monolithic scintillators has so far been hampered by the lengthy and complex procedures needed for position- and time-of-interaction estimation. Here, the algorithms previously developed in our group are revised to make the calibration and operation of a large number of monolithic scintillator detectors in a TOF-PET system practical. In particular, the k-nearest neighbor (k-NN) classification method for x,y-position estimation is accelerated with an algorithm that quickly preselects only the most useful reference events, reducing the computation time for* *position estimation by a factor of $\sim$200 compared to the previously published k-NN 1D method. Also, the procedures for estimating the DOI and time of interaction are revised to enable full detector calibration by means of fan-beam or flood irradiations only. Moreover, a new technique is presented to allow the use of events in which some of the photosensor pixel values and/or timestamps are missing (e.g. due to dead time), so as to further increase system sensitivity. The accelerated methods were tested on a monolithic scintillator detector specifically developed for clinical PET applications, consisting of a 32 mm × 32 mm × 22 mm LYSO:Ce crystal coupled to a digital photon counter (DPC) array. This resulted in a spatial resolution of 1.7 mm FWHM, an average DOI resolution of 3.7 mm FWHM, and a CRT of 214 ps. Moreover, the possibility of using events missing the information of up to 16 out of 64 photosensor pixels is shown. This results in only a small deterioration of the detector performance.*

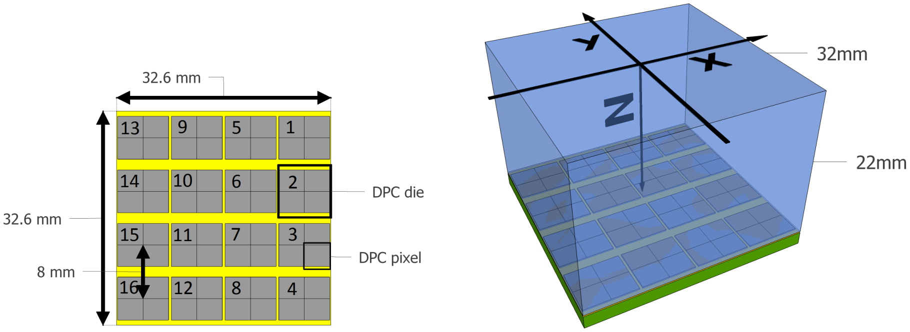

(a) DPC array

(b) Monolithic scintillator detector

Figure 3.1: Sketch of the DPC array (3.1a) and of the monolithic scintillator detector (3.1b) used in this work. The numbering of the DPC die and the coordinate system used in the analysis are also indicated.

## 3.1. Introduction

Monolithic scintillator detectors are based on a single-crystal scintillator with typical edge dimensions of 15-50 mm and a thickness of 10-25 mm, coupled to a pixelated photosensor (Figure 3.1). For each scintillation event, the photosensor registers the light intensity on each of its pixels and acquires one or more timestamps, from which the position-, time- and energy-of-interaction are derived. These detectors can achieve a spatial resolution better than 2 mm full-width-at-half-maximum (FWHM) [1–4] in combination with a coincidence resolving time (CRT) below 200 ps FWHM [5]. In addition, they can provide depth-of-interaction (DOI) information [6–10], high sensitivity, and good energy resolution [3, 11]. Monolithic scintillator detectors thus offer a unique combination of characteristics with an excellent match to the requirements of clinical time-of-flight (TOF) positron emission tomography (PET).

The position of interaction inside the crystal is estimated using analytical or statistical algorithms. Analytical algorithms range from simple center-of-gravity (COG) methods to more complex models of the expected light distribution as a function of the 3D position of interaction [7, 9]. Examples of statistical models are maximum-likelihood positioning [6, 8], neural networks [12, 13], and k-nearest neighbor (k-NN) methods [14, 15].

Statistical methods often provide the best spatial resolution. However, they require meticulous calibration procedures based on a fine sampling of the detector response over a large number of positions, for example by means of pencil beam (PB) irradiations, which translates into long calibration times. Moreover, these algorithms can be computationally demanding. Similar issues affect the methods used to estimate the depth-of-interaction (DOI) and time of interaction, both of which may require position-dependent calibration datasets [5, 10]. These practical difficulties add up if multiple detectors have to be used and have so far hampered the development of clinical TOF-PET systems based on monolithic scintillator detectors.

In this paper we aim to make monolithic scintillator detectors more practical for large-scale application by revising the calibration procedures and estimators for position, time-of-interaction and energy previously developed in our group, in order to reduce their complexity and time consumption and make them more robust with respect to missing data and noise. Accelerated calibration procedures and estimators for position and energy are presented in section 3.2, while an improved version of the time-of-interaction estimation technique is described in section 3.3. In section 3.4 a new approach is introduced to use events with incomplete information (i.e. with missing photosensor pixel values and/or timestamps), so as to improve sensitivity while softening the requirements on the detector operating parameters (dead time, temperature, etc.). In these sections the problems that affected the previously used calibration procedures and estimators are briefly reviewed, after which the general description of the techniques developed to solve these issues is given. The applicability and effectiveness of the new methods are then demonstrated on a monolithic scintillator detector developed for clinical TOF-PET applications, consisting of a 32 mm × 32 mm × 22 mm LYSO:Ce crystal coupled to a digital photon counter (DPC) array. Complete descriptions of the detector and of the measurements performed to calibrate and test it are presented in section 3.5. The practical implementation of the calibration procedures and estimators and the performance that can be achieved with the detector are reported in section 3.6.

## 3.2. Improved calibration procedures and estimators for position and energy

### 3.2.1. x,y-position estimation

Maas *et al.* [14] introduced the k-NN algorithm to estimate the position of interaction in monolithic scintillator detectors. This method compares the light distribution of an unknown event with the light distributions of a large dataset of reference events, i.e. events for which the position of interaction is known. The reference events most similar to the unknown events are selected and their known position of interaction is used to estimate the position of interaction of the unknown event (see section 3.2.1.2). For sufficiently large reference datasets, this method should approach the theoretical minimum of the misclassification probability. However, the implementation by Maas *et al.* required very large reference datasets acquired with a PB at a finely spaced grid on the crystal surface for hundreds of different angles of incidence. A modified version was therefore introduced by van Dam *et al.* [15], which required reference data acquired with a perpendicularly incident PB only, decreasing the calibration time by at least two orders of magnitude. The next implementation of the k-NN method, by Borghi *et al.* [4], utilized independent reference datasets along the x- and y-directions obtained with a fan beam (FB) of annihilation photons, decreasing the calibration time by at least two additional orders of magnitude. Reasonable calibration times of 2-3 hours per detector were thus achieved for monolithic scintillator crystals with edge dimensions of ~2 cm.

Nevertheless, these k-NN implementations still required the calculation of the Euclidean distance of the light distribution of the unknown event to the light distributions of all reference events. Since the number of reference events may be in the order of $10^5$ - $10^6$ and modern photosensors offer a large number of channels per detector, the resulting computational requirements can become prohibitive. Therefore, a new approach is introduced here, which is based on a coarse but fast position pre-estimation for reference and unknown events. Using this pre-estimation, the final, more accurate position estimation can be performed with the k-NN algorithm using only a small fraction of the reference light distributions, viz. those that are estimated to originate in the same region of interaction as the unknown event. Reducing the amount of reference events used in the k-NN algorithm, the method is significantly accelerated.

#### 3.2.1.1. Position pre-estimation algorithms

Position pre-estimation is performed using a clustering method derived from the DOI estimation algorithm introduced by van Dam *et al.* [10], which in turn was inspired by Ling *et al.* [6]. The method uses a parameter correlated to the coordinate to be estimated and a look-up table (LUT). For the detector under study (Figure 3.1), the x- and y-coordinates of the center of gravity of the measured light distribution ($COG_x$ and $COG_y$) were chosen as parameters to perform the classification in the x- and y-directions, whereas the sum of the squared pixel intensity $S$ (SSPI) was used for the DOI:

$$S = \sum_{i=1}^{N_{pxls}} n_i^2 \tag{3.1}$$

Here, $n_i$ is the light intensity on each of the light sensor pixels in the normalized light distribution ($i \in 1, \ldots, N_{pxls}$), with $N_{pxls}$ the total number of pixels. The parameter $S$ can be considered as a measure of how much the light distribution is peaked. The closer the event occurs to the photosensor, the narrower the light distribution and, therefore, the higher is $S$, for events having the same x,y-coordinates. The COG and SSPI were selected because they are simple, robust, and computationally inexpensive parameters for the 3D position pre-estimation.

A calibration dataset containing a sufficient number of events distributed over the whole crystal volume is required to build the LUTs. Knowledge of the real positions of irradiation on the crystal of the events belonging to the calibration dataset is not necessary, therefore a flood irradiation with 511 keV photons could be used. However, given the irradiation condition used to acquire the dataset, it is necessary to know the resulting probability distribution of the energy deposition centroids, i.e. the center of gravity of the different energy deposition points for each gamma-ray interaction, over the crystal volume. This information can be obtained by means of a simple Monte Carlo (MC) simulation.

To obtain the LUT for pre-estimating the x-coordinate ($LUT_x^{PRE}$) the crystal is subdivided into $n_x^{PRE}$ regions of equal width along the x-axis (covering the whole crystal in the y- and z-directions) and the expected fractions $f_x(x)$ of events interacting in each region are derived from the simulated probability distribution of the energy deposition centroids. Next, the $COG_x$ values of the calibration events are calculated and sorted in ascending order, after which the $n_x^{PRE} - 1$ $COG_x$ values demarcating the fractions $f_x(x)$ of the sorted series are selected and stored in $LUT_x^{PRE}$. To pre-estimate the x-position of an unknown event, first its $COG_x$ value is calculated. Then, the x-region delimited by the $LUT_x^{PRE}$ values that are below and above $COG_x$ is selected and its x-position is taken as the pre-estimated position of the unknown event. An equivalent procedure is followed for position pre-estimation along the y-axis.

For DOI pre-estimation, the detector x,y area is divided into $n_x^{PRE-DOI} \times n_y^{PRE-DOI}$ regions in the x,y-plane and in $n_z^{PRE-DOI}$ depth-ranges in the DOI-direction. For each x,y-bin, the fractions $f_z(z|x,y)$ of events interacting in each DOI layer relative to the total number of events interacting in that x,y-bin are derived from the MC simulation. The $COG_x$, $COG_y$ and SSPI values are calculated for each calibration event, which is then assigned to one of the x,y-bins using their pre-estimated x,y position, obtained with $LUT_x^{PRE}$ and $LUT_y^{PRE}$. The events in each x,y-bin are subsequently sorted in ascending order by their SSPI values and the values of the series demarcating the fractions $f_z(z|x,y)$ are used to create the $LUT_{DOI}^{PRE}$, containing $n_x^{PRE-DOI} \times n_y^{PRE-DOI} \times (n_z^{PRE-DOI} - 1)$ reference SSPI values. To pre-estimate the DOI of an unknown event, the appropriate x,y-bin of the $LUT_{DOI}^{PRE}$ is first selected using its pre-estimated x,y-position and then the pre-estimation of the DOI value is derived by comparing the SSPI value of the event to the SSPI values in the $LUT_{DOI}^{PRE}$ for that x,y-bin.

#### 3.2.1.2. Accelerated k-NN 1D method for x,y-position estimation

The more accurate, definitive position estimation is performed using an accelerated version of the Smoothed k-NN 1D method described by Borghi *et al.* [4]. This method requires two reference datasets acquired with a collimated FB of 511 keV photons, one with the FB aligned perpendicularly to the crystal x-axis (x-subset) and one with the FB rotated by 90 degrees (y-subset). For each dataset, a fixed number of full-energy events is acquired at a series of equidistant, accurately known positions along the x- or y-axis, covering the whole crystal surface. The positions of all reference events are subsequently pre-estimated as described in 3.2.1.1. To estimate the x-coordinate of interaction of an unknown event using the accelerated k-NN 1D algorithm, the event position is first pre-estimated with the method described in section 3.2.1.1. Using the pre-estimated positions, the events of the x-subset having a distance to the unknown event in the x,y-plane smaller than an optimized value (defined $r_{xy}^{PRE}$) and a distance in the DOI-direction smaller than another value (defined $r_z^{PRE}$) are selected as the reference dataset for the k-NN algorithm. Then, all the Euclidean distances of the light distribution of the unknown event to the light distributions of all the selected reference events are calculated and the k closest light distributions (nearest neighbors) are found. A 1D histogram of the x-position of the nearest neighbor events is then built and smoothed with a moving average filter n bins wide, whose dimensions are asymmetrically reduced when it approaches the edges. The x coordinate of the unknown event is estimated as the position of the maximum of the histogram. If multiple maxima are present, one of them is randomly chosen. An analogous procedure is used to estimate the y-coordinate.

### 3.2.2. Depth-of-interaction estimation

The more accurate, definitive DOI estimation is performed with a method similar to that used for position pre-estimation. The only difference is that the accelerated k-NN 1D method is used to estimate the x,y-positions of the events of the calibration dataset used to build the final LUT ($LUT_{DOI}$) as well as the x,y-position of the unknown event whose DOI has to be estimated. The advantage of this method over the one described by van Dam *et al.* [10] is that the estimated position of the calibration events instead of their irradiation positions is used to build $LUT_{DOI}$ and therefore it is not necessary to perform PB irradiations to acquire the calibration events.

### 3.2.3. Energy correction for position-dependent detector response

Monolithic scintillator detectors usually show a rather homogeneous energy resolution across the whole crystal volume if they are completely covered with a highly reflective material due to the favorable light-collection conditions [11, 16]. Nevertheless, a simple method to estimate and correct for any remaining energy response variations across the detector volume has been developed. First, the crystal volume is divided into $n_x^{en} \times n_y^{en} \times n_{DOI}^{en}$ voxels. Next, each event of a large calibration dataset distributed over the whole crystal volume is assigned to the voxel containing its position of interaction estimated using the methods described in sections 3.2.1 and 3.2.2. An energy spectrum is created for each voxel and the center position of its 511 keV photopeak is estimated using a Gaussian fit. A correction factor for each voxel is subsequently calculated as the ratio between the photopeak position of the whole detector and the photopeak position of that voxel and stored in a LUT ($LUT_{EN}$). When an unknown event is registered, first its position of interaction is estimated and then its energy is corrected using the factor of the corresponding voxel of $LUT_{EN}$.

## 3.3. Improved calibration procedures and estimators for time of interaction

Pixelated photosensors may register a timestamp for each pixel or group of pixels, providing a maximum of $N_{ts}$ timestamps per event. To distinguish the $N_{pxls}$ photosensor regions that independently measure the amount of incident photons from the $N_{ts}$ regions that provide a timestamp, the formers will be referred to as light-pixels and the latters as time-pixels. If each time-pixel accurately measures the time of arrival of the first scintillation photon(s) detected, the spatio-temporal distribution of the $N_{ts}$ timestamps can be used to correct for the optical transport times of the photons inside the crystal and to calculate more precisely the time of interaction of each gamma photon. In order to optimally perform this correction, a method for maximum-likelihood interaction time estimation (MLITE) was proposed by van Dam *et al.* [5]. Here, this method has been modified in order to make the calibration procedure faster and more practical, as well as to improve the timing performance by selecting only the timestamps with reliable information and using a non-parametric fit for the probability density functions.

The calibration procedure is based on the acquisition of a large calibration dataset of events distributed over the whole crystal volume in coincidence with a fast reference detector. No prior knowledge on their positions of irradiation is needed. We first attempt to remove premature timestamps (e.g. generated by dark counts), as well as late timestamps that do not contain relevant information [17] from the set of $N_{ts}$ timestamps acquired for each scintillation event. This operation makes use of the fact that timestamps acquired in the first part of the scintillation pulse (e.g. in the first ~5 ns for a LYSO crystal) should occur close to each other in time. To perform this operation it is important that no significant time skews are present between the different time-pixels, e.g. due to electronic jitter or readout delays. First, all timestamps of each scintillation event are sorted in order of acquisition (i.e. earliest timestamp in first position, etc.) and the timestamps which are followed by another timestamp in a time period $\Delta t_{ts-seq}^{start}$ are selected. The first valid timestamp is determined as the earliest selected one which is followed by another selected timestamp. Similarly, the last valid timestamp is determined sorting the timestamps in inverse order of acquisition, selecting the timestamps preceded by another timestamp in a time period $\Delta t_{ts-seq}^{end}$ and finding the last selected timestamp preceded by another selected timestamp. All timestamps registered in between the first and last valid ones are also considered valid. To make sure that no useful timestamps are discarded, it is possible to define an additional time window before the first valid timestamp ($\Delta t_{ts}^{start} > \Delta t_{ts-seq}^{start}$) and after the last one ($\Delta t_{ts}^{end} > \Delta t_{ts-seq}^{end}$), accepting also the timestamps acquired in these windows. The length of the four time windows has to be optimized for each type of detector.

Once the valid timestamps are selected the crystal is divided into $n_x^{MLITE} \times n_y^{MLITE} \times n_{DOI}^{MLITE}$ equally sized voxels to which the calibration events are assigned according to their estimated positions of interaction. The interactions in a given voxel are registered by time-pixel $i$ with certain delays, denoted as first photon detection delays (FPDDs), which are determined by the scintillation pulse shape and the optical transport in the crystal. The FPDD probability distribution function (PDF) is estimated for each combination of voxel and time-pixel using the calibration events assigned to that voxel. First, the differences between the valid timestamps acquired by the time-pixel and the corresponding timestamps of the reference detector are calculated and then these values are used to estimate the FPDD PDFs with kernel-density estimation (KDE). This non-parametrical method reduces the influence of statistical fluctuations on the experimentally measured PDFs and, especially at the beginning of the PDFs, preserves more closely their shape compared to the previously proposed method, which employed a fit with an exponentially modified Gaussian [5]. Finally, knowing the geometry of the calibration setup, the difference in the travel times of the paired annihilation quanta to the interaction points in the test and reference detectors can be determined and the zero of the FPDD distributions can be set at the moment of interaction inside the monolithic crystal. Thus, a group of $N_{ts}$ PDFs are obtained per crystal voxel, denoted as $p(t \mid x, y, z, i)$, with $t$ the delay relative to the time of interaction in the monolithic scintillator detector, $(x, y, z)$ the coordinates of the voxel center, and $i$ the index of the sensor time-pixel.

Once an unknown event is detected, its position of interaction is estimated, the event is assigned to the corresponding MLITE voxel and its timestamps are selected using the same validity conditions used to build the FPDD PDFs. Then, the time of interaction $t_{int}$ is estimated using the FPDD distributions of that voxel and a maximum likelihood algorithm. That is, the likelihood of having a set of valid timestamps $\mathbf{t} = t_1, ..., t_{N_{ts}}$ given an interaction time $t_{int}$ is defined as:

$$L(\mathbf{t}|t_{int}) = \prod_{i=1}^{N_{ts}} p(t_i - t_{int}|x, y, z, i) \tag{3.2}$$

The most likely time of interaction $\hat{t}_int$ is obtained by finding the maximum of the likelihood function:

$$\hat{t}_{int} = \arg\max_{t_{int}} L(\mathbf{t}|t_{int}) \tag{3.3}$$

## 3.4. Position, energy, and time of interaction estimators for events with missing information

In part of the events not all light-pixels or time-pixels are acquired, e.g. because a pixel could be in dead time due to the readout or recharge process resulting from an earlier trigger caused by a dark count or a previous scintillation event. If such events with missing information could be used in a practical way to still obtain accurate time, energy and position information, a significant improvement in detector sensitivity could be achieved. Moreover, the method could enable the use of detectors that have some malfunctioning or broken pixels.

In fact, a complete light distribution generally is not essential if statistical methods are used to estimate the position of interaction, since they can be applied to only that part of the information that is available [3]. However, the photon count on the missing pixels is still important for correctly estimating the energy deposited and/or when using analytical methods to estimate the position of interaction, such as the position pre-estimation methods and the DOI estimation algorithm described in sections 3.2.1.1 and 3.2.2. In such cases, missing pixel values can be estimated using analytical methods (e.g. interpolation/extrapolation techniques), methods based on calibration datasets [3], or statistical methods. Here, a new method based on average light distributions and the k-NN algorithm is introduced.

To calculate the average light distributions, a procedure similar to that described in section 3.2.3 to build $LUT_{EN}$ is followed. The monolithic crystal is subdivided into $n_x^{av-ld} \times n_y^{av-ld} \times n_z^{av-ld}$ equal voxels and each event of a large calibration dataset containing only complete light distributions is assigned to a voxel depending on the estimated position of interaction. All light distributions are subsequently normalized to the same total value and the average light distribution for each voxel is calculated.

When an incomplete light distribution is acquired, first a coarse energy discrimination is performed using different energy spectra built with events having different numbers of missing pixels, i.e. spectra built using only events with one missing pixel, two missing pixels, etc. Then the average light distribution that is most similar to the incomplete one is found using the k-NN algorithm. First, all pixels that are missing in the incomplete light distribution are set to zero also in the average light distribution dataset. Then, all distributions are normalized to the same total photon count and the one that is most similar (i.e. having the smallest Euclidean distance) to the incomplete distribution is selected. Finally, the values of the missing pixels of the incomplete light distribution are estimated as:

$$p^j_{inc-ld} = p^j_{av-ld} \cdot \frac{\sum_i p^i_{inc-ld}}{\sum_i p^i_{av-ld}} \tag{3.4}$$

with $p_{inc-ld}$ the pixel values of the incomplete light distribution before normalization, $p_{av-ld}$ the pixel values of the selected average light distribution, $j = 1, ..., N_{misspix}$ the indices of the missing pixels, and $i = 1, ..., N_{acqpix}$ the indices of the acquired pixels.

The estimated photon counts on the missing pixels are used to complement the measured light distribution, from which the total energy of the event is calculated. The complemented light distribution is also used for the position pre-estimation used to select reference events for the accelerated k-NN 1D algorithm. Next, the x,y-position of interaction is determined using the accelerated k-NN 1D method described in section 3.2.1.2. Whereas the complemented distribution is used for position pre-estimation, only the pixels that were acquired during the measurement are used for the definitive position estimation. That is, the pixels missing in the measured light distribution are also set to zero in the pre-selected reference light distributions and all distributions are normalized to the same total photon count. Finally, the complemented light distribution is used once more, this time to estimate the DOI using the method detailed in section 3.2.2.

If an event is missing part of the timestamps, the estimation of the time of interaction with the MLITE method is performed following the approach described in section 3.3, using only the available timestamps to define the likelihood function given in equation 3.2.

## 3.5. Materials and experimental methods

### 3.5.1. Monolithic scintillator detector and reference detectors

The monolithic scintillator detector tested in this work is based on a LYSO:Ce crystal (Crystal Photonics) with a base area of 32 mm × 32 mm, a thickness of 22 mm, and polished surfaces. The four lateral faces were covered with a specular reflector foil (Vikuiti ESR, 3M), whereas the top face was covered with Teflon tape. The 32 mm × 32 mm back surface was coupled to a DPC array developed by Philips Digital Photon Counting (PDPC), model DPC-3200-22-44 (Figure 3.1), using a removable transparent silicone gel (Sylgard 527, Dow Corning).

The DPC array measures 32.6 mm × 32.6 mm and consists of 4 × 4 independent sensors (dies) at a regular pitch of 8 mm, each die containing 2 × 2 light-pixels whose dimensions are 3.2 mm × 3.8775 mm. Each pixel comprises 3200 microcells and is subdivided into 2 × 2 equal subpixels. Each microcell consists of a single photon avalanche photodiode (SPAD) and circuitry to actively quench and recharge the SPAD, read out its status, and selectively enable or disable it. This last feature makes it possible to disable the SPADs that show the highest dark count rates. In this work, the noisiest 5% of microcells on each die were switched off. More details about the sensor architecture can be found in Frach *et al.* [18], Frach *et al.* [19], Schulze [20], and Schaart *et al.* [21].

The subpixels are used to set a statistical threshold for triggering the acquisition sequence of a die at the beginning of a scintillation event [18, 22]. Trigger level $MT_{=1}$ (PDPC notation, see Frach *et al.* [18]) was chosen in this work. With this setting, a die is triggered by the first SPAD firing, upon which a single timestamp is acquired and photon counting is continued during a user-defined validation time (set to 40 ns in this work). At the end of this interval, the die checks whether a higher-energy threshold criterion is met, so as to discard events triggered by dark counts. This validation threshold was set such that at least one pixel should have at least one photon counted on each subpixel (DPC validation threshold notation: '0x7F:AND'). If this condition is not met, the die undergoes a fast (~20 ns) recharge and reset cycle. Otherwise if it is met, the die continues counting for a user-defined integration time (set to 165 ns in this work) and then carries out a readout sequence (680 ns). At the end of this sequence it outputs the photon count of each of the four pixels as well as a single timestamp. Following the definitions given in section 3.3, a die thus corresponds to a time-pixel and contains four light-pixels.

The DPC array is equipped with neighbor logic, which makes it possible to force the readout of neighboring dies or the entire array after the validation of any single die. In this work, the option to force the readout of the entire array was activated.

Several reference detectors similar to the detector under test were assembled to acquire events in coincidence with it. Each detector was built using a different DPC sensor. Two detectors were based on two polished LSO:Ce crystals (Agile Engineering Inc., Knoxville, TN, USA) with dimensions of 32 mm × 32 mm × 20 mm and 16 mm × 16 mm × 20 mm. Three other detectors were assembled using Ca-codoped (0.2% in the melt) LSO:Ce crystals [23] (produced at the Scintillation Materials Research Center, University of Tennessee, and provided by Agile Engineering Inc., Knoxville, TN, USA) with dimensions of 3 mm × 3 mm × 5 mm and a single polished 3 mm × 3 mm face that was coupled to a pixel of a DPC array. The small reference crystals were covered on all the faces with specular reflector foil.

The readout and data acquisition of all detectors was performed using field-programmable gate array (FPGA) based electronic boards and an accompanying computer program provided by PDPC [20].

### 3.5.2. Experimental setup

A slightly modified version of the experimental setup described in Borghi *et al.* [4] was used to perform the calibration and test measurements. Briefly, the setup is based on a paired collimator system that is placed in between the detector under test and a reference detector. It consists of a central tungsten cylinder containing a $^{22}$Na point-source (⌀ 0.5 mm, ~3.5 MBq, IDB Holland BV) and two sets of collimators used to obtain either a ⌀ 0.5 mm PB or a 0.5 mm wide FB of annihilation photons.

The collimator system can be rotated by an angle of 90◦ so that the FB can be aligned perpendicularly to the x- or y-axis of the detector under test. This detector is mounted on two perpendicular linear stages driven by stepper motors (Physics Instruments, M-403.42S stages with C-663 controllers), which precisely move and position the detector in the plane perpendicular to the collimator axis. The entire setup is placed inside a light-tight temperature chamber (Weiss WT 450/70). A Peltier element is mounted on the back of each detector to control its temperature with 0.1 ◦C precision. The working temperature of all detectors was set to -25 ◦C to reduce the dark count rate of the DPC arrays.

### 3.5.3. Data acquisition

Four different sets of events were acquired for calibrating and characterizing the position estimation response of the detector. These are referred to as the FB, perpendicular PB, side PB, and angular PB datasets. The 32 mm × 32 mm × 20 mm LSO:Ce detector was used as a reference detector to acquire the FB dataset while the 16 mm × 16 mm × 20 LSO:Ce detector was used for the other measurements. A count rate profile was performed prior to each measurement in order to find the center of the crystal with respect to the beam position. The use of the different datasets is detailed in section 3.6. The FB dataset was obtained with the FB perpendicularly incident on the crystal front surface. First, the FB was aligned perpendicularly to the crystal x-axis and the x-subset was acquired collecting 12800 full-energy events (see section 3.5.4 for data pre-processing) at a series of reference positions spaced 0.25 mm apart along the x-direction. Subsequently, the FB was rotated by 90° and the y-subset was acquired in an analogous way. The total acquisition time was about 6-7 hours.

The perpendicular PB dataset was acquired with a perpendicularly incident PB at a grid of reference positions with a pitch of 0.25 mm covering the entire crystal front surface. At each point, 100 full-energy events were acquired. The total acquisition time was about 8 days. The side PB dataset was collected by perpendicularly irradiating a crystal side surface with the PB at a grid of reference positions with a pitch of 1 mm in both the x- and z- (DOI-) directions, covering all possible DOIs and spanning from $x = -15.5$ mm to $x = 0.5$ mm. At each position ∼4500 full-energy events were acquired.

Finally, the angular PB dataset was obtained by irradiating half of the crystal front surface at a 0.25 mm pitch reference grid with the PB at a 60° angle of incidence (Figure 3.2). The PB was aligned parallel to the crystal y,z-plane and only the grid positions for which the entry and exit points of the line of irradiation intercepted the front and back face of the crystal were acquired. About 60 full-energy events were acquired per position.

For the calibration and characterization of the time response of the monolithic scintillator detector, the same preliminary measurements described in van Dam *et al.* [5] were performed. Briefly, before the crystal was mounted, the electronic time skews between the dies of the DPC array were determined with a pulsed laser (Hamamatsu PLP-04 laser, wavelength 633 nm, average pulse duration 50 ps). Furthermore, the CRT of each of the three possible combinations of 3 mm ×

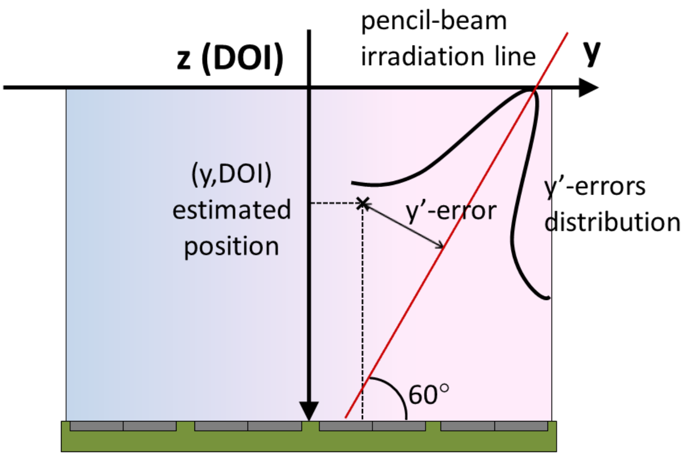

Figure 3.2: Illustration of the angular PB measurement and of the calculation of the y'-error for events incident on the crystal surface at a 60° angle. The coordinate system of the crystal is also shown.

3 mm × 5 mm Ca-codoped LSO:Ce detectors was measured. This permitted us to calculate the single-detector time resolution for each detector. The best reference detector, with a single-detector time resolution of ~89 ps FWHM and an estimated CRT for two identical detectors ($CRT_{ref}$) ~125.9 ps, was chosen as a reference detector for the flood irradiations described below.

Three different datasets were then acquired for the timing calibration and characterization of the monolithic detector. To this end, the uncollimated 22Na point source was placed in between this reference detector and the test detector. The distance between the source and the reference detector was kept at 12 mm, while the monolithic crystal was placed at 22 cm, 24 cm and 26 cm from the source so as to irradiate the whole monolithic crystal surface uniformly. About 4 million and 2 million full-energy coincidence events were acquired at 24 cm and the other distances, respectively. The resulting datasets will be referred to as the 22 cm flood irradiation (22cm-FI), 24cm-FI, and 26cm-FI datasets. A little less than an hour was required to acquire 1 million events during flood irradiation.

### 3.5.4. Data pre-processing

The first pre-processing step for all measurements was to select the events in which no pixel values and timestamps were missing (corresponding to about 65% of all events acquired with the detector settings and operating conditions used in this work) and for which the total energy deposited fell within the full-width-at-ten-maximum (FWTM) of the 511 keV photopeak. For timing measurements, the energy condition was also applied to the reference detector.

A correction to obtain a homogeneous response from the light sensor pixels was subsequently applied so as to obtain more accurate results from the analytical position estimation methods (i.e. the methods used for position pre-estimation and DOI estimation). The perpendicular PB and the FB datasets, which contain events evenly distributed over the crystal surface, were used to build LUTs for uniformity correction ($LUT_{UC}$). The assumption is that the average light distribution over all the events in both datasets should have the same value for all DPC pixels. Therefore, the $LUT_{UC}$ value for each pixel is defined as the ratio between the average value of all pixels and the value of that same pixel in the average light distribution. Since the light-pixels of the DPC array already have a highly uniform response, this correction was mostly performed to remove any effects due to the non-homogeneous quality of the optical coupling and/or possible deficiencies in the crystal wrapping. If necessary, this uniformity correction could be performed regularly, e.g. based on simple flood irradiations, to make the detector response more stable without having to repeat the entire k-NN calibration.

## 3.6. Results and discussion

### 3.6.1. Position estimation

#### 3.6.1.1. Spatial resolution at perpendicular incidence

The perpendicular PB dataset (see section 3.5.3) was used to test the spatial resolution in the x- and y-directions. The positions of all events were estimated using the accelerated k-NN 1D method (see section 3.2.1) as well as the standard k-NN 1D method [4], which calculates the Euclidean distances between the light distributions for all the events in the reference datasets and not for only part of them, selected according to their pre-estimated position of interaction. The FB dataset was used as the reference dataset for both methods. The parameter k was set to 100 and 200 for the standard k-NN 1D and the accelerated k-NN 1D algorithms, respectively. In both cases the smoothing filter had a width of $n = 5$. The FB dataset (the x- and y-subsets together) was also used to create the position pre-estimation LUTs, with $n_x^{PRE} = n_y^{PRE} = 32$ for $LUT_x^{PRE}$ and $LUT_y^{PRE}$. For $LUT_{DOI}^{PRE}$, $n_x^{PRE-DOI} = n_y^{PRE-DOI} = 16$ and $n_z^{PRE-DOI} = 22$. The MC code GATE [24] was used to estimate the energy centroid distributions. The preselection radii were optimized to maintain high spatial resolution while speeding up the positioning algorithm as much as possible: the used values were $r_{xy}^{PRE} = 2mm$ and $r_z^{PRE} = 5mm$. To avoid positioning errors and/or bias due to small differences in the alignment of the crystal with the PB or FB, the misalignment correction procedure presented in Borghi *et al.* [4] was used to correct all results in this section.

Table 3.1 shows the parameters characterizing the average spatial resolution obtained with both k-NN methods, obtained using all events in the PB dataset. The FWHM and FWTM parameters are derived from the 2D point-spread function (2D PSFs), defined as the normalized 2D histogram of the differences between the estimated x,y-positions of interaction and the known x,y positions of irradiation. The FWHM and FWTM are defined, respectively, as the full-width-at-half- and tenth-maximum of the cross-sections along the x- and y-directions of the 2D PSF across

Table 3.1: Average spatial resolution for perpendicularly incident events using the standard 1D k-NN method ('Std.') and the accelerated 1D k-NN method ('Accel.').

| Resolution (mm) | x | | y | | total | |
|---|---|---|---|---|---|---|
| | Std. | Accel. | Std. | Accel. | Std. | Accel. |
| FWHM | 1.45 | 1.68 | 1.49 | 1.70 | - | - |
| FWTM | 4.58 | 4.76 | 4.72 | 5.02 | - | - |
| $r_{50\%}$ | 0.83 | 0.82 | 0.86 | 0.84 | 1.66 | 1.62 |
| $r_{90\%}$ | 3.61 | 3.53 | 3.69 | 3.60 | 5.24 | 5.11 |
| MAE | 1.59 | 1.55 | 1.63 | 1.58 | 2.55 | 2.48 |

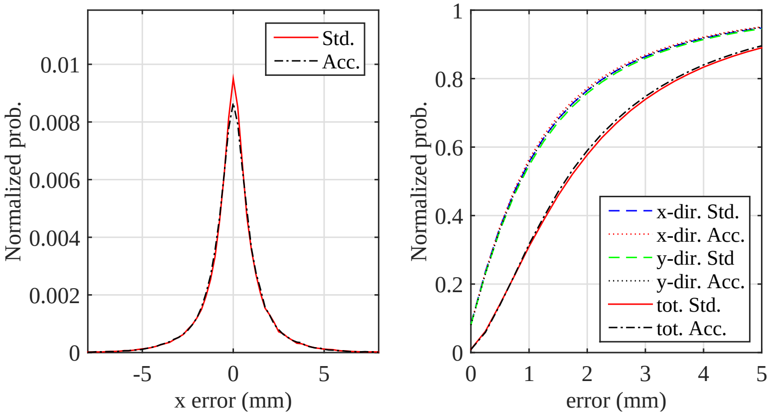

Figure 3.3: Comparison of the cross-sections in the x-direction of the 2D PSFs (left) and of the cumulative distributions of the x-, y- and total errors (right), for the standard 1D k-NN method ('Std.') and the accelerated 1D k-NN method ('Acc.'). All events in the PB datasets are used for these plots.

its maximum (Figure 3.3, left).

Slightly better FWHM and FWTM values are obtained with the standard 1D k-NN method; however, since the 2D PSFs do not have a Gaussian shape this is only due to the difference in height of their central bins and does not represent a real difference in the positioning performance of the methods. For this reason we consider the other parameters reported in Table 3.1 more comprehensive. The $r_{50\%}$ and $r_{90\%}$ values are derived from the normalized cumulative distribution functions (CDFs) of the x-, y- and total errors (Figure 3.3, right), the total error being the length of the error vector. These parameters are defined as the values at which the CDF exceeds 0.5 (i.e. the median error) and 0.9, respectively. The mean absolute error (MAE) is defined as the mean absolute value of the (x-, y- or total) error. A comparison of the CDFs of the two k-NN methods in Figure 3.3 (right) shows that their positioning accuracy is practically equivalent, in fact with slightly better $r_{50\%}$, $r_{90\%}$, and MAE values for the accelerated 1D k-NN method, as reported in Table 3.1.

The MAE and bias vector $\mathbf{b}(\mathbf{v}_{irr}^{i,j})$ were also calculated for the individual irradiation positions $\mathbf{v}_{irr}^{i,j} = (x_{irr}^{i,j}, y_{irr}^{i,j})$ of the PB dataset ($i$ and $j$ being the row and column

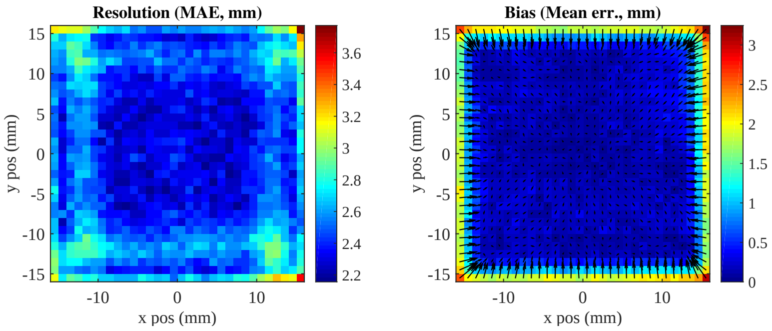

Figure 3.4: Resolution (MAE, left) and bias maps (Mean error, right) for the accelerated 1D k-NN method. Each bin in the plots corresponds to an area of 1 mm × 1 mm.

indices of the irradiation grid). Here, the bias vector is defined as the mean error of the estimated position:

$$\mathbf{b}(\mathbf{v}_{irr}^{i,j}) = \begin{bmatrix} \dfrac{\sum_{m=1}^{M}(\hat{x}_m(\mathbf{v}_{irr}^{i,j}) - x_{irr}^{i,j})}{M} \\ \dfrac{\sum_{m=1}^{M}(\hat{y}_m(\mathbf{v}_{irr}^{i,j}) - y_{irr}^{i,j})}{M} \end{bmatrix} \tag{3.5}$$

where $m$ is the m$^{\text{th}}$ test event acquired at irradiation position $\mathbf{v}_{irr}^{i,j}$, $\hat{\mathbf{v}}_m(\mathbf{v}_{irr}^{i,j}) = (\hat{x}_m(\mathbf{v}_{irr}^{i,j}), \hat{y}_m(\mathbf{v}_{irr}^{i,j}))$ is its estimated position and $M$ is the number of events per position. Figure 3.4 left and Figure 3.4 right respectively show the average MAE value and bias magnitude (calculated as the average Euclidian norm of the bias vectors) in 1 mm × 1 mm regions on the detector front surface, each region containing 16 irradiation positions.

As expected, the spatial resolution is best at the center of the crystal and starts to degrade at about 4-5 mm distance from each edge, for the coordinate perpendicular to that edge [1, 3, 11]. This effect simultaneously occurs for both coordinates in the corners, where the MAE consequently is worse. Nevertheless, the MAE is <3 mm at practically all positions. The bias is negligible (<0.5 mm) except in ~3 mm wide regions near the crystal edges. It becomes substantial (>1.5 mm) only at about 1 mm from the edge, which is attributed to the truncation of the error distributions at the edges.

It has to be noted that all spatial resolution results also include the contributions due to the finite beam diameter, which in this work can be considered negligible, and the errors determined by events which underwent Compton interaction(s) inside the crystal. Compton scattered events can travel a significant distance in thick scintillation crystals and therefore contribute to the tails in the error distributions (PSFs and CDFs) [25].

For the accelerated 1D k-NN method, an average of ~8900 reference events were pre-selected to estimate the x- or y-coordinate of each unknown event, while ~1.6 million reference events were necessary with the standard method. A reduc-

Table 3.2: DOI resolution for events with complete light distributions, for events with the pixel values from up to 4 out of 16 dies (4 pixels per die) missing and for the acquisition conditions used in this work (AC) (see section 3.6.4.2 for details about the results for events with missing pixels).

| Resolution (mm) | No. of missing dies | | | | | |
|---|---|---|---|---|---|---|
| | None | 1 | 2 | 3 | 4 | AC |
| FWHM | 3.73 | 3.88 | 4.03 | 4.25 | 4.43 | 3.8 |
| FWTM | 11.1 | 11.2 | 11.3 | 11.6 | 11.8 | 11.1 |
| $r_{50\%}$ | 1.03 | 1.07 | 1.12 | 1.19 | 1.26 | 1.05 |
| $r_{90\%}$ | 4.70 | 4.82 | 5.00 | 5.23 | 5.51 | 4.77 |
| MAE | 2.23 | 2.30 | 2.39 | 2.50 | 2.64 | 2.27 |

tion by a factor of ~200 in the number of distance calculations, which is the most computing-intensive operation in the k-NN algorithm, has thus been achieved without any degradation of the spatial resolution. The computation time per unknown event using a non-optimized MATLAB implementation of the accelerated 1D k-NN method on a single core was ~5 ms, a significant improvement compared with the value of ~1 s needed with the standard method. This time could still be decreased substantially by replacing the MATLAB script by an optimized code.

#### **3.6.1.2.** DOI resolution

The whole FB dataset was used to create $LUT_{DOI}$ (see section 3.2.2), with $n_x^{DOI} = n_y^{DOI} = 16$ and $n_z^{DOI} = 22$. To assign the calibration events to the x,y-bins of $LUT_{DOI}$, their x,y-position was estimated with the accelerated 1D k-NN method using the leave-one-out technique [16], i.e. removing the event whose position is being estimated from the reference dataset used for k-NN.

The side PB irradiation was used as a test dataset to determine the performance of the DOI estimation. Table 3.2 shows the results. The FWHM and FWTM values were calculated from the 1D distribution of the DOI errors, whereas $r_{50\%}$ and $r_{90\%}$ were obtained from the normalized error CDF.

Figure 3.5 shows the DOI resolution and DOI bias as a function of the z-position of interaction. These plots were obtained by calculating the MAE and the mean error, respectively, for all events acquired at each DOI in the side PB dataset. As expected, the DOI resolution is best near the photosensor and degrades in the upper half of the crystal. The bias is less than 1.5 mm for almost all z-positions, becoming significant in the 3-4 mm near the front crystal surface and the 1-2 mm near the photosensor only, due to truncation of the error distributions. It is noted that these results were obtained with a homogeneous side irradiation; in the case of front irradiation, with more events interacting in the front half of the detector, the average DOI resolution would be slightly worse.

#### **3.6.1.3.** Spatial resolution at non-perpendicular incidence

The angular PB dataset was used to test the spatial resolution at an angle of incidence similar to that occurring in a clinical scanner for events originating at the edge of the radial field of view (FOV). The positioning error was determined for

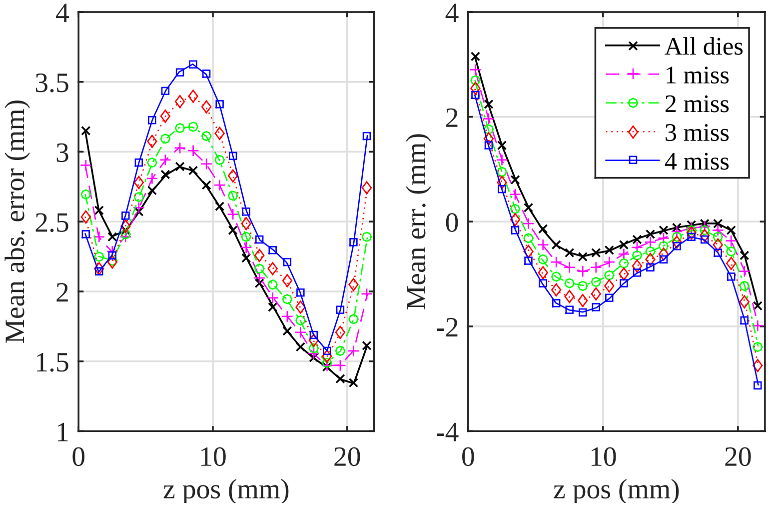

Figure 3.5: DOI resolution (left) and DOI bias (right) as a function of the z-position of interaction for events with the pixel values from up to 4 out of 16 dies (4 pixels per die) missing (see section 3.6.4.2 for details about the results for events with missing pixels).

each event by estimating the position of interaction (x,y,z) and calculating its distance to the true line of response (LOR); see Figure 3.2. The distance between the estimated x-position and the x-coordinate of the plane parallel to the y,z-plane that contains the LOR is denoted as the error in the x-direction. The distance between the estimated y,z-position and the LOR in the plane parallel to the y,z-plane that contains the LOR is called the y′-error. The resolution measures defined in section 3.6.1.1 were calculated on the basis of the x- and y′-errors. To assess the importance of DOI estimation, the calculation was repeated after replacing z by a fixed DOI value of 7.5 mm, equal to the average DOI at $60^\circ$ incidence.

The results are summarized in Table 3.3, while the 1D PSFs (i.e. the projections of the 2D PSFs on the x or y axis) are shown in Figure 3.6. A small resolution degradation is noticeable for the x-coordinate. This could be explained by a small misalignment of the irradiation positions during the non-perpendicular irradiation, which is noticeable in Figure 3.6 as a small offset between the error histograms. Also, the angular PB dataset on average has a smaller DOI than the perpendicular PB dataset and the x,y spatial resolution is worse in the front part of the crystal, which is further away from the DPC arrays.

As for the y′-error, the lower accuracy of the DOI estimation compared to the x,y estimation results in less accurate LOR positioning for non-perpendicular LORs. However, the MAE in the y′-direction is only ~17% higher compared to perpendicular irradiation, which is a large improvement over the ~75% degradation that occurs if the average DOI is used for LOR positioning.

Table 3.3: Spatial resolution for events incident at an angle of $60^{circ}$ on the crystal surface, obtained using the DOI estimated with the method presented in section 3.2.2 ('DOI') and a fixed DOI value of 7.5 mm ('no DOI').

| Resolution (mm) | x | | y′ | | total | |
|---|---|---|---|---|---|---|
| | DOI | no DOI | DOI | no DOI | DOI | no DOI |
| $r_{50\%}$ | 0.93 | 0.93 | 1.12 | 1.84 | 1.94 | 2.97 |
| $r_{90\%}$ | 3.85 | 3.85 | 4.03 | 5.20 | 5.66 | 6.48 |
| MAE | 1.69 | 1.69 | 1.85 | 2.79 | 2.79 | 3.63 |

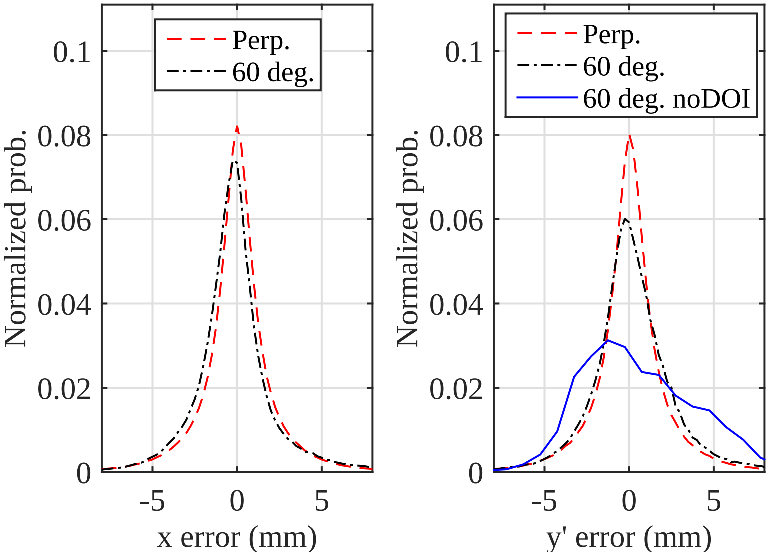

Figure 3.6: 1D PSFs of the x- (left) and y′-errors (right) (y-errors for perpendicular irradiation) in the position estimation for perpendicular irradiation and irradiation at a 60° angle of incidence, with and without DOI correction.

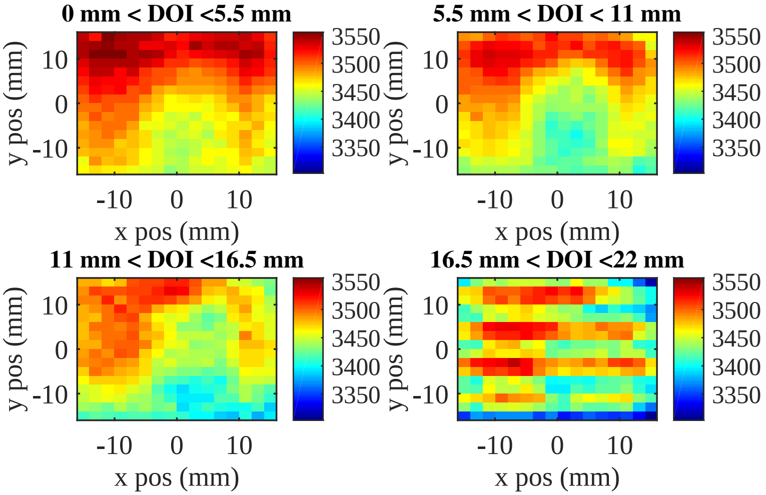

Figure 3.7: Value of the 511 keV photopeak as a function of position of interaction in the crystal (photopeak values are expressed in terms of the number of fired cells corrected using $LUT_{UC}$, as described in section 3.5.4).

### 3.6.2. Energy resolution

The FB dataset was used to create $LUT_{EN}$ (see section 3.2.3), with $n_x^{en} = n_y^{en} = 16$ and $n_z^{en} = 4$. The perpendicular PB dataset was subsequently used to test the influence of the position-dependent energy correction on the detector energy resolution. Only events belonging to the non-corrected 511 keV photopeak were used (see section 3.5.4). The energy resolutions before and after correction were determined with Gaussian fits.

The center position of the 511 keV photopeak as a function of the x,y,z-position of interaction is shown in Figure 3.7. At all DOI, it is possible to notice a region around (x,y) ~ (2,-10) in which the detector shows a reduced energy response, probably due to small defect(s) in the optical coupling. In the DOI layer between 16.5 mm and 22 mm, which is the closest to the DPC array, it is also possible to observe a different response between the regions above the dead areas of the photosensor (y = -16, -8, 0, 8, 16) (Figure 3.1), where the energy response is lower, and the regions centered above the DPC dies (y = -12, -4, 4, 12), where the energy response is higher. This results in a difference in the photopeak position of up to ~200 cells. Despite this variation, the average energy resolution in the energy spectrum of the complete dataset without any correction still equals ~10.25% FWHM (Figure 3.8). If the position-dependent energy correction is applied, an energy resolution of ~9.9% FWHM is achieved.

### 3.6.3. Time resolution

The timestamps of all events in datasets 22 cm FI, 24 cm FI, and 26 cm FI were corrected for the electronic time skews between the DPC dies (see section 3.5.3) and subsequently pre-selected using the method described in section 3.3. The optimized

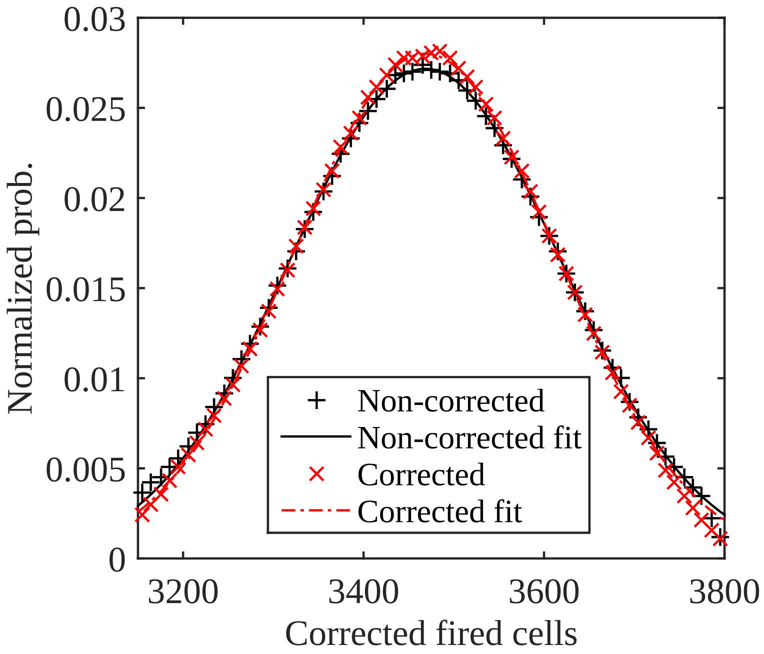

Figure 3.8: Comparison of the 511 keV photopeak of the energy spectrum obtained with all events in the PB dataset before and after position-dependent energy correction.

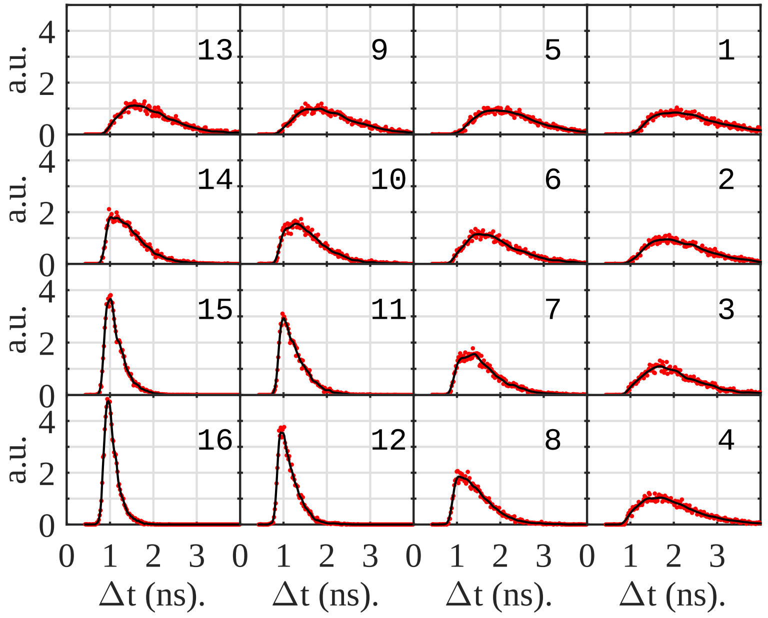

Figure 3.9: Example of FPDD PDFs for events interacting in the crystal voxel having coordinates $(x, y, z) = (-14mm, -14mm, 2.75mm)$, i.e. above die no. 16 (see Figure 3.1) and close to the crystal surface opposite from photosensor surface. Red dots are the experimental histograms whereas black lines are FPDD PDFs estimated using KDE. Numbers in each subplot correspond to die numbering.

values for the time windows were $\Delta t_{ts-seq}^{start} \cong 200ps$, $\Delta t_{ts-seq}^{end} \cong 200ps$, $\Delta t_{ts}^{start} \cong 1ns$ and $\Delta t_{ts}^{end} \cong 3.5ns$. Half of the events of the 24 cm FI dataset (~2 million) were used to determine the FPDD PDFs (Figure 3.9), with $n_x^{MLITE} = n_y^{MLITE} = 16$ and $n_{DOI}^{MLITE} = 4$. The kernel function used for KDE was the Epachenikov (parabolic-shaped) function. To speed up the calculations, the values of all FPDD PDFs were pre-computed on a temporal grid with a spacing equal to 1 DPC time-to-digital converter (TDC) bin (10 ns / $2^9 \cong$ 19.5 ps) and stored in a LUT. Since the absolute time is irrelevant for determining the time resolution, the zero of the FPDD PDFs was left uncorrected for the irradiation geometry.

The remaining half of the 24 cm FI dataset as well as the 22 cm FI and 26 cm FI datasets were used as test datasets. The time of interaction of each event was estimated using MLITE, with the values of the likelihood function $L(\mathbf{t}|t_{int})$ calculated on the same time grid as the FPDDs. The CRT for two identical monolithic scintillator detectors in coincidence was then calculated for each dataset as:

$$CRT = \sqrt{2 \times (CRT_{exp}^2 - (CRT_{ref}^2/2))} \tag{3.6}$$

where $CRT_{exp}$ is the experimentally measured CRT and $CRT_{ref}^2/2$ is the squared value of the single-detector time resolution of the reference detector (see section 3.5.3).

A deterministic timing method was also tested to assess the time resolution that can be achieved without any calibration procedure, apart from the measurement of the time skews between the DPC dies that remains necessary. Specifically, the average value of the first two timestamps registered by the monolithic detector was used as $\hat{t}_int$ [5].

With MLITE, $CRT_{exp}$ is found to be 176 ps FWHM, resulting in a CRT of 214 ps FWHM for two monolithic scintillator detectors in coincidence. With the deterministic method, $CRT_{exp}$ equals 192 ps FWHM, resulting in a CRT of 241 ps FWHM. MLITE thus provides a ~10% improvement of the CRT. The deterministic method still provides a remarkable CRT for a crystal of these dimensions; it has to be noted, however, that this result could only be achieved with a strict selection of reliable timestamps (see section 3.3). The computation time needed with a MATLAB implementation of MLITE running on a single core was ~1 ms per event, which could be further decreased with an optimized code.

The CRT of 214 ps FWHM may be compared with the values reported by van Dam *et al.* [5] for two monolithic scintillator detectors made from Ca-codoped LSO:Ce. These detectors had dimensions of 16 mm × 16 mm × 20 mm and 24 mm × 24 mm × 20 mm and reached CRTs of 185 ps FWHM and 184 ps FWHM, respectively. Since the time resolution of a scintillation detector linearly depends on $sqrt\tau_d$, with $\tau_d$ the decay time constant of the crystal [17] and the decay constants of LYSO:Ce and Ca-codoped LSO:Ce are 43 ns [26] and 33 ns [27], respectively, the value found for the LYSO:Ce monolithic detector is in excellent agreement with what could be expected from the previous measurements with Ca-codoped crystals.

Figure 3.10 shows the three TOF-difference spectra derived from datasets 22 cm FI, 24 cm FI, and 26 cm FI. The CRTs are 175.5 ps FWHM, 176 ps FWHM, and 175 ps FWHM, respectively. The mean times of interaction at 24 cm and 26 cm, relative to the measurement at 22 cm, are 60.3 ps and 135.2 ps, corresponding to distances of 18.1 mm and 40.5 mm, respectively. The differences with the expected distances of 20 mm and 40 mm, respectively, can be explained by the reproducibility of the source position within the setup, which is estimated to be in the order of 1-2 mm.

### 3.6.4. Events with incomplete light distributions

To compare the results obtained with the same statistics, the datasets with complete light distributions that were used in sections 3.6.1, 3.6.2 and 3.6.3 were artificially modified to determine the detector performance for events with incomplete light distributions. That is, four additional versions were created for each dataset, in which the data of 1, 2, 3, or 4 randomly chosen dies (viz., four light-pixel values and one timestamp per die) were deleted. Random deletion is considered justified since the monolithic scintillator detector is operated with full neighbor logic, so dies are expected to be missing only because of dead times caused by dark counts, with essentially equal probability per die.

The FB dataset was used to calculate the average light distributions (section 3.4). The methods described in section 3.4 were used to process the resulting four versions of the perpendicular-PB and side-PB datasets. The analysis used in sections 3.6.1.1, 3.6.1.2 and 3.6.2 was then repeated to determine the spatial,

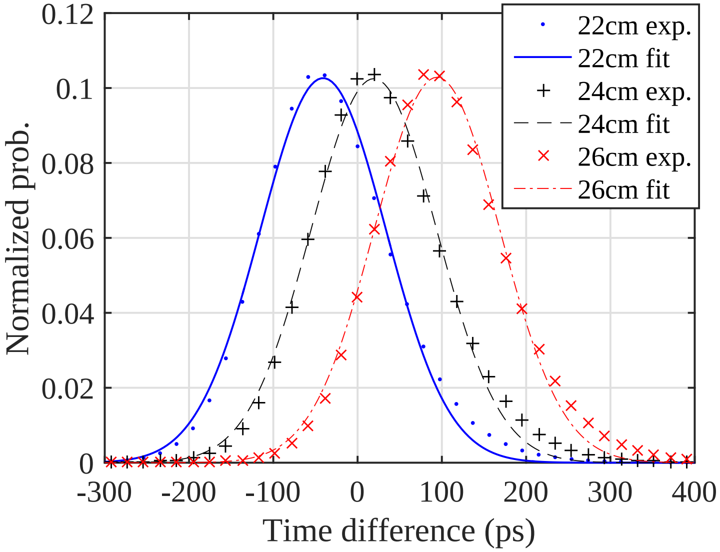

Figure 3.10: TOF-difference spectra obtained for three different distances between the source and the monolithic scintillator detector using the MLITE method.

DOI, and energy resolution as a function of the number of missing dies. Similarly, the analysis in section 3.6.3 was repeated on four versions of the flood irradiation datasets with different numbers of missing dies.

To put these results into perspective, a weighted average of the PSFs, CDFs, energy spectra, and TOF-difference spectra obtained with a variable number of missing dies was also calculated using as weights the fractions of events acquired with up to four missing dies during real measurements. The resulting distributions were used to estimate the performance that would be achieved for the detector settings and operating conditions used in this work if those distributions were accepted. The percentages of the events in which the data from 16, 15, 14, 13, and 12 dies were acquired are 68%, 18%, 6.5%, 2.5%, and 1%, respectively, i.e. ∼96% of the total registered events.

### **3.6.4.1.** Spatial resolution at perpendicular incidence

The parameters that characterize the spatial resolution in the x- and y-directions for perpendicularly incident events with up to four dies missing are reported in Table 3.4. The corresponding error CDFs are shown in Figure 3.11. A small degradation is noticeable for each additional missing die, but total degradations of only ∼10% and ∼15% are found for the MAE and $r_{50\%}$, respectively, when four dies are missing in each event. For the acquisition conditions used in this work (AC), a degradation in the spatial resolution <1.5% would be obtained if events with up to four missing dies were accepted.

Table 3.4: Spatial resolution for perpendicularly incident events with the pixel values from up to 4 out of 16 dies (4 pixels per die) missing and for the acquisition conditions used in this work (AC).

| Resolution (mm) | x | | | | | y | | | | | total | | | | |
|---|---|---|---|---|---|---|---|---|---|---|---|---|---|---|---|
| No. missing dies: | 1 | 2 | 3 | 4 | AC | 1 | 2 | 3 | 4 | AC | 1 | 2 | 3 | 4 | AC |
| FWHM | 1.71 | 1.77 | 1.78 | 1.85 | 1.69 | 1.75 | 1.80 | 1.80 | 1.91 | 1.72 | - | - | - | - | - |
| FWTM | 4.86 | 5.03 | 5.23 | 5.41 | 4.81 | 5.18 | 5.28 | 5.36 | 5.57 | 5.08 | - | - | - | - | - |
| $r_{50\%}$ | 0.84 | 0.87 | 0.91 | 0.95 | 0.83 | 0.87 | 0.90 | 0.93 | 0.98 | 0.85 | 1.66 | 1.72 | 1.79 | 1.86 | 1.64 |
| $r_{90\%}$ | 3.58 | 3.65 | 3.73 | 3.84 | 3.56 | 3.65 | 3.73 | 3.82 | 3.92 | 3.63 | 5.18 | 5.27 | 5.38 | 5.50 | 5.14 |
| MAE | 1.58 | 1.61 | 1.66 | 1.71 | 1.56 | 1.61 | 1.65 | 1.69 | 1.74 | 1.59 | 2.53 | 2.58 | 2.65 | 2.73 | 2.50 |

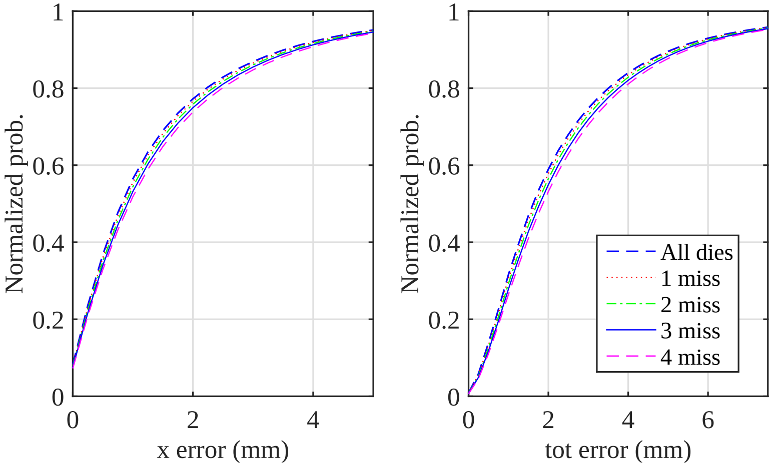

Figure 3.11: CDFs of the x- (left) and total (right) errors in the position estimation for perpendicularly incident events with the pixel values from up to 4 out of 16 dies (4 pixels per die) missing. CDFs of the y-errors are omitted because are similar to CDFs for x-errors.

### 3.6.4.2. DOI resolution

The average DOI resolution as a function of the number of missing dies is reported in Table 3.2. Figure 3.5 shows the DOI resolution and the DOI bias for incomplete light distributions as a function of DOI. The DOI resolution deteriorates by up to ~20% (MAE and $r_{50\%}$) at four missing dies and ~2% for the acquisition conditions used in this work, which is slightly more than the degradation observed in the x- and y-directions. This may be due to the fact that missing information has a twofold influence on the DOI estimation: it affects the x,y-position estimation as well as the SSPI value used to look up the DOI in $LUT_{DOI}$.

It can be noticed that the estimated DOI of events with missing dies tends to be biased towards the crystal front surface, presumably because the algorithm that estimates the missing pixel values has more difficulty in recovering light distributions in which bright pixels are missing.

### 3.6.4.3. Energy resolution

The energy resolutions for incomplete datasets with and without estimated values of the missing pixels are reported in Table 3.5. A degradation of ~55% is observed for the dataset with four missing dies without correction. This is reduced to <10% when using the estimated pixel values, resulting in an energy resolution of 10.6% FWHM, quite an acceptable value for LYSO:Ce. A degradation <1% would be obtained for real measurements accepting events with up to four missing dies.

Figure 3.12 shows the energy spectra obtained with events having two and four missing dies, with and without complemented pixel values, together with the spectrum obtained with events having complete light distributions. It can be noticed that the correction algorithm accurately restores the position of the photopeak and reduces the tail on the left side of the peak.

Table 3.5: Energy resolution for events with complete light distributions, for events with the pixel values from up to 4 out of 16 dies (4 pixels per die) missing (calculated with, ‘Estimated dies’, and without ,‘Missing dies’, estimated values of the missing pixels) and for the acquisition conditions used in this work (AC).

| Energy Resolution | No. of missing dies | | | | | |
|---|---|---|---|---|---|---|
| (% FWHM) | None | 1 | 2 | 3 | 4 | AC |
| Missing dies | - | 11.2 | 12.3 | 13.7 | 15.3 | - |
| Estimated dies | 9.9 | 10.1 | 10.3 | 10.4 | 10.6 | 10.0 |

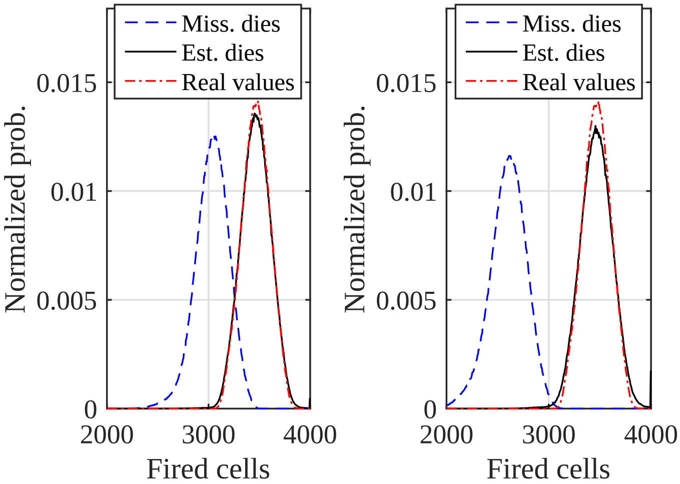

Figure 3.12: Energy spectra obtained with events having complete light distributions (‘Real values’) and having the pixel values from 2 (left) / 4 (right) out of 16 dies (4 pixels per die) missing, calculated with (‘Est. dies’) and without (‘Miss. dies’) estimated values of the missing pixels.

Table 3.6: CRT for events with complete time information, for events with the timestamps from up to 4 out of 16 dies (1 timestamp per die) missing and for the acquisition conditions used in this work (AC). Results are presented for the MLITE method ('MLITE') and the method that uses the average of the first two timestamps ('Av. 2 TS').

| CRT | No. of missing dies | | | | | |
|---|---|---|---|---|---|---|
| | None | 1 | 2 | 3 | 4 | AC |
| MLITE | 214 | 221 | 229 | 239 | 250 | 217 |
| Av. 2 TS | 241 | 251 | 263 | 276 | 292 | 246 |

#### 3.6.4.4. Time resolution

The CRT for events with missing information is shown in Table 3.6. In the case of four missing timestamps, a deterioration of ∼16% is observed with MLITE as well as with the average of the first two timestamps. In this case, MLITE still achieves an excellent CRT of 250 ps even though 25% of the timing information is missing. A degradation ∼1.5% would be obtained if events with up to four missing dies were accepted during the measurements.

## 3.7. Conclusions

New, time-efficient calibration procedures as well as position-, DOI-, energy-, and time-of-interaction estimators for monolithic scintillator detectors were tested experimentally on a detector based on a 32 mm × 32 mm × 22 mm LYSO:Ce crystal and a DPC array. About 9 hours were needed to fully calibrate the detector using a ∼3.5 MBq $^{22}$Na point-source. The possibility of avoiding PB irradiation, which was previously needed for time and DOI calibration and took about 8 days, reduces the calibration time by a factor of at least 20 (see section 3.5.3). Since the detector count rate during FB irradiation was lower than the maximum detector count rate, this time could still be reduced substantially if a stronger source were used. Moreover, considering that the new methods require FB and flood irradiations only, they open up the possibility of calibrating many detectors in parallel.

The accelerated position estimator based on 1D k-NN classification with preselection of the reference events reduces the calculation time by a factor of ∼200 without noticeably reducing the spatial resolution. An average spatial resolution of 1.7 mm FWHM / 1.6 mm MAE is achieved, which is better than or comparable to the best resolutions presented so far for monolithic scintillator detectors with a thickness of 15-20 mm [1, 4]. Additionally, a position-dependent analysis of the spatial resolution and bias showed that monolithic scintillator detectors can achieve quite homogeneous performance over almost all of their volume and that edge effects are reduced using crystals with a low aspect-ratio.

To our knowledge, this is the first time that the experimental DOI performance of a monolithic scintillator detector thicker than 10-15 mm is presented. A MAE better than 3 mm was obtained in the 22 mm LYSO crystal and it was demonstrated that this considerably improves the accuracy of LOR positioning at 60° incidence. This is expected to make the reconstructed image resolution of a typical clinical TOF-PET scanner much more homogeneous throughout its FOV.

A method to correct for the position-dependent energy response of monolithic scintillator detectors was shown to improve the energy resolution from 10.25% FWHM to 9.9% FWHM. This correction would not seem essential, as the uncorrected energy resolution is close to what is achievable with LYSO:Ce already. However, the method was shown to enhance detector performance and, since it can be easily implemented, it could be applied in systems made of many detectors to improve, e.g., the robustness to imperfections occurring during detector manufacturing.

A CRT of 214 ps FWHM was achieved with the MLITE method. This is in excellent agreement with previous results obtained with 20 mm thick monolithic crystals made from Ca-codoped LSO:Ce [5], taking into account the difference in the scintillation decay constants. This suggests that MLITE compensates for the optical photon transport similarly well, even though the present crystal is considerably wider than the previous ones.

A new, statistical method was introduced to estimate the photon count on missing photosensor pixels, which was tested on events in which the data from up to 4 out of 16 DPC dies (corresponding to 4, 8, 12, or 16 out of 64 light-pixels) was artificially removed. The results demonstrate that this method can restore sufficient information to profitably use the deterministic position pre-estimation algorithm of the accelerated 1D k-NN method while maintaining the robustness to missing information typical of statistical position estimation methods [3]. The degradation of the DOI resolution is slightly more pronounced, although parallax errors can still be corrected adequately with up to four missing dies. Finally, the CRT obtained with MLITE showed limited deterioration for events with up to 4 out of 16 timestamps missing. A degradation of all the performance parameters <2% would be observed if events with up to four missing dies were accepted during measurements with the detector settings and operating conditions used in this work, obtaining an improvement in the single-detector sensitivity of about 40% compared with the case in which only complete events are accepted.

In conclusion, this paper shows that monolithic scintillator detectors can be calibrated and operated in a practical way that should allow their use in systems consisting of many detectors. The spatial-, DOI-, energy-, and time-resolution achieved with a 32 mm × 32 mm × 22 mm LYSO:Ce crystal coupled to a DPC array shows an excellent match with the requirements of whole-body clinical TOF-PET imaging.

## Acknowledgements

This work was part of the EU FP7 project SUBLIMA, Grant Agreement 241711; see also www.sublima-pet-mr.eu

# References

[1] X. Li, W. C. J. Hunter, T. K. Lewellen, and R. S. Miyaoka, *Use of cramer–rao lower bound for performance evaluation of different monolithic crystal pet detector designs,* IEEE Transactions on Nuclear Science **59**, 3 (2012).

[2] J. Cabello, P. Barrillon, J. Barrio, M. G. Bisogni, A. Del Guerra, C. Lacasta, M. Rafecas, H. Saikouk, C. Solaz, P. Solevi, C. de La Taille, and G. Llosá, *High resolution detectors based on continuous crystals and sipms for small animal pet,* Nuclear Instruments and Methods in Physics Research Section A: Accelerators, Spectrometers, Detectors and Associated Equipment **718**, 148 (2013).

[3] S. Seifert, G. v. d. Lei, H. T. v. Dam, and D. R. Schaart, *First characterization of a digital sipm based time-of-flight pet detector with 1 mm spatial resolution,* Physics in Medicine and Biology **58**, 3061 (2013).

[4] G. Borghi, V. Tabacchini, S. Seifert, and D. R. Schaart, *Experimental validation of an efficient fan-beam calibration procedure for k-nearest neighbor position estimation in monolithic scintillator detectors,* Nuclear Science, IEEE Transactions on **62**, 57 (2015).

[5] H. T. van Dam, G. Borghi, S. Seifert, and D. R. Schaart, *Sub-200 ps crt in monolithic scintillator pet detectors using digital sipm arrays and maximum likelihood interaction time estimation,* Physics in Medicine and Biology **58**, 3243 (2013).

[6] T. Ling, T. K. Lewellen, and R. S. Miyaoka, *Depth of interaction decoding of a continuous crystal detector module,* Physics in Medicine and Biology **52**, 2213 (2007).

[7] T. Ling, T. H. Burnett, T. K. Lewellen, and R. S. Miyaoka, *Parametric positioning of a continuous crystal pet detector with depth of interaction decoding,* Physics in Medicine and Biology **53**, 1843 (2008).

[8] W. C. J. Hunter, H. H. Barrett, and L. R. Furenlid, *Calibration method for ml estimation of 3d interaction position in a thick gamma-ray detector,* Nuclear Science, IEEE Transactions on **56**, 189 (2009).

[9] Z. Li, M. Wedrowski, P. Bruyndonckx, and G. Vandersteen, *Nonlinear least-squares modeling of 3d interaction position in a monolithic scintillator block,* Physics in Medicine and Biology **55**, 6515 (2010).

[10] H. T. van Dam, S. Seifert, R. Vinke, P. Dendooven, H. Löhner, F. J. Beekman, and D. R. Schaart, *A practical method for depth of interaction determination in monolithic scintillator pet detectors,* Physics in Medicine and Biology **56**, 4135 (2011).

[11] S. Seifert, H. T. v. Dam, J. Huizenga, R. Vinke, P. Dendooven, H. Löhner, and D. R. Schaart, *Monolithic labr 3 :ce crystals on silicon photomultiplier arrays for time-of-flight positron emission tomography,* Physics in Medicine and Biology **57**, 2219 (2012).

[12] P. Bruyndonckx, S. Leonard, L. Jiangui, S. Tavernier, P. Szupryczynski, and A. Fedorov, *Study of spatial resolution and depth of interaction of apd-based pet detector modules using light sharing schemes,* Nuclear Science, IEEE Transactions on **50**, 1415 (2003).

[13] P. Bruyndonckx, S. Leonard, S. Tavernier, C. Lemaitre, O. Devroede, Y. Wu, and M. Krieguer, *Neural network-based position estimators for pet detectors using monolithic lso blocks,* Nuclear Science, IEEE Transactions on **51**, 2520 (2004).

[14] M. C. Maas, D. Van der Laan, D. R. Schaart, J. Huizenga, J. C. Brouwer, P. Bruyndonckx, S. Leonard, C. Lemaitre, and C. W. E. Van Eijk, *Experimental characterization of monolithic-crystal small animal pet detectors read out by apd arrays,* Nuclear Science, IEEE Transactions on **53**, 1071 (2006).

[15] H. T. van Dam, S. Seifert, R. Vinke, P. Dendooven, H. Löhner, F. J. Beekman, and D. R. Schaart, *Improved nearest neighbor methods for gamma photon interaction position determination in monolithic scintillator pet detectors,* Nuclear Science, IEEE Transactions on **58**, 2139 (2011).

[16] M. C. Maas, D. R. Schaart, D. J. v. d. Laan, P. Bruyndonckx, C. Lemaître, F. J. Beekman, and C. W. E. v. Eijk, *Monolithic scintillator pet detectors with intrinsic depth-of-interaction correction,* Physics in Medicine and Biology **54**, 1893 (2009).

[17] S. Seifert, H. T. v. Dam, and D. R. Schaart, *The lower bound on the timing resolution of scintillation detectors,* Physics in Medicine and Biology **57**, 1797 (2012).

[18] T. Frach, G. Prescher, C. Degenhardt, R. de Gruyter, A. Schmitz, and R. Ballizany, *The digital silicon photomultiplier - principle of operation and intrinsic detector performance,* in *Nuclear Science Symposium Conference Record (NSS/MIC), 2009 IEEE* (2009) pp. 1959–1965.

[19] T. Frach, G. Prescher, C. Degenhardt, and B. Zwaans, *The digital silicon photomultiplier - system architecture and performance evaluation,* in *Nuclear Science Symposium Conference Record (NSS/MIC), 2010 IEEE* (2010) pp. 1722–1727.

[20] R. Schulze, *PDPC TEK Manual*, Koninklijke Philips Electronics 2014 (2014).

[21] D. R. Schaart, E. Charbon, T. Frach, and V. Schulz, *Advances in digital sipms and their application in biomedical imaging,* Nuclear Instruments and Methods in Physics Research Section A: Accelerators, Spectrometers, Detectors and Associated Equipment **809**, 31 (2016).

[22] V. Tabacchini, V. Westerwoudt, G. Borghi, S. Seifert, and D. R. Schaart, *Probabilities of triggering and validation in a digital silicon photomultiplier,* Journal of Instrumentation **9**, P06016 (2014).

[23] M. A. Spurrier, P. Szupryczynski, Y. Kan, A. A. Carey, and C. L. Melcher, *Effects of ca2+ co-doping on the scintillation properties of lso:ce,* Nuclear Science, IEEE Transactions on **55**, 1178 (2008).

[24] S. Jan, G. Santin, D. Strul, S. Staelens, K. Assié, D. Autret, S. Avner, R. Barbier, M. Bardiès, P. M. Bloomfield, D. Brasse, V. Breton, P. Bruyndonckx, I. Buvat, A. F. Chatziioannou, Y. Choi, Y. H. Chung, C. Comtat, D. Donnarieix, L. Ferrer, S. J. Glick, C. J. Groiselle, D. Guez, P.-F. Honore, S. Kerhoas-Cavata, A. S. Kirov, V. Kohli, M. Koole, M. Krieguer, D. J. v. d. Laan, F. Lamare, G. Largeron, C. Lartizien, D. Lazaro, M. C. Maas, L. Maigne, F. Mayet, F. Melot, C. Merheb, E. Pennacchio, J. Perez, U. Pietrzyk, F. R. Rannou, M. Rey, D. R. Schaart, C. R. Schmidtlein, L. Simon, T. Y. Song, J.-M. Vieira, D. Visvikis, R. V. d. Walle, E. Wieërs, and C. Morel, *Gate: a simulation toolkit for pet and spect,* Physics in Medicine and Biology **49**, 4543 (2004).

[25] M. C. Maas, D. J. van der Laan, C. W. E. van Eijk, D. R. Schaart, F. J. Beekman, P. Bruyndonckx, and C. Lemaître, *Model of the point spread function of monolithic scintillator pet detectors for perpendicular incidence,* Medical Physics **37**, 1904 (2010).

[26] S. Seifert, J. H. L. Steenbergen, H. T. v. Dam, and D. R. Schaart, *Accurate measurement of the rise and decay times of fast scintillators with solid state photon counters,* Journal of Instrumentation **7**, P09004 (2012).

[27] D. N. ter Weele, D. R. Schaart, and P. Dorenbos, *Comparative study of co-doped and non co-doped lso:ce and lyso:ce scintillators for tof-pet,* Nuclear Science, IEEE Transactions on **62**, 727 (2015).

# 4

# A 32 mm × 32 mm × 22 mm monolithic LYSO:Ce detector with dual-sided digital photon counter readout for ultrahigh-performance TOF-PET and TOF-PET/MRI

This chapter has been published as:
G. Borghi, B. J. Peet, V. Tabacchini, and D. R. Schaart, "A 32 mm × 32 mm × 22 mm monolithic LYSO:Ce detector with dual-sided digital photon counter readout for ultrahigh-performance TOF-PET and TOF-PET/MRI," Phys. Med. Biol., vol. 61, no. 13, pp. 4929–4949, Jul. 2016.
DOI: 10.1088/0031-9155/61/13/4929

***Abstract*** - *New applications for positron emission tomography (PET) and combined PET/magnetic resonance imaging (MRI) are currently emerging, for example in the fields of neurological, breast, and pediatric imaging. Such applications require improved image quality, reduced dose, shorter scanning times, and more precise quantification. This can be achieved by means of dedicated scanners based on ultrahigh-performance detectors, which should provide excellent spatial resolution, precise depth-of-interaction (DOI) estimation, outstanding time-of-flight (TOF) capability, and high detection efficiency. Here, we introduce such an ultrahigh-performance TOF/DOI PET detector,* *based on a 32 mm × 32 mm × 22 mm monolithic LYSO:Ce crystal. The 32 mm × 32 mm front and back faces of the crystal are coupled to a digital photon counter (DPC) array, in so-called dual-sided readout (DSR) configuration. The fully digital detector offers a spatial resolution of ~1.1 mm full width at half maximum (FWHM) / ~1.2 mm mean absolute error (MAE), together with a DOI resolution of ~2.4 mm FWHM, an energy resolution of 10.2% FWHM, and a coincidence resolving time (CRT) of 147 ps FWHM. The time resolution closely approaches the best results (135 ps FWHM) obtained to date with small crystals made from the same material coupled to the same DPC arrays, illustrating the excellent correction for optical and electronic transit time spreads that can be achieved in monolithic scintillators using maximum-likelihood techniques for estimating the time of interaction. The performance barely degrades for events with missing data (up to 6 out of 32 DPC dies missing), permitting the use of almost all events registered under realistic acquisition conditions. Moreover, the calibration procedures and computational methods used for position and time estimation follow recently made improvements that make them fast and practical, opening up realistic perspectives for using DSR monolithic scintillator detectors in TOF-PET and TOF-PET/MRI systems.*

## 4.1. Introduction

Recent studies indicate that new applications for positron emission tomography (PET) are emerging, in part due to the recent development of integrated PET/magnetic resonance imaging (MRI) scanners. Applications for PET/MRI are found in fields where the excellent soft-tissue contrast of MRI provides better anatomical information compared to computed tomography (CT). PET/MRI furthermore offers the possibility to obtain complementary functional and molecular information as well as a substantially reduced radiation dose compared to PET/CT. Promising applications currently under investigation span from research on human brain function [1] to clinical evaluation of neuro-oncological and neurodegenerative diseases, e.g. Alzheimer [2]. Another application of PET/MRI is in pediatric oncology, where dose reduction is most important, especially when repeated imaging sessions are required [3, 4]. Finally, several applications in oncology have demonstrated interesting results, e.g. for the evaluation of lymphoma, head and neck cancers, prostate cancer, and possibly gastrointestinal tumors, gynecological tumors, and breast cancer [5–7].

Although the integration of PET and MRI has posed substantial challenges [8], whole-body clinical PET/MRI scanners have been built and clinically tested [9–12]. However, such whole-body scanners are not optimized for some of the aforementioned applications that involve the imaging of relatively small objects (~20 cm diameter or less), such as the brain, the female breast, and small children. These applications require better spatial resolution than what is currently available. The spatial resolution of whole-body scanners is limited by the large diameter of the PET rings (≥65 cm), which enhances blurring due to photon acollinearity, as well as by the performance of current scintillator detectors, which are typically based on ~4 mm pitch crystal arrays and provide no depth-of-interaction (DOI) correction, resulting in a deterioration of the resolution with increasing radial distance from the scanner central axis, especially in smaller-bore systems [13, 14]. Applications in e.g. pediatrics, neurology, and breast imaging would be much better served with dedicated, small-bore scanners based on ultrahigh-performance detector technology, as for instance demonstrated by the ECAT HRRT brain scanner, which, even 15 years after its introduction, remains a preferred system for brain imaging [15].

Moreover, currently available time-of-flight (TOF)-PET and TOF-PET/MRI scanners have a coincidence resolving time (CRT) larger than 300 ps full-with-at-half-maximum (FWHM) [16], which offers relatively little TOF benefit when imaging objects with a diameter smaller than ~20 cm [17, 18]. Better CRTs are furthermore desirable in integrated TOF-PET/MRI systems since the TOF information could be used for more accurate attenuation correction [19].

In summary, there exists a need for scintillation detectors with much improved spatial resolution, DOI estimation capability, coincidence resolving time, and detection efficiency. Monolithic scintillation detectors have demonstrated to be a promising solution, since they can simultaneously fulfill all of these requirements. That is, previous studies have demonstrated spatial resolutions in the order of ~1 mm FWHM [20–22], accurate DOI correction [23–28], energy resolutions better than 10% FWHM [28], and CRTs well below 200 ps [29]. Moreover, this type of detector can be made MRI compatible when based on analogue or digital silicon photomultipliers (SiPMs) and is less expensive than detectors based on finely-pixelated scintillator matrixes. It is noted that recent studies have introduced more efficient procedures to calibrate the detectors, as well as faster algorithms to estimate the time and position of interaction [22, 28, 30].

Nevertheless, the monolithic scintillation detectors with the best spatial resolutions and CRTs reported to date are relatively thin (≤10 mm) and, therefore, have limited detection efficiency. If the thickness is increased, the spatial, DOI, and time resolutions deteriorate, making them suboptimal for specialized high-resolution applications [22, 28, 31]. An approach that has already demonstrated promising results for simultaneously obtaining high performance and high sensitivity in monolithic scintillator detectors is the so-called dual-sided readout configuration (DSR), in which pixelated photosensors are coupled to both the front and back faces of a thick monolithic crystal [32].

In this work, we present a detector optimized for applications such as pediatric, neurological, and breast imaging, based on a 22 mm thick monolithic LYSO:Ce crystal and two digital photon counter (DPC) arrays in DSR configuration. The detector performance is fully characterized, including the spatial, DOI, energy, and timing performance. The results are compared to those previously reported for a back-sided readout (BSR) detector based on a LYSO:Ce crystal of equal dimensions [28]. Finally, the DSR detector performance is assessed for events in which part of the data acquired by the DPC arrays is missing due to dead time, so as to investigate the robustness of the detector with respect to this potential source of error.

## 4.2. Material and methods

### 4.2.1. Dual-sided readout detector and reference detectors

The DSR detector presented in this paper (Figure 4.1) is based on a polished 32 mm × 32 mm × 22 mm LYSO:Ce crystal (Crystal Photonics, Sanford, USA) and two digital photon counter arrays (model DPC-3200-22-44, Philips Digital Photon Counting). The photosensors are optically coupled to the two opposed 32 mm × 32 mm faces of the crystal using a transparent silicone material (Sylgard 527, Dow Corning). The other faces of the crystal are covered with a specular reflector foil (Vikuiti ESR, 3M).

The DPC arrays have a surface of 32.6 mm × 32.6 mm and consist of 16 independent 7.8775 mm × 7.15 mm silicon dies (at a pitch of 8 mm), each comprising four 3.2 mm × 3.8775 mm sensor pixels and an on-chip time-to-digital converter (TDC). A detailed description of the die architecture can be found in Frach *et al.* [33], Frach *et al.* [34], Schulze [35], Tabacchini *et al.* [36], and Schaart *et al.* [37]. Shortly, each pixel comprehends 3200 microcells, each microcell consisting of a single photon avalanche diode (SPAD) integrated with its own control and readout circuitry, which allows users to switch off SPADs with high dark count rates. For this work, the noisiest 5% of the microcells were disabled.

Each pixel is subdivided into four subpixels, which are connected to a logic network used to implement the trigger threshold. That is, a subpixel assumes a

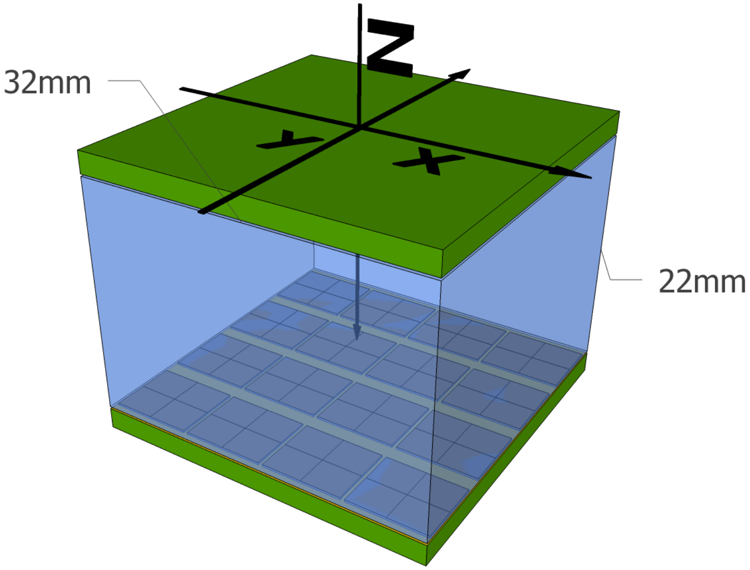

Figure 4.1: Sketch of a partially assembled dual-sided readout detector with the reference system used in the analysis.

logical 'true' state when at least one of its SPADs is fired. The trigger network uses AND/OR operations on the subpixel states to define how many fired subpixels on a pixel will produce a trigger signal. The first pixel that produces such a trigger signal prompts the acquisition of a timestamp and starts the validation sequence [36]. In all measurements performed in this work, the dies were triggered on the first fired subpixel (PDPC notation MT=1), i.e. on the first SPAD discharging on the die.

The validation sequence consists of a user-defined waiting time at the end of which a second, higher threshold has to be reached in order to validate and acquire the event. The validation threshold is implemented by further subdividing the microcells of each subpixel into smaller groups and performing a user-programmable logic operation on these groups using a logic network similar to the one used for the trigger threshold, as described in detail by Tabacchini *et al.* [36]. In the present work, the validation period was set to 40 ns, while the validation threshold was set such that one pixel has to have at least one fired SPAD on each subpixel to validate the event (DPC notation: '0x7F:AND'). If the validation threshold is reached, the die waits for a user-defined integration phase (set to 165 ns in this work) and then reads out the status of all microcells (which takes ~680 ns), providing the number of SPADs fired on each pixel and a single timestamp. If the validation threshold is not reached, a fast recharge-and-reset cycle is performed.

The DPC arrays are equipped with neighbor logic, which was programmed to initiate the acquisition of all the dies of an array after the validation of any single die. The overvoltage Vob was optimized at 2.95 V to limit the amount of undesired triggers resulting from optical cross talk between the two DPCs.

Three additional detectors based on DPC-3200-22-44 arrays were assembled to be used as reference detectors in coincidence measurements. Two of these detectors were based on monolithic LSO:Ce scintillators (Agile Engineering Inc., Knoxville, TN, USA), one measuring 32 mm × 32 mm × 25 mm and the other 16 mm × 16 mm × 20 mm. These crystals were also covered with 3M Vikuiti ESR foil on the side faces, while the top face was covered with Teflon. The last detector was based on a 3 mm × 3 mm × 5 mm calcium co-doped LSO:Ce crystal (0.2% Ca in the melt) [38] (produced at the Scintillation Materials Research Center, University of Tennessee, and provided by Agile Engineering Inc., Knoxville, TN, USA). This crystal was covered with 3M Vikuiti ESR foil on all five sides not coupled to the DPC array.

### 4.2.2. Experimental setup

A paired-collimator setup similar to the one presented in Borghi *et al.* [22] was used for calibrating and assessing the performance of the DSR detector. Shortly, the setup consists of a central tungsten housing for a $^{22}$Na point source (0.5 mm ⌀, ∼3.5 MBq, IDB Holland BV) and two interchangeable sets of collimators which are used to obtain a pencil beam (0.5 mm ⌀) or a fan beam (0.5 mm width) of annihilation photons. The sets are composed of a 80 mm thick tungsten collimator, which shapes the 511 keV beam in the direction of the test detector, and a lead collimator (40 mm or 70 mm thick, for the fan- and pencil-beam set respectively), which confines the beam in the direction of the reference detector.

The DSR detector was mounted on two perpendicular linear stages driven by stepper motors (Physics Instruments, M-403.42S stages with C-663 controllers) to precisely position the detector in front of the collimated beams. The reference detectors were placed at a fixed position on the other side of the collimator. The collimator and the detectors were contained in a light-tight temperature cabinet (Weiss WT 450/70) that was cooled to -28 ° during measurements. Two small fans, one on each side of the DSR detector, were used to dissipate the heat produced by the DPC arrays. During operation the temperature of the DPC tiles stabilized around -25 ° and a bias-voltage adjustment procedure was used to compensate for small (<1 °) temperature drifts.

The detectors were controlled and read out using field-programmable gate array (FPGA) based electronic boards and computer software provided by PDPC [35]. During acquisition, the DPC sensors transmitted all validated die events to the computer where a preliminary selection of coincidence events was performed on-line by the acquisition software using a wide coincidence window. The selected data were stored on hard disk for off-line analysis using MATLAB scripts.

### 4.2.3. Data acquisition

#### 4.2.3.1. Measurements

Four different measurements were performed to calibrate and characterize the spatial response of the DSR detector. They are referred to as the fan-beam (FB), perpendicular pencil-beam (PB), side PB, and angular PB datasets. The detector based on the 32 mm × 32 mm × 25 mm crystal was used as reference detector for the FB measurement, for the other measurements the 16 mm × 16 mm × 20 mm crystal was used instead. Prior to each measurement, count rate profiles were acquired to find the central position of the detector with respect to the fan- or pencil-beam position.

In the FB measurement, two datasets were acquired irradiating the front face of the DSR detector with a perpendicularly incident fan beam. The first dataset was acquired with the fan beam aligned perpendicularly to the crystal x-axis (x-subset) and irradiating the front face of the DSR detector at regular steps of 0.25 mm along the x-axis. For each position, 12800 full-energy events were registered. A similar acquisition was repeated with the fan beam aligned perpendicularly to the crystal y-axis (y-subset) and irradiating the crystal at regular steps of 0.25 mm along the y-axis.

In the perpendicular PB measurement, the whole front face of the detector was irradiated with a perpendicularly incident pencil beam, at a square grid of irradiation positions with a 0.25 mm pitch. A hundred full-energy events per position were registered.

In the side PB measurement, half of a side face of the crystal (0.5 mm ≤ x ≤ 15.5 mm and 0.5 mm ≤ DOI ≤ 21.5 mm) was irradiated with the perpendicularly incident pencil beam at a regular grid having a 1 mm pitch. Here, 3500 full-energy events per position were selected.

Finally, in the angular PB measurement half of the front face of the detector (0 mm ≤ x ≤ 16 mm) was irradiated with the pencil beam incident on it at a 60° angle, aligning the beam such that it was contained in a plane parallel to the plane defined by the y- and z-axis of the crystal. The irradiation was performed at a regular grid having 0.25 mm pitch and only the points for which the entry and the exit points of the irradiation line were on the front and back face of the crystal were irradiated. Fifty full-energy events were acquired per position.

For calibrating and characterizing the timing performance of the DSR detector, a flood irradiation (FI) was performed using the 3 mm × 3 mm × 5 mm LSO:Ce,Ca crystal as a reference detector. The coincidence resolving time of the reference detector ($CRT_{ref}$) was determined using the method described in van Dam *et al.* [29] and was found to be $CRT_{ref} = 128$ ps. The reference and DSR detector were placed at opposed sides of an uncollimated $^{22}$Na point source at a distance of 25 mm and 200 mm, respectively, and a dataset of $\sim 2.8 \cdot 10^6$ full-energy coincidences was acquired.

#### 4.2.3.2. Event selection and homogeneity correction

In the measurements, those events were selected in which all dies of both DPC arrays of the DSR detector were registered and for which the total photon count fell within the full-width-at-tenth-maximum (FWTM) of the 511 keV full-energy peak. For the FI dataset, the same energy condition was imposed on the coincidence detector. Random coincidences were removed in all measurements, except the FI dataset, by first determining a rough estimation of the time of interaction in both detectors - selecting the earliest timestamp that was followed by at least another timestamp in a 1 ns time-window - and applying a coincidence time window of ±2 ns between the DSR detector and the reference detector.

To compensate for a possible non-uniformity in the response of the different DPC pixels, e.g. due to defects in the optical coupling, a uniformity correction look-up table ($LUT_{UC}$) was created. All events of the perpendicular PB irradiation, distributed homogeneously over the front face of the crystal, were used to calculate an average light distribution. The elements of $LUT_{UC}$ were then determined separately for each DPC sensor as the ratio of the mean pixel value and the value of each pixel in the average light distribution measured by that sensor. All light distributions considered in the analysis were corrected by multiplying each DPC pixel value with the corresponding value in $LUT_{UC}$.

### 4.2.4. Data analysis

The methods used to calibrate the DSR detector and to estimate the position-, time-, and energy-of-interaction of the detected gamma quanta are based on the methods described in Borghi *et al.* [28], with slight adaptations for the different photosensor configuration. In the following, a brief summary of these methods, with emphasis on the detector-specific details, is given.

#### 4.2.4.1. Accelerated k-nearest neighbor 1D method for x,y-position estimation

The x,y position of interaction was estimated using the so-called accelerated 1D k-nearest neighbor (k-NN 1D) method developed by Borghi *et al.* [28], which is a greatly accelerated version of the k-NN method [22, 39, 40]. It uses a simple and computationally inexpensive clustering approach to make a preliminary estimation of the position of interaction of an unknown event and then uses this information to select only part of the reference events for the k-NN 1D positioning algorithm that is used for the final position of interaction estimation.

The pre-estimation method is based on look-up tables (LUTs) and requires a measure correlated with each coordinate to be estimated. In this work, the x- and y- coordinates of the center of gravity ($COG_x$ and $COG_y$, respectively) of the total light distribution measured by the two DPC arrays were used as measures of the x and y position of interaction, respectively. Furthermore, the standard deviations $\sigma_{front}$ and $\sigma_{back}$ of the pixel values of the separately normalized light intensity distributions measured by the front and back DPC arrays, respectively, were used to define the measure of the DOI:

$$R_\sigma = \frac{\sigma_{front}}{\sigma_{front} + \sigma_{back}} \tag{4.1}$$

The position pre-estimation LUTs were calculated using the events of the FB dataset as reference data. That is, $LUT_x^{PRE}$ was built by subdividing the detector into 32 equal regions along the x-direction and determining the fractions of events $f_x(x)$ of the FB dataset interacting in each region by means of a GATE Monte Carlo simulation [41]. The reference events were then sorted in ascending order of $COG_x$ value and the values demarcating the fractions $f_x(x)$ of the sorted series were stored in $LUT_x^{PRE}$. The procedure was repeated in the y-direction to determine $LUT_y^{PRE}$. To build $LUT_{DOI}^{PRE}$, the crystal was subdivided into a grid of 16 × 16 × 22 equally sized voxels. The reference events were assigned to the 16 × 16 x,y-bins on the basis of $LUT_x^{PRE}$ and $LUT_y^{PRE}$, while the fractions $f_z(z|x,y)$ of events interacting in each of the 22 DOI layers of each x,y-bin were derived from the Monte Carlo simulation.

The final position estimation is based on the Smoothed k-NN 1D method described by Borghi *et al.* [22]. The method was accelerated by pre-estimating the position of the unknown event as well as the reference events (x- and y-subsets of the FB dataset) on the basis of $LUT_x^{PRE}$, $LUT_y^{PRE}$ and $LUT_{DOI}^{PRE}$ and using for the k-NN calculation only the reference events whose pre-estimated position was in within a certain distance from the pre-estimated position of the unknown event, as described by Borghi *et al.* [28]. This preselection was performed using a 2 mm radius in the x,y-direction and a 2 mm range in the DOI-direction. The number of nearest neighbors used in the Smoothed k-NN 1D method was k = 30 and the width of the smoothing average filter was 5 bins.

#### 4.2.4.2. Depth of interaction estimation

Similar to Borghi *et al.* [28], the method used for the DOI pre-estimation procedure (section 4.2.4.1) was also used to estimate the final DOI value. The only difference is that the final x,y positions determined with the accelerated k-NN 1D method were used to build the look-up table $LUT_{DOI}$, again using a grid of 16 × 16 × 22 voxels, and to determine the x,y-position of the unknown events.

#### 4.2.4.3. Energy resolution

To compensate for possible variation of the energy response with position inside the crystal, a look-up table for energy correction $LUT_{EN}$ was calculated as in Borghi *et al.* [28]. The crystal was subdivided into 16 × 16 × 4 equal voxels (4 DOI layers), to which the events in the FB dataset were assigned based on their estimated positions of interaction. A correction factor was calculated for each voxel as the ratio between the center positions of the 511 keV photopeaks in the energy spectra of the entire detector and of the voxel, using Gaussian fits to determine the peak positions.

#### 4.2.4.4. Electronic skew estimation

A DPC array usually exhibits noticeable electronic time skews between different dies. If an analytical method that combines the timestamps of different dies is used to estimate the time of interaction in the crystal, these skews have to be precisely measured and die timestamps have to be corrected for them. van Dam *et al.* [29] showed that this can be done by illuminating the bare sensor array with short laser pulses. A similar method could be used to measure the time skews between the two arrays used in the DSR detector. However, if the maximum likelihood interaction time estimation (MLITE) method presented in the same paper is used, a precise time alignment of the dies is not necessary and this additional calibration step can be avoided.

In the present work, the MLITE method was adopted (see section 4.2.4.5) and the time differences between the timestamps were used only to select the valid ones, as in Borghi *et al.* [28]. This selection does not require high accuracy in the electronic skew estimation, therefore a procedure was developed to estimate the skews in the already assembled detector, using the data from the FI dataset. The 3D positions of the events were first estimated using the methods described in sections 4.2.4.1 and 4.2.4.2. Then, for each die, the events in the 8 mm × 8 mm × 4 mm crystal volume directly on top of that die were used to determine the distribution of the differences between the timestamps recorded on that die and the reference detector. This distribution was fitted with an exponentially modified Gaussian and the center position of the Gaussian component of the fit was taken as the skew estimation for the die. The estimated skews were then used to correct all timestamps in the FI datasets.

#### 4.2.4.5. Maximum likelihood interaction time estimation

The time of interaction inside the DSR detector is estimated using the MLITE method [29]. This method is based on a maximum-likelihood algorithm and uses all the timestamps acquired in a monolithic scintillator detector to correct for the delays arising from the transport of the scintillation photons inside the crystal (as well as potential electronic skews), so as to obtain a more precise estimation of the time of interaction.

In this work, ∼2.3 million events from the FI dataset were used for MLITE calibration. First, a timestamp selection was performed for each event so as to remove early timestamps triggered by dark counts and late timestamps containing little information about the interaction time [28]. The first valid timestamp in each sequence was taken as the earliest timestamp that was followed by at least two more timestamps within a 1 ns time window and all timestamps generated 1.5 ns later than the first one were neglected. Then the crystal was divided into 8 × 8 × 6 equal voxels (6 DOI layers) to which the calibration events were assigned based on their estimated position of interaction. Finally, for each combination of voxel and DPC die, the probability distribution of the first photon detection delays (FPDDs) was determined by calculating the differences between the timestamps of that die and the reference detector and by using kernel density estimation (KDE). The kernel function used for KDE was the Epachenikov (parabolic-shaped) function. To accelerate the MLITE method, all FPDD probability distribution functions (PDFs) were pre-computed on a temporal grid with a spacing equal to 1 DPC TDC-bin (10 ns / $2^9 \cong 19.5$ ps) and stored in a LUT.

To estimate the time of interaction of an unknown event, the relevant timestamps were first selected using the same selection procedure used above for the reference events. The MLITE method was then used to estimate the most likely time of interaction.

#### 4.2.4.6. Detector performance for events with missing data

Even if neighbor logic is enabled, DPC arrays do not always register the photon counts and time stamps from all dies, for example because a die may be in a recharge/reset sequence after a non-validated trigger has been generated by a dark count. For the detector settings and measurement conditions used in this work, approximately 55% of the 511 keV events are acquired with the data of at least one die missing (Figure 4.2). However, only ∼3% of events have more than 6 (out of a total of 32) dies missing, therefore most of the incomplete events should

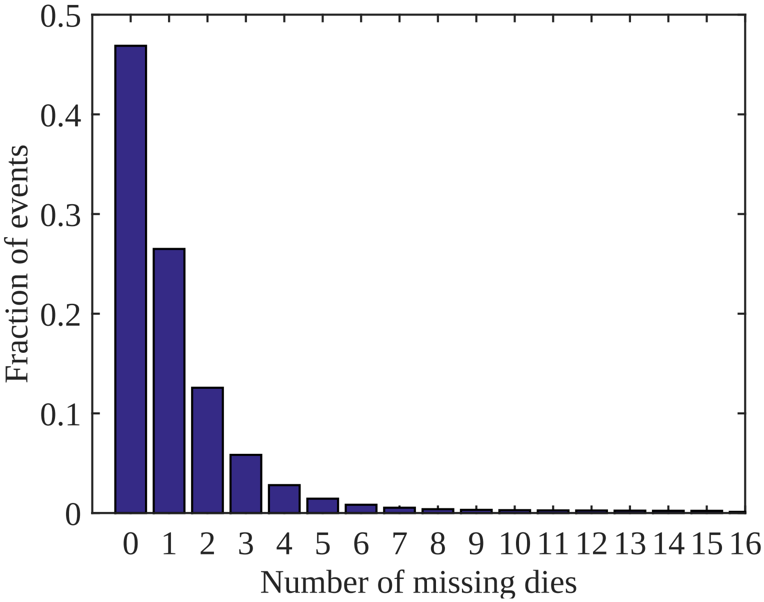

Figure 4.2: Fraction of events having a certain number of missing dies for the measurement conditions and DPC settings used this study.

still contain sufficient information to obtain an accurate estimation of the position and time of interaction.

A method to use the events with missing data was therefore implemented using the same techniques used in Borghi *et al.* [28]. Shortly, the crystal was subdivided into 16 × 16 × 4 voxels, to which the events (without any missing data) from the FB dataset were assigned. The average measured light distribution was then calculated for each voxel. In case of an event with missing data, the average light distribution most similar to the incomplete one was determined using k-NN algorithm ($k = 1$) and its renormalized pixel values were assigned to the corresponding missing pixels of the incomplete light distribution. The estimated pixel values were then used to calculate the total energy (which was also corrected for position dependence as described in section 4.2.4.3), to pre-estimate the 3D position of the event, and to determine the final DOI value. However, only the measured, incomplete data were used for the k-NN 1D and MLITE algorithms, since these statistical methods allow the missing data simply to be ignored [28].

## 4.3. Results and discussion

### 4.3.1. Spatial resolution for perpendicularly incident events

The x,y spatial resolution of the DSR detector was determined using the perpendicular PB dataset as test dataset. The positions of interaction of all its events were estimated using the accelerated k-NN 1D method (section 4.2.4.1) and the position-

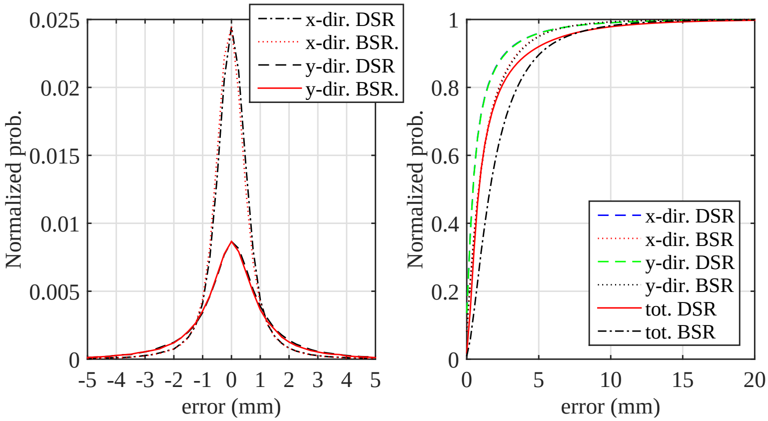

Figure 4.3: The cross sections of the 2D point spread function in both the x- and the y-direction (left) and the cumulative distribution functions of the x- and the y- and total errors (right), for the DSR detector and, for comparison, the BSR detector [28].

ing errors were calculated as the differences between these estimated positions and the known positions of irradiation. To correct for small misalignments (<0.2 mm translation, <1° rotation) between this dataset and the FB calibration dataset used for detector calibration, the corresponding correction procedure described in Borghi *et al.* [22] was applied. The computation time required to estimate the position of an unknown event using a non-optimized MATLAB code on a single core was ~5-10 ms, which could be decreased using optimized software.

Traditionally, the measures used to define the spatial resolution of monolithic scintillator detectors are the FWHM and FWTM of the cross sections through the maximum of the 2D histogram of the positioning errors, in other words the detector 2D point spread function (2D PSF) (Figure 4.3, left). However, as discussed by Borghi *et al.* [28], these values do not provide complete information in case the PSFs do not have a Gaussian shape. Therefore, also other measures, based on the cumulative distribution functions (CDFs) of the x, y, and total errors (Figure 4.3, right) were calculated. These measures are the error values at which the CDFs exceed 50% and 90%, called $r_{50\%}$ (or median error) and $r_{90\%}$, respectively, as well as the mean absolute errors (MAE), i.e. the average of the absolute values of the errors.

The results are reported in Table 4.1; it should be noted that these values are not corrected for the ~0.7 mm FWHM width of the pencil beam. In order to make a direct comparison, the equivalent values, previously obtained with a BSR detector based on a LYSO:Ce crystal of equal dimensions [28], are reported in the same table. The DSR detector shows excellent results, e.g. ~1.1 mm FWHM and $r_{50\%}$ <0.5 mm for the resolution in the x- and y-directions. Particularly noteworthy are the $r_{50\%}$ values, which are essentially halved compared to the BSR detector. In fact, $r_{50\%}$ is probably the measure that best indicates the intrinsic detector positioning accuracy, since the other measures (FWTM, $r_{90\%}$, MAE) are more strongly affected

Table 4.1: Comparison of the spatial resolution of the DSR detector in the x- and y-directions with a BSR detector of the same dimensions [28], for perpendicularly incident events.

| Resolution (mm) | x | | y | | total | |
|---|---|---|---|---|---|---|
| | DSR | BSR | DSR | BSR | DSR | BSR |
| FWHM | 1.09 | 1.68 | 1.10 | 1.70 | - | - |
| FWTM | 2.54 | 4.76 | 2.51 | 5.02 | - | - |
| $r_{50\%}$ | 0.43 | 0.82 | 0.43 | 0.84 | 0.85 | 1.62 |
| $r_{90\%}$ | 2.67 | 3.53 | 2.71 | 3.60 | 4.27 | 5.11 |
| MAE | 1.18 | 1.55 | 1.19 | 1.58 | 1.87 | 2.48 |

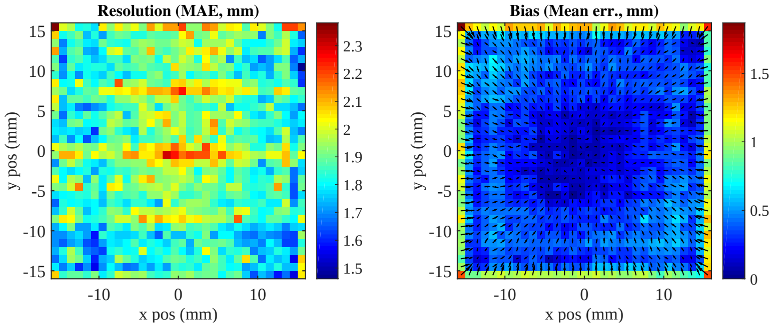

Figure 4.4: Maps of the mean absolute error (left) and position estimation bias (right) for each 1 mm × 1 mm region of the detector surface.

by events that undergo one or more Compton interactions inside the crystal (i.e. >50% of all events). In such an event a significant fraction of the total energy may be deposited at some distance from the position of first interaction, making accurate positioning of the event more difficult even if the intrinsic detector performance is improved.

In order to study the positioning performance of the DSR detector as a function of the x,y position of interaction, the detector surface was subdivided into 1 mm × 1 mm regions and the MAE values were calculated for each region considering only the events whose position of irradiation was in that area (Figure 4.4, left). The mean error in each region was also calculated, in order to study the positioning bias of the detector (Figure 4.4, right) [28, 42]. The spatial resolution is found to be fairly homogeneous across the detector surface, while the bias is smaller than 1 mm, except in the regions near the edges (≤2 mm), where it increases to ~1.5 mm.

### 4.3.2. DOI resolution

The depth-of-interaction resolution of the DSR detector was determined by estimating the DOI of all events in the side PB dataset, calculating the 1D histogram of the errors (1D PSF) with respect to the known irradiation depths, and computing the corresponding FWHM/FWTM and MAE values. The average resolution is 2.4 mm

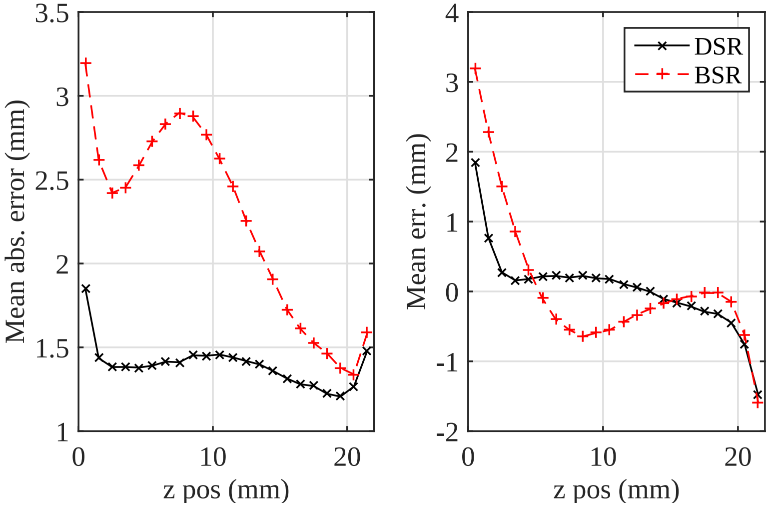

Figure 4.5: DOI resolution (left) and DOI bias (right) for the DSR and BSR detectors plotted as a function of the DOI.

FWHM and 5.6 mm FWTM, whereas the average MAE is 1.4 mm. These values represent a considerable improvement compared to the BSR detector, which achieves average values of 3.7 mm FWHM, 11.1 mm FWTM, and 2.2 mm MAE.

To investigate the DOI resolution and bias as a function of the DOI, the MAE and the mean error (bias) were also calculated for each individual z-position of irradiation (Figure 4.5). For comparison, the equivalent results obtained with the BSR detector are shown in the same plot. The DOI resolution of the DSR detector appears to be homogeneous over practically the whole DOI range, whereas the BSR detector shows a substantial deterioration in the front part of the crystal. The bias of the DSR detector is negligible, except in the regions close to photosensors, where it increases due to the truncation of the error distributions by the crystal edges.

### 4.3.3. Positioning accuracy for non-perpendicularly incident events

The angular PB dataset was used to test the position estimation accuracy of the DSR detector for non-perpendicular irradiation conditions. The x-error was defined as the distance between the estimated position of interaction and the plane parallel to the y,z-plane that contains the true line of response (LOR). The y′-error was defined as the distance between the estimated y,z position of interaction and the true LOR within the y,z-plane which contains the true LOR.

The results obtained with DOI correction are reported in Table 4.2, together with the values obtained when a fixed DOI value of 7.5 mm is used. This value corresponds to the mean depth of the energy deposition centroid for 511 keV gamma rays entering the crystal at an angle of 60° with respect to the detector front face.

Table 4.2: Spatial resolution for events incident at 60° with respect to the crystals front face, obtained using either the estimated DOI ('DOI') or a fixed DOI value of 7.5 mm ('no DOI').

| Resolution (mm) | x | | y′ | | total | |
|---|---|---|---|---|---|---|
| | DOI | no DOI | DOI | no DOI | DOI | no DOI |
| $r_{50\%}$ | 0.50 | 0.50 | 0.72 | 2.11 | 1.19 | 2.57 |
| $r_{90\%}$ | 3.02 | 3.02 | 3.18 | 5.90 | 4.96 | 6.73 |
| MAE | 1.29 | 1.29 | 1.43 | 2.81 | 2.15 | 3.39 |

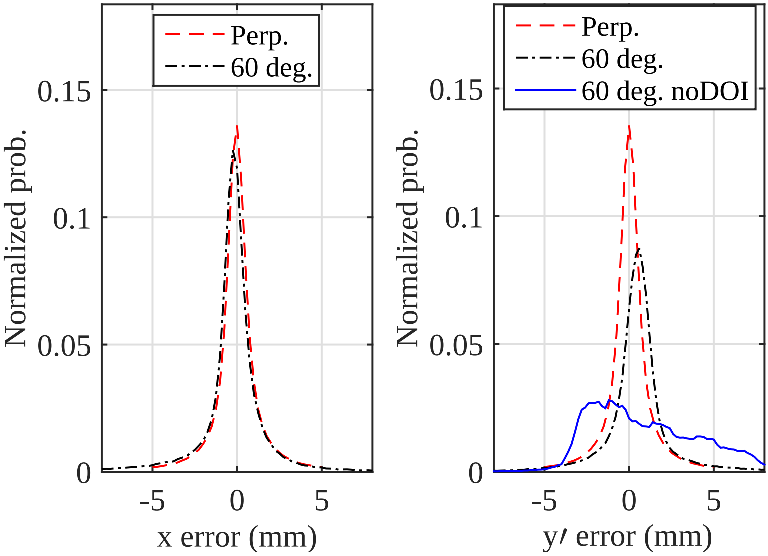

Figure 4.6: The 1D PSFs derived from the irradiation with the pencil-beam at an angle of 60° with respect to the detector front face. The results with DOI correction ('60 Deg') are compared to the case when a fixed DOI value of 7.5 mm is being used ('60 deg. no DOI', only for y′-direction) and to the 1D PSF obtained for the perpendicular pencil-beam irradiation ('Perp.').

If DOI correction is applied, only a small degradation compared to the measurement with perpendicular irradiation can be noticed for the total error. In contrast, significant deterioration is observed if a fixed DOI value is assumed.

To further demonstrate the importance of precise DOI estimation, the 1D histograms of the errors in the x- and y′-directions (1D PSFs) for the three cases are compared in Figure 4.6. It is noted that the 1D PSF for the y′-errors shows some bias at 60° incidence. This could be due to inaccurate alignment of the crystal, since the positioning procedure is less precise when the crystal is not aligned perpendicularly to the beam.

These results show that an accurate DOI estimation capability is necessary for high resolution detectors to maintain their excellent positioning performance also for non-perpendicularly incident events. This capability is particularly essential in small-diameter scanners for dedicated applications such as pediatric, neurological, and breast imaging. In these systems a significant fraction of events are expected

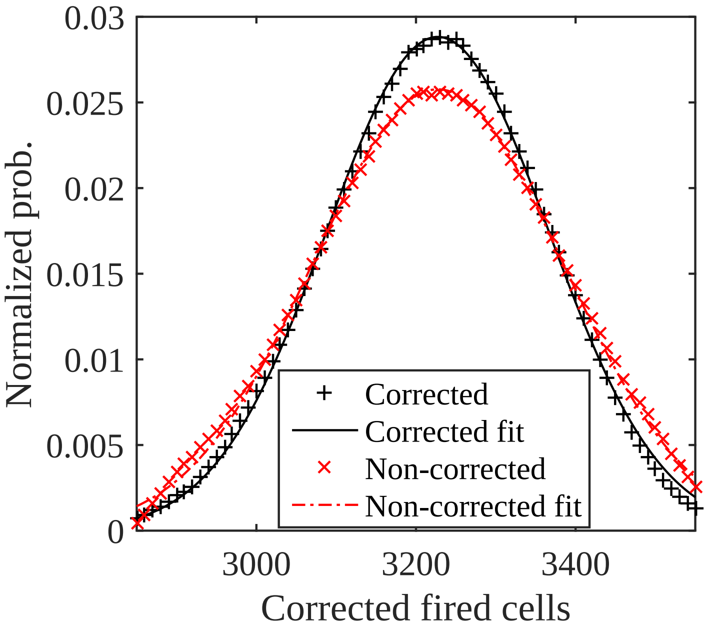

Figure 4.7: The energy distributions for complete light distributions with and without position-dependent energy correction. The energy resolution for the corrected energy spectrum is 10.2% FWHM. The resolution of the uncorrected spectrum is 11.5% FWHM.

to be incident at a large angle on the detectors and therefore precise DOI estimation is of utmost importance to obtain a homogeneous resolution across the whole FOV.

### 4.3.4. Energy resolution

The energy resolution of the DSR detector was determined using the perpendicular PB dataset, considering only the events within the FWTM of the non-corrected 511 keV photopeak. The total energy of these events was corrected using the method described in section 4.2.4.3 and a Gaussian fit was used to determine the FWHM of the non-corrected and corrected peaks (Figure 4.7). Without correction, the energy resolution equals 11.5% FWHM, while it improves to 10.2% FWHM with energy correction. This improvement could be explained by a different quality in the optical coupling of the two photosensors, resulting in a dependence of the photon collection efficiency on the position and depth of interaction.

### 4.3.5. Time resolution

The events of the FI dataset which had not been employed for the MLITE calibration procedure (0.5 million events) were used to determine the coincidence resolving time of the DSR detector. About 1-2 ms were needed to estimate each single timestamp using a MATLAB implementation of MLITE running on a single

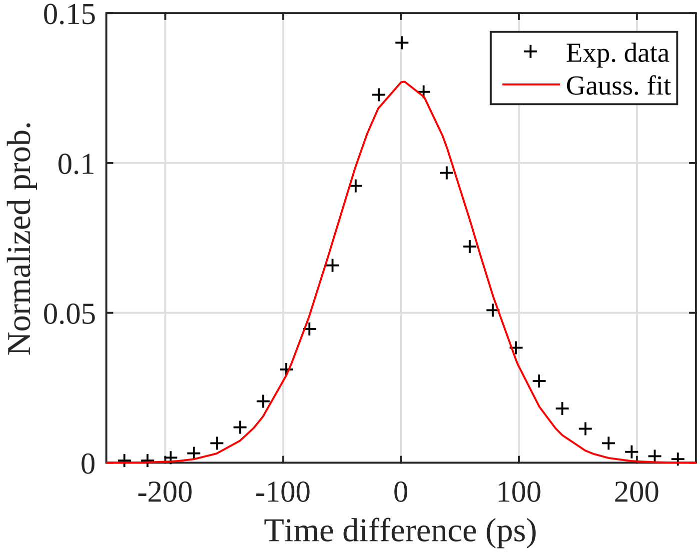

Figure 4.8: The timing spectrum of the DSR detector in coincidence with a fast 3 mm × 3 mm × 5 mm LSO:Ce (0,2% Ca) crystal. The FWHM of the Gaussian fit of this spectrum is 137.5 ps, which translates into a CRT of ~147 ps FWHM for two DSR detectors in coincidence.

core, which could be reduced using optimized code. The MLITE values (section 4.2.4.5) were used to obtain a time difference spectrum in coincidence with the reference detector (Figure 4.8). The slightly asymmetric shape of the spectrum is probably caused by early timestamps in the reference detector generated by dark counts, which cannot be discriminated if they arrive too close in time to the scintillation event. The FWHM of a Gaussian fit of the coincidence spectrum is 137.5 ps and therefore the coincidence resolving time of two DSR detectors in coincidence ($CRT_{DSR}$) can be estimated as:

$$CRT_{DSR} = \sqrt{2 \times (CRT_{exp}^2 - CRT_{ref}^2)} \sim 147psFWHM \tag{4.2}$$

where $CRT_{exp}$ is the experimental CRT and $CRT_{ref}$ that of the reference detector (~128 ps FWHM).

A simpler, analytical method which estimates the time of interaction as the average of the first two valid timestamps in the DSR detector was also tested [29]. This resulted in a $CRT_{DSR}$ ~185 ps FWHM using a Gaussian fit. It has to be noted that this value could probably be improved slightly if optimal corrections for the die and tile skews were performed.

Given the large size of the LYSO:Ce crystal (32 mm × 32 mm × 22 mm), the DSR detector can be said to achieve an excellent CRT. It performs significantly better than the BSR detector, which reached a $CRT_{BSR}$ ~215 ps FWHM with the MLITE method and a $CRT_{BSR}$ ~240 ps FWHM with the analytical method. The CRT of the DSR detector is also better than the value of ~160 ps FWHM previously obtained with thinner (10 mm) monolithic crystals based on Ca-codoped LSO:Ce, which in fact is a significantly faster scintillator than standard LYSO:Ce [38, 43]. The improvement in the DSR detector is probably due to the smaller transit time spread of the scintillation photons inside the crystal, which on average undergo a smaller number of reflections before they are detected [44, 45]. Also the increased number of timestamps acquired may contribute to the CRT improvement [46].

### 4.3.6. Effect of missing data on detector performance

To tests the performance of the DSR detector for events with missing data, the analyses described in the previous sections were repeated after artificially deleting the photon counts and timestamps of n randomly selected dies from the test datasets (n = 1, 2, ..., 6). The same test datasets were used in order to maintain even statistics. Random deletion was justified because full neighbor logic was used on the DPC arrays, so missing dies were expected only because of dead time following dark-count triggers, which have similar probabilities for each die. The spatial, time, and energy resolutions were then determined as a function of n.

This information was subsequently used to estimate the spatial, DOI, time, and energy resolutions if all events with up to six missing dies were accepted under the acquisition conditions (AC) and DPC settings used in this work. This estimation was obtained from the pertinent error histograms of the datasets having from zero up to six missing dies (e.g. the 2D PSFs for the spatial resolution) and calculating their weighted sum, using as weights the fractions of events having n missing dies reported in Figure 4.2.

The x,y positioning accuracy as a function of n is reported in Table 4.3, while the results for the DOI resolution are shown in Table 4.4. The deterioration of the spatial resolution is ≤10% in all cases, whereas the DOI resolution worsens by ~20% in the case of 6 missing dies. The estimated performance for the measurement conditions used in this work show that there would be a negligible degradation for the x,y resolution and a degradation <4% for the DOI resolution if events with up to 6 missing dies were accepted.

The results on the energy resolution are presented in Table 4.5 (position-dependent energy correction was applied in all cases). The performance degradation is limited; even in case of 6 missing dies an energy resolution of 11.6% FWHM is obtained, which is still adequate for a clinical scanner. For the acquisition conditions used in this work, energy resolution would deteriorate only by ~3%. In Figure 4.9, the energy spectra for events with 3 and 6 missing dies are plotted, before and after the missing pixels have been estimated and the energy correction has been performed: it can be observed that the estimation of missing pixel values correctly restores the position of the photopeak.

Finally, the effect of missing timestamps on the detector timing performance is reported in Table 4.6. A degradation of about 20% is found for 6 missing dies and of ~4% under real measurement conditions if events with up to six missing dies were accepted. The slightly higher deterioration compared to spatial resolution may be caused by the combination of missing time information and less precise information

Table 4.3: Spatial resolution for perpendicularly incident events as a function of the number of missing dies and for the acquisition conditions used in this work (AC). Since the behavior of the resolution in the y-direction is similar to that in the x-direction, only the second one is reported.

| Resolution (mm) | x | | | | | | | total | | | | | | |
|---|---|---|---|---|---|---|---|---|---|---|---|---|---|---|
| No. missing dies: | 1 | 2 | 3 | 4 | 5 | 6 | AC | 1 | 2 | 3 | 4 | 5 | 6 | AC |
| FWHM | 1.10 | 1.11 | 1.11 | 1.13 | 1.16 | 1.17 | 1.10 | - | - | - | - | - | - | - |
| FWTM | 2.56 | 2.60 | 2.64 | 2.72 | 2.74 | 2.78 | 2.57 | - | - | - | - | - | - | - |
| $r_{50\%}$ | 0.44 | 0.45 | 0.46 | 0.47 | 0.48 | 0.49 | 0.44 | 0.86 | 0.88 | 0.90 | 0.92 | 0.94 | 0.97 | 0.86 |
| $r_{90\%}$ | 2.70 | 2.73 | 2.75 | 2.79 | 2.82 | 2.85 | 2.70 | 4.31 | 4.35 | 4.39 | 4.43 | 4.48 | 4.52 | 4.31 |
| MAE | 1.19 | 1.20 | 1.22 | 1.23 | 1.24 | 1.26 | 1.19 | 1.89 | 1.91 | 1.93 | 1.96 | 1.98 | 2.00 | 1.89 |

Table 4.4: DOI resolution for events with complete light distributions, for events with a given number of missing dies and for the acquisition conditions used in this work (AC).

| Resolution (mm) | No. of missing dies (4 pixels for each die) | | | | | | | |
|---|---|---|---|---|---|---|---|---|
| | None | 1 | 2 | 3 | 4 | 5 | 7 | AC |
| FWHM | 2.42 | 2.52 | 2.60 | 2.68 | 2.77 | 2.87 | 2.95 | 2.50 |
| FWTM | 5.61 | 5.94 | 6.25 | 6.57 | 6.88 | 7.2 | 7.57 | 5.91 |
| MAE | 1.40 | 1.45 | 1.50 | 1.54 | 1.59 | 1.65 | 1.69 | 1.45 |

Table 4.5: Energy resolution as a function of the number of missing dies and for the acquisition conditions used in this work (AC). Results are reported for incomplete light distributions ('Miss. dies') and for incomplete light distributions in which the missing data has been estimated ('Est. dies').

| Energy Resolution | No. of missing dies (4 pixels for each die) | | | | | | | |
|---|---|---|---|---|---|---|---|---|
| (% FWHM) | None | 1 | 2 | 3 | 4 | 5 | 6 | AC |
| Missing dies | 10.2 | 12.4 | 13.2 | 14.2 | 15.3 | 16.5 | 17.7 | - |
| Estimated dies | - | 10.6 | 10.8 | 11.0 | 11.2 | 11.4 | 11.6 | 10.5 |

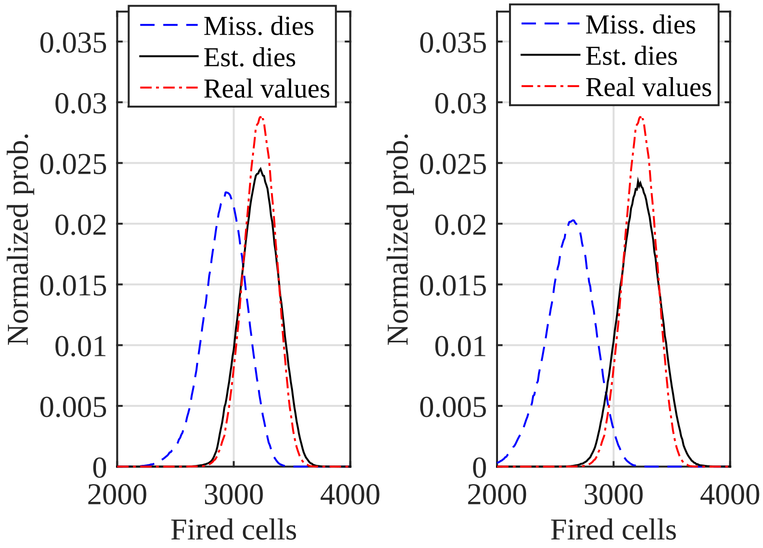

Figure 4.9: The energy distributions for events with the data from 3 and 6 DPC dies missing. The energy distributions are provided with ('Est. Dies') and without ('Miss. Dies') estimated photon counts for the missing pixels and compared with the energy distribution obtained with the real energy values.

Table 4.6: Coincidence resolving time as a function of the number of missing dies and for the acquisition conditions used in this work (AC). Results are reported for the MLITE method ('MLITE') and for the method that uses the average of the first two timestamps ('Av. 2 ts.).

| CRT | No. of missing dies (1 timestamp for each die) | | | | | | | |
|---|---|---|---|---|---|---|---|---|
| | None | 1 | 2 | 3 | 4 | 5 | 6 | AC |
| MLITE | 147 | 156 | 160 | 165 | 170 | 175 | 180 | 153 |
| Av. 2 TS | 185 | 189 | 193 | 198 | 203 | 208 | 215 | 189 |

on the position of interaction, which is also necessary for time estimation.

In summary, the performance degradation for all parameters is within acceptable limits even with 6 dies missing. In a realistic situation the sensitivity of a TOF-PET ring based on DSR detectors could thus be kept at the highest level without compromising the scanner performance.

## 4.4. Conclusions

A monolithic TOF/DOI PET detector based on a 32 mm × 32 mm × 22 mm LYSO:Ce crystal and two DPC arrays in dual-sided readout configuration has been built and fully characterized. Essential detector performance results include a spatial resolution in the x- and y-directions of ~1.1 mm FWHM / ~1.2 mm MAE; a DOI resolution of ~2.4 mm FWHM; an energy resolution of 10.2% FWHM; and a CRT of 147 ps FWHM, when the data from all DPC dies is acquired. These performance parameters were shown to barely degrade under the acquisition conditions used in this work if events having up to 6 missing DPC dies were accepted, which means that no compromise needs to be made between performance and sensitivity in realistic acquisition conditions. Thanks to the short DPC dead time that follows each acquired event, no degradation in the detector performance is expected even for singles count-rates that may be expected in typical clinical PET acquisitions.

A comparison of these results to those obtained with an equally sized LYSO:Ce crystal read out from the back side only (spatial resolution ~1.7 mm FWHM / ~1.6 mm MAE; DOI resolution ~3.7 mm FWHM; energy resolution ~9.9%; CRT ~215 ps FWHM) [28] shows - for the first time - that not only the spatial resolution and the DOI estimation, but also the timing performance is significantly improved when using monolithic scintillator detectors in dual-sided readout configuration. Indeed, the CRT achieved with this 32 mm × 32 mm × 22 mm crystal approaches the best CRT achieved with (non-codoped) 3 mm × 3 mm × 5 mm LYSO:Ce crystals and DPC-3200-22-44 arrays to date, which to our knowledge equals ~135 ps FWHM [47]. This clearly illustrates the excellent correction of the optical and electronic transit time spreads that can be achieved with the MLITE algorithm [29].

It should be noted that the present results were obtained using standard-grade, commercially available LYSO:Ce material. Thus, the timing resolution could be further improved (perhaps towards a CRT of 120-130 ps FWHM) if a faster scintillator material such as LSO:Ce,0.2%Ca were used [38, 43, 46].

In conclusion, the detector presented in this paper offers a unique combination of excellent spatial, DOI, energy, and time resolution, potential MR-compatibility, and high sensitivity. Moreover, the calibration procedures and computational methods used for position and time estimation follow recently made improvements [28] and as such are many times faster and more practical than the ones used previously, making it possible to calibrate the detectors in a few hours. This opens up realistic perspectives for using DSR monolithic scintillator detectors in TOF-PET and TOF-PET/MRI systems.

The excellent performance of the DSR detector appears especially beneficial for clinical scanners with a relatively small diameter, such as dedicated devices for neurological, breast, and pediatric imaging [48]. Nevertheless, recent Monte Carlo system simulations based on the experimentally characterized spatial responses of the BSR and DSR detectors indicate that the DSR detector could significantly improve the performance of whole-body clinical scanners as well, even if the influence of photon acollinearity and statistical limitations are taken into account [49].

## Acknowledgements

This work was part of the EU FP7 project SUBLIMA, Grant Agreement 241711; see also www.sublima-pet-mr.eu

# References

[1] H. F. Wehrl, M. Hossain, K. Lankes, C.-C. Liu, I. Bezrukov, P. Martirosian, F. Schick, G. Reischl, and B. J. Pichler, *Simultaneous pet-mri reveals brain function in activated and resting state on metabolic, hemodynamic and multiple temporal scales,* Nat Med **19**, 1184 (2013).

[2] P. Werner, H. Barthel, A. Drzezga, and O. Sabri, *Current status and future role of brain pet/mri in clinical and research settings,* European Journal of Nuclear Medicine and Molecular Imaging **42**, 512 (2015).

[3] S. Purz, O. Sabri, A. Viehweger, H. Barthel, R. Kluge, I. Sorge, and F. W. Hirsch, *Potential pediatric applications of pet/mr,* Journal of Nuclear Medicine **55**, 32S (2014).

[4] K. Zukotynski, F. Fahey, M. Kocak, L. Kun, J. Boyett, M. Fouladi, S. Vajapeyam, T. Treves, and T. Y. Poussaint, *18f-fdg pet and mr imaging associations across a spectrum of pediatric brain tumors: A report from the pediatric brain tumor consortium,* Journal of Nuclear Medicine (2014), 10.2967/jnumed.114.139626.

[5] F. Fraioli and S. Punwani, *Clinical and research applications of simultaneous positron emission tomography and mri,* The British Journal of Radiology **87**, 20130464 (2014).

[6] H. Jadvar and P. M. Colletti, *Competitive advantage of pet/mri,* European Journal of Radiology **83**, 84 (2014).

[7] C. B. Hruska and M. K. O'Connor, *Nuclear imaging of the breast: Translating achievements in instrumentation into clinical use,* Medical Physics **40**, 050901 (2013), https://aapm.onlinelibrary.wiley.com/doi/pdf/10.1118/1.4802733 .

[8] S. Vandenberghe and P. K. Marsden, *Pet-mri: a review of challenges and solutions in the development of integrated multimodality imaging,* Physics in Medicine and Biology **60**, R115 (2015).

[9] G. Delso, S. Fürst, B. Jakoby, R. Ladebeck, C. Ganter, S. G. Nekolla, M. Schwaiger, and S. I. Ziegler, *Performance measurements of the siemens mmr integrated whole-body pet/mr scanner,* Journal of Nuclear Medicine **52**, 1914 (2011).

[10] A. Drzezga, M. Souvatzoglou, M. Eiber, A. J. Beer, S. Fürst, A. Martinez-Möller, S. G. Nekolla, S. Ziegler, C. Ganter, E. J. Rummeny, and M. Schwaiger, *First clinical experience with integrated whole-body pet/mr: Comparison to pet/ct in patients with oncologic diagnoses,* Journal of Nuclear Medicine **53**, 845 (2012).

[11] H. H. Quick, C. von Gall, M. Zeilinger, M. Wiesmüller, H. Braun, S. Ziegler, T. Kuwert, M. Uder, A. Dörfler, W. A. Kalender, and M. Lell, *Integrated whole-body pet/mr hybrid imaging: Clinical experience,* Investigative Radiology **48**, 280 (2013).

[12] G. Delso, M. Khalighi, M. Hofbauer, M. Porto, P. Veit-Haibach, and G. von Schulthess, *Preliminary evaluation of image quality in a new clinical tof-pet/mr scanner,* EJNMMI Physics **1**, A41 (2014).

[13] S. Surti, A. R. Shore, and J. S. Karp, *Design study of a whole-body pet scanner with improved spatial and timing resolution,* Nuclear Science, IEEE Transactions on **60**, 3220 (2013).

[14] H. Thoen, V. Keereman, P. Mollet, R. V. Holen, and S. Vandenberghe, *Influence of detector pixel size, tof resolution and doi on image quality in mr-compatible whole-body pet,* Physics in Medicine and Biology **58**, 6459 (2013).

[15] H. W. A. M. de Jong, F. H. P. van Velden, R. W. Kloet, F. L. Buijs, R. Boellaard, and A. A. Lammertsma, *Performance evaluation of the ecat hrrt: an lso-lyso double layer high resolution, high sensitivity scanner,* Physics in Medicine and Biology **52**, 1505 (2007).

[16] M. Miller, J. Zhang, K. Binzel, J. Griesmer, T. Laurence, M. Narayanan, D. Natarajamani, S. Wang, and M. Knopp, *Characterization of the vereos digital photon counting pet system,* Journal of Nuclear Medicine **56**, 434 (2015).

[17] W. W. Moses, *Fundamental limits of spatial resolution in pet,* Nuclear Instruments and Methods in Physics Research Section A: Accelerators, Spectrometers, Detectors and Associated Equipment **648, Supplement 1**, S236 (2011).

[18] L. Eriksson and M. Conti, *Randoms and tof gain revisited,* Physics in Medicine and Biology **60**, 1613 (2015).

[19] M. Defrise, A. Rezaei, and J. Nuyts, *Time-of-flight pet data determine the attenuation sinogram up to a constant,* Physics in Medicine and Biology **57**, 885 (2012).

[20] J. Cabello, P. Barrillon, J. Barrio, M. G. Bisogni, A. Del Guerra, C. Lacasta, M. Rafecas, H. Saikouk, C. Solaz, P. Solevi, C. de La Taille, and G. Llosá, *High resolution detectors based on continuous crystals and sipms for small animal pet,* Nuclear Instruments and Methods in Physics Research Section A: Accelerators, Spectrometers, Detectors and Associated Equipment **718**, 148 (2013).

[21] S. Seifert, G. v. d. Lei, H. T. v. Dam, and D. R. Schaart, *First characterization of a digital sipm based time-of-flight pet detector with 1 mm spatial resolution,* Physics in Medicine and Biology **58**, 3061 (2013).

[22] G. Borghi, V. Tabacchini, S. Seifert, and D. R. Schaart, *Experimental validation of an efficient fan-beam calibration procedure for k-nearest neighbor position estimation in monolithic scintillator detectors,* Nuclear Science, IEEE Transactions on **62**, 57 (2015).

[23] T. Ling, T. K. Lewellen, and R. S. Miyaoka, *Depth of interaction decoding of a continuous crystal detector module,* Physics in Medicine and Biology **52**, 2213 (2007).

[24] T. Ling, T. H. Burnett, T. K. Lewellen, and R. S. Miyaoka, *Parametric positioning of a continuous crystal pet detector with depth of interaction decoding,* Physics in Medicine and Biology **53**, 1843 (2008).

[25] W. C. J. Hunter, H. H. Barrett, and L. R. Furenlid, *Calibration method for ml estimation of 3d interaction position in a thick gamma-ray detector,* Nuclear Science, IEEE Transactions on **56**, 189 (2009).

[26] Z. Li, M. Wedrowski, P. Bruyndonckx, and G. Vandersteen, *Nonlinear least-squares modeling of 3d interaction position in a monolithic scintillator block,* Physics in Medicine and Biology **55**, 6515 (2010).

[27] H. T. van Dam, S. Seifert, R. Vinke, P. Dendooven, H. Löhner, F. J. Beekman, and D. R. Schaart, *A practical method for depth of interaction determination in monolithic scintillator pet detectors,* Physics in Medicine and Biology **56**, 4135 (2011).

[28] G. Borghi, V. Tabacchini, and D. R. Schaart, *Towards monolithic scintillator based tof-pet systems: practical methods for detector calibration and operation,* Physics in Medicine and Biology **61**, 4904 (2016).

[29] H. T. van Dam, G. Borghi, S. Seifert, and D. R. Schaart, *Sub-200 ps crt in monolithic scintillator pet detectors using digital sipm arrays and maximum likelihood interaction time estimation,* Physics in Medicine and Biology **58**, 3243 (2013).

[30] R. S. Miyaoka, L. Tao, C. Lockhart, X. Li, and T. K. Lewellen, *Calibration procedure for a continuous miniature crystal element (cmice) detector,* Nuclear Science, IEEE Transactions on **57**, 1023 (2010).

[31] X. Li, W. C. J. Hunter, T. K. Lewellen, and R. S. Miyaoka, *Use of cramer–rao lower bound for performance evaluation of different monolithic crystal pet detector designs,* IEEE Transactions on Nuclear Science **59**, 3 (2012).

[32] M. C. Maas, D. R. Schaart, D. J. v. d. Laan, P. Bruyndonckx, C. Lemaître, F. J. Beekman, and C. W. E. v. Eijk, *Monolithic scintillator pet detectors with intrinsic depth-of-interaction correction,* Physics in Medicine and Biology **54**, 1893 (2009).

[33] T. Frach, G. Prescher, C. Degenhardt, R. de Gruyter, A. Schmitz, and R. Ballizany, *The digital silicon photomultiplier - principle of operation and intrinsic detector performance,* in *Nuclear Science Symposium Conference Record (NSS/MIC), 2009 IEEE* (2009) pp. 1959–1965.

[34] T. Frach, G. Prescher, C. Degenhardt, and B. Zwaans, *The digital silicon photomultiplier - system architecture and performance evaluation,* in *Nuclear Science Symposium Conference Record (NSS/MIC), 2010 IEEE* (2010) pp. 1722–1727.

[35] R. Schulze, *PDPC TEK Manual*, Koninklijke Philips Electronics 2014 (2014).

[36] V. Tabacchini, V. Westerwoudt, G. Borghi, S. Seifert, and D. R. Schaart, *Probabilities of triggering and validation in a digital silicon photomultiplier,* Journal of Instrumentation **9**, P06016 (2014).

[37] D. R. Schaart, E. Charbon, T. Frach, and V. Schulz, *Advances in digital sipms and their application in biomedical imaging,* Nuclear Instruments and Methods in Physics Research Section A: Accelerators, Spectrometers, Detectors and Associated Equipment **809**, 31 (2016).

[38] M. A. Spurrier, P. Szupryczynski, Y. Kan, A. A. Carey, and C. L. Melcher, *Effects of ca2+ co-doping on the scintillation properties of lso:ce,* Nuclear Science, IEEE Transactions on **55**, 1178 (2008).

[39] M. C. Maas, D. Van der Laan, D. R. Schaart, J. Huizenga, J. C. Brouwer, P. Bruyndonckx, S. Leonard, C. Lemaitre, and C. W. E. Van Eijk, *Experimental characterization of monolithic-crystal small animal pet detectors read out by apd arrays,* Nuclear Science, IEEE Transactions on **53**, 1071 (2006).

[40] H. T. van Dam, S. Seifert, R. Vinke, P. Dendooven, H. Löhner, F. J. Beekman, and D. R. Schaart, *Improved nearest neighbor methods for gamma photon interaction position determination in monolithic scintillator pet detectors,* Nuclear Science, IEEE Transactions on **58**, 2139 (2011).

[41] S. Jan, G. Santin, D. Strul, S. Staelens, K. Assié, D. Autret, S. Avner, R. Barbier, M. Bardiès, P. M. Bloomfield, D. Brasse, V. Breton, P. Bruyndonckx, I. Buvat, A. F. Chatziioannou, Y. Choi, Y. H. Chung, C. Comtat, D. Donnarieix, L. Ferrer, S. J. Glick, C. J. Groiselle, D. Guez, P.-F. Honore, S. Kerhoas-Cavata, A. S. Kirov, V. Kohli, M. Koole, M. Krieguer, D. J. v. d. Laan, F. Lamare, G. Largeron, C. Lartizien, D. Lazaro, M. C. Maas, L. Maigne, F. Mayet, F. Melot, C. Merheb, E. Pennacchio, J. Perez, U. Pietrzyk, F. R. Rannou, M. Rey, D. R. Schaart, C. R. Schmidtlein, L. Simon, T. Y. Song, J.-M. Vieira, D. Visvikis, R. V. d. Walle, E. Wieërs, and C. Morel, *Gate: a simulation toolkit for pet and spect,* Physics in Medicine and Biology **49**, 4543 (2004).

[42] S. Seifert, H. T. v. Dam, J. Huizenga, R. Vinke, P. Dendooven, H. Löhner, and D. R. Schaart, *Monolithic labr 3 :ce crystals on silicon photomultiplier arrays for time-of-flight positron emission tomography,* Physics in Medicine and Biology **57**, 2219 (2012).

[43] D. N. ter Weele, D. R. Schaart, and P. Dorenbos, *Comparative study of co-doped and non co-doped lso:ce and lyso:ce scintillators for tof-pet,* Nuclear Science, IEEE Transactions on **62**, 727 (2015).

[44] D. N. ter Weele, D. R. Schaart, and P. Dorenbos, *Picosecond time resolved studies of photon transport inside scintillators,* Nuclear Science, IEEE Transactions on **62**, 1961 (2015).

[45] D. N. ter Weele, D. R. Schaart, and P. Dorenbos, *Scintillation detector timing resolution; a study by ray tracing software,* Nuclear Science, IEEE Transactions on **62**, 1972 (2015).

[46] S. Seifert, H. T. v. Dam, and D. R. Schaart, *The lower bound on the timing resolution of scintillation detectors,* Physics in Medicine and Biology **57**, 1797 (2012).

[47] J. Y. Yeom, R. Vinke, and C. S. Levin, *Side readout of long scintillation crystal elements with digital sipm for tof-doi pet,* Medical Physics **41**, 122501 (2014).

[48] E. Mikhaylova, V. Tabacchini, G. Borghi, P. Mollet, E. D'Hoe, D. R. Schaart, and S. Vandenberghe, *Optimization of an ultralow-dose high-resolution pediatric pet scanner based on monolithic scintillators with dual-sided digital sipm readout: A simulation study,* in preparation (2016).

[49] V. Tabacchini, S. Surti, G. Borghi, B. J. Peet, J. S. Karp, and D. R. Schaart, *Improved image quality using monolithic scintillator detectors with dual-sided readout in a whole-body tof-pet ring: a simulation study,* in preparation (2016).

# 5

# Sub-3 mm, near-200 ps TOF/DOI-PET imaging with monolithic scintillator detectors in a 70 cm diameter tomographic setup

This chapter has been published as:
G. Borghi, V. Tabacchini, R. Bakker, and D. R. Schaart, "Sub-3 mm, near-200 ps TOF/DOI-PET imaging with monolithic scintillator detectors in a 70 cm diameter tomographic setup," Phys. Med. Biol., vol. 63, no. 15, p. 155006, Jul. 2018.
DOI: 10.1088/1361-6560/aad2a6

***Abstract*** - *Recently, a monolithic scintillator detector for time-of-flight (TOF) / depth-of-interaction (DOI) positron emission tomography (PET) was developed. It has a detector spatial resolution of ~ 1.7 mm full-width-at-half-maximum (FWHM), a coincidence resolving time (CRT) of ~215 ps FWHM, and ~4.7 mm FWHM DOI resolution. Here, we demonstrate, for the first time, the imaging performance of this detector in a 70 cm diameter PET geometry. We built a tomographic setup representative of a whole-body clinical scanner, comprising two coaxially rotating arms, each carrying a detector module, and a central, rotating phantom table. The fully automated setup sequentially acquires all possible lines of response (LORs) of a complete detector ring, using a step-and-shoot acquisition approach. The modules contained 2 × 2 detectors, each detector consisting of a 32 mm × 32 mm × 22 mm LYSO crystal*

*and a digital silicon photomultiplier (dSiPM) array. The system spatial resolution was assessed using a* $^{22}$*Na point source at different radial distances in the field-of-view (FOV). Using 2D filtered back projection (2D FBP, non-TOF), tangential and radial spatial resolutions of ~2.9 mm FWHM were obtained at the center of the FOV. The use of DOI information resulted in almost uniform spatial resolution throughout the FOV up to a radial distance of 25 cm, where the radial and tangential resolution are ~3.3 mm FWHM and ~4.7 mm FWHM, respectively, whereas without DOI the resolution deteriorates to ~9 mm FWHM. Additional measurements were performed with a* $^{22}$*Na filled Derenzo-like phantom at different locations within the FOV. Images reconstructed with a TOF maximum-likelihood expectation-maximization (TOF ML-EM) algorithm show that the system is able to clearly resolve 3 mm diameter hot rods up to 25 cm radial distance. The excellent and uniform spatial resolution, combined with an energy resolution of 10.2% FWHM and a CRT of ~212 ps FWHM, indicates a great potential for monolithic scintillators as practical high-performance detectors in TOF/DOI-PET systems.*

## 5.1. Introduction

Positron emission tomography (PET) is a well-established in vivo molecular imaging technique, both in research and in clinical practice. PET plays a key role in an increasing number of applications in different fields, such as oncology, neurology, functional studies, and drug development. Depending on the radio-tracer chosen, PET can provide a variety of functional and metabolic information. In modern PET scanners, these data are usually combined with the anatomical information obtained with an integrated computed tomography (CT) or magnetic resonance imaging (MRI) system.

Much research in PET instrumentation focuses on the development of high-performance detector technology. The main challenge in the context of clinical PET is to obtain a precise estimation of the gamma-ray position of interaction, combined with high sensitivity, an excellent coincidence resolving time (CRT), and good energy resolution. An important innovation that could be introduced in clinical scanners is the capability of estimating the depth of interaction (DOI) of gamma rays inside the detectors, without compromising on other performance parameters. This additional information would allow scanners to achieve a higher and more homogeneous spatial resolution throughout the field of view (FOV) [1, 2]. At present, benefits of DOI estimation have been experimentally demonstrated only in preclinical PET scanners or demonstrators [3, 4], whereas there are no results available for PET scanners or demonstrators having ring dimensions compatible with clinical applications.

Current clinical whole-body scanners are usually built with detectors based on segmented scintillator-crystal matrices whose pixels typically have edge dimensions of 4-5 mm and a thickness of 20-30 mm. These crystal arrays are read out using either light sharing techniques or one-to-one coupling, by means of arrays of photomultiplier tubes (PMTs), position sensitive PMTs (PS-PMTs), or arrays of silicon photomultipliers (SiPMs). In state-of-the-art clinical scanners these detectors typically achieve a CRT of 300-350 ps full-width-at-half-maximum (FWHM) and an energy resolution of about 10.5%-11% FWHM, but none of them provides DOI estimation [5].

Prototype pixelated scintillation detectors with improved performance compared to the clinical state-of-the-art have been presented in literature. These detectors are typically based on smaller crystals (~2 mm pixels) [6–8], while numerous designs have been proposed to obtain DOI estimation. For instance, 3D crystal arrays [9], stacked matrices made of different materials with different decay times (phoswich) [10, 11], phosphor-coated crystals with pulse-shape classification [12], light sharing techniques that encode the DOI in the width of the registered light distribution [7], and crystals with double-sided-readout (DSR) [13, 14]. Often, such improvements come at the expense of other key performance parameters, such as time resolution and energy resolution, and/or result in increased cost and complexity.

An interesting alternative to pixelated detectors is represented by monolithic scintillator detectors, in which a continuous scintillator (typically a cuboidal crystal) is coupled to an array of photosensors. Monolithic scintillator detectors have shown an excellent combination of spatial resolution, coincidence resolving time, and detection efficiency [15–17]. For example, our group has recently presented a detector based on a 32 mm × 32 mm × 22 mm LYSO:Ce crystal and a digital photon counter (DPC) array which achieved a x-y spatial resolution ~1.7 mm FWHM / ~ 1.6 mm mean absolute error (MAE), a DOI resolution ~3.7 mm FWHM / ~2.2 mm MAE, and a CRT of ~215 ps FWHM [18]. Also, new methods have been proposed to increase the efficiency of the calibration procedures and of the time and position estimation algorithms [19], which had previously been considered a limitation for the practical application of this technology.

Thus, monolithic detectors are becoming a serious option for clinical TOF/DOI-PET scanners. Nevertheless, monolithic and pixelated scintillator detectors have inherently different responses and it is not possible to simply compare e.g. the FWHM spatial resolution of a monolithic detector with the crystal pitch of a pixelated detector [2]. Hence, realistic tomographic image acquisition measurements are warranted to assess the performance of monolithic scintillator detectors at the full-scanner level.

In this work we aim to experimentally predict the imaging performance of a 70 cm diameter whole-body TOF/DOI-PET scanner based on monolithic scintillator crystals coupled to DPC arrays using a new tomographic setup, which has been developed to perform full PET acquisitions using only two detector modules. The setup comprises two rotating arms, each one carrying a detector module, as well as a central rotating phantom table. The setup can be used to sequentially acquire all possible combinations of detector modules of a complete PET ring, using a step-and-shoot acquisition procedure. A detailed description of the detector modules and of the experimental setup is presented in section 5.2, while the time, energy, and spatial resolution obtained in the tomographic experiments are reported in section 5.3.

## 5.2. Methods

### 5.2.1. Module design and sensor settings

The two PET modules used in this work are based on DPC3200-22-44-M22 sensor modules produced by Philips Digital Photon Counting (PDPC) (Figure 5.1). Each module hosts 2 × 2 digital silicon photomultiplier (dSiPM) arrays (model DPC3200-22-44) at a distance of ~0.5 mm one from each other and dedicated readout electronics. The DPC arrays measure 32.6 mm × 32.6 mm and are composed of 4 × 4 independent sensors (dies) at a pitch of 8 mm. Each die is subdivided into four pixels and is equipped with an on-silicon integrated TDC system. When a die acquires a light signal, it registers the intensity of the light on each pixel, i.e. the exact number of fired single photon avalanche photodiodes (SPADs), and a single timestamp. Therefore, DPC arrays can provide an 8 × 8 pixel light distribution and 16 timestamps when read out fully. More detailed descriptions of the DPC array working principle can be found in Frach *et al.* [20], Frach *et al.* [21], Schaart *et al.* [22], and Schulze [23]. The modules were controlled and read out by a field-programmable gate array (FPGA) based electronic board and a computer software provided by PDPC.

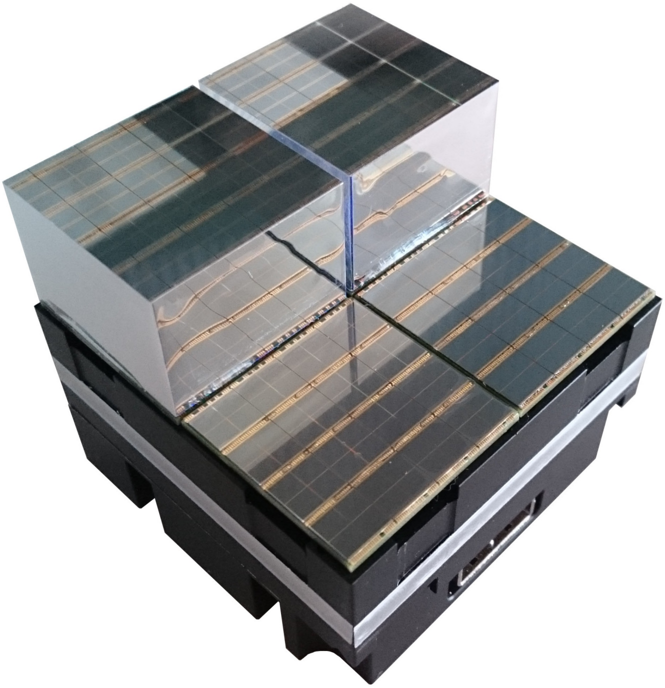

Figure 5.1: Photograph of a DPC3200-22-44-M22 detector module partly assembled using 32 mm × 32 mm × 22 mm LYSO:Ce crystals.

Eight monolithic scintillator detectors based on 32 mm × 32 mm × 22 mm LYSO:Ce crystals (Crystal Photonics, Sanford, USA) and DPC3200-22-44 arrays were assembled to fully populate the modules. The lateral faces of the crystals were covered with a specular reflector foil (Vikuiti ESR, 3M), while the top faces were covered with Teflon tape. The crystals were permanently glued to the photosensors using UV-curing glue (DELO Photobond 4436).

The sensor settings [24] were optimized to maximize the timing performance and the sensitivity for monolithic scintillator detectors operated at reduced temperatures (-20/-15 °C). On all sensors, the noisiest 10% of the SPADs were disabled. The trigger threshold was set at the first photon interacting on a die (DPC notation: $\mathrm{MT}_{=1}$), the validation interval was set to 40 ns, the validation threshold setting required at least one photon per pixel to validate an event on a die (DPC notation: 0x:7F:AND) and the integration interval equaled 165 ns. Considering also the readout and reset time (680 ns), DPC sensors have a total dead time per acquired event <1 $\mu$s. However, the bandwidth of current DPC sensor tile is artificially limited by the event storage memory available on the tile FPGA: the present sensor tile can handle a maximum of about 120 kcps per chip, i.e. each monolithic crystal detector used in this work has a maximum theoretical count rate of ~120 kcps. The neighbor logic was activated so that all dies on a sensor were acquired every time that one of the dies registered a validated event.

A hardware gating signal was defined between the modules using the FPGA electronic board to register only the events occurring within a coincidence window of ~100 ns. This broad coincidence pre-selection requirement was imposed with the sole purpose of reducing the single-event rate registered on the sensors and to minimize the amount of data to be transferred to the data acquisition computer through a USB 2.0 connection [24]. A more accurate coincidence selection was performed during the offline analysis (see section 5.2.3).

### 5.2.2. Time and position estimators for monolithic scintillator detectors

Monolithic scintillator detectors require individual calibration and optimized estimation algorithms to achieve their best spatial and timing performance. In Borghi *et al.* [19] and in Borghi *et al.* [18], new calibration methods were presented that made it possible to fully characterize the response of a detector in few hours using fan-beam and flood irradiations. In the same papers, several modifications to the statistical estimators for the position-, energy-, and time-of-interaction were introduced to accelerate these estimators and make them practically applicable. The same methods and estimators were used in the present work to calibrate the detectors on the PET modules and to process the acquired data.

In particular, for x,y position estimation an accelerated version of the k-nearest neighbor (k-NN) method was used, which requires the acquisition of a reference dataset for each single detector using a fan-beam irradiation. The same datasets were used to calculate the look-up tables (LUTs) needed to correct for the position-dependent energy response of the detectors and to estimate the DOI. The spatial sampling used to estimate the position of interaction inside the crystal was 0.25

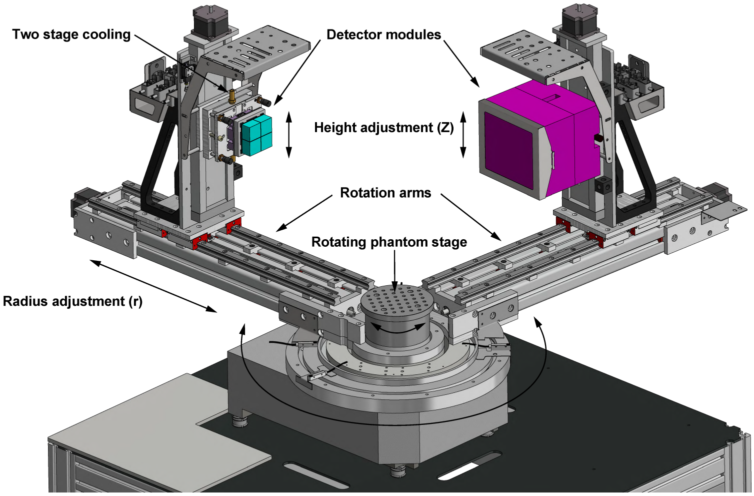

Figure 5.2: Technical drawing (isometric projection) of the tomographic setup.

mm × 0.25 mm × 1 mm in the x, y and DOI direction, respectively.

A separate calibration dataset, acquired by means of a simple flood irradiation, was used to calibrate the maximum likelihood interaction estimation method (MLITE), the statistical method used to estimate the time of interaction [17].

A short description of the calibration procedures and estimators is given in appendix, section 5.5. In particular, the small adaptations that were necessary to adjust the methods to the measurement conditions used in this work are highlighted there. For a complete description of the methods, the reader is referred to the papers cited.

### 5.2.3. Tomographic setup

A new setup was designed and built to perform complete tomographic acquisitions using only two detector modules (Figure 5.2). This setup is constructed such that PET scans with different axial extents and with the modules at different radial positions can be acquired. The setup achieves a module positioning accuracy ≤0.2-0.3 mm even at the largest radii, thus preventing image artifacts or degradations in the imaging performance that might otherwise occur from inaccurate mechanical precision.

The setup is based on a precision goniometer originally developed for an x-ray diffractometer (Bruker) with two coaxially rotating stages capable of a full rotation. The rotational accuracy is $<0.01^\circ$ and each rotating stage is equipped with a mechanical arm. On each arm, two perpendicular, custom-made linear stages driven by stepper motors are used to support and move a PET module, such that its radial position r and height z can be adjusted. The range of the r and z linear stages are 450 mm and 250 mm, respectively. The positioning accuracy of both stages is <0.05 mm. At the center of the goniometer, an additional rotating stage (accuracy

∼0.05°) is mounted, so that the central platform onto which the sources are placed can be rotated. All stages make use of closed-loop control. A dedicated control unit based on a CNC protocol was developed that interfaces with a PC, allowing the experimenter to easily control the setup (Berkelaar MRT, Delft).

Precise alignment of the modules was obtained by means of fine-adjustment mechanisms that allow correction of the unavoidable small inaccuracies that occur when large machineries are assembled. Alignment was performed using a 3D measuring arm (Romer Absolute Arm, 6 axis) that could determine the spatial position of the various components with a precision of <0.02 mm. The detector modules are mounted using a high-precision docking system that defines their position accurately even if they are removed and re-mounted.

The setup also includes a two-stage cooling system designed to control the temperature of the DPC sensors and to dissipate the heat produced by the detectors during operation. The first cooling stage is a liquid cooling machine (Integral XT 150, LAUDA) used to stabilize the temperature of a cooling plate at the back of each module at ∼15 °C. The second cooling stage consists of high-power Peltier elements mounted in between the cooling plates and the modules, which can cool the modules down to about -20 °C. The modules and Peltier elements are enclosed by insulating foam boxes purged with dry nitrogen to avoid condensation of moisture.

Complete tomographic acquisition are performed acquiring all module pair positions (or views) that are measured in a full 3D PET ring, i.e. all module pair positions that define LORs that intersect the FOV. For a given module pair position, possible LORs include all lines connecting all the points on the surface of the detectors of one module with all the points on the surface of the detectors of the other module. A given view can be obtained by moving either the arms, the central plate, or both. For each view a measurement of the same time duration has to be registered. A LabVIEW program was developed to perform such acquisition sequences in a completely automated way. No angular constraints are applied on the possible LORs, so tomographic measurements are performed in full 3D PET mode. Coincidences are saved in list mode.

For the tomographic acquisitions performed in this work, the inner diameter (module-to-module maximum distance) of the system was set to 70 cm, thus representing a whole-body clinical scanner made of 32 modules. The FOV has a diameter of 50 cm and an axial extent of 6.5 cm, corresponding to the size of a single detector module. A representation of the PET ring emulated with the tomographic setup is shown in Figure 5.3.

Coincidence events were selected offline, using a 4 ns wide software coincidence window and an energy window corresponding with the full-width-at-ten-maximum (FWTM) of the uncorrected 511 keV photopeaks of the different detectors, which on average corresponds to a ∼100 keV wide energy window (see appendix, section 5.5.1).

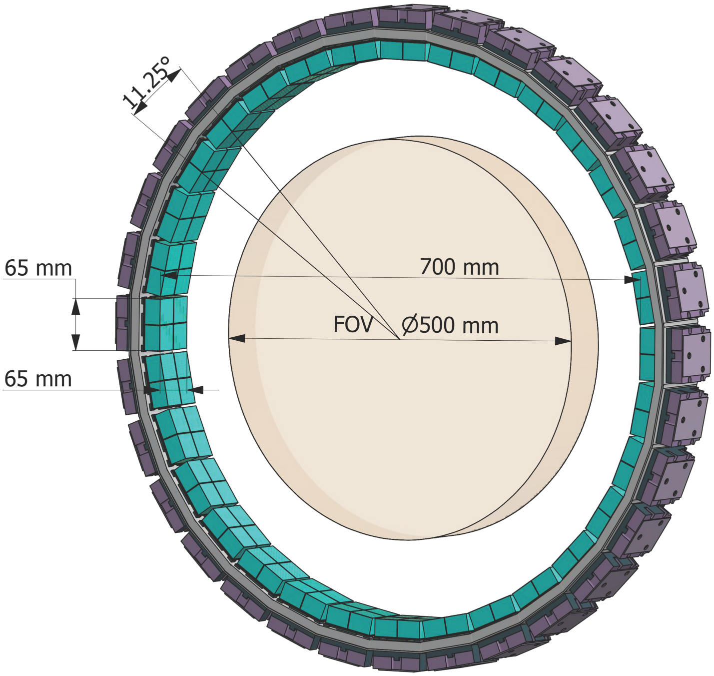

Figure 5.3: Representation of the PET ring emulated with the tomographic setup. The scanner is composed of a single ring of 32 modules. Each module has an active area of ~65 mm × 65 mm. The inner diameter of the scanner is 70 cm (module-to-module distance), while the angular distance between modules is 11.25°. The FOV has a diameter of 50 cm and an axial extent of 6.5 cm.

### 5.2.4. System characterization

#### 5.2.4.1. Energy resolution and coincidence resolving time

The energy resolution and CRT of the tomographic setup were determined from a complete tomographic acquisition of a $^{22}$Na point source (∼3 MBq) placed at the center of the FOV. The energy resolution was calculated by creating, for each of the 8 detectors, a calibrated spectrum corrected for the position-dependent detector response (see appendix, 5.5.3) and summing the obtained spectra. Detector calibration was performed as a simple linear calibration using only the 511 keV photopeak as a calibration point. The single-detector and overall energy resolutions were determined with Gaussian fits.

A system TOF-difference spectrum was obtained by calculating the differences between the detector timestamps for all coincidences acquired during the measurement. Detector timestamps were corrected for die and tile electronic skews, which were determined as described in appendix, 5.5.4. No further correction to align the spectra obtained at the different combinations of module positions was performed. The system CRT was determined with a Gaussian fit of the spectrum.

#### 5.2.4.2. Spatial resolution measurements with point sources

Complete tomographic acquisitions of a single $^{22}$Na point source (⌀ 0.5 mm, ∼3 MBq) were performed at different positions along the x-axis of the scanner, from the center of the FOV up to a radial offset of 25 cm, at a pitch of 5 cm. A scan time of ∼3 minutes per module position was used at each radial offset, which resulted in a total number of 4.5 to 5.5 million coincidences per scan, depending on the source position.

The images were reconstructed projecting all the LORs on a single plane and using 2D filtered back projection without considering TOF information (2D FBP, non-TOF), with pixel dimensions of 0.5 mm × 0.5 mm, with no smoothing or apodization. The LORs were rebinned with an angular sampling of 0.5° and a radial sampling of 0.25 mm. The radial and tangential resolutions were defined as the FWHM of a line profile across the reconstructed point sources in the two directions, respectively. The FWHMs were calculated using spline interpolation of the 1D line profiles through the point sources. In order to investigate the accuracy and the impact of DOI estimation, images were reconstructed both with and without DOI information incorporated in the reconstruction. In case no DOI estimation was used, the center of the crystal was used as a fixed value for the DOI.

#### 5.2.4.3. Spatial resolution measurements with Derenzo-like phantom

A custom, Derenzo-like resolution phantom was built using PMMA (polymethyl methacrylate) plastic to qualitatively assess the spatial resolution and the imaging performance of the PET scanner (Figure 5.4). The hot-rod insert of the phantom has a diameter of 10 cm, a height of 7 cm and is subdivided into six sectors, with rod diameters of 2.5 mm, 3.0 mm, 3.5 mm, 4.0 mm, 5.0 mm, and 7.0 mm. The distance between the centers of adjacent rods within each sector always equals twice the rod diameter. A total activity of ∼20 MBq of $^{22}$Na was used to prepare the homogeneous aqueous solution with which the phantom was filled. Considering the

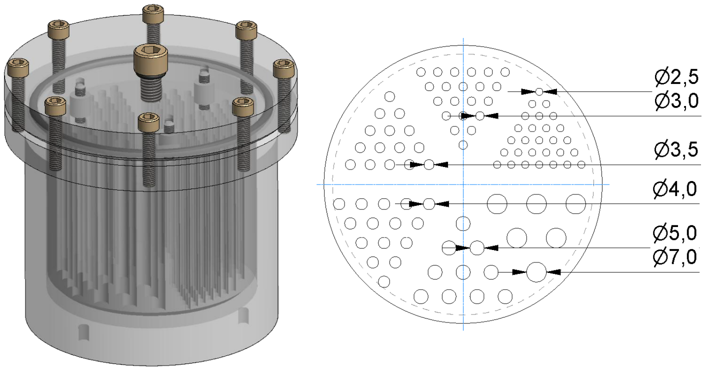

Figure 5.4: Technical drawings of the Derenzo-like resolution phantom: isometric projection of the entire phantom (left) and top-view of the of the hot-rod insert (right).

total volume of solution, which is partly outside the hot rods, the estimated activity concentration was ~150-200 kBq/cm$^3$.

The phantom was scanned at three radial distances from the center of the FOV, viz. 0 cm, 15 cm and 20 cm. At each radial distance, the scan time at each module position equaled ~40 min, which resulted in a total number of ~50 million coincidence events for each complete tomographic scan.

Image reconstruction was performed using a list-mode 3D TOF maximum-likelihood expectation-maximization (TOF ML-EM) algorithm [25] with a voxel size of 1 mm × 1 mm × 1 mm. Siddon ray tracing was used to calculate the elements of the system matrix [26]. No resolution modelling was used for image reconstruction. Normalization, scatter and random correction were not applied, since normalization and random correction are not expected to have an influence on spatial resolution, whereas scatter correction has only a minor effect on the tails of the measured activity distribution. Attenuation correction was applied using an analytical model of the phantom, of which the geometry, composition and position inside the scanner are accurately known. Attenuation correction was part of the image reconstruction, no prior correction was performed on the measured data. A sensitivity map (in the image space) was calculated by backprojecting LORs on the image matrix. In order to calculate the sensitivity map in the image space, a number of 10000 LORs were randomly sampled for each monolithic detector pair and backprojected on the image matrix, i.e. the end-points of each LOR were randomly sampled in the (continuous) volume of each crystal. All images were obtained with 10 EM iterations, since additional iterations did not provide any significant visual improvement. As only the transaxial resolution is of interest for this measurement, the 50 central image slices were averaged in order to increase count statistics.

All images were reconstructed twice, once using the estimated DOI and once using the center of the crystal as a fixed DOI value.

Table 5.1: Single-detector and scanner energy resolution with position-dependent energy response correction.

| Module | M1 | M1 | M1 | M1 | M2 | M2 | M2 | M2 | Total |
|---|---|---|---|---|---|---|---|---|---|
| Detector | D1 | D2 | D3 | D4 | D1 | D2 | D3 | D4 | |
| Energy res. (% FWHM) | 11.1 | 10.2 | 10.1 | 10.1 | 10.6 | 10.3 | 10.3 | 10.1 | 10.2 |

# 5.3. Results and discussion

## 5.3.1. Energy resolution and coincidence resolving time

The energy resolutions of the single detectors are reported in Table 5.1. All of them lie between 10.6% FWHM and 10.1% FWHM, except for the resolution of detector 1 on module 1, which is slightly worse. An overall system resolution of 10.2% FWHM is found, which is competitive with state-of-the-art detectors used in commercial scanners based on pixelated scintillators.

For comparison, the recent GE Healthcare Signa TOF-PET/MRI scanner, which is based on analog SiPMs, has an energy resolution of 10.3% [27]. For the Philips Vereos TOF-PET/CT scanner, which is based on arrays of 4 mm × 4 mm LYSO:Ce crystals coupled to the same DPC sensors as used in this work, an energy resolution of 11.1% FWHM has been reported [28]. Similar values have been reported for other prototype detectors and scanners based on pixelated crystals coupled to DPC sensors [6, 29, 30] or PMTs [8], which achieved energy resolutions between 10.7% FWHM and 11.4% FWHM. The slightly improved energy resolution of monolithic scintillator detectors compared to pixelated detector, when the same type of photosensor is used, can be explained by the more efficient light collection process due to the favorable aspect ratio of monolithic crystals.

In previous work on a prototype monolithic detector (similar to the ones used in this work) we reported an even better value for the energy resolution, viz. less than 10% FWHM [18]. The difference can probably be explained by the higher percentage of DPC cells disabled in the present work (10% instead of 5%) and by the slightly larger sensor temperature fluctuations observed during operation (∼1 °C instead of 0.1-0.2 °C).

A system CRT of ∼212 ps FWHM was obtained using the MLITE method discussed in section 5.2.2. Figure 5.5 shows the corresponding time difference histogram. This result is consistent with the CRT values that were measured independently with 8 different couples of monolithic crystals (see appendix, section 5.5.4), which were all between 210 ps FWHM and 220 ps FWHM.

For comparison, CRTs of ∼315 ps FWHM and of 385 ps FWHM have been reported recently for the Vereos TOF-PET/CT scanner [28] and for the Signa TOF-PET/MRI scanner (GE) [27], respectively. For research scanners, a CRT of ∼266 ps FWHM was measured by Degenhardt *et al.* [29] on a prototype PET scanner based on DPC sensors and one-to-one coupled 4 mm × 4 mm × 22 mm LYSO:Ce crystals. In Schug *et al.* [30], a CRT of ∼ 213 ps FWHM was reported for a prototype small-diameter scanner based on DPC sensors and 4 mm × 4 mm crystals with a thickness of only 10 mm. This comparison indicates that monolithic scintillator detectors can achieve better timing performance than segmented crystals of equal

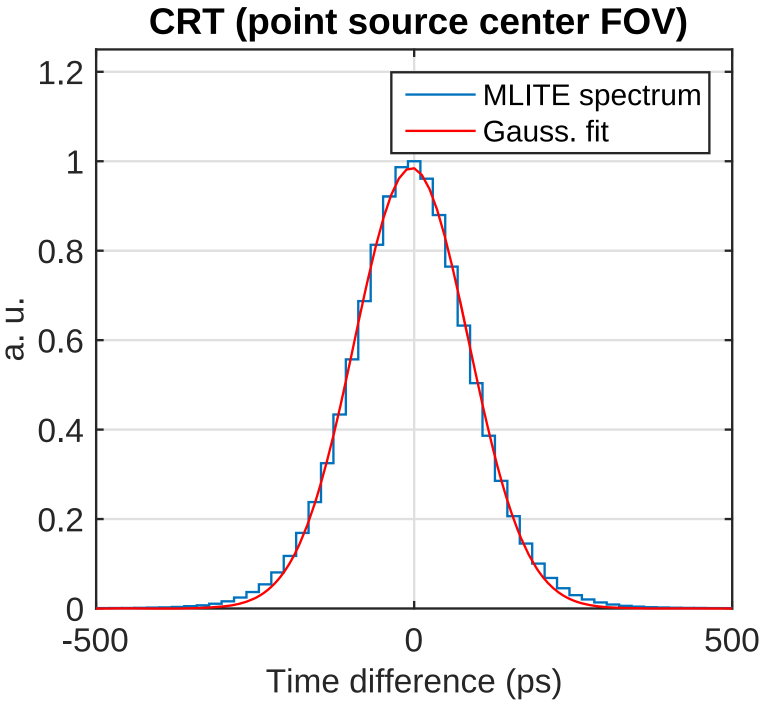

Figure 5.5: Timing histogram containing all coincidences obtained at all detector positions in a full tomographic acquisition of a ~3 MBq $^{22}$Na point source at the center of the FOV. Timestamps were derived using the MLITE method [17, 18].

Table 5.2: Spatial resolution in the radial and tangential directions at different radial distances, with and without using the DOI information in the FBP reconstruction of the $^{22}$Na point source images.

| Radial position | Radial resolution (mm FWHM) | | Tangential resolution (mm FWHM) | |
|---|---|---|---|---|
| | DOI | no DOI | DOI | no DOI |
| 0 cm | 2.9 | 3.1 | 2.9 | 3.1 |
| 5 cm | 3.0 | 3.4 | 3.2 | 3.3 |
| 10 cm | 3.0 | 4.4 | 3.4 | 3.6 |
| 15 cm | 3.2 | 5.4 | 3.5 | 4.1 |
| 20 cm | 3.2 | 7.0 | 4.0 | 4.9 |
| 25 cm | 3.3 | 8.8 | 4.7 | 9.0 |

thickness, due to the favorable light collection conditions and the possibility to correct for the influence of the optical transport of the scintillation photons within the crystal, using techniques such as MLITE [17].

Finally, the same data used to calculate the CRT with MLITE were used to determine the CRT that could be achieved using a simple, analytical method to estimate the time of interaction, viz. using the average of the first two valid timestamps [17]. This approach provides a CRT of ~233 ps FWHM, indicating that it is possible to achieve excellent timing performance even without MLITE. It is noted that this result furthermore implies that the skew correction based on a simple flood irradiation of the detectors (see appendix, section 5.5.4) works very well, as this analytical approach is expected to be rather sensitive to any remaining skews.

## 5.3.2. Spatial resolution

### 5.3.2.1. Spatial resolution with point sources

The radial and tangential spatial resolutions measured with point sources and 2D FBP at different radial offsets are reported in Table 5.2 and Figure 5.6 (red squares). A spatial resolution of ~2.9 mm FWHM is measured at the center of the FOV, while very little degradation is observed at radial distances of up to 25 cm, where the radial and tangential resolutions become ~3.3 mm FWHM and ~4.7 mm FWHM, respectively. Such a homogeneous spatial resolution across the entire FOV shows that monolithic scintillator detectors can accurately estimate the DOI.

For comparison, when the same datasets are reconstructed using no DOI information, the spatial resolution rapidly deteriorates as the point source is moved away from the center of the FOV (Figure 5.6, black circles). At a radial distance of 25 cm, the radial and tangential resolutions become ~8.6 mm FWHM and ~9.0 mm FWHM, respectively.

The spatial resolution of our system outperforms the resolution reported for all currently available whole-body clinical scanners. For instance, radial and tangential spatial resolutions of 4.44 mm FWHM and 4.10 mm FWHM at 1 cm and of 8.44 mm FWHM and 5.23 mm FWHM at 20 cm were recently reported for the Signa TOF-PET/MRI scanner [31]. Similar results were reported for the Vereos TOF-PET/CT scanner, which achieves a transverse spatial resolution of 4.11 mm FWHM at 1 cm

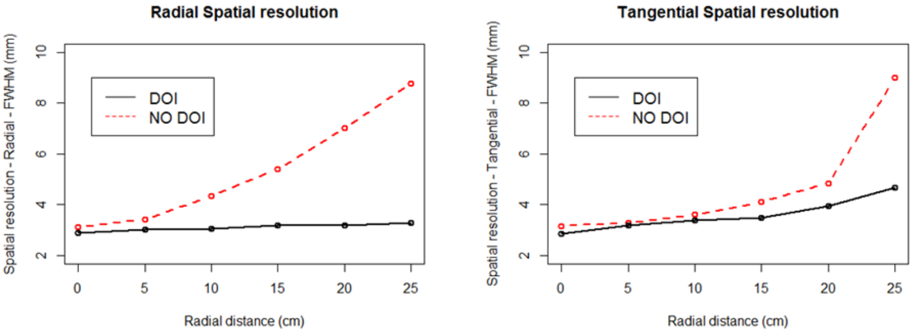

Figure 5.6: Radial (left) and tangential (right) spatial resolution as a function of the radial distance of the point source, with (black circles) and without (red squares) using the DOI information in the FBP reconstruction of the $^{22}$Na point source images. The lines connecting the symbols are only included to guide the eye.

and of 5.79 mm FWHM at 20 cm, respectively [28].

To our knowledge, a spatial resolution of about 3 mm FWHM in a whole-body clinical PET system has so far only been achieved by Wong *et al.* [8], who built a prototype scanner based on small LYSO:Ce crystals (2.35 mm × 2.35 mm × 15.2 mm) coupled to PMTs. With this scanner an impressive resolution of ∼2.9 mm FWHM and ∼3.7 mm FWHM was measured at the center of the FOV and at 24 cm radial distance, respectively. The relatively small influence of DOI in this system can be attributed to its relatively thin (15.2 mm) crystals and relatively large scanner diameter (∼87 cm). Unfortunately, both of these factors tend to reduce system sensitivity.

### 5.3.2.2. Derenzo-like phantom images

The TOF ML-EM reconstructed image of the Derenzo-like phantom acquired with the phantom positioned at the center of the FOV is shown in Figure 5.7. All rods with a diameter of ≥3 mm are clearly distinguishable, while most of the rods in the 2.5 mm sector can be recognized.

Because of the accurate DOI information provided by the monolithic scintillator detectors, essentially the same results are obtained when the phantom is imaged at different positions throughout the FOV. Specifically, when the phantom is positioned with its center at 15 cm radial offset (Figure 5.8), the image looks quite similar to Figure 5.7. Even when the phantom is positioned at 20 cm radial offset (Figure 5.9), in which case the smallest rods are located at radial distances of up to ∼25 cm, little degradation of image quality is observed. For a visual impression of the benefit of including DOI information in the reconstruction process, Figure 5.7, Figure 5.8 and Figure 5.9 show also images of the Derenzo-like phantom reconstructed without (right) DOI correction. As expected, a comparison of the images with and without DOI information demonstrates that DOI information is more important to improve image quality at larger radial distances in the FOV. When the phantom is positioned

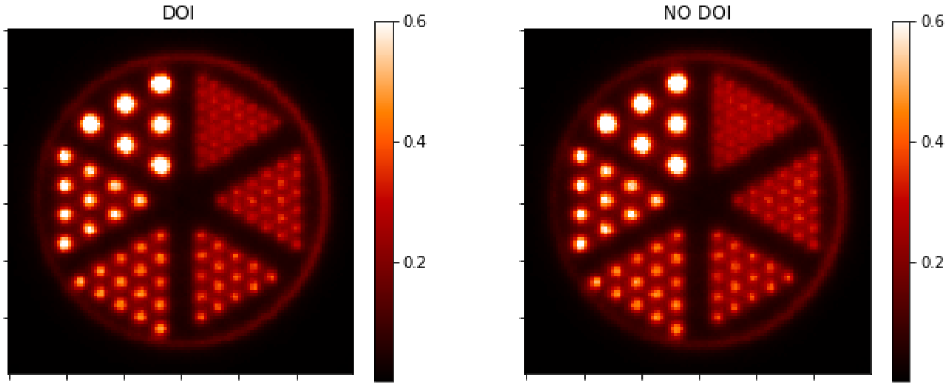

Figure 5.7: TOF ML-EM reconstructed image of the Derenzo-like phantom at the center of the FOV. DOI information is used in the reconstruction of the left-hand image and discarded in the right-hand image. The diameter of the rods in the different sectors is 2.5 mm, 3.0 mm, 3.5 mm, 4.0 mm, 5.0 mm, and 7.0 mm. The pixel intensity values obtained from image reconstruction were normalized from 0 to 1. The image was obtained with 10 EM iterations. The 50 central image slices were averaged in order to increase count statistics.

at the center of the FOV there are no noticeable differences between the DOI and non-DOI images. However, when the phantom is positioned at 15 or 20 cm radial offset only the sectors with the rods having a diameter >4 mm can be resolved.

The excellent quality of the images obtained with the Derenzo-like phantom confirms the outstanding spatial resolution of the tomographic system measured with the point sources and the capability of the system to maintain an almost uniform spatial resolution throughout the whole FOV thanks to the DOI information. However, a direct comparison between the two results cannot be made, since point-source spatial resolution cannot be reliably estimated using ML-EM reconstruction [32].

## 5.4. Conclusions

Two complete PET modules, each containing four 32 mm × 32 mm × 22 mm LYSO:Ce crystals read out by digital photon counter arrays, were assembled and fully calibrated. The modules were installed on the two rotating arms of an experimental setup capable of acquiring all LORs of a complete tomographic PET acquisition in a step-and-shoot approach. The system was used to emulate a 70 cm diameter PET ring based on monolithic scintillator detectors and to experimentally estimate its energy resolution, timing performance and spatial resolution.

An average energy resolution of ~10.2% FWHM and a CRT of ~212 ps FWHM were obtained. A spatial resolution of ~2.9 mm FWHM was measured at the center of the FOV, using a single $^{22}$Na point source and 2D FBP reconstruction. The resolution remained almost constant throughout the FOV because of the accurate DOI estimation of the detectors. At the largest radial distance tested (25 cm), the resolution increased to only 3.3 mm FWHM and 4.7 mm FWHM in the radial and

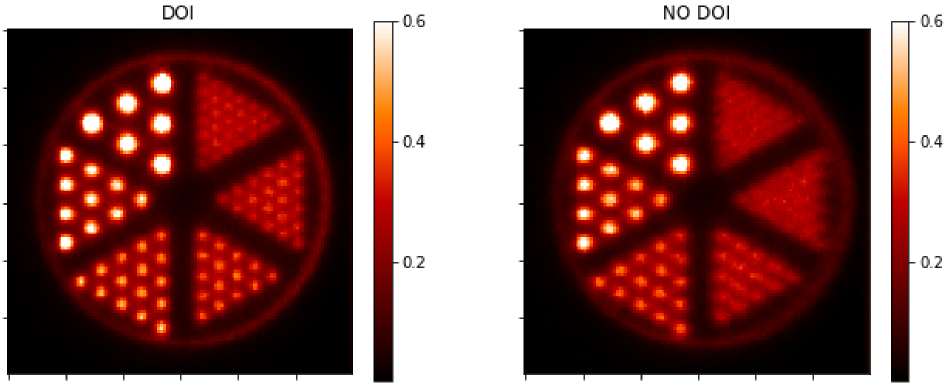

Figure 5.8: TOF ML-EM reconstructed images of the Derenzo-like phantom with its center positioned at 15 cm radial distance, such that the smallest rods are located at radial distances of up to ~20 cm. DOI information is used in the reconstruction of the left-hand image and discarded in the right-hand image. The diameter of the rods in the different sectors is 2.5 mm, 3.0 mm, 3.5 mm, 4.0 mm, 5.0 mm, and 7.0 mm. The pixel intensity values obtained from image reconstruction were normalized from 0 to 1. The image was obtained with 10 EM iterations. The 50 central image slices were averaged in order to increase count statistics.

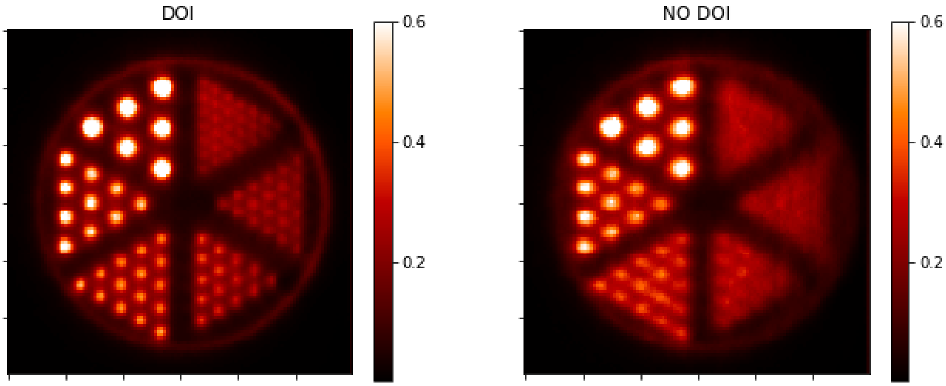

Figure 5.9: TOF ML-EM reconstructed images of the Derenzo-like phantom with its center positioned at 20 cm radial distance, such that the smallest rods are located at radial distances of up to ~25 cm. DOI information is used in the reconstruction of the left-hand image and discarded in the right-hand image. The diameter of the rods in the different sectors is 2.5 mm, 3.0 mm, 3.5 mm, 4.0 mm, 5.0 mm, and 7.0 mm. The pixel intensity values obtained from image reconstruction were normalized from 0 to 1. The image was obtained with 10 EM iterations. The 50 central image slices were averaged in order to increase count statistics.

tangential direction, respectively.

Furthermore, PET acquisitions of a Derenzo-like phantom were performed and reconstructed using a TOF ML-EM algorithm. The results show that the tomographic setup is able to clearly resolve 3 mm hot rods up to a radial distance of ~25 cm.

We emphasize that no resolution modelling was used in the reconstruction of any of the images presented in this work. Future research will include investigating the potential benefit of modelling the detector response in the image reconstruction. Future work should also include a detailed study of the count-rate capabilities of the detector, which could not be performed with the current experimental setup because of the limitations of the readout electronics. Nevertheless, due to the short dead time of DPC sensors ($<1$ $\mu$s per event) and the bandwidth of the DPC-sensor array ($>100$ kcps), we do not expect count-rate limitations for monolithic detectors in realistic whole-body clinical PET acquisition conditions.

In conclusion, we built a proof-of-concept tomographic setup to investigate, for the first time, the imaging performance of 32 mm × 32 mm × 22 mm LYSO:Ce monolithic scintillator detectors developed at our lab in a 70 cm diameter TOF/DOI-PET geometry. These results are particularly meaningful because no group has yet shown tomographic images experimentally obtained with thick monolithic detectors in a tomographic setup having a diameter compatible with clinical applications. Moreover, to the best of our knowledge, these are the first experimental results (obtained either with monolithic or with pixelated detectors) that show how DOI information can improve the spatial resolution of a clinical PET scanner at large radial distances. The results obtained demonstrate the excellent potential of monolithic scintillator detectors as a practical high-performance detector for clinical TOF/DOI-PET.

## Acknowledgements

This work was part of the EU FP7 project SUBLIMA, Grant Agreement 241711; see also www.sublima-pet-mr.eu

## 5.5. Appendix: time and position estimation methods and detector calibration procedures

All calibration measurements were performed in a dedicated setup built in a climate chamber (Weiss WT 450/70), which was cooled to about -20 °C, resulting in a sensor temperature of about -17/-16 °C during operation. All measurements were acquired selecting one detector on one module for calibration and using one detector on the other module as a reference. The module containing the detector to be calibrated was assembled on a pair of perpendicular stages driven by stepper motors (Physics Instruments, M-403.42S stages with C-663 controllers) which were used to correctly position it and move it when necessary.

### 5.5.1. Data pre-processing

A few pre-processing operations were performed for all measurements done in this work, both the calibration measurements reported in this section and the characterization measurements described in section 5.2.4.

The first step consisted of selecting only the events in which no pixel values or time stamps were missing and for which the total (uncorrected) deposited energy fell within the full-width-at-ten-maximum (FWTM) of the 511 keV photopeak. Before applying any energy correction, the mean energy resolution of the detectors (which have practically Gaussian photopeaks) is 10.6% (minimum is 10.3%, maximum is 12%), therefore on average the FWTM is ~19.3% (min ~18.8%, max 21.9%), which corresponds to an energy window ~100 keV wide (min ~96 keV, max ~112 keV).

The second step consisted of correcting the values of all light distributions for possible non-uniformities in the DPC array response which could be due to small defects in crystal wrapping or in the optical coupling between the crystals and the sensor. The homogeneity correction maps used for this operation were calculated with the method reported in Borghi *et al.* [18] using the fan-beam irradiation measurement described in section 5.5.2.

### 5.5.2. Spatial response calibration and position estimation algorithms

An accelerated version of the k-nearest neighbor (k-NN) classification algorithm [18] was used for estimating the x-y position of interaction of each gamma ray inside the PET detectors. The basic idea of this method is to first perform a rapid but coarse pre-estimation of the 3D position of interaction of an incident gamma ray by using analytical parameters of the light distributions and calibrated LUTs. For this purpose we used (i) the center of gravity (COG) of the light distribution for the x and y position and (ii) the sum of the squared pixel intensities for the DOI. Once a pre-estimated position is obtained, a more accurate estimation is obtained by running the k-NN 1D algorithm on a subset of the reference dataset composed of only reference events whose pre-estimated positions of interactions are close to the pre-estimated positon of the unknown event. Since the k-NN algorithm is run on a significantly smaller subset of the training dataset, the overall computational time is greatly reduced. The same method used for DOI pre-estimation was also used for the final estimation of the DOI, except that the x-y coordinates estimated with the k-NN algorithm were used to build the LUT and to calculate the DOI [33].

The acquisition of training (or reference) events for position estimation was performed by irradiating the crystals of the detectors with a narrow fan beam of annihilation photons at precise x or y positions, while uniformly irradiating the crystals along the other direction [19]. The fan beam was obtained using a $^{22}$Na source (⌀ 0.5 mm, ~3 MBq, IDB Holland BV) and a 80 mm tungsten slit collimator with a slit width of about 0.5 mm. For each detector, two datasets of reference events were acquired, one collected along a series of equally spaced positions (0.25 mm pitch) on the x axis (x-subset) and the other one on the y axis (y-subset). At each position, 12800 full-energy events were collected. These datasets were used to calibrate the pre-positioning LUTs and as x- or y-reference datasets for the accelerated 1D k-NN algorithm. An estimation of the distribution of the x-y-z positions of interaction of the calibration events inside the crystals, which is needed to calculate the position pre-estimation LUTs and the LUT for the final DOI estimation, was obtained with Monte Carlo simulations performed using GATE [34].

### 5.5.3. Energy response calibration

Monolithic scintillator detectors can have small variations in their energy response depending on the position of interaction of the gamma rays inside the crystal. An energy correction LUT was therefore calculated for each detector [18] by subdividing the crystal into 2 mm × 2 mm × 5.5 mm 'voxels' and determining a correction factor for each voxel. This correction factor was equal to the ratio between the 511 keV photopeak position of the total energy spectrum and the photopeak position of the spectrum obtained for that voxel. For this calibration procedure, the same datasets acquired with fan-beam irradiation for x,y position estimation were used.

### 5.5.4. Electronic skew estimation and MLITE calibration

Detector calibration for the MLITE algorithm [17, 18] consisted of two steps. First, the electronic time skews between the different dies on each sensor were estimated. Then, the probability distributions of the first photon detection delays (i.e. the delays between the time of interaction of the gamma-ray and the time of detection of the first visible photon interacting on a die) for a grid of positions inside the crystal and for each die were determined. For this purpose, a flood irradiation was acquired for each crystal using a $^{22}$Na point source (~3 MBq). The monolithic crystal to be calibrated was placed at a distance of about 390 mm from the source while the distance of the reference monolithic crystal was about 60 mm, so that the coincidence event would be localized in a region of the reference detector smaller than a die. About 20 million coincidence events were acquired for each detector to be calibrated and their position of interaction inside the detectors was estimated using the methods described in section 5.5.2.

The die skews were estimated for each single detector using all events registered during the flood irradiation. To estimate the die skew between two vertically, horizontally or diagonally adjacent dies, all the events interacting in the 8 × 8 mm2 region in between the dies and at a DOI between 0 mm and 10 mm (from the crystal top face) were selected. The differences of the timestamps acquired by the two dies were then calculated and used to estimate their probability distribution function with kernel density estimation (KDE). The mode of the distribution was then considered an estimation of the skew. Using the relative time distances between adjacent dies, time skews of all dies with respect to a single die were then calculated.

To determine the accuracy of this skew-estimation method, it was tested on a detector similar to the detectors used in this work for which the values of the die skews measured with a laser were available [18]. The test showed that the average difference between the values obtained with the new method and the values measured with a laser was smaller than 20 ps (i.e. the width of the TDC bins of the DPC sensors), while the maximum differences were smaller than 40-50 ps. This result shows that the new method provides excellent estimation and its accuracy can be considered comparable with the accuracy achievable performing a measurement with a laser.

To estimate the detector FPDDs, four million reference events were selected for each detector among the events acquired during the flood irradiations. The events were selected so that their estimated position of interaction in the reference detector was above the die on which the flood irradiation was electronically collimated and their estimated DOI was comprised between 0 mm and 6 mm (from the crystal top face). The reference timestamps were calculated as the average of the first two timestamps registered on the reference detector and were used to estimate the FPDDs of the sensor being calibrated, following the procedure described in Borghi *et al.* [18]. Using this procedure it was possible to avoid the use of small, fast reference detectors for the MLITE calibration.

To estimate the electronic skews in between tiles and modules, an additional measurement was necessary. First, all detectors of one module were measured in coincidence with a single detector of the other module using an un-collimated $^{22}$Na point source placed exactly in the center between them (~20 cm distance from each detector). The same measurement was repeated after inverting the modules. One million events per detector combination were acquired and the resulting time spectra were calculated. The position of the timing spectra acquired for all eight combinations were used to calculate the skews between detectors.

# References

[1] S. Surti, A. R. Shore, and J. S. Karp, *Design study of a whole-body pet scanner with improved spatial and timing resolution,* Nuclear Science, IEEE Transactions on **60**, 3220 (2013).

[2] H. Thoen, V. Keereman, P. Mollet, R. V. Holen, and S. Vandenberghe, *Influence of detector pixel size, tof resolution and doi on image quality in mr-compatible whole-body pet,* Physics in Medicine and Biology **58**, 6459 (2013).

[3] A. J. González, A. Aguilar, P. Conde, L. Hernández, L. Moliner, L. F. Vidal, F. Sánchez, S. Sánchez, C. Correcher, C. Molinos, J. Barberá, K. Lankes, S. Junge, T. Bruckbauer, P. Bruyndonckx, and J. M. Benlloch, *A pet design based on sipm and monolithic lyso crystals: Performance evaluation,* IEEE Transactions on Nuclear Science **63**, 2471 (2016).

[4] M. S. Lee, K. Y. Kim, G. B. Ko, and J. S. Lee, *Prototype pre-clinical PET scanner with depth-of-interaction measurements using single-layer crystal array and single-ended readout,* Physics in Medicine and Biology **62**, 3983 (2017).

[5] S. Vandenberghe, E. Mikhaylova, E. D'Hoe, P. Mollet, and J. S. Karp, *Recent developments in time-of-flight pet,* EJNMMI Physics **3**, 3 (2016).

[6] R. Marcinkowski, S. España, R. V. Holen, and S. Vandenberghe, *Optimized light sharing for high-resolution tof pet detector based on digital silicon photomultipliers,* Physics in Medicine and Biology **59**, 7125 (2014).

[7] M. S. Lee and J. S. Lee, *Depth-of-interaction measurement in a single-layer crystal array with a single-ended readout using digital silicon photomultiplier,* Physics in Medicine and Biology **60**, 6495 (2015).

[8] W.-H. Wong, H. Li, Y. Zhang, R. Ramirez, S. An, C. Wang, S. Liu, Y. Dong, and H. Baghaei, *A high-resolution time-of-flight clinical pet detection system using a gapless pmt-quadrant-sharing method,* Nuclear Science, IEEE Transactions on **62**, 2067 (2015).

[9] D. R. Schaart, H. T. v. Dam, S. Seifert, R. Vinke, P. Dendooven, H. Löhner, and F. J. Beekman, *A novel, sipm-array-based, monolithic scintillator detector for pet,* Physics in Medicine and Biology **54**, 3501 (2009).

[10] J. P. Schmall, S. Surti, and J. S. Karp, *Characterization of stacked-crystal pet detector designs for measurement of both tof and doi,* Physics in Medicine and Biology **60**, 3549 (2015).

[11] C.-M. Chang, J. W. Cates, and C. S. Levin, *Time-over-threshold for pulse shape discrimination in a time-of-flight/depth of interaction phoswich pet detector,* in *2016 IEEE Nuclear Science Symposium, Medical Imaging Conference and Room-Temperature Semiconductor Detector Workshop (NSS/MIC/RTSD)* (2016) pp. 1–3.

[12] M. Kaul, S. Surti, and J. S. Karp, *Combining surface treatments with shallow slots to improve the spatial resolution performance of continuous, thick lyso detectors for pet,* Nuclear Science, IEEE Transactions on **60**, 44 (2013).

[13] S. Seifert and D. R. Schaart, *Improving the time resolution of tof-pet detectors by double-sided readout,* Nuclear Science, IEEE Transactions on **PP**, 1 (2014).

[14] H. G. Kang, G. B. Ko, J. T. Rhee, K. M. Kim, J. S. Lee, and S. J. Hong, *A dual-ended readout detector using a meantime method for sipm tof-doi pet,* IEEE Transactions on Nuclear Science **62**, 1935 (2015).

[15] S. Seifert, H. T. v. Dam, J. Huizenga, R. Vinke, P. Dendooven, H. Löhner, and D. R. Schaart, *Monolithic labr 3 :ce crystals on silicon photomultiplier arrays for time-of-flight positron emission tomography,* Physics in Medicine and Biology **57**, 2219 (2012).

[16] S. Seifert, G. v. d. Lei, H. T. v. Dam, and D. R. Schaart, *First characterization of a digital sipm based time-of-flight pet detector with 1 mm spatial resolution,* Physics in Medicine and Biology **58**, 3061 (2013).

[17] H. T. van Dam, G. Borghi, S. Seifert, and D. R. Schaart, *Sub-200 ps crt in monolithic scintillator pet detectors using digital sipm arrays and maximum likelihood interaction time estimation,* Physics in Medicine and Biology **58**, 3243 (2013).

[18] G. Borghi, V. Tabacchini, and D. R. Schaart, *Towards monolithic scintillator based tof-pet systems: practical methods for detector calibration and operation,* Physics in Medicine and Biology **61**, 4904 (2016).

[19] G. Borghi, V. Tabacchini, S. Seifert, and D. R. Schaart, *Experimental validation of an efficient fan-beam calibration procedure for k-nearest neighbor position estimation in monolithic scintillator detectors,* Nuclear Science, IEEE Transactions on **62**, 57 (2015).

[20] T. Frach, G. Prescher, C. Degenhardt, R. de Gruyter, A. Schmitz, and R. Ballizany, *The digital silicon photomultiplier - principle of operation and intrinsic detector performance,* in *Nuclear Science Symposium Conference Record (NSS/MIC), 2009 IEEE* (2009) pp. 1959–1965.

[21] T. Frach, G. Prescher, C. Degenhardt, and B. Zwaans, *The digital silicon photomultiplier - system architecture and performance evaluation,* in *Nuclear Science Symposium Conference Record (NSS/MIC), 2010 IEEE* (2010) pp. 1722–1727.

[22] D. R. Schaart, E. Charbon, T. Frach, and V. Schulz, *Advances in digital sipms and their application in biomedical imaging,* Nuclear Instruments and Methods in Physics Research Section A: Accelerators, Spectrometers, Detectors and Associated Equipment **809**, 31 (2016).

[23] R. Schulze, *PDPC TEK Manual*, Koninklijke Philips Electronics 2014 (2014).

[24] R. Schulze, *PDPC Module TEK Manual*, Koninklijke Philips Electronics 2014 (2014).

[25] S. Vandenberghe, Y. D'Asseler, M. Koole, L. Bouwens, R. V. de Walle, I. L. Lemahieu, and R. A. Dierckx, *Iterative list mode reconstruction for coincidence data of gamma camera,* in *Medical Imaging 2000: Image Processing*, Vol. 3979, edited by K. M. Hanson, International Society for Optics and Photonics (SPIE, 2000) pp. 1538 – 1546.

[26] R. L. Siddon, *Fast calculation of the exact radiological path for a three-dimensional ct array,* Medical Physics **12**, 252 (1985), https://aapm.onlinelibrary.wiley.com/doi/pdf/10.1118/1.595715 .

[27] C. S. Levin, S. H. Maramraju, M. M. Khalighi, T. W. Deller, G. Delso, and F. Jansen, *Design features and mutual compatibility studies of the time-of-flight pet capable ge signa pet/mr system,* IEEE Transactions on Medical Imaging **35**, 1907 (2016).

[28] M. Miller, J. Zhang, K. Binzel, J. Griesmer, T. Laurence, M. Narayanan, D. Natarajamani, S. Wang, and M. Knopp, *Characterization of the vereos digital photon counting pet system,* Journal of Nuclear Medicine **56**, 434 (2015).

[29] C. Degenhardt, P. Rodrigues, A. Trindade, B. Zwaans, O. Mulhens, R. Dorscheid, A. Thon, A. Salomon, and T. Frach, *Performance evaluation of a prototype positron emission tomography scanner using digital photon counters (dpc),* in *Nuclear Science Symposium and Medical Imaging Conference (NSS/MIC), 2012 IEEE* (2012) pp. 2820–2824.

[30] D. Schug, J. Wehner, P. M. Dueppenbecker, B. Weissler, P. Gebhardt, B. Goldschmidt, A. Salomon, F. Kiessling, and V. Schulz, *Pet performance and mri compatibility evaluation of a digital, tof-capable pet/mri insert equipped with clinical scintillators,* Physics in Medicine and Biology **60**, 7045 (2015).

[31] A. M. Grant, T. W. Deller, M. M. Khalighi, S. H. Maramraju, G. Delso, and C. S. Levin, *Nema nu 2-2012 performance studies for the sipm-based tof-pet component of the ge signa pet/mr system,* Medical Physics **43**, 2334 (2016).

[32] K. Gong, S. R. Cherry, and J. Qi, *On the assessment of spatial resolution of PET systems with iterative image reconstruction,* Physics in Medicine and Biology **61**, N193 (2016).

[33] H. T. van Dam, S. Seifert, R. Vinke, P. Dendooven, H. Löhner, F. J. Beekman, and D. R. Schaart, *A practical method for depth of interaction determination in monolithic scintillator pet detectors,* Physics in Medicine and Biology **56**, 4135 (2011).

[34] S. Jan, G. Santin, D. Strul, S. Staelens, K. Assié, D. Autret, S. Avner, R. Barbier, M. Bardiès, P. M. Bloomfield, D. Brasse, V. Breton, P. Bruyndonckx, I. Buvat, A. F. Chatziioannou, Y. Choi, Y. H. Chung, C. Comtat, D. Donnarieix, L. Ferrer, S. J. Glick, C. J. Groiselle, D. Guez, P.-F. Honore, S. Kerhoas-Cavata, A. S. Kirov, V. Kohli, M. Koole, M. Krieguer, D. J. v. d. Laan, F. Lamare, G. Largeron, C. Lartizien, D. Lazaro, M. C. Maas, L. Maigne, F. Mayet, F. Melot, C. Merheb, E. Pennacchio, J. Perez, U. Pietrzyk, F. R. Rannou, M. Rey, D. R. Schaart, C. R. Schmidtlein, L. Simon, T. Y. Song, J.-M. Vieira, D. Visvikis, R. V. d. Walle, E. Wieërs, and C. Morel, *Gate: a simulation toolkit for pet and spect,* Physics in Medicine and Biology **49**, 4543 (2004).

# 6

# Concluding Remarks and Discussion

***Abstract*** - *This thesis focuses on developing novel monolithic scintillator detectors for clinical PET applications and on improving the calibration and event-reconstruction methods required by these detectors. For this purpose, a novel method for calibrating the k-NN position-estimation algorithms is developed (Chapter 2) and all the algorithms used to reconstruct the energy and the time/position of interaction of gamma rays are reviewed (Chapter 3). This makes it possible to fully calibrate a detector only with flood and fan-beam irradiations. Moreover, the position-estimation algorithm is speeded up by introducing a novel position-pre-estimation technique and all the event-reconstruction algorithms are improved to reconstruct also events with incomplete light distributions and missing time information (Chapter 3). Using these new methods, two monolithic detector prototypes based on wide and thick crystals (32 mm × 32 mm × 22 mm) and on DPC digital silicon photomultipliers (dSiPMs) are fully calibrated and then characterized. The first of these prototypes is read out by a single dSiPM array from the back side (Chapter 3) and is developed for whole-body clinical PET applications. The second one, instead, is read out from the front and back side and is developed for high-resolution organ-specific scanners (Chapter 4). Finally, the imaging performance of the back-side-readout detector are investigated in a tomographic setup representative of a whole-body clinical scanner (70 cm diameter) (Chapter 5). In this final chapter, all these results are reviewed, extending the discussion also to the most recent experimental works of other research groups. Finally, some concluding remarks and an outlook on future use of monolithic detectors are presented.*

## 6.1. General overview of the field before the beginning of this research work

As discussed in Chapter 1 (section 1.3.3.2), monolithic detectors have received extensive attention as a possible alternative to pixelated detectors in PET applications since the early 2000's, especially for preclinical systems [1–5]. To a large extent, this was made possible by the development of finely-segmented photosensors (in particular APD arrays and, later, SiPM arrays) that could sample the scintillation light distribution more accurately. By the beginning of the 2010's, it was well established that monolithic detectors could potentially provide a unique combination of characteristics such as good spatial resolution, even in the order of 1 mm FWHM in 10 mm thick crystals [6, 7], DOI estimation capabilities [8, 9], good energy resolution [6, 7] and excellent CRT [10], even below 200 ps for 20 mm thick crystals.

The possibility to combine all these features is a peculiar property of monolithic detectors. In pixelated detectors with single-side readout, the architectures that can provide good spatial resolution and/or DOI estimation are usually based on small crystals and light sharing techniques. These architectures cause scintillation photons to undergo a large number of reflection before they are detected by the photosensor and therefore determine a slower and inefficient extraction of the light, which degrades the timing and energy resolution. For this reason, in pixelated detectors it is usually necessary to compromise between timing and energy resolution on one side, for which a single layer of wider crystals is preferable, and spatial resolution and DOI capability on the other side, for which thinner crystals, light sharing techniques and stacked crystal matrixes should be used.

In monolithic scintillator detectors, instead, it is not necessary to compromise between the different performance parameters since the favorable aspect ratio of the crystals facilitates a fast and efficient light collection, which benefits spatial resolution, energy resolution and timing performance at the same time. Monolithic detectors also have several other practical advantages. First of all, their production cost is lower, since they are easier to be assembled and less crystal polishing and surface processing is required for a single monolithic crystal compared to a pixelated crystal array. Then, monolithic detectors seems to be more robust with respect to photosensor deterioration: for example, if some photosensors pixels are damaged, monolithic crystals can still provide good performance (see Chapter 3), whereas in pixelated detectors this could lead to a significant distortion in the flood map or to a dead crystals element, if 1:1 coupling is used. Finally, monolithic crystals do not have dead material in their active volume, whereas pixelated crystal arrays have to include reflecting material between the pixels to optically isolate them. Therefore, monolithic crystals have an higher sensitivity, especially compared to high resolution crystal arrays. For example, if a reflecting foil of 100 $\mu m$ is used, the sensitive volume of a crystal array with 2 mm crystal pitch is reduced to ~90% of its total volume.

Despite all these advantages, monolithic detectors have found applications (mostly in recent years) only in few pre-clinical systems [11–14], in dedicated breast PET systems [15, 16], in an MR-insert for brain PET [17], and in a commercial dedicated brain PET system [18]. They have not yet been implemented in whole-body PET scanners, mainly because they are considered more complex to be calibrated and operated compared to pixelated detectors, especially if the best achievable performance is pursued.

As discussed in Chapter 1, section 1.3.3.2, there are many different methods that have been proposed to estimate the position of interaction of gamma rays inside monolithic detectors. These methods can be broadly divided into two large categories: the first one comprehends all analytical algorithms, e.g. algorithms based on COG or on models of the light distribution, whereas the second one includes the algorithms based on statistical or machine-learning techniques. These latter methods usually provide superior positioning performance: however, they are typically based on calibration datasets that are obtained with long and complex procedures. Moreover, statistical or machine-learning methods usually require significant resources in terms of memory and computational power to store the detector calibration datasets and process the acquired events. So far, these calibration and computational requirements made monolithic detectors unpractical for application in large systems and hampered their use in clinical scanners. Another issue that hampered the use of monolithic detectors is that, before the beginning of this work, no one had ever demonstrated the possibility to combine all the aforementioned advantages in a single detector having an appropriate sensitivity (i.e. thickness) for whole-body scanners.

Therefore, the work presented in this thesis has been dedicated to investigate these calibration and operational issues, to develop optimized detector architectures for clinical applications and to show the imaging capabilities of monolithic detectors, in order to demonstrate the potentiality of such detectors as an all-around high-performance solution for the next generation of TOF-PET clinical scanners.

## 6.2. Calibration and event reconstruction for monolithic scintillator detectors

### 6.2.1. Calibration procedures

Usually, statistical and machine-learning methods used to estimate the position of interaction inside monolithic detectors require to collect comprehensive datasets of calibration events on a fine grid of reference positions. These datasets can be used to train neural networks [19–21], to calibrate algorithms based on maximum-likelihood estimation [3] or as reference events for methods based on the k-nearest neighbor (k-NN) classification method [4, 22]. Due to the large number of positions and events required for a proper calibration and to the low count-rate that can be obtained with a well-collimated pencil beam (diameter ~0.5 mm), these calibration scans can last for days or even weeks. Therefore, they are a serious bottleneck for a practical use of monolithic detectors, since calibrating all detectors that are necessary in a real scanner would not be possible in a reasonable amount of time. Several authors have tried to compromise, e.g. by reducing the number of calibration positions or increasing the dimension of the pencil beam. However, none of these approaches completely solve the issue and in any case they tend to degrade the final performance, which is not desirable in high-resolution detectors.

A possible solution to this problem is presented in Chapter 2, in which an innovative calibration method based on fan-beam irradiation is experimentally tested for the first time. This method, originally proposed in van Dam *et al.* [22], uses a fan-beam irradiation to collect two separate datasets of reference events, each one composed of events for which only one coordinate is known, and then uses a modified version of the k-NN position estimation method to independently determine the two coordinates. The new method is tested with two monolithic detectors having a footprint of 16 mm × 16 mm and a thickness of 10 mm and 20 mm. In both cases, the new method demonstrates to be equivalent to the previous method based on pencil-beam calibration, enabling the detectors to achieve outstanding spatial resolutions of ~1.1 mm FWHM and of ~1.5 mm FWHM for the 10 mm and 20 mm thick detectors, respectively.

The concept of fan-beam calibration has been recently applied to another position estimation method based on gradient tree boosting (GTB) regression, a supervised machine-learning method [23]. Also in that case, the fan-beam calibration provided the same performance of the pencil beam calibration.

These works demonstrate that the best strategy to obtain a fast and optimal spatial calibration of a monolithic detector is to use a fan-beam irradiation to independently characterize the spatial response in the x and y directions and then to use an estimation method that separately determines the two coordinates. The fan-beam calibration method reduces the number of calibration position from $n_{pos,x} \times n_{pos,y}$ to $n_{pos,x} + n_{pos,y}$ (where $n_{pos,x}$ and $n_{pos,y}$ are the number of calibration position in the x and y direction) and proved to be more than one order of magnitude faster than pencil-beam calibration (when the same point source is used), making it possible to calibrate the detectors in just a few hours. Moreover, this method could be further accelerated by using line sources, which can contain a significantly higher amount of activity compared to point sources. This could further reduce the calibration time by another order of magnitude, making it possible to obtain a complete spatial calibration in just a few minutes.

An additional advantage of fan-beam calibration is the possibility to obtain irradiation conditions similar to the ones used for calibrating single detectors also in a PET ring, for example by using multiple line-sources in combination with mechanical and/or electronic collimation. This would be of particular importance if a procedure for acquiring reference events in an assembled PET scanner had to be developed, for example for regular calibration and quality-assurance procedures.

Besides the calibration technique used for the x-y position estimation algorithm, also the calibration procedures for DOI and time-of-interaction estimation methods have to be simply implementable. Several techniques have been proposed to estimate the DOI and some of them require a calibration scan acquired with a side irradiation of the detectors [1, 21, 24]. Although a fan-beam irradiation might be used to speed up the process in these cases as well, a side irradiation complicates the calibration procedure and cannot be implemented in an already assembled scanner. Therefore, methods that use calibration datasets obtained with frontal irradiation should probably be preferred [8, 9]. However, also these methods usually rely on calibration datasets obtained with a pencil-beam scan on a regular grid of positions, which are used to build calibrated look-up tables (LUT) for each point in the grid. Similarly, also the statistical method proposed by van Dam *et al.* [10] to improve the timing performance of monolithic detectors by using the multiple timestamps acquired on wide pixelated photosensors necessitates calibration events for which the position of interaction is known.

In Chapter 3, new DOI and time-of-interaction calibration procedures are proposed that do not require pencil-beam scans. Since the optimized x-y positioning methods developed in Chapter 2 already have an accuracy that is comparable with the pitch of the LUTs built during the DOI and time-of-interaction calibration procedures, fan-beam scans or even flood irradiations can be used to build these LUTs; the reconstructed positions are then used as the positions of the reference events. This approach showed good results, demonstrating that flood irradiations can be used to calibrate DOI estimation methods, time-of-interaction estimation methods and methods used to correct the spatial dependence of the energy measurement. A similar approach can also be used for other calibration procedures, as for example the procedure introduced in Chapter 5 (Appendix A.4) for estimating the electronic skew between different dies of an SiPM array.

A different approach to reduce the calibration burden is to develop methods that do not need collimated scans for obtaining calibration data. One of the most interesting methods proposed in literature is based on self-organizing maps (SOMs), a machine-learning technique that is able to cluster events with similar features and organize them in a map representing the geometry of the detector [25]. This method proved to be effective for thin detectors but turned out to be much more complex in thick detectors (15-20 mm) due to their different response at different DOIs, which requires to use 3D SOMs instead of 2D SOMs. However, some preliminary tests showed that SOMs might also be used in thicker detectors with reasonable results (S. Seifert, 2013, private communication). Also the clustering method used in Chapter 3 to pre-estimate the position of the events before using k-NN demonstrated good positioning performance, despite its simplicity (see section 6.2.2).

Another approach proposed in literature to avoid calibration measurements is to produce a calibration dataset for statistical positioning methods by using Monte Carlo simulations, as shown for neural networks in Iborra *et al.* [26]. However, Monte Carlo simulations typically assume ideal responses and thus may not accurately reproduce the small non-ideal characteristics (uneven roughness and wrapping of the crystals, nonhomogeneous coupling between the crystal and the photosensor) of individual detectors.

In conclusion, the results presented in this thesis and obtained by other research groups demonstrate that the calibration data required to achieve optimal performance by monolithic detectors can be obtained with a combination of flood and fan-beam irradiations. With such irradiations, together with some *a priori* assumptions and Monte Carlo simulations, it is possible to obtain in just a couple of hours per detector (and potentially in few minutes) the calibration data required to fully exploit the potential of statistical and machine-learning methods used to estimate the position of interaction (xy and DOI), the time of interaction, and the deposited energy.

For completion, it is noted that other methods that require only flood irradiations or no calibration data at all have been developed, even if they have not demonstrated yet the capability to obtain the best possible performance. However, these methods might be used if the performance deterioration that they introduce at scanner level are considered acceptable. Alternatively, they might be used to speed up the calibration procedures in a mixed approach, in which these methods are used for a preliminary calibration that is then refined with a reduced dataset of real reference events.

### 6.2.2. Position estimation algorithms

An extensive list of the different methods developed to estimate the position of interaction (x, y and DOI) of gamma rays inside monolithic detectors has been reported in Chapter 1, section 1.3.3.2. So far, methods based on statistical or machine-learning techniques have widely demonstrated to be capable of providing superior positioning performance compared to analytical algorithms. Most often, the former methods rely on a calibration (or reference) dataset that characterizes the detector response. Thanks to this characterization, they often utilize the information encoded in the light distribution of the unknown events more accurately than analytical methods. In general, the more the calibration dataset is complete in describing the detector response, the more precise the positon of interaction can be estimated. The major challenge in developing statistical and machine-learning methods thus consists in developing calibration procedures and estimation algorithms that make efficient use of the limited available resources, i.e. that can provide results close to the intrinsic detector resolution while using calibration datasets acquired in a fast and practical way and requiring limited computational resources.

As discussed in section 6.2.1, it has been demonstrated in different studies (and for the first time in the experimental work presented in Chapter 2) that it is possible to develop statistical or machine-learning methods that use fast calibration procedures based on fan-beam irradiation. This procedure requires only few hours (and potentially only few minutes) and allow detectors to achieve the same positioning performance obtained with standard calibration datasets based on pencil-beam irradiation. The issue that still remains to be solved is therefore the development of an optimal positioning algorithm that can be implemented with the limited computational resources available in a PET scanner.

In this research work, the k-NN position estimation method [4] was chosen to develop and test the xy positioning performance of new monolithic detectors. This method is based on the nearest neighbor pattern classification algorithm and should approach the minimum probability for misclassification, i.e. mispositioning [27], for sufficiently large reference datasets. Thus it can be used to provide an estimation of the intrinsic spatial resolution of a monolithic detector.

Several optimized versions of this method were already developed over the years to make it more practical, e.g. to use more effectively the information contained in smaller reference datasets or in datasets acquired with fan-beam irradiation [22]. However, the computational burden imposed by k-NN-based algorithms still hampered their practical application. For each unknown event, these algorithms require to compute the distance of its light distribution from the light distributions of all the events in the reference datasets (usually defined as the Euclidean distance between the pixel intensities), to sort these distances, to choose the k events with the smallest distances and then to make an histogram of their known positions. Considering that appropriate reference datasets can contain up to a few hundred thousands of events, these operations require a computational power that is excessive for standard processing electronics embedded in PET modules, such as field-programmable gate arrays (FPGAs) and microcontrollers. Moreover, processing all the data in (nearly) real time in a central processing computer would require computational resources that might be unpractical for a PET scanner. Moreover, this second approach would further complicate data transmission and storage, since it would not be possible to preliminary discriminate the events at module level and the raw data of each event (pixel intensities and TDC values) should be transmitted to and stored in the central processing system.

Therefore, in Chapter 3 a new positioning method based on the k-NN approach is developed, with the aim to reduce the computational power required for position estimation. This methods relies on a fast position pre-estimation algorithm, based on a clustering method similar to the methods proposed by Ling *et al.* [8] and by van Dam *et al.* [9] to estimate the DOI. In practice, position pre-estimation is performed by using a parameter correlated to the coordinate to be estimated (in this case, the simple COG values for the x and y coordinates and the summed squared pixel intensity for the DOI) and calibrated look-up tables (LUTs). Using the pre-estimated position of the unknown event and of the reference events, only the reference events whose position is estimated to be close to the unknown event are selected and used for the k-NN estimation. As demonstrated in Chapter 3, this approach makes possible to obtain a spatial resolution that is essentially equivalent to standard methods, reducing at the same time the number of events used for k-NN calculation by two orders of magnitude. This improvement appeared to be crucial for the experimental work presented in Chapter 5, since it made possible to reconstruct the position of interaction inside monolithic detector modules in a reasonable amount of time. However, despite the large reduction in the computational-power requirements, this new k-NN algorithm still has considerable memory requirements, since each reference dataset is several hundred MBs. Therefore, further modifications of the method might still be needed to adapt it to the memory resources available in PET modules.

Similarly, also the other statistical methods proposed so far have analogous limitations: for example, also ML estimation has large computational and, to a lesser extent, memory requirements; moreover, it has not been demonstrated yet the possibility to implement this method with fan-beam calibration. Therefore, further improvements are still needed by all statistical methods before they can be practically implemented in real clinical scanners.

Currently, machine learning techniques are another family of techniques that are drawing large interest for position estimation in monolithic detectors. Several of these techniques have already provided remarkable results and demonstrated to be promising methods for obtaining fast and precise positioning algorithms that require limited memory and computational resources. Usually, machine learning techniques are quite robust and can efficiently use calibration data even in case of reduced datasets. Moreover, they are used in many other applications (e.g. artificial intelligence in consumer electronics) and therefore the field of monolithic detectors could significantly benefit of the numerous research efforts carried on for other purposes.

Some of the machine-learning methods that have already been tested for position estimation comprehend neural networks [20, 26], self-organizing maps [25], and methods based on gradient tree boosting (GTB) [23, 24]. As for statistical methods, also for these methods the major challenges lie in developing algorithms that can be efficiently calibrated, provide accurate positioning and are compatible with the computational resources available in clinical PET modules. An interesting approach to this problem has been shown in Müller *et al.* [23] and in Müller *et al.* [24], in which a systematic study of the tradeoffs between positioning accuracy and memory requirements has been presented.

A drawback of machine-learning methods is that so far they have demonstrated to be effective only in relatively thin crystals (10-12 mm), if single-sided readout is used. Therefore, further efforts to make them reliable also for thicker crystals are needed. To this purpose, a collaboration has been established between TU Delft and Aachen University, which aims at testing the GTB methods developed by Aachen University on the data used for the experimental work presented in Chapter 3 and at adapting these methods to thicker crystals.

It is interesting to note that so far there are no comparative studies that clearly show which of the proposed statistical or machine-learning methods is more suitable for the task of estimating the position of interaction inside monolithic detectors and can provide superior performances in terms of calibration efficiency, positioning accuracy and computational requirements. Such a study is difficult to set up, since it would require that all the methods are computationally optimized; however, the results of a proper comparison of the different methods would make future algorithm developments more efficient.

There are some additional points that have to be considered when developing position estimation algorithms for monolithic detectors and when comparing different methods. First of all, it is important to consider that practically all the methods mentioned above could also be combined with data compression methods, such as the principal components analysis (PCA) [23, 28]. Such compression methods could potentially be very important to reduce the memory and computational requirements of the position estimation algorithms without degrading the performance. However, they further complicate the algorithm optimization, since they also require careful implementation in order to be efficient in reducing the amount of data while maintaining the information contained therein.

Second, the positioning methods should have the capability to estimate the position of interaction also in case the light distributions registered by the detectors are not complete, e.g. in case one of the photosensor pixels is not triggered or is in dead time when the interaction occurs. For example, in Chapter 3 a new statistical method has been introduced to estimate the values of the missing pixels and use this values to perform the standard xy and DOI position estimation. This methods showed excellent positioning capabilities also for events that are missing up to 25% of the total information (4 dies out of 16), demonstrating the robustness of monolithic detectors to this issue.

Third, many positioning methods provide error distributions which are not Gaussian. Some methods provide distributions which are more peaked but have longer tails, while others may have a more frequent occurrence of small errors but be more efficient in reducing the tails of the distributions. In this regard, it would be interesting to set up a simulation study that investigates how different error distributions influence the scanner performance and the final image resolution. This study could also be used to determine which is the most important parameter in defining detectors resolution among the many parameters that have been proposed so far, e.g. the FWHM or the RMS values of the 1D or 2D error distribution functions, the mean absolute error (MAE), the median value (defined also $r_{50\%}$) of the cumulative error distribution functions, etc. (see Chapter 3 for a discussion about these parameters). In fact, since many statistical or machine-learning positioning methods can be optimized for minimizing a single resolution parameter (e.g. the parameter used by machine learning-algorithms during the training phase to evaluate the algorithm performance), a better understanding of what is the most important one would also be important to properly implement all these methods.

Such a study about the influence of the shape of the error distribution on the PET system performance would also be interesting if it were performed for different types of systems, such as whole-body clinical scanners and dedicated scanners for brain imaging, breast imaging or pediatric applications. In different scanners, the final image quality is differently influenced by the detector spatial resolution and therefore different position estimation techniques might be used for different applications, depending on the necessity to maximize the detectors spatial resolution or to use algorithms that are more computationally efficient. In whole-body PET, for example, the most advanced methods might not be necessary, since in such systems the factors that limit most image resolution are usually statistical noise (sensitivity) and photon acollinearity. Therefore, in these scanners optimized analytical methods might already provide the necessary positioning accuracy.

For example, the pre-positioning method presented in Chapter 3 provides an overall error distribution that is less peaked and a bit wider compared to the accelerated k-NN method also presented in Chapter 3 (Figure 6.1). Therefore, the pre-positioning method seem to perform much worse than the k-NN method when the FWHM spatial resolution is considered (Table 6.1). However, the comparison of the cumulative distribution functions and of the $r_{50\%}$, $r_{90\%}$ and the MAE values obtained with the two methods show that the positioning accuracy of the pre-positioning method is only slightly worse compared to the k-NN method and is still remarkable considering the simplicity of the algorithm.

In conclusion, the results presented in this thesis and in literature show that in

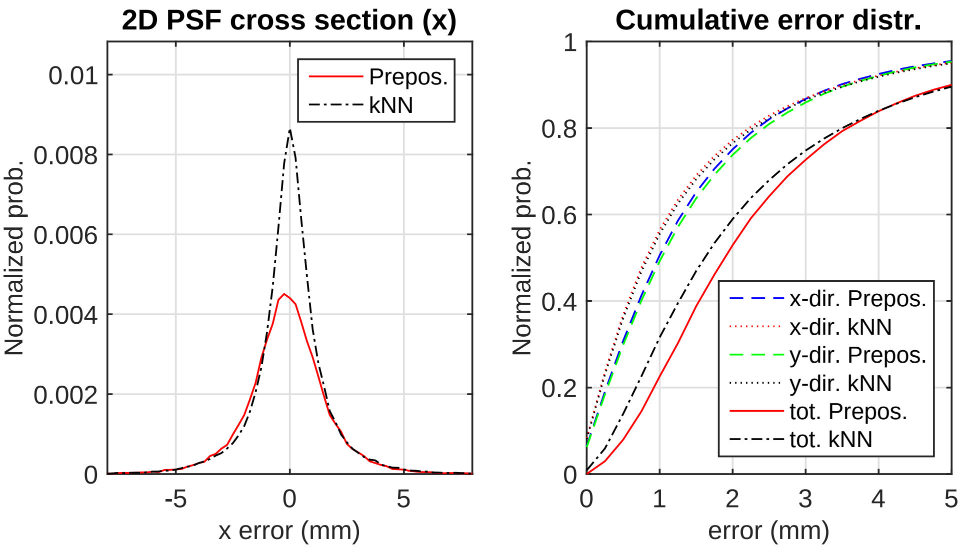

Figure 6.1: Comparison of (left) the cross-sections in the x direction of the 2D PSFs and (right) of the cumulative error distributions functions (x, y and total positioning errors) obtained using the prepositioning algorithm and the accelerated k-NN positioning algorithm, both presented in Chapter 3.

Table 6.1: Average spatial resolution for perpendicularly incident events using the prepositioning method (Prepos.) and the accelerated 1D k-NN method (Acc.k-NN).

| | x | | y | | total | |
|---|---|---|---|---|---|---|
| | Prepos. | Acc. k-NN | Prepos. | Acc. k-NN | Prepos. | Acc. k-NN |
| FWHM – 2D PSF | 2.85 | 1.68 | 2.95 | 1.70 | - | - |
| FWTM – 2D PSF | 6.74 | 4.76 | 6.95 | 5.02 | - | - |
| $r_{50\%}$ | 0.99 | 0.82 | 1.03 | 0.84 | 1.9 | 1.62 |
| $r_{90\%}$ | 3.48 | 3.53 | 3.58 | 3.6 | 5.01 | 5.11 |
| MAE | 1.62 | 1.55 | 1.67 | 1.58 | 2.60 | 2.48 |

recent years statistical or machine-learning methods have made substantial steps forward towards a practical application, reducing their requirements in terms of calibration data and computational resources. Despite none of the proposed methods has been implemented in a real scanner yet, the new elements proposed in these works show interesting approaches that could be combined to obtain optimal positioning results with reasonable computational requirements. Among these innovations, the most interesting are the data reduction techniques (e.g. PCA), the more and more refined machine-learning techniques, the use of flood irradiations to calibrate DOI and time-of-interaction estimation methods (Chapter 3), and the use of pre-positioning methods based on analytical algorithms to reduce the calculation burden on the statistical and machine-learning techniques. Besides statistical or machine-learning methods, also optimized analytical method (e.g. the prepositioning method presented in Chapter 3) showed good results and may be a viable option in systems whose performance are not deteriorated by the limited degradation in the spatial resolution that they achieve.

## 6.3. Monolithic detectors for clinical PET scanners

### 6.3.1. Monolithic detectors for whole-body scanners

In Chapter 3, a monolithic scintillator detector designed for whole-body PET applications is fully characterized and the calibration and event-reconstruction methods developed to operate it are described in detail. As discussed in Chapter 1, section 1.3.1, detectors for this application should have excellent detector sensitivity (crystal thickness $\geq$ 20 mm), excellent CRT, good spatial resolution (2-3 mm FWHM) and good energy resolution ($\leq$ 12 %). Moreover, considering the large number of detectors required in a scanner, they should also be easy to be assembled and not too expensive, in order to limit the complexity and the cost of the system.

The detector presented in Chapter 3 is based on a wide monolithic crystal (32 mm × 32 mm × 22 mm, LYSO) read out from the back side by a DPC digital SiPM array, similar to the photosensor array used in commercial Vereos PET/CT scanners (Philips) [29]. When only events with complete light distributions are considered, the detector achieves a spatial resolution of 1.7 mm FWHM ($r_{50\%} \sim 0.83$ mm, MAE $\sim$ 1.57 mm), an average DOI resolution of 3.7 mm FWHM (MAE $\sim$ 2.23 mm), a CRT of 214 ps and an energy resolution of $\sim$9.9%. The performance of the detector are also characterized when events with a variable number of missing dies are used: with the detector settings and operating conditions used for the experimental characterization, a degradation of all the performance parameters <2% would be observed if events with up to four missing dies were accepted.

#### 6.3.1.1. Comparison with detectors used in commercial PET scanners

Compared to the detector modules currently used in commercial PET scanners and in the uEXPLORER scanner (see Chapter 1, Table 1.4), the back-side-readout (BSR) monolithic detector presented in Chapter 3 equals or outperforms them with respect to all the performance parameters. Considering the detector positioning accuracy, a direct comparison of the BSR monolithic detector spatial resolution with the crystal pitch used in pixelated detectors does not provide a complete comparison of their performances. However, it is reasonable to assume that the spatial resolution of the monolithic detector should be at least comparable with the resolution of the modules used in the Vision PET scanner (Siemens), having a crystal pitch of 3.2 mm, and of the uEXPLORER scanner, having a crystal pitch of 2.85 mm, which are the modules with the smallest crystal pitch among the currently available whole-body clinical TOF-PET scanners. The timing and energy resolution of the BSR monolithic detector are also comparable to the best values reported for commercial scanners, which correspond to a CRT of 210 ps for the Vision PET scanner (Siemens) and to an energy resolution equal to 9.5% for the Discovery MI PET/CT scanner (GE). The real advantage of the monolithic detector lies in its capability to estimate the DOI, which is not present in none of the modules employed in commercial scanner. This capability greatly improves the image spatial resolution in the outer regions of the FOV, as discussed in Chapter 55 and in section 6.4 of this chapter.

#### 6.3.1.2. Comparison with other monolithic detector prototypes

Compared to most of the other monolithic detector prototypes reported in literature or used in research and commercial scanners, the BSR detector presented in this thesis is one of the most sensitive ever presented. Most of the times, the thickness of monolithic detectors is limited to 12-15 mm in order to reduce the issues related to poor position reconstruction close to the crystal edges. In this work, a 22-mm-thick detector was chosen to achieve the sensitivity required in whole-body PET scanners, in which crystals with a thickness between 20 and 25 mm are usually employed (see Chapter 1, Table 1.4). The optimization of the position estimation methods made it possible to obtain a spatial resolution that is comparable with the resolution obtained with thinner detectors. For example, recently an xy spatial resolution of 1.55 mm FWHM ($r_{50\%}$ ~0.66 mm) for a 12 mm thick crystals [23] and of 1.8 mm FWHM for a 15 mm thick crystals [30] have been reported. Also the DOI resolution is comparable with the resolution reported for the 15 mm thick detector (3.7 mm FWHM), while it is slightly worse than the resolution achieved by the 12 mm thick detector (2.1 mm FWHM) [24], even if it can be considered comparable if only the volume of the crystal closest to the photosensor array is considered (see **Figure 4**, Chapter 3).

It is to be noted that promising results in terms of xy spatial resolution (~1.5 mm) and DOI resolution (~4 mm FWHM) have been reported for 20 mm thick monolithic scintillator detectors [31, 32]. However, in these works only the central part of the detector was considered in the characterization, excluding 5 mm of the crystal surface on each side. Therefore, a direct comparison with the detector presented in this thesis cannot be made.

One of the most distinctive characteristics of the detector presented in this thesis compared to the other thick monolithic detectors (≥15 mm) presented in literature is its excellent timing resolution. The timing properties of many monolithic detectors found in literature have not been optimized and the scanner based on them do not have TOF capabilities [15, 17, 18]. Only in Lamprou *et al.* [33] the TOF capability of a 15-mm-thick monolithic detector is investigated in depth: in this case, a modest CRT of ~500 ps is reported. The detector presented here achieves an excellent CRT of 214 ps. This is in agreement with previous results obtained with similar detectors based on 20 mm thick crystals made from Ca-codoped LSO:Ce [10], taking into account the slower decay time of the crystal used in this work.

#### 6.3.1.3. Comparison with pixelated detector prototypes

The detector presented in Chapter 1.4 shows a combination of characteristics that has not been matched yet even by prototype pixelated detectors developed for whole-body PET applications. A complete review of these prototypes is outside the scopes of this thesis, however few interesting examples will be discussed below in order to give an idea of the state of the art in this field.

For example, a high-resolution and high-sensitivity module has been presented by Marcinkowski *et al.* [34], based on 2 mm × 2 mm × 22 mm crystals. This module is based on the same photosensor used for the monolithic detector and has comparable or better spatial resolution. However, it has a slightly worse timing resolution (~300 ps), in part probably due also to the higher operating temperature (6-7 °C), and does not provide DOI information. A similar high-resolution detector based on 2 mm × 2 mm × 20 mm crystals and DPC sensors has also been presented in [35]. This detector features also DOI estimation capability, thanks to a special arrangement of the reflector between the crystals. However, its DOI resolution (4.67 mm) is slightly worse compared to the monolithic detector presented in Chapter 1.4 and the CRT is only 1.2 ns FWHM. This poor timing resolution might be partly explained by the higher operating temperature (0 °C) and by different sensor settings; however, it is probably also determined by the light-sharing technique used to obtain DOI estimation. A similar detector concept with DOI estimation capabilities has also been proposed by Kuang *et al.* [36], however also in that detector the final timing resolution (~500 ps) is worse compared to the BSR monolithic detector.

Another detector prototype with good spatial resolution, high sensitivity and DOI estimation capability has been presented in Hirano *et al.* [37]. This detectors is based on a position-sensitive PMT (PS-PMT) and on a stack of 4 crystal arrays, each one made of 16 × 16 GSO crystals having dimensions of 2.9 mm × 2.9 mm × 7.5 mm. Crystal identification is obtained through a special reflector arrangement that univocally positions each crystal in the 2D flood histogram. This detector was first developed for an in-beam PET prototype and then applied in several brain PET prototypes (see section 6.3.2). As a proof of concept, it was also tested in a whole-body PET scanner prototype [38] to experimentally demonstrate for the first time in a complete PET scanner that DOI-estimation capability improves the spatial resolution in the outer regions of the FOV (see section 6.4). However, the timing resolution of this detector is quite poor (>2 ns), also due to the scintillator material used (GSOZ). Therefore, despite the detector is interesting for the results obtained in the prototype scanner, it may not be a viable solution for modern whole-body TOF-PET systems.

Among the recently-developed pixelated detector prototypes with DOI estimation capabilities, one of the most promising one has been presented in Pizzichemi *et al.* [39] and in Stringhini *et al.* [40]. This prototype is based on a crystal array made of small (1.6 mm pitch) and relatively thick (15 mm) depolished LYSO:Ce crystals, coupled on one side with an SiPM array and on the other side with a glass light guide. Thanks to the depolished surfaces, the ratio of the amount of light extracted from the two ends of the crystals is strongly dependent on the DOI. The light extracted from the crystal side coupled with the photosensor makes possible to precisely determine the time and xy position of interaction. The light redirected and shared among multiple crystals by the light guide on top of the crystal array is used instead to estimate the DOI with an analytical method. This method uses as DOI measure the ratio between the light read by the SiPM directly coupled to the crystal and the total amount of light allows the detector to achieve a DOI resolution in the order of ~3 mm. In a following work, Pizzichemi *et al.* [41] demonstrated that the timing resolution of such a detector concept and of standard pixelated detectors without light sharing are equivalent, if appropriate methods to estimate the time of interaction are used. In particular, they demonstrated that even using this light-sharing technique it is still possible to achieve a CRT in the order of ~160 ps, both using crystal arrays based on small crystals (1.6 mm pitch) and arrays made of wider crystals (3.2 mm pitch). This result is remarkable, especially considering that standard LYSO:Ce crystals (not co-doped) are used in this word. Such a detector concept is therefore very promising both for organ-dedicated scanners and for whole-body scanners. However, whole-body scanners would require to use thicker crystals, in order to achieve the necessary sensitivity, which could deteriorate the timing and DOI performance. In Zatcepin *et al.* [42], further improvements in the DOI and timing resolution are obtained using statistical and machine-learning methods. However, these methods introduce further complications in the data analysis, as for monolithic crystals, and should therefore be optimized to be practically applicable in real scanners.

In conclusion, the detector presented in Chapter 3 presents one of the most interesting combinations of characteristics in the field of PET detectors for whole-body applications thanks to its high sensitivity, excellent timing and energy resolution, good spatial resolution and DOI estimation capability. This last characteristic in particular could provide significant improvements to the image quality of PET scanners compared to the current state-of-the-art detectors and is probably more relevant than a more extreme spatial resolution. Indeed, in a whole-body scanner the system spatial resolution is mainly limited by acollinearity and statistical noise, therefore an higher detector spatial resolution might not provide relevant benefits, whereas the DOI estimation capability can determine a significant improvement of the spatial resolution in the outer regions of the FOV (see Chapter 5).

### 6.3.2. Monolithic detectors for dedicated high-resolution clinical PET scanners

In Chapter 4, an ultrahigh-performance TOF/DOI PET detector is presented and fully characterized. This detector is developed for possible applications in high-resolution organ-dedicated clinical PET scanners, which are currently an active field of research in particular for brain [43] and breast [44, 45] imaging, or in dedicated high-resolution pediatric scanners, which are a new concept of scanners investigated in simulation studies [46]. The development of these scanners is motivated by the need for improved sensitivity and spatial resolution compared to whole-body scanners, in order to image smaller structures, reduce the dose delivered to patients (in particular to children and patients undergoing periodic screenings) and improve the temporal resolution (i.e. the time required to obtain an image) in dynamic studies.

Since these scanners usually have a small diameter (≤45 cm in organ-dedicated scanners), photon acollinearity poses lower limitations on image spatial resolution compared to whole-body scanners. Therefore, high detector spatial resolution is fundamental to pursue the best possible system performance. At the same time, parallax error is enhanced by the smaller scanner radius. Thus, good DOI estimation capability is also a strict requirement to obtain a good and more homogeneous image resolution in the whole FOV. Thick detectors (≥15/20 mm) are also crucial in these applications to achieve high sensitivity, even if sometimes a compromise is necessary if DOI estimation capability is absent or limited. Also in high-resolution scanners, TOF capability can be used to enhance the SNR of the final images, to improve the temporal resolution in dynamic studies or the reduce the dose delivered to patients. However, in comparison with whole-body scanners, a better detector timing resolution (≤200 ps FWHM) is required in high-resolution scanners to obtain a significant performance enhancement, due to the reduced diameter of the imaged objects (see Chapter 1, section 1.2.5). Considering that a reduced number of modules is needed, in dedicated high-resolution scanners a higher complexity and/or cost of the detectors (compared to detectors for whole-body PET) can be considered a suitable tradeoff if it determines a significant improvement in the final system performance.

The detector presented in Chapter 4 is based on a monolithic scintillator crystal (32 mm × 32 mm × 22 mm, LYSO) read out on two sides by DPC digital SiPM arrays. When only events with complete light distributions are considered, the detector achieves a spatial resolution of 1.1 mm FWHM ($r_{50\%}$ ~0.43 mm, MAE ~1.18 mm), an average DOI resolution of 2.4 mm FWHM (MAE ~1.4 mm), a CRT of 147 ps and an energy resolution of ~10.2%. When events with up to six missing dies are accepted (using the detector settings and operating conditions employed for the experimental characterization), no substantial deterioration of these results is determined.

Compared to pixelated detectors used in commercial or prototype brain and breast scanners, the dual-sided readout (DSR) monolithic detector presented in Chapter 4 equals or outperforms most of them in their performance characteristics. For a quick comparison, a summary of the specifications of some of the most advanced pixelated detectors used in those scanners is reported in Table 6.2. A recent and more comprehensive review of the scanners developed for brain imaging can be found in [43], whereas an extensive review of the scanners developed for breast imaging can be found in Hsu *et al.* [45].

As shown in Table 6.2, the xy crystal pitch of those detectors is comprised between 1.2 mm and ~3 mm and most of them are based on crystal arrays composed of several layers, whose thickness is comprised between 3 and 10 mm. In multi-layer detectors, DOI is usually estimated identifying the layer in which the

Table 6.2: Characteristics of some of the most advanced pixelated detectors used in commercial or prototype brain and breast scanners.

| Scanner | Brain / breast | Crystal dimensions (mm3) | Array dimensions | DOI layers | DOI technique | Photosensor | Crystal material |
|---|---|---|---|---|---|---|---|
| ECAT-HRRT [47, 48] | Brain | 2.1×2.1×7.5 | 8×8 | 2 | Phoswich | PMT | LSO |
| jPET-D4 [49] | Brain | 2.9×2.9×7.5 | 16×16 | 4 | Phoswich + reflector arrangement | PS-PMT | GSO |
| NEURO-PET [50] | Brain | 2.3×2.3×10 | 22×22 (inner)<br>21×21 (outer) | 2 | Offset arrays | SiPM | LYSO |
| Brain PET - HAMAMATSU [51] | Brain | 1.2×1.2×3/4/5/8 | 32×32 | 4 | 4 independent arrays | SiPM | LYSO |
| Brain PET - PRESCIENT IMAGING [43] | Brain | 1.76×1.76×? | 14×14 (inner)<br>13×13 (outer) | 2 | Offset arrays | SiPM | LFS |
| HELMET PET [52, 53] | Brain | 1.5×1.5×10 | 32×32 | 1 | - | SiPM | LYSO |
| HEMISPHERE+CHIN [37, 54] | Brain | 2.8×2.8×7.5 | 16×16 | 4 | Reflector arrangement | PS-PMT | GSO |
| ADD-ON PET (MR-compatible) [55] | Brain | 2×2×5 | 19×6×4 | 4 | Reflector arrangement | SiPM | LYSO |
| Shimazdu Breast PET [56] | Breast | 1.44×1.44×4.5 | 32×32×4 | 4 | Reflector arrangement | PS-PMT | LGSO |
| Clear PEM [57, 58] | Breast | 2×2×20 | 4×8×1 | ~2 mm FWHM | Double-side pixel readout (continuous DOI estimation) | APD | LYSO |

interaction occurs by means of the phoswich technique or of several light sharing methods, e.g. introducing a special reflector arrangement or shifting the position of the crystal layers. However, other DOI estimation techniques are also used, e.g. using several independent detectors stacked one on top of each other (Brain PET – Hamamatsu). The only detector that uses a different approach for DOI estimation is the detector used in the ClearPEM system, which is based on long crystal pixels (20 mm) read out on two sides. In this detector, a continuous DOI estimation is obtained using the ratio of the light extracted from each crystal side as DOI measure and a DOI resolution ~2 mm FWHM is achieved. As also discussed in the previous section, a direct comparison of the 3D crystal pitch used in pixelated DOI detectors with the spatial resolution and DOI resolution of a monolithic detector does not provide an accurate comparison of their performance. However, it is reasonable to assume that the DSR-detector spatial resolution and DOI resolution are comparable if not better than those of the detectors shown in Table 6.2, since the smallest crystal pitch in the xy direction is 1.5 mm and in the z direction is 5 mm.

Only the prototype detector module developed by Hamamatsu and presented in Watanabe *et al.* [51] could have a spatial and DOI resolution that is comparable (at least for the thinnest crystal layers) with the DSR monolithic detector. However, this module is composed of a stack of four independent detectors, each one based on an SiPM array and on an arrays of 1.2 mm × 1.2 mm crystals with variable thickness (3/4/5/8 mm). Therefore, the monolithic DSR detector is probably less complex to assemble and less expensive.

As regards sensitivity, the modules based on LSO/LYSO that are reported in Table 6.2 have a total crystal thickness comprised between 10 mm and 20 mm, therefore the DSR monolithic detector has a sensitivity that is equivalent or higher compared to them. The modules based on GSO, instead, are built using a thicker crystal array (30 mm); however, they have a similar or just slightly higher sensitivity compared to the monolithic detector, since GSO crystals are less dense than LYSO/LSO crystals.

The characteristic that makes the DSR monolithic detector superior compared to the modules presented in Table 6.2 is its outstanding timing resolution of ~150 ps (with a non-codoped LYSO crystal). This CRT could substantially improve the image SNR also in small-diameter scanners, whereas none of the detectors used in brain and breast scanners have a timing resolution that enables the systems to use the TOF technique. In many cases, this is probably due to the complex crystal geometry and reflector arrangement used to obtain DOI estimation, which make light extraction slower and less efficient and therefore deteriorate the intrinsic timing capabilities of the detectors. Only the detector presented in Watanabe *et al.* [51] could potentially achieve a good CRT, since it is based on thin crystals and SiPMs: however in that system the readout electronics is not optimized for timing.

Among the pixelated detector prototypes developed for high-resolution scanners, one of the most interesting is the small-crystal detector presented in Pizzichemi *et al.* [41], which is also mentioned in section 6.3.1.3. This detector is based on 1.5 mm crystals read out from a single side and achieves a DOI resolution in the order of 3 mm and a CRT in the order of 160 ps. Compared to the DSR monolithic detector, this prototype shows almost comparable (even if slightly worse) spatial and timing resolution. However, it is based on 15 mm crystals, therefore is has lower sensitivity. The single-side readout configuration of this prototype is an advantage oved the dual-side readout configuration of the monolithic detector, since it requires to cover a smaller surface with SiPMs. However, to achieve these performance the prototype uses small SiPM pixels, having a 3 mm pitch versus the 4 mm pixel pitch of the dSiPMs used in the DSR monolithic detector, which translates in an almost equivalent number of channel for an equivalent detector surface. Moreover, also the DOI estimation technique used in the pixelated detector seem to provide the best performance when more refined estimation techniques based on machine learning are used [42]. Therefore, this prototype might not be significantly more practical to be operated compared to the DSR monolithic detector.

Several high-resolution scanners based on monolithic crystals and dedicated to brain and breast imaging have also been developed in recent years by the i3M research group in Valencia and by the company Oncovision. The systems developed for breast imaging are the MAMMI dedicated breast PET scanner [15], which is commercially available, and the MAMMOCARE PET prototype [16], an improved version of the MAMMI PET scanner that integrates a biopsy system. The systems developed for brain imaging are the CareMiBrain dedicated brain PET scanner [18], which is also commercially available, and the MINDView PET scanner [17], a prototype system that can be used as an insert in an MRI scanner for simultaneous PET and MR imaging. The detectors used in the brain scanners are the most advanced ones and differentiate for their thickness, since in the CareMiBrain scanner 15-mm-thick crystals are used [30], whereas the MINDView PET scanner is based on 20-mm-thick crystals [32]. As also reported in section 6.3.1.2, promising results have been claimed for these detectors in terms of xy spatial resolution (~1.5 mm) and DOI resolution (~4 mm FWHM). However, the DSR monolithic detector has better overall spatial resolution compared to these detectors. Moreover, it does not show the same limitations in the positioning accuracy in the border regions. As also discussed for pixelated detectors, the characteristic that truly makes the DSR monolithic detector superior compared to the other monolithic detectors is its timing resolution, since none of them can achieve timing performance that make possible to use the TOF technique.

In conclusions, the detector presented in Chapter 4 has optimal characteristics for being used in dedicated high-resolution scanners and equals or outperforms all the detector developed for these applications, either based on pixelated or monolithic crystals. The DSR monolithic detectors combines excellent spatial resolution (xy and DOI), high sensitivity, very good energy resolution and state-of-the-art timing resolution, which could be further improved using Ca-codoped L(Y)SO crystals. This last characteristic in particular could determine sensible improvements in the performance of high-resolution scanners, since it would make possible to fully exploit the TOF technique also in small-diameter systems. The dual-side readout configuration makes the detector more expensive and more challenging to be operated compared to detectors that have a single-side readout. However, the DSR monolithic detectors can achieve excellent performance also using photosensors with a rather large pixel pitch (4 mm), therefore it has a channel density which is comparable with other high-resolution detectors read out from a single side. In any case, the drawbacks of the DSR configuration are compensated by a significant improvement of the detector performance, which could significantly boost also the scanner performance. Therefore, the detector presented in Chapter 4 is an interesting prototype for high-resolution applications, as demonstrated also in a recent simulation study regarding the optimization of a pediatric scanner [46].

## 6.4. Imaging performance of BSR monolithic detectors and comparison with current PET scanners

The BSR monolithic detector presented in Chapter 3 was developed specifically for whole-body clinical PET scanners. As discussed in Chapter 1 (section 1.3.1), detectors for this application are required to have excellent sensitivity (crystal thickness ≥20 mm), excellent CRT, good energy resolution (≤12 %), good spatial resolution (2-3 mm FWHM), and, if possible, DOI estimation capability. Despite none of the commercially-available whole-body scanners is based on detectors that have this capability, its importance has been shown in several simulation studies. These studies demonstrated that DOI estimation can improve the image spatial resolution in the outer region of the FOV and make the image quality more homogeneous throughout the whole FOV [59, 60].

To conclude this research work, in Chapter 5 the imaging capabilities of the BSR monolithic detector are investigated in a 70 cm diameter PET geometry. Two complete PET modules based on such detectors are developed and employed in a tomographic setup representative of a whole-body clinical scanner. The fully automated setup, based on two coaxially rotating arms and a central rotating phantom table, sequentially acquires all possible LORs of a complete detector ring, using a step-and-shoot acquisition approach.

During the system characterization procedure, a complete tomographic acquisition of a $^{22}$Na point source positioned at the center of the FOV is used to determine the timing and energy resolution of the system, which achieves a CRT of ~212 ps FWHM and an energy resolution of 10.2%.

The system spatial resolution is quantitatively assessed imaging the $^{22}$Na point source at different radial distances from the system axis and reconstructing the images using 2D filtered-back-projection (FBP) method, adapting the standard NEMA procedure [61] to the particular characteristics of the tomographic system. An excellent radial and tangential resolution of ~2.9 mm are obtained at the center of the imaged region. Thanks to the DOI estimation capability of the monolithic detectors, the resolution remains almost constant in the whole FOV: at a radial distance of 20 cm, the radial and tangential spatial resolutions are 3.2 mm and 4.0 mm, respectively, whereas at 25 cm they become 3.3 mm and 4.7 mm. For comparison, when no DOI information is used to reconstruct the same datasets, at a radial distance of 20 cm the radial and tangential spatial resolutions degrade to 7.0 mm and 4.9 mm, respectively, whereas at 25 cm they become 8.8 mm and 9.0 mm.

The system spatial resolution is also qualitatively assessed by imaging a Derenzo-like phantom at different locations within the FOV. The images, which are reconstructed using a TOF maximum-likelihood expectation-maximization (ML-EM) method, show that the system is able to resolve 3-mm-diameter hot rods up to 25 cm radial distance.

These results can be compared with the performance of current state-of-the-art commercial scanners, which are summarized in Chapter 1, Table 1.4. The tomographic system based on monolithic detectors equals or outperforms all of them in terms of timing and energy resolution. Only the Vision scanner (Siemens) achieves a similar CRT of 210 ps, whereas the Cartesian Prime scanner (Canon) has a comparable CRT of 255 ps. The VEREOS system (Philips), which is based on the same DPC sensors used for the monolithic BSR detectors, has a timing resolution of ~310 ps and all the other scanners have a CRT in the order of ~400 ps. As for the energy resolution, the Discovery MI and the Signa scanners (GE) achieve an energy resolution of 9.5% and 10.3%, respectively, which are slightly better or comparable to the resolution obtained with the scanner based on monolithic detectors. All the other scanners, instead, have an energy resolution ≥11%.

The system based on monolithic detectors achieves similar or better results than commercial scanners also in terms of spatial resolution. At the center of the FOV, where the monolithic-detector scanner achieves an average transaxial spatial resolution of ~2.9 mm, resolutions ≥3.5 mm are reported for most of commercial scanners. Only the the uMI500 (United Imaging) and the uEXPLORER (United Imaging) scanners achieve a comparable average transaxial resolution of ~3.0 mm, thanks to the small crystal pixels employed in those systems. At 10 cm radial distance from the center of the FOV, the radial and tangential resolution of commercial scanners is in the range of 3.3-5.8 mm and 3.1-4.6 mm, respectively, whereas the system based on monolithic detectors has a radial and tangential resolution of 3.0 mm and 3.5 mm. At 20 cm radial distance, the radial and tangential resolutions of commercial scanners are in the range of 4.1-8.4 mm and 3.6-5.2 mm, respectively, whereas the tomographic system presented in this thesis has a radial and tangential resolution of 3.2 mm and 4.0 mm. Especially if we consider the radial resolution, which deteriorates more significantly with radial distance, the system based on monolithic detectors can achieve better results than commercial scanners thanks to its DOI estimation capability. The effectiveness of this characteristic can be further stressed considering that the system presented in this thesis has a smaller diameter (70 cm) and uses thicker crystals (22 mm) compared to the Vereos (Philips), the Vision (Siemens), the uMI550 (United Imaging) and the uEXPLORER (United Imaging) systems, which are the commercial systems providing the best spatial performance.

The performance of the monolithic-detector system can be also compared with some recent PET scanner prototypes. The first of them is the so-called PennPET Explorer, a long-axial-FOV system based on the Vereos PET scanner technology [62]. The spatial resolution reported for this scanner at the center of the FOV is 4.2 mm / 3.9 mm / 4.1 mm in the radial / tangential / axial direction, respectively, and the energy resolution is ~12%,. These results are similar to those obtained with the VEREOS scanner. Besides the increased sensitivity, the major improvement of this system compared to the Vereos is its timing resolution: thanks to a better cooling system, in the PennPET Explorer scanner the DPC sensors can be operated at lower temperature (~5 °C) and therefore with a lower trigger threshold, allowing the system to achieve a CRT of 256 ps at low activities. Compared to the PennPET Explorer, the system based on monolithic detectors can achieve a better spatial and energy resolution and a slightly better CRT, even if this last results is favored also by the lower temperature at which the monolithic detectors are operated.

Another interesting PET scanner prototype has been recently presented by Akamatsu *et al.* [38]. The system is based on the detector module presented in Hirano *et al.* [37], which were mainly developed for brain-PET applications and are also described in section 6.3.1.3 of this Chapter. The overall performance of the scanner are limited by the limited performance of the detectors, in particular in terms of timing resolution and, to a lesser extent, of positioning accuracy, mainly due to the complex structure of the crystal array and to the chosen scintillator material. However, it is interesting to report the results obtained with this system in terms of spatial resolution because this is the first complete whole-body scanner based on pixelated detectors with DOI estimation capability. At 1 cm from the center of the FOV, a radial resolution of 4.1 mm is reported, which degrades to 4.8 mm at 10 cm and to 5.9 mm at 20 cm. If no DOI information is used, the radial resolution degrades to 6.9 mm at 10 cm and to 11.4 mm at 20 cm. These are meaningful results to demonstrate the effectiveness of DOI estimation in improving image quality in the outer part of the FOV, especially considering the small diameter of the detector ring (66 cm), and support the findings obtained with the tomographic system based on monolithic detectors.

Finally, another scanner prototype worth to be mentioned has been reported in Wong *et al.* [63]. Despite the scanner has been developed as a low-cost system and is based on PMTs, it can achieve an excellent spatial resolution. At the center of the FOV, a transaxial resolution of 2.87 mm is reported, which becomes 3.40 mm, 3.69 mm and 3.91 mm at a radial distance of 16 cm, 24 cm and 28 cm, respectively. These results are remarkable and are made possible by the small dimension and the reduced thickness of the crystal pixels (2.44 mm pitch, 15.2 mm thickness) and by the large ring diameter (87 cm). The system also achieves a fair timing resolution (473 ps) and a reasonable energy resolution (11.2%). Compared to the tomographic system based on monolithic detectors, the system developed by Wong *et al.* achieves a comparable or even better spatial resolution, especially at larger radial distances. However, this system has a worse timing resolution, lower detector sensitivity and a large ring diameter, which also decreases the scanner sensitivity. Therefore, the overall imaging performance might be limited with respect to a system based on monolithic detectors, especially in terms of statistical noise and signal-to-noise ratio.

In conclusion, the tomographic system presented in Chapter 5 demonstrates that monolithic detectors are a very interesting option for whole-body PET applications. The system achieves a spatial resolution that is comparable or better than the resolution of current state-of-the-art commercial and prototype scanners at the center of the FOV. Moreover, thanks to its DOI estimation capability, it has an excellent spatial resolution also in the outer regions of the FOV, despite its reduced ring diameter in comparison to most of the other scanners. Finally, the monolithic detectors used in the system can guarantee an high sensitivity and achieve an excellent timing resolution. Therefore, it would be interesting to develop a complete prototype scanner based on this type of detectors, to study the other system performance (sensitivity, counting rate statistics, etc.) and bring this technology closer to clinical applications.

## 6.5. Final considerations and outlook - The prospects of monolithic detectors for clinical PET

In the previous sections the most important findings of this thesis have been reviewed and summarized, extending the discussion of these results also to the most recent experimental works presented by other research groups after the papers constituting the central part of this thesis were published.

As discussed in section 6.1 of this Chapter, two issues hampered the use of monolithic detectors in clinical systems at the beginning of the 2010's, namely the lack of practical calibration procedures and position estimation algorithms. Thanks to the new findings presented in recent years, several of which have been introduced in this work, these issues can be considered solved or close to be solved today.

In Chapters 2 and 3 of this thesis (and in other research works) it has been demonstrated that fan-beam irradiations and flood irradiations can provide proper reference data for a complete detector calibration, without degrading the performance compared to pencil-beam irradiations. A remaining challenge is the development of methods for detector quality assurance and detector calibration in an assembled scanner. Flood irradiations using point sources, line sources or homogeneous phantoms cannot be used in a straightforward way for such checks in complete systems based on monolithic detectors, contrary to systems based on pixelated detectors. However, as discussed also in section 6.2.1 of this Chapter, the use of mechanical and electronic collimation could make it possible to obtain reference datasets similar to a fan-beam irradiation also in complete PET scanners. In combination with optimized analysis algorithms, these datasets would provide the required information to perform quality assurance and calibration checks. This approach should be investigated in more detail and for different possible scanner geometries, however preliminary considerations showed its feasibility (V. Tabacchini, private communication).

As regards the position and time estimation algorithms, a number of statistical and machine-learning methods have already demonstrated very promising results for developing algorithms that can provide the best detector performance using computational and memory requirements compatible with a real PET scanner. In particular, there are several approaches that could be combined to achieve this goal. In my opinion, the most interesting are: position pre-estimation using simple analytical algorithms, in order to reduce the computational burden of statistical and machine-learning algorithms; data compression, using principal-component analysis or similar techniques; machine-learning methods with reduced computational requirements, such as neural networks or gradient-tree boosting. Therefore, it can be expected that this goal will be achieved soon, also considering that machine-learning methods are rapidly evolving since they are an active topic of research for many other applications. In any case, as discussed in section 6.2.2 of this Chapter, it is already possible to implement analytical methods that can be used in real systems, at the expense of a limited deterioration of the performance.

The results presented in Chapters 3 and Chapter 4 of this thesis, reviewed also in section 6.3 of this chapter, show that monolithic detectors can equal or outperform current state-of-the-art pixelated detectors, both for whole-body and for organ-specific high-resolution PET applications. In particular, their peculiar characteristic is that they can combine high sensitivity, remarkable spatial resolution, DOI estimation, excellent timing performance, and good energy resolution, also using a single-sided readout architecture. DOI estimation in particular would be an important feature for modern scanners with long axial field-of-view, since it would allow these systems to accept coincidences with larger incidence angle, further improving the sensitivity without degrading the system resolution. A similar combination of characteristics is difficult to be obtained in pixelated detectors and in any case would require complex light-sharing and position reconstruction techniques, making their employment at least as challenging as for monolithic detectors.

Tabacchini *et al.* [64] used the experimental characterization of the BSR and DSR monolithic detectors (Chapters 3 and Chapter 4 of this thesis) to model their spatial responses and simulate their imaging performance in a clinical PET system. They concluded that at scanner level the imaging capabilities of these detectors are equivalent to pixelated detectors that have a crystal pitch of 3.2 mm and 1.3 mm, respectively, as well as the same crystal thickness (22 mm) and the capability to classify the position of interaction in three DOI layers. Currently, only the Vision PET/CT scanner (Siemens) and the scanners produced by United Imaging (uMI550 PET/CT and uEXPLORER PET/CT) have a pixel pitch equal or smaller than 3.2 mm, that is, 3.2 mm and 2.85 mm, respectively (see Chapter 1, Table 1.4). However, they all have lower sensitivity, they do not have DOI estimation capability, and the United Imaging scanners have worse timing resolution. Therefore, a complete PET scanner based on the BSR detector can be expected to achieve overall imaging capabilities that should be better than current commercial scanners.

Indeed, the measurements presented in Chapter 5 with a tomographic setup based on the BSR detector demonstrate that a clinical whole-body PET scanner based on such technology could improve the performance of current commercial scanners. In particular, the characterization of the system spatial resolution using point sources shows that monolithic detectors can obtain an excellent and almost homogeneous resolution across the whole FOV, thanks to their DOI estimation capability. This characteristic, combined with the excellent timing resolution and high sensitivity, makes the BSR monolithic detector a very promising technology for whole-body and total-body PET scanners.

From the system point of view, monolithic detectors pose few additional challenges compared to detectors based on crystal arrays. In standard pixelated detectors, the light signal is usually read on a single or on a limited number of photosensor channels. In monolithic detectors, instead, the light signal is spread on a wider photodetector area and is therefore affected by the noise of a larger number of channels. Because of this reason, monolithic detectors require a photosensor with low noise and high PDE to achieve the best performance, and also optimized readout electronics. These requirements are necessary to obtain a good SNR on all the photosensor channels, in order to precisely sample the light distribution and to acquire accurate timestamps on multiple pixels. In this work, the DPC3200-22-44 digital SiPMs arrays (Philips) have been used to build monolithic detectors. These sensors were chosen because they have a good PDE, good timing performance, and because they have an integrated readout and time-pick-off system. This last characteristic in particular simplified the development of the monolithic scintillator detector prototypes, which require advanced readout electronics for a large number of channels. To obtain the best timing performance, the detectors were operated at low temperature (about -20/-15 °C in the tomographic setup) so that the lowest trigger level could be used without an excessive number of false triggers due to dark counts. This is a challenging requirement, however it should be achievable also at system level with a proper design of the cooling system. For example, the PennPET Explorer scanner (which is based on the same DPC sensors) has been designed to be operated at about 0/5 °C [62], demonstrating that PET systems can be successfully operated at temperatures lower than the ones used in current commercial scanners (usually running at a temperature ≥15 °C). In any case, the cooling requirements could be reduced using different, more recent SiPM technologies. In particular, state-of-the-art analog SiPMs have a much lower DCR compared to dSiPM, since they are produced using custom processes which determine a lower noise compared to the more complex processes required to produce dSiPM with integrated readout electronics. Most recent analog SiPMs have also excellent PDE [65] and SPTR [66]: these characteristics, in combination with state-of-the-art low-noise multichannel readout ASICs, could make it possible to develop monolithic detectors with even better performance compared to the detectors presented in Chapter 3 and Chapter 4.

In conclusion, the results presented in this thesis and in other recent papers demonstrate that it is possible to develop practical techniques to operate monolithic scintillator detectors in clinical PET systems. Using standard scintillation material (LYSO:Ce) and a digital SiPM array already employed in commercial scanners, it is possible to develop detectors which overall outperform the detectors currently employed in commercial whole-body and organ-dedicated scanners, and also most of the prototype detectors presented in literature. The results obtained with the tomographic setup presented in Chapter 5 confirm that a scanner based on a BSR monolithic detector could achieve superior imaging performance compared to current state-of-the-art whole-body scanners based on pixelated detectors, since the monolithic detector has similar timing and positioning performance, better sensitivity and DOI estimation capability. Even better performance could be obtained with reasonable developments, using most recent scintillation materials (L(Y)SO:Ce,Ca) and state-of-the-art SiPM technologies and ASICs.

Therefore, monolithic scintillator detectors could be the enabling technology to develop the next generation of clinical PET scanners, both for whole-body or high-resolution systems. In whole-body and total-body scanners, back-sided-readout monolithic detectors could make it possible to achieve a system CRT ≤150 ps and an image spatial resolution approaching the limit set by physical constraints (~2-2.5 mm), whereas in organ-dedicated scanners dual-sided readout detectors could enable the system to achieve a timing resolution ≤100 ps and an image spatial resolution ~1 mm. In both cases, these results could be obtained in combination with a very high sensitivity (22-mm-thick crystals) and an almost homogeneous spatial resolution throughout the whole FOV, thanks to the DOI estimation capability. Such scanners would significantly improve the diagnostic capability of current commercial scanners, opening up new clinical and research applications.

## References

[1] P. Bruyndonckx, S. Leonard, L. Jiangui, S. Tavernier, P. Szupryczynski, and A. Fedorov, *Study of spatial resolution and depth of interaction of apd-based pet detector modules using light sharing schemes,* Nuclear Science, IEEE Transactions on **50**, 1415 (2003).

[2] P. Bruyndonckx, C. Lemaitre, S. Leonard, D. R. Schaart, D. J. van der Laan, M. C. Maas, O. Devroede, W. Yibao, M. Krieguer, and S. Tavernier, *Initial characterization of a nonpixelated scintillator detector in a pet prototype demonstrator,* Nuclear Science, IEEE Transactions on **53**, 2543 (2006).

[3] T. Ling, K. Lee, and R. Miyaoka, *Performance comparisons of continuous miniature crystal element (cmice) detectors,* Nuclear Science, IEEE Transactions on **53**, 2513 (2006).

[4] M. C. Maas, D. Van der Laan, D. R. Schaart, J. Huizenga, J. C. Brouwer, P. Bruyndonckx, S. Leonard, C. Lemaitre, and C. W. E. Van Eijk, *Experimental characterization of monolithic-crystal small animal pet detectors read out by apd arrays,* Nuclear Science, IEEE Transactions on **53**, 1071 (2006).

[5] R. S. Miyaoka, X. Li, W. Hunter, L. A. Pierce, W. McDougald, P. E. Kinahan, and T. K. Lewellen, *Resolution properties of a prototype continuous miniature crystal element (cmice) scanner,* Nuclear Science, IEEE Transactions on **58**, 2244 (2011).

[6] S. Seifert, H. T. v. Dam, J. Huizenga, R. Vinke, P. Dendooven, H. Löhner, and D. R. Schaart, *Monolithic labr 3 :ce crystals on silicon photomultiplier arrays for time-of-flight positron emission tomography,* Physics in Medicine and Biology **57**, 2219 (2012).

[7] S. Seifert, G. v. d. Lei, H. T. v. Dam, and D. R. Schaart, *First characterization of a digital sipm based time-of-flight pet detector with 1 mm spatial resolution,* Physics in Medicine and Biology **58**, 3061 (2013).

[8] T. Ling, T. K. Lewellen, and R. S. Miyaoka, *Depth of interaction decoding of a continuous crystal detector module,* Physics in Medicine and Biology **52**, 2213 (2007).

[9] H. T. van Dam, S. Seifert, R. Vinke, P. Dendooven, H. Löhner, F. J. Beekman, and D. R. Schaart, *A practical method for depth of interaction determination in monolithic scintillator pet detectors,* Physics in Medicine and Biology **56**, 4135 (2011).

[10] H. T. van Dam, G. Borghi, S. Seifert, and D. R. Schaart, *Sub-200 ps crt in monolithic scintillator pet detectors using digital sipm arrays and maximum likelihood interaction time estimation,* Physics in Medicine and Biology **58**, 3243 (2013).

[11] F. Sánchez, A. Orero, A. Soriano, C. Correcher, P. Conde, A. González, L. Hernández, L. Moliner, M. J. Rodríguez-Alvarez, L. F. Vidal, J. M. Benlloch, S. E. Chapman, and W. M. Leevy, *Albira: A small animal pet/spect/ct imaging system*, Medical Physics **40**, 051906 (2013).

[12] A. J. González, A. Aguilar, P. Conde, L. Hernández, L. Moliner, L. F. Vidal, F. Sánchez, S. Sánchez, C. Correcher, C. Molinos, J. Barberá, K. Lankes, S. Junge, T. Bruckbauer, P. Bruyndonckx, and J. M. Benlloch, *A pet design based on sipm and monolithic lyso crystals: Performance evaluation*, IEEE Transactions on Nuclear Science **63**, 2471 (2016).

[13] P. Mollet, K. Deprez, B. Vandeghinste, S. Neyt, R. Marcinkowski, S. Vandenberghe, and R. Van Holen, *The β-cube, a high-end compact preclinical benchtop pet for total body imaging*, Journal of Nuclear Medicine **58**, 393 (2017).

[14] S. Krishnamoorthy, E. Blankemeyer, P. Mollet, S. Surti, R. V. Holen, and J. S. Karp, *Performance evaluation of the MOLECUBES β-CUBE—a high spatial resolution and high sensitivity small animal PET scanner utilizing monolithic LYSO scintillation detectors*, Physics in Medicine & Biology **63**, 155013 (2018).

[15] L. Moliner, A. J. González, A. Soriano, F. Sánchez, C. Correcher, A. Orero, M. Carles, L. F. Vidal, J. Barberá, L. Caballero, M. Seimetz, C. Vázquez, and J. M. Benlloch, *Design and evaluation of the mammi dedicated breast pet*, Medical Physics **39**, 5393 (2012).

[16] L. Moliner, C. Correcher, D. Hellingman, J. Alamo, V. Carrilero, A. Orero, A. J. González, and J. M. Benlloch, *Performance characteristics of the mammocare pet system based on nema standard*, Journal of Instrumentation **12**, C01014 (2017).

[17] A. J. Gonzalez, A. Gonzalez-Montoro, L. F. Vidal, J. Barbera, S. Aussenhofer, L. Hernandez, L. Moliner, F. Sanchez, C. Correcher, E. J. Pincay, G. Cañizares, E. Lamprou, S. Sanchez, J. V. Catret, S. Jiménez-Serrano, J. Cabello, M. Schwaiger, A. Iborra, T. Merlin, D. Visvikis, and J. M. Benlloch, *Initial results of the mindview pet insert inside the 3t mmr*, IEEE Transactions on Radiation and Plasma Medical Sciences **3**, 343 (2019).

[18] L. Moliner, M. J. Rodríguez-Alvarez, J. V. Catret, A. González, V. Ilisie, and J. M. Benlloch, *Nema performance evaluation of caremibrain dedicated brain pet and comparison with the whole-body and dedicated brain pet systems*, Scientific Reports **9**, 15484 (2019).

[19] P. Bruyndonckx, S. Leonard, S. Tavernier, C. Lemaitre, O. Devroede, Y. Wu, and M. Krieguer, *Neural network-based position estimators for pet detectors using monolithic lso blocks*, Nuclear Science, IEEE Transactions on **51**, 2520 (2004).

[20] P. Bruyndonckx, C. Lemaitre, D. J. van der Laan, M. Maas, D. Schaart, W. Yonggang, L. Zhi, M. Krieguer, and S. Tavernier, *Evaluation of machine learning*

*algorithms for localization of photons in undivided scintillator blocks for pet detectors,* Nuclear Science, IEEE Transactions on **55**, 918 (2008).

[21] Y. Wang, W. Zhu, X. Cheng, and D. Li, *3d position estimation using an artificial neural network for a continuous scintillator pet detector,* Physics in Medicine and Biology **58**, 1375 (2013).

[22] H. T. van Dam, S. Seifert, R. Vinke, P. Dendooven, H. Löhner, F. J. Beekman, and D. R. Schaart, *Improved nearest neighbor methods for gamma photon interaction position determination in monolithic scintillator pet detectors,* Nuclear Science, IEEE Transactions on **58**, 2139 (2011).

[23] F. Müller, D. Schug, P. Hallen, J. Grahe, and V. Schulz, *Gradient tree boosting-based positioning method for monolithic scintillator crystals in positron emission tomography,* IEEE Transactions on Radiation and Plasma Medical Sciences **2**, 411 (2018).

[24] F. Müller, D. Schug, P. Hallen, J. Grahe, and V. Schulz, *A novel doi positioning algorithm for monolithic scintillator crystals in pet based on gradient tree boosting,* IEEE Transactions on Radiation and Plasma Medical Sciences **3**, 465 (2019).

[25] S. España, K. Deprez, R. V. Holen, and S. Vandenberghe, *Fast calibration of spect monolithic scintillation detectors using un-collimated sources,* Physics in Medicine and Biology **58**, 4807 (2013).

[26] A. Iborra, A. J. González, A. González-Montoro, A. Bousse, and D. Visvikis, *Ensemble of neural networks for 3d position estimation in monolithic PET detectors,* Physics in Medicine & Biology **64**, 195010 (2019).

[27] D. J. van der Laan, M. C. Maas, P. Bruyndonckx, and D. R. Schaart, *Limits on the spatial resolution of monolithic scintillators read out by apd arrays,* Physics in Medicine and Biology **57**, 6479 (2012).

[28] L. A. Pierce, S. Pedemonte, D. DeWitt, L. MacDonald, W. C. J. Hunter, K. V. Leemput, and R. Miyaoka, *Characterization of highly multiplexed monolithic PET / gamma camera detector modules,* Physics in Medicine & Biology **63**, 075017 (2018).

[29] I. Rausch, A. Ruiz, I. Valverde-Pascual, J. Cal-González, T. Beyer, and I. Carrio, *Performance evaluation of the vereos pet/ct system according to the nema nu2-2012 standard,* Journal of Nuclear Medicine **60**, 561 (2019).

[30] A. González-Montoro, F. Sánchez, R. Martí, L. Hernández, A. Aguilar, J. Barberá, J. V. Catret, G. Cañizares, P. Conde, E. Lamprou, F. Martos, S. Sánchez, L. F. Vidal, J. M. Benlloch, and A. J. González, *Detector block performance based on a monolithic lyso crystal using a novel signal multiplexing method,* Nuclear Instruments and Methods in Physics Research Section A: Accelerators, Spectrometers, Detectors and Associated Equipment **912**, 372 (2018).

[31] A. J. González, S. Majewski, F. Sánchez, S. Aussenhofer, A. Aguilar, P. Conde, L. Hernández, L. F. Vidal, R. Pani, M. Bettiol, A. Fabbri, J. Bert, D. Visvikis, C. Jackson, J. Murphy, K. O'Neill, and J. M. Benlloch, *The mindview brain pet detector, feasibility study based on sipm arrays,* Nuclear Instruments and Methods in Physics Research Section A: Accelerators, Spectrometers, Detectors and Associated Equipment **818**, 82 (2016).

[32] A. González-Montoro, A. Aguilar, G. Cañizares, P. Conde, L. Hernández, L. F. Vidal, M. Galasso, A. Fabbri, F. Sánchez, J. M. Benlloch, and A. J. González, *Performance study of a large monolithic lyso pet detector with accurate photon doi using retroreflector layers,* IEEE Transactions on Radiation and Plasma Medical Sciences **1**, 229 (2017).

[33] E. Lamprou, A. J. Gonzalez, F. Sanchez, and J. M. Benlloch, *Exploring tof capabilities of pet detector blocks based on large monolithic crystals and analog sipms,* Physica Medica **70**, 10 (2020).

[34] R. Marcinkowski, S. España, R. V. Holen, and S. Vandenberghe, *Optimized light sharing for high-resolution tof pet detector based on digital silicon photomultipliers,* Physics in Medicine and Biology **59**, 7125 (2014).

[35] M. S. Lee and J. S. Lee, *Depth-of-interaction measurement in a single-layer crystal array with a single-ended readout using digital silicon photomultiplier,* Physics in Medicine and Biology **60**, 6495 (2015).

[36] Z. Kuang, Q. Yang, X. Wang, X. Fu, N. Ren, S. Wu, C. Zhang, B. Zhao, Z. Sang, Z. Hu, J. Du, D. Liang, X. Liu, H. Zheng, and Y. Yang, *Performance of a depth encoding PET detector module using light sharing and single-ended readout with SiPMs,* Physics in Medicine & Biology **64**, 085012 (2019).

[37] Y. Hirano, M. Nitta, N. Inadama, F. Nishikido, E. Yoshida, H. Murayama, and T. Yamaya, *Performance evaluation of a depth-of-interaction detector by use of position-sensitive pmt with a super-bialkali photocathode,* Radiological Physics and Technology **7**, 57 (2014).

[38] G. Akamatsu, H. Tashima, Y. Iwao, H. Wakizaka, T. Maeda, A. Mohammadi, S. Takyu, M. Nitta, F. Nishikido, H. Rutherford, A. Chacon, M. Safavi-Naeini, E. Yoshida, and T. Yamaya, *Performance evaluation of a whole-body prototype PET scanner with four-layer DOI detectors,* Physics in Medicine & Biology **64**, 095014 (2019).

[39] M. Pizzichemi, G. Stringhini, T. Niknejad, Z. Liu, P. Lecoq, S. Tavernier, J. Varela, M. Paganoni, and E. Auffray, *A new method for depth of interaction determination in pet detectors,* Physics in Medicine and Biology **61**, 4679 (2016).

[40] G. Stringhini, M. Pizzichemi, A. Ghezzi, A. Stojkovic, M. Paganoni, and E. Auffray, *Development and evaluation of a practical method to measure the depth*

*of interaction function for a single side readout pet detector,* Journal of Instrumentation **11**, P11014 (2016).

[41] M. Pizzichemi, A. Polesel, G. Stringhini, S. Gundacker, P. Lecoq, S. Tavernier, M. Paganoni, and E. Auffray, *On light sharing TOF-PET modules with depth of interaction and 157 ps FWHM coincidence time resolution,* Physics in Medicine & Biology **64**, 155008 (2019).

[42] A. Zatcepin, M. Pizzichemi, A. Polesel, M. Paganoni, E. Auffray, S. I. Ziegler, and N. Omidvari, *Improving depth-of-interaction resolution in pixellated PET detectors using neural networks,* Physics in Medicine & Biology **65**, 175017 (2020).

[43] C. Catana, *Development of dedicated brain pet imaging devices: Recent advances and future perspectives,* Journal of Nuclear Medicine **60**, 1044 (2019).

[44] W. A. Berg, *Nuclear breast imaging: Clinical results and future directions,* Journal of Nuclear Medicine **57**, 46S (2016).

[45] D. F. Hsu, D. L. Freese, and C. S. Levin, *Breast-dedicated radionuclide imaging systems,* Journal of Nuclear Medicine **57**, 40S (2016).

[46] E. Mikhaylova, V. Tabacchini, G. Borghi, P. Mollet, E. D'Hoe, D. R. Schaart, and S. Vandenberghe, *Optimization of an ultralow-dose high-resolution pediatric PET scanner design based on monolithic scintillators with dual-sided digital SiPM readout: a simulation study,* Physics in Medicine & Biology **62**, 8402 (2017).

[47] K. Wienhard, M. Schmand, M. E. Casey, K. Baker, J. Bao, L. Eriksson, W. F. Jones, C. Knoess, M. Lenox, M. Lercher, P. Luk, C. Michel, J. H. Reed, N. Richerzhagen, J. Treffert, S. Vollmar, J. W. Young, W. D. Heiss, and R. Nutt, *The ecat hrrt: performance and first clinical application of the new high resolution research tomograph,* IEEE Transactions on Nuclear Science **49**, 104 (2002).

[48] H. W. A. M. de Jong, F. H. P. van Velden, R. W. Kloet, F. L. Buijs, R. Boellaard, and A. A. Lammertsma, *Performance evaluation of the ecat hrrt: an lso-lyso double layer high resolution, high sensitivity scanner,* Physics in Medicine and Biology **52**, 1505 (2007).

[49] T. Yamaya, E. Yoshida, T. Obi, H. Ito, K. Yoshikawa, and H. Murayama, *First human brain imaging by the jpet-d4 prototype with a pre-computed system matrix,* IEEE Transactions on Nuclear Science **55**, 2482 (2008).

[50] K. S. Grogg, T. Toole, J. Ouyang, X. Zhu, M. D. Normandin, Q. Li, K. Johnson, N. M. Alpert, and G. El Fakhri, *National electrical manufacturers association and clinical evaluation of a novel brain pet/ct scanner,* Journal of Nuclear Medicine **57**, 646 (2016).

[51] M. Watanabe, A. Saito, T. Isobe, K. Ote, R. Yamada, T. Moriya, and T. Omura, *Performance evaluation of a high-resolution brain PET scanner using four-layer MPPC DOI detectors,* Physics in Medicine & Biology **62**, 7148 (2017).

[52] S. Majewski, J. Proffitt, J. Brefczynski-Lewis, A. Stolin, A. Weisenberger, W. Xi, and R. Wojcik, *Helmetpet: A silicon photomultiplier based wearable brain imager,* in *2011 IEEE Nuclear Science Symposium Conference Record* (2011) pp. 4030–4034.

[53] S. Melroy, C. Bauer, M. McHugh, G. Carden, A. Stolin, S. Majewski, J. Brefczynski-Lewis, and T. Wuest, *Development and design of next-generation head-mounted ambulatory microdose positron-emission tomography (am-pet) system,* Sensors **17** (2017), 10.3390/s17051164.

[54] H. Tashima, E. Yoshida, Y. Iwao, H. Wakizaka, T. Maeda, C. Seki, Y. Kimura, Y. Takado, M. Higuchi, T. Suhara, T. Yamashita, and T. Yamaya, *First prototyping of a dedicated PET system with the hemisphere detector arrangement,* Physics in Medicine & Biology **64**, 065004 (2019).

[55] F. Nishikido, M. Fujiwara, H. Tashima, M. S. H. Akram, M. Suga, T. Obata, and T. Yamaya, *Development of a full-ring "add-on pet" prototype: A head coil with doi-pet detectors for integrated pet/mri,* Nuclear Instruments and Methods in Physics Research Section A: Accelerators, Spectrometers, Detectors and Associated Equipment **863**, 55 (2017).

[56] K. K. Miyake, K. Matsumoto, M. Inoue, Y. Nakamoto, S. Kanao, T. Oishi, S. Kawase, K. Kitamura, Y. Yamakawa, A. Akazawa, T. Kobayashi, J. Ohi, and K. Togashi, *Performance evaluation of a new dedicated breast pet scanner using nema nu4-2008 standards,* Journal of Nuclear Medicine **55**, 1198 (2014).

[57] M. C. Abreu, J. D. Aguiar, F. G. Almeida, P. Almeida, P. Bento, B. Carrico, M. Ferreira, N. C. Ferreira, F. Goncalves, C. Leong, F. Lopes, P. Lousa, M. V. Martins, N. Matela, P. R. Mendes, R. Moura, J. Nobre, N. Oliveira, C. Ortigao, L. Peralta, R. Pereira, J. Rego, R. Ribeiro, P. Rodrigues, J. Sampaio, A. I. Santos, L. Silva, J. C. Silva, P. Sousa, I. C. Teixeira, J. P. Teixeira, A. Trindade, and J. Varela, *Design and evaluation of the clear-pem scanner for positron emission mammography,* IEEE Transactions on Nuclear Science **53**, 71 (2006).

[58] M. C. Abreu, D. Aguiar, E. Albuquerque, F. G. Almeida, P. Almeida, P. Amaral, E. Auffray, P. Bento, P. Bruyndonckx, R. Bugalho, B. Carriço, H. Cordeiro, M. Ferreira, N. C. Ferreira, F. Gonçalves, P. Lecoq, C. Leong, F. Lopes, P. Lousã, J. Luyten, M. V. Martins, N. Matela, P. R. Mendes, R. Moura, J. Nobre, N. Oliveira, C. Ortigão, L. Peralta, J. Rego, R. Ribeiro, P. Rodrigues, A. I. Santos, J. C. Silva, M. M. Silva, S. Tavernier, I. C. Teixeira, J. P. Teixeira, A. Trindade, J. Trummer, and J. Varela, *Clear-pem: A pet imaging system dedicated to breast cancer diagnostics,* Nuclear Instruments and Methods in Physics Research Section A: Accelerators, Spectrometers, Detectors and Associated Equipment **571**, 81 (2007).

[59] H. Thoen, V. Keereman, P. Mollet, R. V. Holen, and S. Vandenberghe, *Influence of detector pixel size, tof resolution and doi on image quality in mr-compatible whole-body pet,* Physics in Medicine and Biology **58**, 6459 (2013).

[60] S. Surti, A. R. Shore, and J. S. Karp, *Design study of a whole-body pet scanner with improved spatial and timing resolution,* Nuclear Science, IEEE Transactions on **60**, 3220 (2013).

[61] NEMA-NU2, *Performance Measurements of Positron Emission Tomographs (PETS)*, NEMA Standards Publication NU 2-2012 (National Electrical Manufacturers Association (NEMA), 2012).

[62] J. S. Karp, V. Viswanath, M. J. Geagan, G. Muehllehner, A. R. Pantel, M. J. Parma, A. E. Perkins, J. P. Schmall, M. E. Werner, and M. E. Daube-Witherspoon, *Pennpet explorer: Design and preliminary performance of a whole-body imager,* Journal of Nuclear Medicine **61**, 136 (2020).

[63] W.-H. Wong, H. Li, Y. Zhang, R. Ramirez, S. An, C. Wang, S. Liu, Y. Dong, and H. Baghaei, *A high-resolution time-of-flight clinical pet detection system using a gapless pmt-quadrant-sharing method,* Nuclear Science, IEEE Transactions on **62**, 2067 (2015).

[64] V. Tabacchini, S. Surti, G. Borghi, J. S. Karp, and D. R. Schaart, *Improved image quality using monolithic scintillator detectors with dual-sided readout in a whole-body tof-pet ring: a simulation study,* Physics in Medicine and Biology **62**, 2018 (2017).

[65] A. Gola, F. Acerbi, M. Capasso, M. Marcante, A. Mazzi, G. Paternoster, C. Piemonte, V. Regazzoni, and N. Zorzi, *Nuv-sensitive silicon photomultiplier technologies developed at fondazione bruno kessler,* Sensors **19**, 308 (2019).

[66] J. W. Cates, S. Gundacker, E. Auffray, P. Lecoq, and C. S. Levin, *Improved single photon time resolution for analog SiPMs with front end readout that reduces influence of electronic noise,* Physics in Medicine & Biology **63**, 185022 (2018).

# Acknowledgements

This thesis is the conclusion of a long work that began when I started my PhD program at TU Delft University and, for different reasons, has been protracted for several years after I left from the Netherlands. During all these years many and many people helped me in my experimental work and during the writing process, supported me at work and in my private life, encouraged me to conclude this project also when other urgencies pushed it in the background. Therefore, I would like to use these pages to express my gratitude to all of them, who have been fundamental to achieve this goal. Considering the length of the list, I am afraid that inevitably I will not remember someone, therefore I would like first to apologize to those people I will forget to mention and assure them I attribute great value also to their support.

First of all, I would like to gratefully acknowledge my promotors Dennis Schaart and Harry van der Graaf. Dennis, I am very thankful for the opportunity that you gave me when you offered me the PhD position at TU Delft and for all the time and efforts that you invested in me and in my work. In particular, I have always appreciated the style that you used to mentor and guide me: you never tried to impose your point of view and your opinions and you always trusted me and left me the freedom to decide the most interesting topics to investigate. Nevertheless, you always supported my work and helped me when I needed, also providing for all the resources that were necessary for my research. Our discussions have been invaluable to me to have a clear feedback on my work, gain new insights into the issues I was investigating and find new ideas to inspire my research. I have also deeply appreciated your support and your positive attitude during this long time it took me to write the thesis: it has been precious to me for finding the motivation to get the work done. Harry, thank you for your support, your feedback on my thesis and your always timely help, especially in this last period during which I finalized my thesis: your contribution has been important to improve my work and speed up the defense process.

The other people who contributed most to the (hopefully) positive outcome of this work are my colleagues and office mates Herman van Dam, Stefan Seifert and Valerio Tabacchini. Herman and Stefan, in the period during which we worked together you taught me a lot about PET and monolithic detectors and for sure I would have never been able to achieve all the results shown in this thesis if I had not started from your excellent work. More than that, you have also been an example of how to conduct rigorous scientific research, investigating in depth all aspects of the problems and achieving solid results. Valerio, we shared office for four years and, besides our days, we also shared most of our scientific works. The continuous discussions with you has been invaluable to have a suitably critical opinion on my research and has been fundamental to spot errors and find new and better ideas. We had complementary abilities and I think that we have been a

great team: I consider the PET demonstrator that we built together an outstanding achievement and it would have never been possible without you.

I also want to thank all the staff members of TU Delft University who gave me their support during my permanence there. First of all, I want to thank the staff of DEMO, who always found a way to give a shape to the ideas that I had for my experimental setups. In particular, I want to thank William van Goozen, who helped me during my first years, and René Bakker, who has been the great mind behind the construction of the mechanical structure of the fabulous TTG. René, without your creativity and your skills we would have never been able to achieve the excellent results that we obtained. Beside that, you have also been a fun and interesting person to work with: I always enjoyed the time spent together and all our discussions, during working hours and coffee breaks, about technical projects and artistic machinery. You are a positive person and I wish I had a colleague like you in all the places where I work. Another sincere thank goes to Jan Huizenga and Folkert Geurink, who always helped me to fix all the electronics issues in my setups and also gave their valuable support to build the PET demonstrator. I would also like to thank all the people in the radio-protection service, who gave us their support in all our 'hot' experiments. Among them, a special thank goes to Koos van Kammen, not only for his constructive collaboration during working hours but also for all our adventures in bars and at the climbing gym. Koos, thank you for all the fun moments that you organized, for sure you made my staying in Delft much more enjoyable. A special thank goes also to José Buurman, Thea Miedema and Anouk Nieuwesteeg for their administrative support. Again, thanks to all of you, it was a pleasure to work with you.

Besides the people who directly contributed to my work, I would also like to thank all the former and present member of the department with whom I shared lunches and coffees, my working hours and my free time, nights at the 't Koepeltje and in the city. You welcomed me when I arrived and you created a friendly atmosphere that made my working days enjoyable and my time in the Netherlands a great experience. In random order, thank you Patricia, Francesco, Robin, Antonia, Vallin, Pablo, Guzman, Edith, Mikhail, Rupali, and thanks to all the other people I had the pleasure to work with. A special mention goes to Alessia, who has been and still is a great friend. Your presence was a great support for me and your positivity and your liveliness always cheered me up also during the long Dutch winters. Alessia, thank you for all the fun moments that we spent together in Delft, for the help that you have always given me, and especially for still being present in my life despite the distance.

Finally, the most difficult part to be written of this thesis. Among all the people who supported me, inspired me and motivated me, undoubtedly the most important ones are the members of my family. Without them, I would have never been able to achieve this result. I am afraid that my words will be inadequate to express all of my gratitude and my love for them but I hope that in their heart they know anyway how important they are for me.
*Infine, la parte piú difficile da scrivere di questa tesi. Tra tutte le persone che mi hanno sostenuto, ispirato e motivato, senza dubbio le piú importanti sono i membri*

*della mia famiglia poiché senza di loro non sarei mai riuscito a raggiungere questo risultato. Ho il timore che le mie parole saranno inadeguate ad esprimere tutta la mia gratitudine e il mio amore nei loro confronti ma spero che comunque nel loro cuore sappiano quanto loro siano importanti per me.*

My first thank goes to my parents, Emanuela e Donato, who have always been a guide and an example for me. Mum, dad, thank you for teaching me the value of the hard work and for always encouraging me to follow my passions and my interests, even if that meant being far away from each other. Your support and love have been fundamental for me, I found my own path in life thanks to you. Sometimes I made the right choices and sometimes I made the wrong ones but I always knew that I could count on you. Mum, thank you for always encouraging me and being close to me: the years I spent in the Netherlands were not easy for you and nevertheless you never complained that we were far apart but instead you always found a way to make me feel your support. Dad, unfortunately you could just see the beginning of this journey but not the end and during these years I often missed you. In any case, I like to think that this achievement would have made you happy and also a bit proud.
*Il mio primo ringraziamento va ai miei genitori, Emanuela e Donato, che sono sempre stati una guida e un esempio per me. Mamma, papá, grazie per avermi insegnato il valore dell'impegno e del lavoro e per avermi sempre incoraggiato a seguire le mie passioni e i miei interessi, anche se questo ha significato non poter sempre essere vicini. Il vostro sostegno e il vostro amore sono stati fondamentali per me, é grazie a voi che ho potuto trovare la mia strada, facendo scelte giuste e scelte sbagliate ma sapendo sempre di poter contare su di voi. Mamma, grazie per avermi incoraggiato e per essermi stata vicina: gli anni che ho passato in Olanda non sono stati facili per te, eppure non mi hai mai fatto pesare il fatto che fossimo lontani ed anzi hai sempre trovato il modo di farmi sentire il tuo supporto. Papá, purtroppo tu hai potuto vedere solo l'inizio di questo percorso ma non la fine e durante questi anni ho spesso sentito la tua mancanza. Mi piace comunque pensare che questo traguardo ti avrebbe reso felice e un pochino orgoglioso.*

Lucia, Giovanni, thank you for being close siblings, for always supporting and encouraging me. Besides being great siblings, you are also my friends and my advisors. Knowing that you are always with me, that I can count on you also when we are far apart has always given me strength and serenity.
*Lucia, Giovanni, grazie per essere stati un fratello e una sorella presenti, per essermi sempre stati vicini e per avermi sempre fatto sentire il vostro incoraggiamento. Oltre che essere un fratello e una sorella fantastici, siete stati anche amici e consiglieri. Sapere che voi ci siete, che posso contare su di voi anche quando siamo lontani, mi ha sempre dato e mi dará sempre forza e tranquillitá.*

Lodoviga, you met me when this project had been started since a long time and could appear a bit improbable and distant. Instead, you always believed in me and in the importance of concluding it. You always supported and encouraged me when I spent my free evenings and weekends writing, despite often that meant to have less time for the two of us. Your love and your respect have been fundamental for me and I cannot find the words to express my gratitude for supporting me especially

during this last year, during which the time, energies and dedication that I needed to conclude the thesis made me distracted and absent-minded also in moments during which you were the person who deserved to be supported. This thesis and this achievement would have never been possible without you and I hope that you can feel that they are also a bit yours. I love you too and I know that I am lucky to have you on my side in my life. Thank you for everything.
*Lodoviga, tu mi hai conosciuto quando questo progetto era cominciato da tempo e poteva sembrare una cosa un po' improbabile e lontana. Invece tu hai sempre creduto in me e nell'importanza di portarlo a termine. Mi hai sostenuto e mi hai incoraggiato quando nel mio tempo libero passavo le serate e i fine settimana a scrivere, nonostante questo spesso volesse dire avere meno tempo per noi. Il tuo amore e la tua considerazione sono stati fondamentali per me e non so esprimere a parole la mia gratitudine per avermi sostenuto in particolare durante quest'ultimo anno, durante il quale il tempo, le energie e l'impegno che mi sono serviti per concludere la tesi mi hanno reso a volte distratto e distante in momenti in cui saresti stata tu ad avere bisogno del mio sostegno. Questa tesi e questo traguardo non sarebbero stati possibili senza di te e spero che tu possa sentirli un pochino anche tuoi. Anche io ti amo e so di essere fortunato ad averti accanto come compagna di vita. Grazie di tutto.*

Finally, the last words are for my daughter Clara, the last one arrived in the family, the apple of my eye. I hope that one day you will read these words and you will know that your arrival has been a fundamental source of motivation and inspiration for me to conclude this thesis. I hope that I will be able to support and guide you in the same way my parents and your mum have always done with me and I wish that your life will be full of wonderful adventures and great achievements.
*Infine, le mie ultime parole sono per mia figlia Clara, l'ultima arrivata della famiglia, la luce dei miei occhi. Mi auguro che un giorno leggerai queste parole e saprai che il tuo arrivo é stato per me una fondamentale fonte di ispirazione e motivazione per poter concludere questa tesi. Spero che io sapró sostenerti e guidarti come i miei genitori e la tua mamma hanno sempre fatto con me e ti auguro che la tua vita possa essere piena di fantastiche avventure e grandiose soddisfazioni.*

# Curriculum Vitæ

Giacomo Borghi was born in Cantù (Italy) in 1986. He obtained his secondary school degree (Maturità Scientifica) at the scientific high school *Liceo Scientifico Paolo Giovio*, Como (Italy) in 2005. In the same year, he joined the physics program at the *Università degli Studi di Milano-Bicocca* (Milan, Italy). In 2008, he received the B.Sc. degree in Physics with specialization in Elementary Particles with a thesis entitled "Bolometric Detector with Double Light-Heat Readout", following a 3-month internship in the collaboration working on the CUORE experiment. During his M.Sc. program, he worked for 15 months (2010/2011) as a research intern in the AQUA group of TERA Foundation, an Italian Research Foundation based at CERN (Geneva) focusing on the development of new instrumentation for hadrontherapy. In 2011, he received the M.Sc. degree in Physics with specialization in Physics of Fundamental Interactions with a thesis entitled "Development of a Positron Tomography System that employs Time of Flight for Diagnostic in Hadrontherapy".

From 2011 until 2016 he was employed as a Ph.D. student at *Delft University of Technology*, in the faculty of Applied Sciences, in the department of Radiation Science and Technology. In particular, he focused his research on the development and experimental characterization of new detectors for time-of-flight positron emission tomography (TOF-PET) based on monolithic scintillation crystals and digital silicon photomultipliers. The results of the research carried on during this period are presented in this thesis.

Since 2016 until now, he has been employed as researcher in the field of silicon sensors at *Fondazione Bruno Kessler* (FBK), Trento (Italy), in the Sensors and Devices Center. As a researcher in FBK, he focuses on developing innovative silicon sensors for the detection of ionizing radiation and visible light. In particular, he works on the development and design of silicon drift detectors (SDDs), low-gain avalanche diode (LGAD) detectors, silicon photomultipliers (SiPMs), and pixel and strip detectors.

# List of Publications

[1] P. King, M. Gugiatti, M. Carminati, L. Buonanno, G. Borghi, G. Pepponi, P. Lechner, D. Siegmann, K. Urban, T. Houdy, S. Mertens, and C. Fiorini, *Design and characterization of Kerberos: a 48-channel analog pulse processing and data acquisition platform,* Journal of Instrumentation **16**, T07007 (2021).

[2] G. Utica, E. Fabbrica, M. Carminati, G. Borghi, N. Zorzi, F. Ficorella, A. Picciotto, I. Allegretta, G. Falkenberg, and C. Fiorini, *ARDESIA-16: a 16-channel SDD-based spectrometer for energy dispersive X-ray fluorescence spectroscopy,* Journal of Instrumentation **16**, P07057 (2021).

[3] G. Paternoster, G. Borghi, R. Arcidiacono, M. Boscardin, N. Cartiglia, M. Centis Vignali, G. F. Dalla Betta, M. Ferrero, F. Ficorella, M. Mandurrino, L. Pancheri, F. Siviero, V. Sola, and M. Tornago, *Novel strategies for fine-segmented Low Gain Avalanche Diodes,* Nuclear Instruments and Methods in Physics Research Section A: Accelerators, Spectrometers, Detectors and Associated Equipment **987**, 164840 (2021).

[4] M. Missiaggia, E. Pierobon, M. Castelluzzo, A. Perinelli, F. Cordoni, M. Centis Vignali, G. Borghi, E. V. Bellinzona, E. Scifoni, F. Tommasino, V. Monaco, L. Ricci, M. Boscardin, and C. La Tessa, *A Novel Hybrid Microdosimeter for Radiation Field Characterization Based on the Tissue Equivalent Proportional Counter Detector and Low Gain Avalanche Detectors Tracker: A Feasibility Study ,* (2021).

[5] M. Tornago, R. Arcidiacono, N. Cartiglia, M. Costa, M. Ferrero, M. Mandurrino, F. Siviero, V. Sola, A. Staiano, A. Apresyan, K. Di Petrillo, R. Heller, S. Los, G. Borghi, M. Boscardin, G.-F. Dalla Betta, F. Ficorella, L. Pancheri, G. Paternoster, H. Sadrozinski, and A. Seiden, *Resistive AC-Coupled Silicon Detectors: Principles of operation and first results from a combined analysis of beam test and laser data,* Nuclear Instruments and Methods in Physics Research Section A: Accelerators, Spectrometers, Detectors and Associated Equipment **1003**, 165319 (2021).

[6] M. Capasso, F. Acerbi, G. Borghi, A. Ficorella, N. Furlan, A. Mazzi, S. Merzi, V. Mozharov, V. Regazzoni, N. Zorzi, G. Paternoster, and A. Gola, *FBK VUV-sensitive Silicon Photomultipliers for cryogenic temperatures,* Nuclear Instruments and Methods in Physics Research Section A: Accelerators, Spectrometers, Detectors and Associated Equipment **982**, 164478 (2020).

[7] G. Paternoster, G. Borghi, M. Boscardin, N. Cartiglia, M. Ferrero, F. Ficorella, F. Siviero, A. Gola, and P. Bellutti, *Trench-Isolated Low Gain Avalanche Diodes (TI-LGADs),* IEEE Electron Device Letters **41**, 884 (2020).

[8] M. Sammartini, M. Gandola, F. Mele, G. Bertuccio, F. Ambrosino, P. Bellutti, G. Borghi, R. Campana, M. Caselle, D. Cirrincione, Y. Evangelista, M. Feroci, F. Ficorella, M. Fiorini, F. Fuschino, M. Grassi, C. Labanti, P. Malcovati, A. Picciotto, A. Rachevski, I. Rashevskaya, G. Zampa, N. Zampa, N. Zorzi, and A. Vacchi, *Pixel Drift Detector (PixDD) – SIRIO: an X-ray spectroscopic system with high energy resolution at room temperature,* Nuclear Instruments and Methods in Physics Research Section A: Accelerators, Spectrometers, Detectors and Associated Equipment **953**, 163114 (2020).

[9] M. Grassi, M. Gandola, F. Mele, G. Bertuccio, P. Malcovati, F. Fuschino, R. Campana, C. Labanti, M. Fiorini, Y. Evangelista, R. Piazzolla, M. Feroci, G. Zampa, N. Zampa, A. Rachevski, P. Bellutti, G. Borghi, E. Demenev, F. Ficorella, A. Picciotto, N. Zorzi, I. Rashevskaya, A. Vacchi, F. Fiore, and L. Burderi, *X-/$\gamma$-Ray Detection Instrument for the HERMES Nano-Satellites Based on SDDs Read-Out by the LYRA Mixed-Signal ASIC Chipset,* in *2020 IEEE International Instrumentation and Measurement Technology Conference (I2MTC)* (IEEE, 2020) pp. 1–6.

[10] M. Ferrero, R. Arcidiacono, G. Borghi, M. Boscardin, N. Cartiglia, M. Costa, G. D. Betta, F. Ficorella, M. Mandurrino, M. Obertino, L. Pancheri, G. Paternoster, F. Siviero, V. Sola, A. Staiano, M. Tornago, and M. C. Vignali, *Evolution of the design of ultra fast silicon detector to cope with high irradiation fluences and fine segmentation,* Journal of Instrumentation **15**, C04027 (2020).

[11] R. Arcidiacono, G. Borghi, M. Boscardin, N. Cartiglia, M. Costa, G. Dalla Betta, F. Fausti, M. Ferrero, F. Ficorella, M. Mandurrino, S. Mazza, E. Olave, L. Pancheri, G. Paternoster, H.-F. Sadrozinski, V. Sola, A. Staiano, A. Seiden, F. Siviero, M. Tornago, and Y. Zhao, *State-of-the-art and evolution of UFSD sensors design at FBK,* Nuclear Instruments and Methods in Physics Research Section A: Accelerators, Spectrometers, Detectors and Associated Equipment **978**, 164375 (2020).

[12] N. Cartiglia, R. Arcidiacono, G. Borghi, M. Boscardin, M. Costa, Z. Galloway, F. Fausti, M. Ferrero, F. Ficorella, M. Mandurrino, S. Mazza, E. Olave, G. Paternoster, F. Siviero, H. F. Sadrozinski, V. Sola, A. Staiano, A. Seiden, M. Tornago, and Y. Zhao, *LGAD designs for Future Particle Trackers,* Nuclear Instruments and Methods in Physics Research Section A: Accelerators, Spectrometers, Detectors and Associated Equipment **979**, 164383 (2020).

[13] F. Fuschino, R. Campana, C. Labanti, L. Amati, E. Virgilli, L. Terenzi, P. Bellutti, G. Bertuccio, G. Borghi, F. Ficorella, M. Gandola, M. Grassi, G. La Rosa, P. Lorenzi, P. Malcovati, F. Mele, P. Orleański, A. Picciotto, A. Rachevski, I. Rashevskaya, A. Santangelo, P. Sarra, G. Sottile, C. Tenzer, A. Vacchi, Z. Gianluigi, N. Zampa, N. Zorzi, P. Hedderman, M. Winkler, A. Gemelli, I. Kuvvetli,

S. M. Pedersen, D. Tcherniak, and L. C. Bune Jensen, *The XGIS instrument on-board THESEUS: the detection plane and on-board electronics,* in Space Telescopes and Instrumentation 2020: Ultraviolet to Gamma Ray, Vol. 11444, edited by J.-W. A. den Herder, K. Nakazawa, and S. Nikzad (SPIE, 2020) p. 277.

[14] F. Fuschino, R. Campana, C. Labanti, Y. Evangelista, F. Fiore, M. Gandola, M. Grassi, F. Mele, F. Ambrosino, F. Ceraudo, E. Demenev, M. Fiorini, G. Morgante, R. Piazzolla, G. Bertuccio, P. Malcovati, P. Bellutti, G. Borghi, G. Dilillo, M. Feroci, F. Ficorella, G. La Rosa, P. Nogara, G. Pauletta, A. Picciotto, I. Rashevskaya, A. Rashevsky, S. Giuseppe, A. Vacchi, E. Virgilli, G. Zampa, N. Zampa, N. Zorzi, T. Chen, Y. Xu, N. Gao, J. Cao, and L. Wang, *An innovative architecture for wide band transient monitor on board HERMES nano-satellite constellations,* in Space Telescopes and Instrumentation 2020: Ultraviolet to Gamma Ray, Vol. 11444, edited by J.-W. A. den Herder, K. Nakazawa, and S. Nikzad (SPIE, 2020) p. 167.

[15] Y. Evangelista, F. Fiore, F. Fuschino, R. Campana, F. Ceraudo, E. Demenev, A. Guzman, C. Labanti, G. La Rosa, M. Fiorini, M. Gandola, M. Grassi, F. Mele, G. Morgante, P. Nogara, R. Piazzolla, S. Pliego Caballero, I. Rashevskaya, F. Russo, G. Sciarrone, G. Sottile, D. Milankovich, A. Pál, F. Ambrosino, N. Auricchio, M. Barbera, P. Bellutti, G. Bertuccio, G. Borghi, J. Cao, T. Chen, G. Dilillo, M. Feroci, F. Ficorella, U. Lo Cicero, P. Malcovati, A. Morbidini, G. Pauletta, A. Picciotto, A. Rachevski, A. Santangelo, C. Tenzer, A. Vacchi, L. Wang, Y. Xu, G. Zampa, N. Zampa, N. Zorzi, L. Burderi, M. Lavagna, R. Bertacin, P. Lunghi, A. Monge, B. Negri, S. Pirrotta, S. Puccetti, A. Sanna, F. Amarilli, G. Amelino-Camelia, M. Bechini, M. Citossi, A. Colagrossi, S. Curzel, G. Della Casa, M. Cinelli, M. Del Santo, T. Di Salvo, C. Feruglio, F. Ferrandi, M. Fiorito, D. Gacnik, G. Galgóczi, A. F. Gambino, G. Ghirlanda, A. Gomboc, M. Karlica, P. Efremov, U. Kostic, A. Clerici, B. Lopez Fernandez, A. Maselli, L. Nava, M. Ohno, D. Ottolina, A. Pasquale, M. Perri, M. Piccinin, J. Prinetto, A. Riggio, J. Ripa, A. Papitto, S. Piranomonte, F. Scala, D. Selcan, S. Silvestrini, T. Rotovnik, E. Virgilli, I. Troisi, N. Werner, G. Zanotti, A. Anitra, A. Manca, and A. Clerici, *The scientific payload on-board the HERMES-TP and HERMES-SP CubeSat missions,* in Space Telescopes and Instrumentation 2020: Ultraviolet to Gamma Ray, Vol. 11444, edited by J.-W. A. den Herder, K. Nakazawa, and S. Nikzad (SPIE, 2020) p. 168.

[16] C. Labanti, L. Amati, F. Frontera, S. Mereghetti, J. L. Gasent-Blesa, C. Tenzer, P. Orleanski, I. Kuvvetli, R. Campana, F. Fuschino, L. Terenzi, E. Virgilli, G. Morgante, M. Orlandini, R. C. Butler, J. B. Stephen, N. Auricchio, A. De Rosa, V. Da Ronco, F. Evangelisti, M. Melchiorri, S. Squerzanti, M. Fiorini, G. Bertuccio, F. Mele, M. Gandola, P. Malcovati, M. Grassi, P. Bellutti, G. Borghi, F. Ficorella, A. Picciotto, V. Zanini, N. Zorzi, E. Demenev, I. Rashevskaya, A. Rachevski, G. Zampa, A. Vacchi, N. Zampa, G. Baldazzi, G. La Rosa, G. Sottile, A. Volpe, M. Winkler, V. Reglero, P. H. Connell, B. Pinazo-Herrero, J. Navarro-González, P. Rodríguez-Martínez, A. J. Castro-Tirado, A. Santangelo, P. Hedderman,

P. Lorenzi, P. Sarra, S. M. Pedersen, D. Tcherniak, C. Guidorzi, P. Rosati, A. Trois, and R. Piazzolla, *The X/Gamma-ray Imaging Spectrometer (XGIS) on-board THESEUS: design, main characteristics, and concept of operation,* in *Space Telescopes and Instrumentation 2020: Ultraviolet to Gamma Ray*, Vol. 11444, edited by J.-W. A. den Herder, K. Nakazawa, and S. Nikzad (SPIE, 2020) p. 303.

[17] M. Gugiatti, M. Carminati, C. Fiorini, G. Borghi, and F. Ficorella, *A Coin-Sized Detector for Room-Temperature X-Ray Photons and Electron Spectroscopy,* in *2020 27th IEEE International Conference on Electronics, Circuits and Systems (ICECS)* (2020) pp. 1–4.

[18] M. M. Patil, M. Caselle, L. Rota, A. Dierlamm, M. Baselga Bacardit, G. Niehues, E. Bründermann, M. Weber, A.-S. Müller, G. Borghi, and M. Boscardin, *Novel P-in-N Si-Sensor technology for high resolution and high repetition-rate experiments at accelerator facilities,* in *Proceedings of Topical Workshop on Electronics for Particle Physics — PoS(TWEPP2018)*, Vol. 343 (Sissa Medialab, Trieste, Italy, 2019) p. 045.

[19] M. Andrä, J. Zhang, A. Bergamaschi, R. Barten, C. Borca, G. Borghi, M. Boscardin, P. Busca, M. Brückner, N. Cartiglia, S. Chiriotti, G.-F. Dalla Betta, R. Dinapoli, P. Fajardo, M. Ferrero, F. Ficorella, E. Fröjdh, D. Greiffenberg, T. Huthwelker, C. Lopez-Cuenca, M. Meyer, D. Mezza, A. Mozzanica, L. Pancheri, G. Paternoster, S. Redford, M. Ruat, C. Ruder, B. Schmitt, X. Shi, V. Sola, D. Thattil, G. Tinti, and S. Vetter, *Development of low-energy X-ray detectors using LGAD sensors,* Journal of Synchrotron Radiation **26**, 1226 (2019).

[20] I. Hafizh, G. Bellotti, M. Carminati, G. Utica, M. Gugiatti, A. Balerna, V. Tullio, G. Borghi, A. Picciotto, F. Ficorella, N. Zorzi, A. Capsoni, S. Coelli, L. Bombelli, and C. Fiorini, *ARDESIA: A fast silicon drift detector X-ray spectrometer for synchrotron applications,* X-Ray Spectrometry **48**, 382 (2019).

[21] J. Bufon, M. Altissimo, G. Aquilanti, P. Bellutti, G. Bertuccio, F. Billè, R. Borghes, G. Borghi, G. Cautero, S. Ciano, A. Cicuttin, D. Cirrincione, M. L. Crespo, S. Fabiani, F. Ficorella, M. Gandola, A. Gianoncelli, D. Giuressi, R. Grisonich, G. Kourousias, K. S. Mannatunga, F. Mele, R. H. Menk, L. Olivi, G. Orzan, A. Picciotto, A. Rachevski, I. Rashevskaya, M. Sammartini, S. Schillani, A. Stolfa, G. Zampa, N. Zampa, N. Zorzi, and A. Vacchi, *Large solid angle and high detection efficiency multi-element silicon drift detectors (SDD) for synchrotron based x-ray spectroscopy,* in *AIP Conference Proceedings*, Vol. 2054 (2019) p. 060061.

[22] I. Hafizh, G. Bellotti, M. Carminati, G. Utica, M. Gugiatti, A. Balerna, V. Tullio, G. Lepore, G. Borghi, F. Ficorella, A. Picciotto, N. Zorzi, A. Capsoni, S. Coelli, L. Bombelli, and C. Fiorini, *Characterization of ARDESIA: a 4-channel SDD X-ray spectrometer for synchrotron measurements at high count rates,* Journal of Instrumentation **14**, P06027 (2019).

[23] S. Zhang, A. Santangelo, M. Feroci, Y. Xu, F. Lu, Y. Chen, H. Feng, S. Zhang, S. Brandt, M. Hernanz, L. Baldini, E. Bozzo, R. Campana, A. De Rosa, Y. Dong, Y. Evangelista, V. Karas, N. Meidinger, A. Meuris, K. Nandra, T. Pan, G. Pareschi, P. Orleanski, Q. Huang, S. Schanne, G. Sironi, D. Spiga, J. Svoboda, G. Tagliaferri, C. Tenzer, A. Vacchi, S. Zane, D. Walton, Z. Wang, B. Winter, X. Wu, J. J. M. in' t Zand, M. Ahangarianabhari, G. Ambrosi, F. Ambrosino, M. Barbera, S. Basso, J. Bayer, R. Bellazzini, P. Bellutti, B. Bertucci, G. Bertuccio, G. Borghi, X. Cao, F. Cadoux, R. Campana, F. Ceraudo, T. Chen, Y. Chen, J. Chevenez, M. Civitani, W. Cui, W. Cui, T. Dauser, E. Del Monte, S. Di Cosimo, S. Diebold, V. Doroshenko, M. Dovciak, Y. Du, L. Ducci, Q. Fan, Y. Favre, F. Fuschino, J. L. Gálvez, M. Gao, M. Ge, O. Gevin, M. Grassi, Q. Gu, Y. Gu, D. Han, B. Hong, W. Hu, L. Ji, S. Jia, W. Jiang, T. Kennedy, I. Kreykenbohm, I. Kuvvetli, C. Labanti, L. Latronico, G. Li, M. Li, X. Li, W. Li, Z. Li, O. Limousin, H. Liu, X. Liu, B. Lu, T. Luo, D. Macera, P. Malcovati, A. Martindale, M. Michalska, B. Meng, M. Minuti, A. Morbidini, F. Muleri, S. Paltani, E. Perinati, A. Picciotto, C. Piemonte, J. Qu, A. Rachevski, I. Rashevskaya, J. Rodriguez, T. Schanz, Z. Shen, L. Sheng, J. Song, L. Song, C. Sgro, L. Sun, Y. Tan, P. Uttley, B. Wang, D. Wang, G. Wang, J. Wang, L. Wang, Y. Wang, A. L. Watts, X. Wen, J. Wilms, S. Xiong, J. Yang, S. Yang, Y. Yang, N. Yu, W. Zhang, G. Zampa, N. Zampa, A. A. Zdziarski, A. Zhang, C. Zhang, F. Zhang, L. Zhang, T. Zhang, Y. Zhang, X. Zhang, Z. Zhang, B. Zhao, S. Zheng, Y. Zhou, N. Zorzi, and J. F. Zwart, *The enhanced X-ray Timing and Polarimetry mission—eXTP,* Science China Physics, Mechanics & Astronomy **62**, 29502 (2019), arXiv:1812.04020 .

[24] A. Rachevski, M. Ahangarianabhari, G. Aquilanti, P. Bellutti, G. Bertuccio, G. Borghi, J. Bufon, G. Cautero, S. Ciano, A. Cicuttin, D. Cirrincione, M. Crespo, S. Fabiani, F. Ficorella, M. Gandola, D. Giuressi, K. Mannatunga, F. Mele, R. Menk, L. Olivi, G. Orzan, A. Picciotto, I. Rashevskaya, M. Sammartini, S. Schillani, G. Zampa, N. Zampa, N. Zorzi, and A. Vacchi, *The XAFS fluorescence detector system based on 64 silicon drift detectors for the SESAME synchrotron light source,* Nuclear Instruments and Methods in Physics Research Section A: Accelerators, Spectrometers, Detectors and Associated Equipment **936**, 719 (2019).

[25] L. Buonanno, M. Carminati, C. Fiorini, P. King, G. Borghi, N. Furlan, N. Zorzi, and L. Gironi, *Passivated SDD-Based Detection Unit to Improve Reliability in Scintillation Detection,* in *2019 IEEE Nuclear Science Symposium and Medical Imaging Conference (NSS/MIC)* (IEEE, 2019) pp. 1–3.

[26] G. Batignani, S. Bettarini, G. Borghi, M. Boscardin, A. Ciarrocchi, M. Crivellari, C. Coletti, A. Di Gaspare, A. Di Lieto, F. Forti, D. Goretti, N. Mishra, E. Paoloni, G. Rizzo, J. Scherzinger, A. Tredicucci, L. Vicarelli, and N. Zorzi, *Development of graphene-based ionizing radiation sensors,* Nuclear Instruments and Methods in Physics Research Section A: Accelerators, Spectrometers, Detectors and Associated Equipment **936**, 666 (2019).

[27] G. Kourousias, F. Billè, G. Cautero, J. Bufon, A. Rachevski, S. Schillani, D. Cirrincione, M. Altissimo, R. Menk, G. Zampa, N. Zampa, I. Rashevskaya, R. Borghes, M. Gandola, A. Picciotto, G. Borghi, F. Ficorella, N. Zorzi, P. Bellutti, G. Bertuccio, A. Vacchi, and A. Gianoncelli, *XRF topography information: Simulations and data from a novel silicon drift detector system,* Nuclear Instruments and Methods in Physics Research Section A: Accelerators, Spectrometers, Detectors and Associated Equipment **936**, 80 (2019).

[28] F. Fuschino, R. Campana, C. Labanti, Y. Evangelista, M. Feroci, L. Burderi, F. Fiore, F. Ambrosino, G. Baldazzi, P. Bellutti, R. Bertacin, G. Bertuccio, G. Borghi, D. Cirrincione, D. Cauz, F. Ficorella, M. Fiorini, M. Gandola, M. Grassi, A. Guzman, G. L. Rosa, M. Lavagna, P. Lunghi, P. Malcovati, G. Morgante, B. Negri, G. Pauletta, R. Piazzolla, A. Picciotto, S. Pirrotta, S. Pliego-Caballero, S. Puccetti, A. Rachevski, I. Rashevskaya, L. Rignanese, M. Salatti, A. Santangelo, S. Silvestrini, G. Sottile, C. Tenzer, A. Vacchi, G. Zampa, N. Zampa, and N. Zorzi, *HERMES: An ultra-wide band X and gamma-ray transient monitor on board a nano-satellite constellation,* Nuclear Instruments and Methods in Physics Research Section A: Accelerators, Spectrometers, Detectors and Associated Equipment **936**, 199 (2019), arXiv:1812.02432 .

[29] M. Carminati, A. Amirkhani, M. Gugiatti, E. Ferrara, C. Fiorini, E. Demenev, G. Pepponi, S. Ronchin, F. Ficorella, G. Borghi, N. Zorzi, E. Borovin, and L. Lutterotti, *32-Channel Detection Unit for Combined XRF-XRD in Mining Transportable Applications,* in *2019 IEEE Nuclear Science Symposium and Medical Imaging Conference (NSS/MIC)* (IEEE, 2019) pp. 1–3.

[30] G. Utica, M. Gugiatti, M. Carminati, E. Fabbrica, I. Hafizh, A. Balerna, G. Borghi, F. Ficorella, A. Picciotto, N. Zorzi, A. Capsoni, S. Coelli, A. Tocchio, E. Welter, and C. Fiorini, *Towards Efficiency and Count-Rate Enhancement of X-ray ARDESIA Spectrometer,* in *2019 IEEE Nuclear Science Symposium and Medical Imaging Conference (NSS/MIC)* (IEEE, 2019) pp. 1–4.

[31] D. Cirrincione, M. Ahangarianabhari, F. Ambrosino, I. Bajnati, P. Bellutti, G. Bertuccio, G. Borghi, J. Bufon, G. Cautero, F. Ceraudo, Y. Evangelista, S. Fabiani, M. Feroci, F. Ficorella, M. Gandola, F. Mele, G. Orzan, A. Picciotto, M. Sammartini, A. Rachevski, I. Rashevskaya, S. Schillani, G. Zampa, N. Zampa, N. Zorzi, and A. Vacchi, *High precision mapping of single-pixel Silicon Drift Detector for applications in astrophysics and advanced light source,* Nuclear Instruments and Methods in Physics Research Section A: Accelerators, Spectrometers, Detectors and Associated Equipment **936**, 239 (2019).

[32] M. Rebai, D. Rigamonti, S. Cancelli, G. Croci, G. Gorini, E. Perelli Cippo, O. Putignano, M. Tardocchi, C. Altana, M. Angelone, G. Borghi, M. Boscardin, C. Ciampi, G. Cirrone, A. Fazzi, D. Giove, L. Labate, G. Lanzalone, F. La Via, S. Loreti, A. Muoio, P. Ottanelli, G. Pasquali, M. Pillon, S. Puglia, A. Santangelo, A. Trifiro, and S. Tudisco, *New thick silicon carbide detectors: Response to 14 MeV neutrons and comparison with single-crystal diamonds,* Nuclear

Instruments and Methods in Physics Research Section A: Accelerators, Spectrometers, Detectors and Associated Equipment **946**, 162637 (2019).

[33] M. Feroci, V. Karas, P. Orleański, A. Santangelo, S. Schanne, X. Wu, S. Zane, S. Zhang, A. Vacchi, S. Paltani, P. Bellutti, G. Ambrosi, E. Bozzo, Y. XU, A. Zdziarski, A. De Rosa, F. Ambrosino, M. Barbera, O. Limousin, M. Ahangarianabhari, A. Argan, B. Bertucci, G. Bertuccio, J. Bayer, G. Borghi, F. Cadeaux, R. Campana, F. Ceraudo, D. Cirrincione, E. Del Monte, S. Di Cosimo, Y. Evangelista, S. Diebold, Y. Favre, F. Ficorella, F. Fuschino, O. Gevin, M. Grassi, T. Kennedy, C. Labanti, U. Lo Cicero, P. Malcovati, A. Martindale, A. Meuris, M. Michalska, A. Morbidini, F. Muleri, E. Perinati, A. Picciotto, M. Pohl, I. Rashvskaya, J. Svoboda, K. Skup, C. Tenzer, D. Walton, B. Winter, G. Zampa, N. Zampa, N. Zorzi, S. Zhang, T. Chen, Q. Fan, B. Hong, H. Mao, F. Lu, T. Luo, Y. Zhou, L. Zhang, W. Zhang, T. Pan, and X. Zhang, *The large area detector onboard the eXTP mission,* in *Space Telescopes and Instrumentation 2018: Ultraviolet to Gamma Ray*, Vol. 10699, edited by J.-W. A. den Herder, K. Nakazawa, and S. Nikzad (SPIE, 2018) p. 47.

[34] Y. Evangelista, F. Ambrosino, M. Feroci, P. Bellutti, G. Bertuccio, G. Borghi, R. Campana, M. Caselle, D. Cirrincione, F. Ficorella, M. Fiorini, F. Fuschino, M. Gandola, M. Grassi, C. Labanti, P. Malcovati, F. Mele, A. Morbidini, A. Picciotto, A. Rachevski, I. Rashevskaya, M. Sammartini, G. Zampa, N. Zampa, N. Zorzi, and A. Vacchi, *Characterization of a novel pixelated Silicon Drift Detector (PixDD) for high-throughput X-ray astrophysics,* Journal of Instrumentation **13**, P09011 (2018), arXiv:1808.08041 .

[35] G. Bellotti, A. D. Butt, M. Carminati, C. Fiorini, L. Bombelli, G. Borghi, C. Piemonte, N. Zorzi, and A. Balerna, *ARDESIA Detection Module: A Four-Channel Array of SDDs for Mcps X-Ray Spectroscopy in Synchrotron Radiation Applications,* IEEE Transactions on Nuclear Science **65**, 1355 (2018).

[36] S. K. Brandt, M. Hernanz, M. Feroci, P. Orleański, A. Santangelo, S. Schanne, X. Wu, J. in't Zand, S. Zhang, P. E. Olsen, C. Mansanet, R. Campana, F. Fuschino, C. Labanti, G. Zampa, N. Zampa, P. Bellutti, G. Borghi, F. Ficorella, A. Picciotto, N. Zorzi, O. Limousin, A. Meris, Y. Xu, E. Bozzo, Y. Evangelista, J. L. Gálvez, C. Tenzer, F. Zwart, F. Lu, S. Zhang, T. Cheng, F. Ambrosino, A. Argan, E. Del Monte, C. Budtz-Jorgensen, N. Lund, A. Rachevski, A. Vacchi, and I. Rashevskaya, *The wide field monitor onboard the eXTP mission,* in *Space Telescopes and Instrumentation 2018: Ultraviolet to Gamma Ray*, Vol. 10699, edited by J.-W. A. den Herder, K. Nakazawa, and S. Nikzad (SPIE, 2018) p. 149.

[37] G. Borghi, V. Tabacchini, R. Bakker, and D. R. Schaart, *Sub-3 mm, near-200 ps TOF/DOI-PET imaging with monolithic scintillator detectors in a 70 cm diameter tomographic setup,* Physics in Medicine & Biology **63**, 155006 (2018).

[38] J. Bufon, S. Schillani, M. Altissimo, P. Bellutti, G. Bertuccio, F. Billè, R. Borghes, G. Borghi, G. Cautero, D. Cirrincione, S. Fabiani, F. Ficorella, M. Gandola, A. Gianoncelli, D. Giuressi, G. Kourousias, F. Mele, R. Menk, A. Picciotto, A. Rachevski, I. Rashevskaya, M. Sammartini, A. Stolfa, G. Zampa, N. Zampa, N. Zorzi, and A. Vacchi, *A new large solid angle multi-element silicon drift detector system for low energy X-ray fluorescence spectroscopy,* Journal of Instrumentation **13**, C03032 (2018).

[39] S. Tudisco, F. La Via, C. Agodi, C. Altana, G. Borghi, M. Boscardin, G. Bussolino, L. Calcagno, M. Camarda, F. Cappuzzello, D. Carbone, S. Cascino, G. Casini, M. Cavallaro, C. Ciampi, G. Cirrone, G. Cuttone, A. Fazzi, D. Giove, G. Gorini, L. Labate, G. Lanzalone, G. Litrico, G. Longo, D. Lo Presti, M. Mauceri, R. Modica, M. Moschetti, A. Muoio, F. Musumeci, G. Pasquali, G. Petringa, N. Piluso, G. Poggi, S. Privitera, S. Puglia, V. Puglisi, M. Rebai, S. Ronchin, A. Santangelo, A. Stefanini, A. Trifirò, and M. Zimbone, *SiCILIA—Silicon Carbide Detectors for Intense Luminosity Investigations and Applications,* Sensors **18**, 2289 (2018).

[40] F. Acerbi, A. Gola, V. Regazzoni, G. Paternoster, G. Borghi, N. Zorzi, and C. Piemonte, *High Efficiency, Ultra-High-Density Silicon Photomultipliers,* IEEE Journal of Selected Topics in Quantum Electronics **24**, 1 (2018).

[41] I. Hafizh, G. Utica, M. Gugiatti, G. Bellotti, M. Carminati, A. Balerna, V. Tullio, G. Borghi, A. Picciotto, F. Ficorella, N. Zorzi, A. Capsoni, S. Coelli, L. Bombelli, and C. Fiorini, *Qualification of ARDESIA SDD X-ray Spectrometer in Synchrotron Measurements,* in *2018 IEEE Nuclear Science Symposium and Medical Imaging Conference Proceedings (NSS/MIC)* (IEEE, 2018) pp. 1–4.

[42] F. Acerbi, A. Gola, V. Regazzoni, G. Paternoster, G. Borghi, C. Piemonte, and N. Zorzi, *Ultra-high cell-density silicon photomultipliers with high detection efficiency,* in *Proceedings of SPIE - The International Society for Optical Engineering*, Vol. 10212, edited by M. A. Itzler and J. C. Campbell (2017) p. 102120I.

[43] M. Caselle, L. Rota, M. Balzer, M. Brosi, S. Funkner, B. Kehrer, M. J. Nasse, G. Niehues, M. Patil, P. Schönfeldt, M. Schuh, J. L. Steinmann, M. Yan, E. Bründermann, M. Weber, A. S. Müller, G. Borghi, M. Boscardin, and S. Ronchin, *Single-shot longitudinal beam profile and terahertz diagnostics at MHz- Towards GHz-rates with high-throughput electronics,* in *Proceedings of the 6th International Beam Instrumentation Conference, IBIC 2017* (2017) pp. 136–140.

[44] E. Mikhaylova, V. Tabacchini, G. Borghi, P. Mollet, E. D'Hoe, D. R. Schaart, and S. Vandenberghe, *Optimization of an ultralow-dose high-resolution pediatric PET scanner design based on monolithic scintillators with dual-sided digital SiPM readout: a simulation study,* Physics in Medicine & Biology **62**, 8402 (2017).

[45] V. Tabacchini, S. Surti, G. Borghi, J. S. Karp, and D. R. Schaart, *Improved image quality using monolithic scintillator detectors with dual-sided readout in a whole-body TOF-PET ring: a simulation study,* Physics in Medicine and Biology **62**, 2018 (2017).

[46] G. Bellotti, I. Hafizh, A. D. Butt, M. Carminati, C. Fiorini, A. Balerna, V. Tullio, G. Borghi, C. Piemonte, N. Zorzi, A. Capsoni, S. Coelli, E. Viscione, and L. Bombelli, *ARDESIA: 4-Channels Fast SDD X-ray Spectrometer for Synchrotron Applications,* in *2017 IEEE Nuclear Science Symposium and Medical Imaging Conference (NSS/MIC)* (IEEE, 2017) pp. 1–4.

[47] A. Amirkhani, G. Bellotti, A. D. Butt, M. Carminati, D. Ferrari, C. Fiorini, G. Ripamonti, G. Borghi, C. Piemonte, N. Zorzi, M. Bazzi, M. Iliescu, and M. Miliucci, *Characterization and Analysis of Cross-Talk on Monolithic SDD Arrays for the SIDDHARTA Experiment,* in *2017 IEEE Nuclear Science Symposium and Medical Imaging Conference (NSS/MIC)* (IEEE, 2017) pp. 1–3.

[48] M. Feroci, E. Bozzo, S. Brandt, M. Hernanz, M. van der Klis, L.-P. Liu, P. Orleanski, M. Pohl, A. Santangelo, S. Schanne, L. Stella, T. Takahashi, H. Tamura, A. Watts, J. Wilms, S. Zane, S.-N. Zhang, S. Bhattacharyya, I. Agudo, M. Ahangarianabhari, C. Albertus, M. Alford, A. Alpar, D. Altamirano, L. Alvarez, L. Amati, C. Amoros, N. Andersson, A. Antonelli, A. Argan, R. Artigue, B. Artigues, J.-L. Atteia, P. Azzarello, P. Bakala, D. Ballantyne, G. Baldazzi, M. Baldo, S. Balman, M. Barbera, C. van Baren, D. Barret, A. Baykal, M. Begelman, E. Behar, O. Behar, T. Belloni, F. Bernardini, G. Bertuccio, S. Bianchi, A. Bianchini, P. Binko, P. Blay, F. Bocchino, M. Bode, P. Bodin, I. Bombaci, J.-M. Bonnet Bidaud, S. Boutloukos, F. Bouyjou, L. Bradley, J. Braga, M. S. Briggs, E. Brown, M. Buballa, N. Bucciantini, L. Burderi, M. Burgay, M. Bursa, C. Budtz-Jørgensen, E. Cackett, F. Cadoux, P. Cais, G. A. Caliandro, R. Campana, S. Campana, X. Cao, F. Capitanio, J. Casares, P. Casella, A. J. Castro-Tirado, E. Cavazzuti, Y. Cavechi, S. Celestin, P. Cerda-Duran, D. Chakrabarty, N. Chamel, F. Château, C. Chen, Y. Chen, Y. Chen, J. Chenevez, M. Chernyakova, J. Coker, R. Cole, A. Collura, M. Coriat, R. Cornelisse, L. Costamante, A. Cros, W. Cui, A. Cumming, G. Cusumano, B. Czerny, A. D'Aì, F. D'Ammando, V. D'Elia, Z. Dai, E. Del Monte, A. De Luca, D. De Martino, J. P. C. Dercksen, M. De Pasquale, A. De Rosa, M. Del Santo, S. Di Cosimo, N. Degenaar, J. W. den Herder, S. Diebold, T. Di Salvo, Y. Dong, I. Donnarumma, V. Doroshenko, G. Doyle, S. A. Drake, M. Durant, D. Emmanoulopoulos, T. Enoto, M. H. Erkut, P. Esposito, Y. Evangelista, A. Fabian, M. Falanga, Y. Favre, C. Feldman, R. Fender, H. Feng, V. Ferrari, C. Ferrigno, M. Finger, M. H. Finger, G. W. Fraser, M. Frericks, M. Fullekrug, F. Fuschino, M. Gabler, D. K. Galloway, J. L. Gálvez Sanchez, P. Gandhi, Z. Gao, E. Garcia-Berro, B. Gendre, O. Gevin, S. Gezari, A. B. Giles, M. Gilfanov, P. Giommi, G. Giovannini, M. Giroletti, E. Gogus, A. Goldwurm, K. Goluchová, D. Götz, L. Gou, C. Gouiffes, P. Grandi, M. Grassi, J. Greiner, V. Grinberg, P. Groot, M. Gschwender, L. Gualtieri, M. Guedel, C. Guidorzi, L. Guy, D. Haas, P. Haensel, M. Hailey, K. Hamuguchi, F. Hansen, D. H.

Hartmann, C. A. Haswell, K. Hebeler, A. Heger, M. Hempel, W. Hermsen, J. Homan, A. Hornstrup, R. Hudec, J. Huovelin, D. Huppenkothen, S. C. Inam, A. Ingram, J. J. M. In’t Zand, G. Israel, K. Iwasawa, L. Izzo, H. M. Jacobs, F. Jetter, T. Johannsen, P. A. Jenke, P. Jonker, J. Josè, P. Kaaret, K. Kalamkar, E. Kalemci, G. Kanbach, V. Karas, D. Karelin, D. Kataria, L. Keek, T. Kennedy, D. Klochkov, W. Kluzniak, E. Koerding, K. Kokkotas, S. Komossa, S. Korpela, C. Kouveliotou, A. F. Kowalski, I. Kreykenbohm, L. M. Kuiper, D. Kunneriath, A. Kurkela, I. Kuvvetli, F. La Franca, C. Labanti, D. Lai, F. K. Lamb, C. Lachaud, P. P. Laubert, F. Lebrun, X. Li, E. Liang, O. Limousin, D. Lin, M. Linares, D. Linder, G. Lodato, F. Longo, F. Lu, N. Lund, T. J. Maccarone, D. Macera, S. Maestre, S. Mahmoodifar, D. Maier, P. Malcovati, J. Malzac, C. Malone, I. Mandel, V. Mangano, A. Manousakis, M. Marelli, J. Margueron, M. Marisaldi, S. B. Markoff, A. Markowitz, A. Marinucci, A. Martindale, G. Martínez, I. M. McHardy, G. Medina-Tanco, M. Mehdipour, A. Melatos, M. Mendez, S. Mereghetti, S. Migliari, R. Mignani, M. Michalska, T. Mihara, M. C. Miller, J. M. Miller, T. Mineo, G. Miniutti, S. Morsink, C. Motch, S. Motta, M. Mouchet, G. Mouret, J. Mulačová, F. Muleri, T. Muñoz-Darias, I. Negueruela, J. Neilsen, T. Neubert, A. J. Norton, M. Nowak, A. Nucita, P. O’Brien, M. Oertel, P. E. H. Olsen, M. Orienti, M. Orio, M. Orlandini, J. P. Osborne, R. Osten, F. Ozel, L. Pacciani, F. Paerels, S. Paltani, M. Paolillo, I. Papadakis, A. Papitto, Z. Paragi, J. M. Paredes, A. Patruno, B. Paul, F. Pederiva, E. Perinati, A. Pellizzoni, A. V. Penacchioni, U. Peretz, M. A. Perez, M. Perez-Torres, B. M. Peterson, V. Petracek, C. Pittori, J. Pons, J. Portell, A. Possenti, K. Postnov, J. Poutanen, M. Prakash, I. Prandoni, H. Le Provost, D. Psaltis, J. Pye, J. Qu, D. Rambaud, P. Ramon, G. Ramsay, M. Rapisarda, A. Rashevski, I. Rashevskaya, P. S. Ray, N. Rea, S. Reddy, P. Reig, M. Reina Aranda, R. Remillard, C. Reynolds, L. Rezzolla, M. Ribo, R. de la Rie, A. Riggio, A. Rios, D. H. Rischke, P. Rodríguez-Gil, J. Rodriguez, R. Rohlfs, P. Romano, E. M. R. Rossi, A. Rozanska, A. Rousseau, B. Rudak, D. M. Russell, F. Ryde, L. Sabau-Graziati, T. Sakamoto, G. Sala, R. Salvaterra, D. Salvetti, A. Sanna, J. Sandberg, T. Savolainen, S. Scaringi, J. Schaffner-Bielich, H. Schatz, J. Schee, C. Schmid, M. Serino, N. Shakura, S. Shore, J. D. Schnittman, R. Schneider, A. Schwenk, A. D. Schwope, A. Sedrakian, J.-Y. Seyler, A. Shearer, A. Slowikowska, M. Sims, A. Smith, D. M. Smith, P. J. Smith, M. Sobolewska, V. Sochora, P. Soffitta, P. Soleri, L. Song, A. Spencer, A. Stamerra, B. Stappers, R. Staubert, A. W. Steiner, N. Stergioulas, A. L. Stevens, G. Stratta, T. E. Strohmayer, Z. Stuchlik, S. Suchy, V. Suleimanov, F. Tamburini, T. Tauris, F. Tavecchio, C. Tenzer, F. K. Thielemann, A. Tiengo, L. Tolos, F. Tombesi, J. Tomsick, G. Torok, J. M. Torrejon, D. F. Torres, E. Torresi, A. Tramacere, I. Traulsen, A. Trois, R. Turolla, S. Turriziani, S. Typel, P. Uter, P. Uttley, A. Vacchi, P. Varniere, S. Vaughan, S. Vercellone, M. Vietri, F. H. Vincent, V. Vrba, D. Walton, J. Wang, Z. Wang, S. Watanabe, R. Wawrzaszek, N. Webb, N. Weinberg, H. Wende, P. Wheatley, R. Wijers, R. Wijnands, M. Wille, C. A. Wilson-Hodge, B. Winter, S. J. Walk, K. Wood, S. E. Woosley, X. Wu, R. Xu, W. Yu, F. Yuan, W. Yuan, Y. Yuan, G. Zampa, N. Zampa, L. Zampieri, L. Zdunik, A. Zdziarski, A. Zech, B. Zhang,

C. Zhang, S. Zhang, M. Zingale, and F. Zwart, *The LOFT mission concept: a status update,* in *Space Telescopes and Instrumentation 2016: Ultraviolet to Gamma Ray*, Vol. 9905, edited by J.-W. A. den Herder, T. Takahashi, and M. Bautz (2016) p. 99051R.

[49] F. Fuschino, C. Labanti, R. Campana, G. C. Gangemi, M. Marisaldi, L. P. Rignanese, G. Baldazzi, I. Elmi, Y. Evangelista, M. Feroci, G. Zampa, N. Zampa, A. Rashevsky, A. Vacchi, I. Rashevskaya, S. Fabiani, N. Zorzi, C. Piemonte, P. Bellutti, F. Ficorella, G. Borghi, and L. Burderi, *Characterization of a LaBr 3 scintillator with multi-cell Silicon Drift Detector (SDD) readout,* in *Space Telescopes and Instrumentation 2016: Ultraviolet to Gamma Ray*, Vol. 9905, edited by J.-W. A. den Herder, T. Takahashi, and M. Bautz (2016) p. 99056J.

[50] G. Borghi, B. J. Peet, V. Tabacchini, and D. R. Schaart, *A 32 mm × 32 mm × 22 mm monolithic LYSO:Ce detector with dual-sided digital photon counter readout for ultrahigh-performance TOF-PET and TOF-PET/MRI,* Physics in Medicine and Biology **61**, 4929 (2016).

[51] G. Borghi, V. Tabacchini, and D. R. Schaart, *Towards monolithic scintillator based TOF-PET systems: practical methods for detector calibration and operation,* Physics in Medicine and Biology **61**, 4904 (2016).

[52] A. Carimatto, S. Mandai, E. Venialgo, T. Gong, G. Borghi, D. R. Schaart, and E. Charbon, *A 67,392-SPAD PVTB-compensated multi-channel digital SiPM with 432 column-parallel 48ps 17b TDCs for endoscopic time-of-flight PET,* in *Digest of Technical Papers - IEEE International Solid-State Circuits Conference*, Vol. 58 (IEEE, 2015) pp. 202–203.

[53] G. Borghi, V. Tabacchini, S. Seifert, and D. R. Schaart, *Experimental Validation of an Efficient Fan-Beam Calibration Procedure for k-Nearest Neighbor Position Estimation in Monolithic Scintillator Detectors,* IEEE Transactions on Nuclear Science **62**, 57 (2015).

[54] V. Tabacchini, G. Borghi, and D. R. Schaart, *Time-based position estimation in monolithic scintillator detectors,* Physics in Medicine and Biology **60**, 5513 (2015).

[55] U. Amaldi, G. Borghi, M. Bucciantonio, R. Kieffer, J. Samarati, F. Sauli, and D. Watts, *Development of TOF-PET detectors based on the Multi-Gap Resistive Plate Chambers,* Nuclear Instruments and Methods in Physics Research, Section A: Accelerators, Spectrometers, Detectors and Associated Equipment **778**, 85 (2015).

[56] M. Georgiou, G. Borghi, S. V. Spirou, G. Loudos, and D. R. Schaart, *First performance tests of a digital photon counter (DPC) array coupled to a CsI(Tl) crystal matrix for potential use in SPECT,* Physics in Medicine and Biology **59**, 2415 (2014).

[57] V. Tabacchini, V. Westerwoudt, G. Borghi, S. Seifert, and D. R. Schaart, *Probabilities of triggering and validation in a digital silicon photomultiplier,* Journal of Instrumentation **9**, P06016 (2014).

[58] H. T. van Dam, G. Borghi, S. Seifert, and D. R. Schaart, *Sub-200 ps CRT in monolithic scintillator PET detectors using digital SiPM arrays and maximum likelihood interaction time estimation,* Physics in Medicine and Biology **58**, 3243 (2013).

[59] D. Watts, G. Borghi, F. Sauli, and U. Amaldi, *The use of multi-gap resistive plate chambers for in-beam PET in proton and carbon ion therapy,* Journal of Radiation Research **54**, i136 (2013).